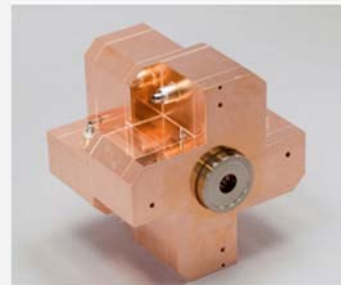# CERN ADVANCED ACCELERATOR SCHOOL
September 2017
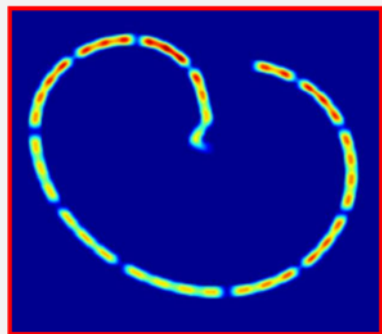

Support
Booklet for the
Beam Instrumentation Course

- ## Beam Position Measurement
- ## Tune Measurement
- ## Profile and Emittance Measurement
- ## Beam Loss Monitoring
- ## Bunch Length Measurement

Marek Gasior, Thibaut Lefevre, Rhodri Jones, Hermann Schmickler (CERN)
Kay Wittenburg (DESY)

Royal Holloway University of London
(3-15 September 2017)

Index

Chapter 1

Beam Position Measurement

1.1   Introduction

Introduction to Beam Position Measurement Systems
Extracted from the CAS proceedings, Trondheim, Norway 2013

Introduction to Beam Position Measurement Systems

(Extracted from the Advanced CAS Proceedings, Trondheim, Norway, 2013 [1])

M. Gasior, R. Jones, T. Lefevre, H. Schmickler
CERN, Geneva, Switzerland

K. Wittenburg
DESY, Hamburg, Germany

1   Beam Position Measurement

The Beam Position Monitor (BPM) can be found in every accelerator. Its role is to provide information on the position of the beam in the vacuum chamber at the monitor location. For linacs and transfer lines the BPMs are used to measure and correct beam trajectories, while for synchrotrons such monitors are distributed around the ring and used to calculate the closed orbit. In circular machines, their location is usually chosen close to the main quadrupole magnets where the β-functions are largest and so any orbit distortion a maximum. For 90° lattices a typical layout involves placing horizontal monitors near the focusing quadrupoles (where the horizontal β-function is large) and the vertical monitors near the defocusing quadrupoles (where the vertical β-function is large). Apart from closed orbit measurements, the BPMs are also used for trajectory measurements (the first turn trajectory is particularly important for closing the orbit on itself) and for accelerator physics experiments, where turn-by-turn data, and even bunch-to-bunch data is often required.

In the early days a BPM monitoring system simply consisted of an oscilloscope linked directly to the pick-up signals. Since then, enormous advances in the acquisition and processing electronics have been made, turning beam position monitors into very complex systems. Modern BPMs are capable of digitising individual bunches separated by a few nanoseconds, with a spatial resolution of a micrometre or less, while the resulting orbit or trajectory collected from several hundred pick-ups can be displayed in a fraction of a second.

1.1   Pick-ups

The measurement of beam position relies on processing the information from pick-up electrodes located in the beam pipe. Five pick-up families are commonly employed:

- Electrostatic – including so-called 'button' and 'shoe-box' pick-ups
- Electromagnetic – stripline couplers
- Resonant cavity – especially suited for high frequency linacs
- Resistive
- Magnetic

An excellent in depth analysis of most of these pick-ups is presented in Ref. [2]. Here we will briefly describe the three most commonly used, namely the electrostatic, electromagnetic and cavity pick-up.

1.1.1   *Electrostatic (Capacitive)*

The electrostatic or capacitive pick-up is the most widely used in circular accelerators. It consists of metallic electrodes situated on opposite sides of the vacuum chamber at the location where the beam is to be measured. As the beam passes through, electric charges are induced on the electrodes, with more induced on the side which is closer to the beam than the one furthest from the beam. By measuring the difference in the charge induced, the position can be calculated.

Fig. 1: Cross-section and photo of an LHC button electrode

Let us analyse the properties of button pick-ups (see Fig. 1) since they are the most popular due to their low cost and ease of construction.

The image current associated with the beam will induce a charge on the button which is proportional to the beam intensity and inversely proportional to the position of the beam from the electrode. A schematic representation is given in Fig. 2.

Fig. 2: Schematic of a capacitively coupled electrode

The figure of merit for any electrode is its transfer impedance (the ratio of the pick-up output voltage, V, to the beam current, I_B). For a capacitive pick-up the signal is proportional to the rate of change of beam current at low frequencies, while for high frequencies the capacitance 'integrates' the signal and the transfer impedance tends to its maximum. For the case of a button electrode of area A and capacitance C situated at a distance d from the beam, the maximum transfer impedance (i.e. the value it tends to at high frequency) can be approximated by:

$$Z_{T\infty} = \frac{A}{2\pi d(\beta c)\,C}$$

where β is the relativistic β and c the speed of light.

Impedance transformation can be used to improve the low frequency response at the expense of that at high frequency. Figure 3(a) shows the frequency response of an 8pF button electrode for the matched

2

50Ω impedance case (1:1) and after two different impedance transformations. The time response of the button for different bunch lengths can be seen in Fig. 3(b).

When designing such pick-ups care must be taken to limit the impedance variations when the transmission line used for signal extraction passes from the vacuum to a feedthrough or cable dielectric (such as ceramic, glass or air). Any such mismatch will produce unwanted reflections, often at high frequency, which could perturb the processing electronics. For this reason most processing chains introduce a low-pass filter on the button output. Special care must also be taken to pair the electrodes on opposite sides of the chamber to minimise offsets in the position reading. This pairing can be made less sensitive to capacitance variations if the high frequency cut-off for the processing electronics sits on the linear part of the button response, with the disadvantage that the overall signal amplitude is reduced.

Fig. 3: (a) Frequency response and (b) time response of a button electrode

1.1.2   *Electromagnetic (stripline)*

The electromagnetic pick-up is a transmission line (stripline) which couples to the transverse electromagnetic (TEM) field of the beam. The transmission line is formed between the stripline and the wall of the vacuum chamber and is excited by the beam only at the gaps on either end of the stripline where a longitudinal field occurs. Figure 4 shows the layout of such an electromagnetic stripline electrode.

Consider a bunch travelling from left to right (upstream to downstream). While it is over the upstream port there is a voltage V_r across R_U, causing a voltage wave of that amplitude to be launched to the right. The stripline forms a transmission line with the wall of the vacuum chamber of characteristic impedance Z_0. The voltage wave is therefore accompanied by a right travelling current wave of amplitude $I_r = V_r / Z_0$. This current flows along the bottom surface of the electrode whilst an equal and opposite current flows along the chamber wall. In addition an image current of amplitude ηI_B travels along the top surface of the electrode. The voltage V_r across R_U can therefore be expressed as

$$V_r = (-I_r + \eta I_B)R_U = \eta I_B \frac{R_U Z_0}{R_U + Z_0} \quad \Rightarrow \quad V_r = \tfrac{1}{2}\eta I_B Z_0 \text{ for a matched stripline } (R_U = Z_0)$$

3

When the beam is over the downstream port it produces a voltage $-V_r = -\frac{1}{2}\eta I_B Z_0$ across R_D in the same way as it produced a voltage $+V_r$ across R_U. This launches a left-travelling wave of the same magnitude, but different sign to the right-travelling wave, which propagates along the transmission line formed by the stripline and the chamber wall and will produce an inverted signal upon arrival at the upstream port a time L/c later. The final signal observed at the upstream port will therefore be a bipolar pulse with the maxima separated by $2L/c$ (see Fig. 5(a)).

r = chamber radius
h = stripline gap height
w = stripline width
L = stripline length
$\Delta\phi$ = angle subtended by the electrode
$\eta = \Delta\phi/(2\pi)$ = fraction of azimuth subtended by electrode
I_B = beam current
R_U/R_D = upstream/downstream termination resistance
Z_0 = characteristic impedance of the stripline

Fig. 4: Schematic and photo of an electromagnetic stripline pick-up

When the RF wavelength of the beam is equal to multiples of 2L, the reflection and the signal from next bunch will cancel and there will be no net signal from the stripline. A maximum in the frequency response will be observed when L is a quarter of an RF period, and hence the stripline pick-up length is usually chosen accordingly. The full frequency response of a 60cm long stripline is shown in Fig. 5(b) and has a lobe structure, with the minima located at multiples of $c/(2L)$.

(a)

(b)

Fig. 5: (a) Time response and (b) frequency response of a 60cm long electromagnetic stripline pick-up

For a relativistic beam the voltage due to the beam passing the downstream port is produced at the same time as the right-travelling wave propagating between the stripline and the wall arrives at the

4

downstream port. The two equal and opposite voltages therefore cancel producing no net signal at the downstream port. The electromagnetic stripline pick-up is therefore said to be "directional", i.e. a signal is only observed on the upstream port with respect to the beam direction. These pick-ups are therefore used in all locations where there are two counter rotating beams in the same vacuum chamber. Due to imperfections in the stripline and feedthrough impedance matching, the best directivity one can hope to obtain for a real stripline is generally around 25-30dB (i.e. the voltage signal of one beam with respect to the other is attenuated by a factor between 18-32).

1.1.3   *Resonant Cavity*

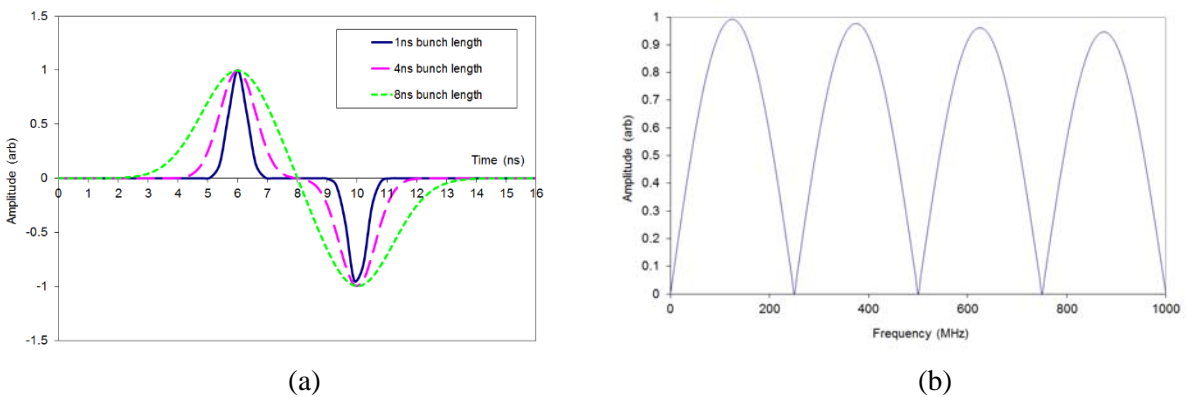Resonant structures, e.g. "pill-box" or rectangular cavities, coaxial resonators and more complex waveguide-loaded resonators, have become very popular to fulfil the high resolution, single-pass beam position monitoring demands of next generation, high energy, linear accelerators [3,4], or for driving a SASE-FEL beam-line [5].
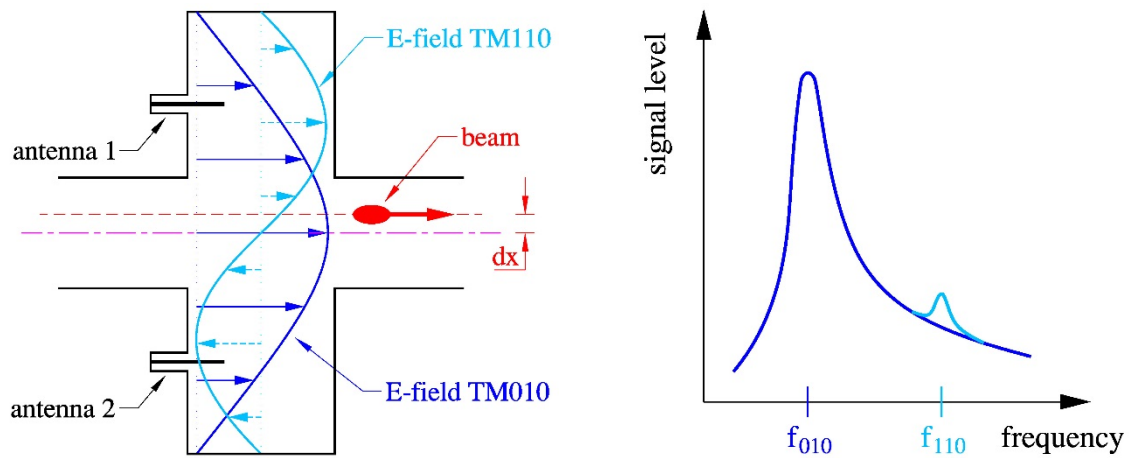
Fig. 6: Principle and frequency response of a cavity BPM

These are constructed to exploit the fact that an off-centre beam excites a dipole mode (TM_{110}) in the cavity, with the amplitude of excitation almost linearly dependent on the off-axis displacement of the beam (Fig. 6). This dipole mode has a slightly different frequency from the main monopole mode (TM_{010}) of the cavity, which allows the processing electronics to select only the frequency of interest (dipole TM_{110}) and so suppress much of the large, unwanted, intensity related signal (monopole TM_{010}).

Fig. 7: Principle and example of a waveguide coupled cavity pick-up (ATF2, KEK, Japan)

5

1.2 Further Reading I:

Overview of Recent Trends and Developments for BPM Systems
M. Wendt, Proceedings of Beam Instrumentation Workshop DIPAC, 2011

OVERVIEW OF RECENT TRENDS AND DEVELOPMENTS FOR BPM SYSTEMS*

M. Wendt[#], Fermilab, Batavia, IL 60510, U.S.A.

Abstract

Beam position monitoring (BPM) systems are the workhorse of beam diagnostics for almost any kind of charged particle accelerator: linear, circular or transport-lines, operating with leptons, hadrons or heavy ions. BPMs are essential for beam commissioning, accelerator fault analysis and trouble shooting, machine optics, as well as lattice measurements, and finally, for accelerator optimization, in order to achieve the ultimate beam quality.

This presentation summarizes the efforts of the beam instrumentation community on recent developments and advances on BPM technologies, i.e. BPM pickup monitors and front-end electronics (analog and digital). Principles, examples, and state-of-the-art status on various BPM techniques, serving hadron and heavy ion machines, sync light synchrotron's, as well as electron linacs for FEL or HEP applications are outlined.

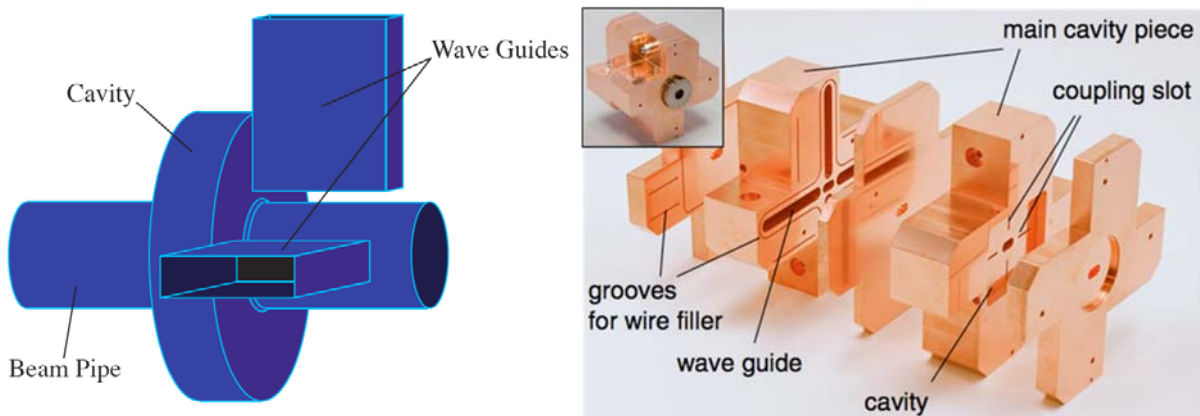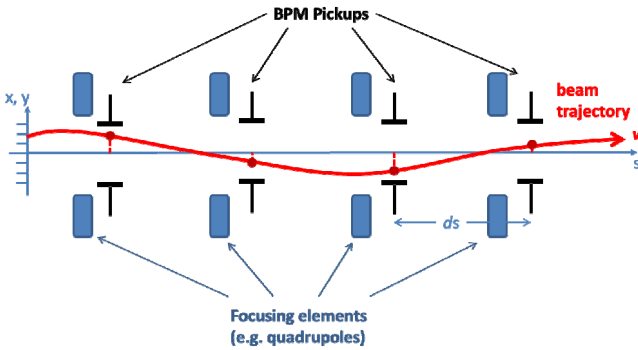# INTRODUCTION

Figure 1: Measurement of the beam trajectory.

The observation of the beam trajectory

$$u(s) = A\sqrt{\beta}\,\sin(Q\varphi + \delta) \qquad (1)$$

with $u = (x, y)$ as the transverse coordinates, A the amplitude of the oscillation, β the beta-function, Q the betatron tune, $\varphi = 0\ldots2\pi$, and δ an initial condition, is one of the most fundamental beam measurements in any particle accelerator. A series of beam position monitors (BPM) are distributed along the beam-line, preferably near the focusing elements (e.g. quadrupole magnets), see Figure 1. The BPMs monitor the transverse beam displacement (x, y) at their locations s_n, knowing the distance ds between two monitors we may also get the slope (x', y') of the beam trajectory – if no optical elements are in-between.
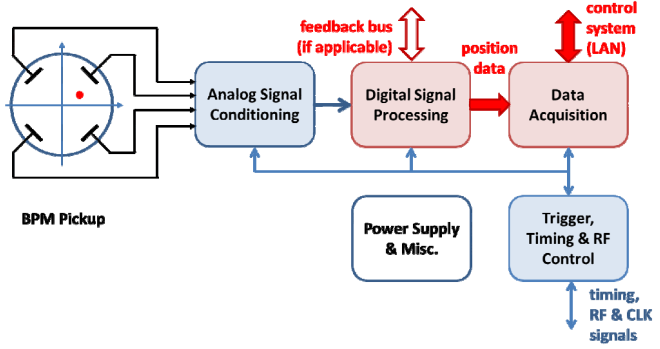
Figure 2: Schematics of a beam position monitor.

Each beam position monitor consists of a BPM pickup, with two or four symmetrically arranged electrodes, followed by a readout electronics system for signal conditioning and processing (Fig. 2). The pickup electrodes sense a part of the electromagnetic field of the passing beam and convert it to an electrical signal. The read-out electronics extract the beam position information out of the electrode signals by conditioning the analog signal, followed by digital signal processing techniques. The position data and other controls of the BPM read-out system are handled by a data acquisition interface, typically a CPU processor, which interfaces to the accelerator control system. The digital signal processing and data acquisition has to be supported by timing and clock signals, which are also used for time stamping, i.e. synchronizing BPM data across the entire system, as well as accelerator event and RF signals (for analog signal conditioning).
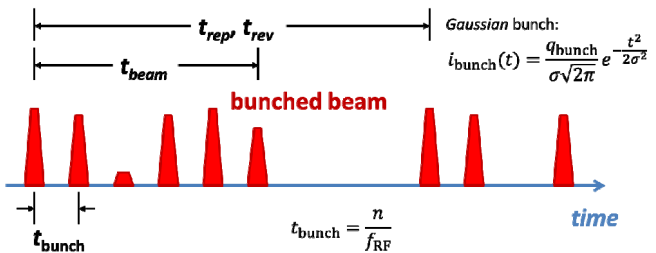
Figure 3: Beam structure.

The particle beam is a bunched stimulus signal for the BPM, with $t_{bunch} = n/f_{RF}$. As Figure 3 indicates, the beam bunches may have different intensities, sometimes even missing bunches. The beam structure spans t_{beam}, and typically repeats with t_{rep} in linacs and transport-lines, and t_{rev} in circular accelerators. Depending on the measurement or integration time of the BPM, we can resolve the beam position of single or all individual bunches, or the average over one or several beam pulses

or turns. Multipurpose accelerators, such as the CERN PS or the Fermilab Main Injector may accelerate different beam structures, apply sophisticated RF gymnastics and even use different particle species, which further complicates the operating conditions for the BPM system [1].

Some important characteristics of a BPM system are:

* *Measurement / integration time,* as described.
* *Position resolution*, i.e. the minimum beam displacement difference the BPM can resolve (typically depends a lot on the integration time).
* *Linearity and accuracy,* i.e. the absolute error of the reported beam position, over a part or the complete range of the beam pipe aperture.
* *x-y coupling*
* *Dynamic range,* in terms of beam intensity. The reported beam position has to be independent of the beam intensity, saturation or noise effects will appear at high / low beam intensities and compromise linearity and position resolution.
* *Reproducibility and long term stability* are important for storage rings and beam lattices which critically rely on references orbits.
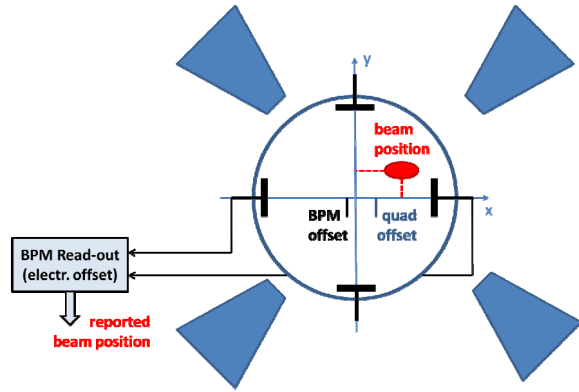
Figure 4: BPM and quadrupole offsets.

The zero-order effect of the linearity correction is the so-called *BPM-offset*. Fig. 4 illustrates the BPM and quadrupole offsets with respect to the vacuum pipe. A beam-based alignment (BBA) procedure can be performed to characterize the BPM-to-quadrupole offset and tilt, including the effects of the electronics [2], [3]. [4].

Digital signal processing allows us to simultaneously output BPM data with different integration times, e.g. multiturn averaged position data, single pass / turn-by-turn, or even single bunch displacement information. This enables besides the beam orbit characterization, a large variety of direct and indirect beam measurements and observations, e.g. injection oscillations, betatron and synchrotron tunes, dispersion and beam energy, x-y coupling, beam optics, magnet alignment and errors, non-linear field effects, etc. [5]. For machine commissioning the processing of the beam intensity signal is of great value, while precise, RF derived clock signals also enable beam phase and time-of-flight measurements with today's BPM systems.

BPM PICKUP

The BPM pickup is an arrangement of electromagnetic antennas or a resonant device, and part of the accelerator vacuum system. In a simplistic view, for relativistic beams ($v \approx c_0$), the output signal of a BPM pickup can be expressed:

$$V_{\text{elec}}(x, y, \omega) = s(x, y) Z(\omega) I_{\text{beam}}(\omega) \quad (2a)$$

$$V_{\Delta}(x, y, \omega) = s(x, y, \omega) Z(\omega) I_{\text{beam}}(\omega) \quad (2b)$$

where V is the output signal for a broadband pickup electrode (2a) or a resonant cavity (2b), $Z(\omega)$ is the frequency dependent transfer function or shunt impedance of the pickup, and $s(x,y,\omega)$ is sensitive to the beam position (x,y), and eventually also frequency dependent. The beam current $I_{\text{beam}}(\omega)$ can often be approximated by a Gaussian function for the bunch signal, with a repetition similar as shown in Fig. 3. Most BPM pickups can be classified as either broadband or resonant. Besides being an RF or microwave device, the BPM pickup has to be UHV certified, and in some superconducting cryogenic installations also must operate at cryogenic temperatures and meet special cleanroom requirements.

Broadband BPM Pickups
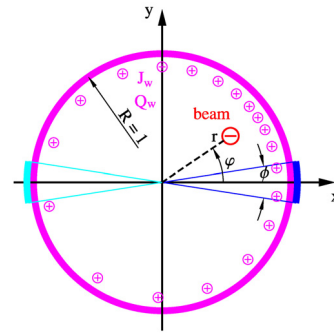
Figure 5: Beam and image currents.

For a broadband BPM pickup the sensitivity *s* in eq. (2a) is independent of ω. Broadband BPMs operate in terms of the image current model (Fig. 5), this *Laplace* problem was solved analytically for a beam pipe with circular or elliptical cross-section [6], [7], [8]:

$$J_{\text{w}}(R = 1, \phi_w) = I_0 \frac{1 - \rho^2}{1 + \rho^2 - 2\rho \cos(\phi_w - \varphi)} \quad (3)$$

Eq. (3) returns the image current density J_{w} at the surface of the beam pipe ($R=1$, ϕ_w) for a beam position at ($\rho=r/R$, φ), where $I_0=I_{\text{beam}}/2\pi$. Integrating ϕ_w over the range of the BPM electrode ϕ gives the electrode current I_{elec}, for which the geometric part is (note: cylindrical coordinates)

$$s(\rho, \varphi) = \phi + 4 \sum_{n=1}^{\infty} \frac{\rho^n}{n} \cos(n\varphi) \sin\left(\frac{n\phi}{2}\right) \quad (4)$$

Two symmetric arranged electrodes A, B (e.g. horizontal, as in Fig. 5) can now perform as BPM:

$$\text{beam pos.} = f\left(\frac{A - B}{A + B}\right) \text{ or } = f\left(20 \log_{10}\left(\frac{A}{B}\right)\right) \quad (5)$$

With typical pickup dimensions, e.g. R=25 mm, ϕ=30^0, the sensitivity computes to 2.75 dB/mm around the beam pipe center. As eq. (2a) indicates, all broadband BPMs, suffer from a strong I_{beam} common mode term in the output signal, with a small amplitude modulation component due to the beam position *(x,y)*. The position sensitivity is basically fixed by the geometry and the related image current distribution, eq. (3), (4), (5).

Most prominent and widely applied member of the broadband BPM family is the electrostatic (capacitive) coupling so-called "button BPM" (different commercial button BPM feedthroughs are available). Also the stripline BPM (electromagnetic coupling) is popular, the length of the striplines, allows to match Z(ω) to the bunch spectrum $I_{bunch}(\omega)$. Circular split-plane ("shoe-box") BPMs have an almost linear position dependence, which also can be achieved with large capacitive electrodes, spanning $\phi \approx 60^0$. [9] uses BPMs with magnetic coupling loop antennas for beam position monitoring near the dump, and [10] gives further theoretical background on magnetic BPMs, also for detection of the beam angle. [11] developed a inductive BPM with single pass capability and sub-micrometer resolution.

While all broadband BPMs basically follow with their position characteristics the image current model, they differ in their frequency behavior Z(ω), which is discussed extensively [12], [13], [14]. The numerical solution of the Laplace equation allows a more precise approach to evaluate *s(x,y)*, also for non-circular cross-sections of the beam pipe. The results can be fitted with 2-D polynomials or look-up tables, allowing a linearization in the post-processing of the BPM data.

The effect of non-relativistic beams to the sensitivity of different BPM electrode shapes has been studied in great detail with help of numerical methods [15].
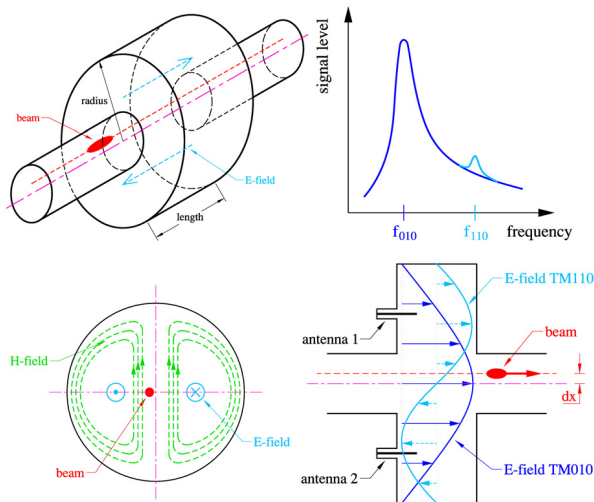
Resonant BPM Pickups

Figure 6: "Pillbox" cavity as BPM.

A cylindrical "pillbox" with conductive walls of length ℓ and radius R resonates at its eigenfrequencies

$$f_{mnp} = \frac{1}{2\pi\sqrt{\mu_0\varepsilon_0}}\sqrt{\left(\frac{j_{mn}}{R}\right)^2 + \left(\frac{p\pi}{\ell}\right)^2} \quad (6)$$

This resonator can be utilized as passive, beam driven cavity BPM by providing beam pipe ports (Fig. 6). A subset of the eigenmodes eq. (6) is excited by the bunched beam, for the application as BPM the lowest transverse-magnetic dipole mode TM$_{110}$ is of interest. Its

$$E_z = C\, J_1\left(\frac{j_{11}r}{R}\right)e^{i\omega t}\cos\varphi \quad (7)$$

field component couples to the beam with an almost linear dependence to the beam displacement *r*, and vanishes when the beam is in the center (*r* = 0). Four symmetrically arranged pin antenna feedthroughs fix the polarization of TM$_{110}$ to the horizontal and vertical axis, and provide the unnormalized difference signal Δ = $f(x,y,I_{beam})$, the beam intensity is hidden in the constant *C*.

Resonant structures, e.g. "pill-box" or rectangular cavities, also coaxial resonators, and more complex waveguide-loaded resonators, became very popular to fulfil the high resolution, single-pass beam position monitoring demands of linear accelerators for the high luminosity final focus lattice [16], [17], or driving a SASE-FEL beam-line [18]. In [19] the operation of a simple cavity BPM inside a cryostat is presented. The discussion on the theoretical background was recently updated [20]. The x-y decoupling of the TM$_{110}$ polarization is addressed in [21]. The high resolution potential of a BPM system with C-Band choke-mode resonators was demonstrated the first time at the SLAC final focus test beam, achieving 25 nm single-bunch, single-pass position resolution [22].
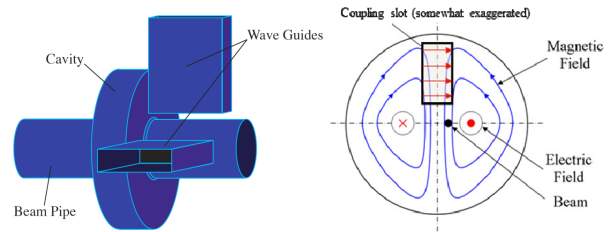
Figure 7: Waveguide-loaded cavity BPM.

The presence of the fundamental TM$_{010}$ monopole mode adds a strong common mode component to the dipole-mode position signal, and even having a different frequency f_{010}, it limits the performance of the cavity BPM. A waveguide of width *a*, with a cut-off frequency

$$f_{010} \quad < \quad f_{10} = \frac{1}{2a\sqrt{\mu\varepsilon}} \quad < \quad f_{110} \quad (8)$$

acts as very efficient, internal high-pass filter, and makes the cavity BPM quasi "common-mode free" (Fig. 7). The coupling slot between resonator and waveguide also helps to align the TM$_{110}$ polarization planes, and minimizes the x-y coupling. However, the finite Q-value of the resonances still causes an unwanted leakage of the

monopole-mode at the frequency f_{110} of the dipole mode, thus limiting the resolution.

The first test of a system of three waveguide-loaded 14 GHz cavity BPMs was performed at BNL, demonstrating 150 nm beam position resolution [23]. Separate waveguide-loaded rectangular resonators (Fig. 8), operating at different C-Band frequencies achieved 8.7 nm resolution at the ATF2 final focus test beam-line [24].
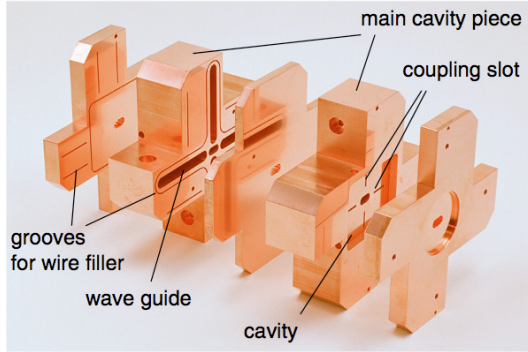
Figure 8: The ATF2 IP-BPM.

A magnetic waveguide-to-coaxial port coupling was introduced for the C-Band cavity BPMs at SPring-8 [25], a similar construction is tested for the XFEL [26]. The monopole-mode (TM_{010}) reference resonator, required to deliver beam intensity and phase reference signals to the read-out electronics, is also used as beam arrival time monitor, showing a 25 fsec temporal resolution performance. A low-Q, mass-producible X-Band cavity BPM for the CLIC main linac is under development, targeting <50 nm spatial resolution at <50 nsec integration time. Details on the effects of tolerances are discussed, as well as performance limitations due to mode leaking, and a comparison between single vs. multi-bunch beam stimulus [27].

Beam position monitoring based on TEM coaxial resonators, the so-called re-entrant cavity BPM, has also been studied, and is proposed to operate inside the cryomodule at the European XFEL project [28]. A waveguide-loaded version demonstrated sub-micron resolution, when tested under single-bunch, single-pass beam conditions [29].

Beam excited dipole mode signals from the HOM-couplers of standing wave accelerating structures have been studied at the FLASH FEL facility. An online SVD algorithm was used to orthogonalize the signals, thus make HOM signals usable as beam position monitor [30].

READ-OUT ELECTRONICS

The read-out system interfaces the BPM pickup to the accelerator data acquisition (control) system (Fig. 2). Signal conditioning, normalization and linearization of the position signals / data have to be provided for the time stamped beam position data. To achieve long term stability, calibration signals for gain-correction, or other correction methods are added to the system. The BPM data may also serve in beam orbit feedback systems, thus

a low latency of the signal processing is of important value.
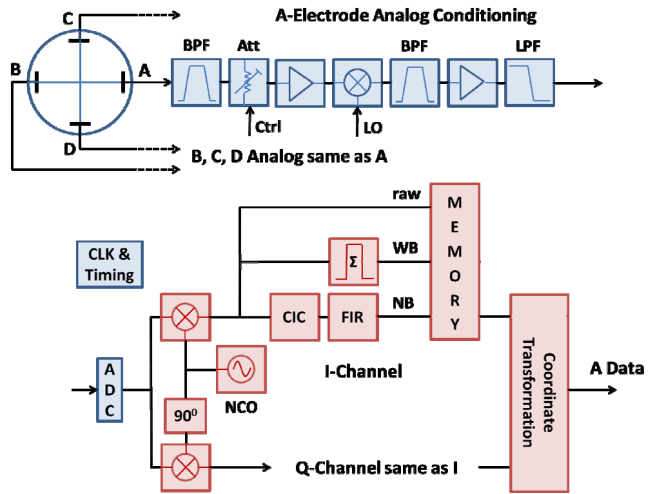
Figure 9: Key elements of the BPM read-out electronics.

An overview of "traditional" BPM read-out techniques was summarized in [31]. Today the BPM read-out electronics is typically based on frequency domain signal processing techniques, which were developed for the telecommunications market [32]. Bandpass filters in the analog section prepare the BPM pickup signals into sinewave-like burst signals, for waveform singal sampling and processing in the digital section. Microwave and RF analog components, 12-16 bit pipeline ADCs, FPGAs and clock distribution chips with sub-psec jitter are some of the key hardware elements. Figure 9 illustrates a typical electronics arrangement for a broad-band BPM pickup, 1-of-4 channels is shown. In some cases the analog down-mixer can be omitted, for cavity BPMs the schematics is similar, here the analog mixer is still required. The digital signal processing takes place in a FPGA, the I-Q down-conversion to baseband is required if the ADC clock is not locked to the accelerator RF.

As Figure 9 indicates, the measurement of the pickup electrodes signals (A, B, C, and D) is performed separately, normalization and linearization takes place in the FPGA or CPU. Drifts and aging effects have to be compensated by a calibration tone signal [33], or a channel switching scheme [34]. The effect of ADC clock jitter is discussed in various application notes [35], this becomes particulary critical in systems with heavy undersampling ($f_{signal} \gg f_{CLK}$). The digital data stream can be filtered and decimated in various ways, Fig. 8 indicates how narrow-band, wide-band and raw signals can be handled simultaneously. We usually down-convert f_{signal}-f_{NCO} not exactly to DC, but to a low frequency with an integer number of oscillations over the measurement period, this avoids a crawling phase.

ACKNOWLEGEMENTS

REFERENCES

[1] B. Banerjee, et.al., "Fermilab Main Injector Beam Position Monitor Upgrade," BIW'06, Batavia, IL, USA, May 2006, AIP Conf. Proc. **868** (2006), pp. 540-548.

[2] R. Brinkmann and M. Boege, "Beam-Based Alignment and Polarization Optimization in the HERA Electron Ring," EPAC'94, London, UK, June/July 1994, pp. 938-940.

[3] C. E. Adolphsen, et.al., "Beam-Based Alignment Technique for the SLC Linac," PAC'89, Chicago, IL, USA, March 1989, Proc. of IEEE (1998), SLAC-PUB-4902

[4] M. Boege, et.al., "The Swiss Light Source A "Test-Bed" for Damping Ring Optimization," IPAC'10, Kyoto, Japan, May 2010, WEPE091, pp. 3560-62 (2010).

[5] A. Hofmann, "Beam Diagnostics and Applications," BIW'98, Stanford, CA, USA, May 1998, AIP Conf. Proc. **451** (1998), pp. 3-22.

[6] J. Cuperus, "Monitoring of Particle Beams at High Frequencies," CERN, Geneva, Switzerland, November 1976, CERN/PS/LIN 76-7.

[7] K. Satoh, "New Beam Position Monitor by detecting Wall Currents," Rev. Sci. Instr. **4** (1979), p. 450.

[8] R. C. Shafer, "Characteristics of Directional Coupler Beam Position Monitors," PAC'85, Vancouver, BC, Canada, May 1985, IEEE Trans. Nucl. Sci. **32** (1985), pp. 1933-37.

[9] N. Baboi, et.al., "Magnetic Coupled Beam Position Monitor for the FLASH Dump Line," BIW'10, Santa Fe, NM, USA, May 2010, TUPSM039, pp. 214-217 (2010).

[10] X. He, et.al., "Direct Measurement of the Beam Deflection Angle using the axial B-dot Field," APS Phys. Rev. 2011, to be published

[11] I. Podadera, et.al., "Precision Beam Position Monitor for EUROTeV," DIPAC'07, Venice, Italy, May 2007, TUPB03, pp. 57-59 (2007).

[12] R. C. Shafer, "Beam Position Monitoring," BIW'89, Uptown, NY, USA, October 1989, AIP Conf. Proc. **212** (1989), pp. 26-58.

[13] D. P. McGinnis, "The Design of Beam Pickup and Kickers," BIW'94, Vancouver, BC, Canada, October 1994, AIP Conf. Proc. **333** (1994), pp. 64-85.

[14] F. Marcellini, et.al., "DAΦNE Broad-Band Button Electrodes," INFN-LNF Frascati, January 16, 1996, Note: **CD-6**.

[15] P. Kowina, et.al., "FEM Simulations – A Powerful Tool for BPM Design," DIPAC'09, Basel, Switzerland, May 2009, MOOC03, pp. 35-37 (2009).

[16] S. Walson, et.al., "Performance of a High Resolution Cavity Beam Position Monitor System," NIM-A, **578** (2007), pp. 1-22.

[17] S. T. Boogert, et.al., "Cavity Beam Position Monitor System for ATF2," IPAC'10, Kyoto, Japan, May 2010, MOPE070, pp. 1140-42 (2010).

[18] S. Smith, et.al., "LCLS Cavity Beam Position Monitors," DIPAC'09, Basel, Switzerland, May 2009, TUOC03, pp. 285-287 (2009).

[19] R. Lorenz, "Cavity Beam Position Monitors," BIW'98, Stanford, CA, USA, May 1998, AIP Conf. Proc. **451** (1998), pp. 53-73.

[20] D. Lipka, et.al., "Cavity BPM Designs, Related Electronics and Measured Performances," DIPAC'09, Basel, Switzerland, May 2009, MOPD07, pp. 280-284 (2009).

[21] V. Sargsyan, "Cavity Beam Position Monitor for the TESLA Cryomodule – Cross-Talk Minimization," Ph. D. thesis, Technical University Berlin, Germany (2003).

[22] T. Slaton, et.al., "Development of Nanometer Resolution C-Band Radio Frequency Beam Position Monitors in the Final Focus Test Beam," SLAC-PUB-7921, August 1998

[23] V. Balakin, et.al., "Experimental Results form a Microwave Cavity Beam Position Monitor," PAC'99, New York, NY, USA, March/April 1999, IEEE Proc. (1999), pp. 461-464.

[24] T. Nakamura, et.al., "High Resolution Cavity BPM for ILC Final Focus System (IP-BPM)," LCWS/ILC 2007, Hamburg, Germany, May/June 2007, arXiv:0709.2254v1, eConf C0705302.

[25] H. Maesaka, et.al., "Development of the RF Cavity BPM of XFEL/Spring-8," DIPAC'09, Basel, Switzerland, May 2009, MOPD07, pp. 56-58 (2009).

[26] D. Lipka, et.al., "Orthogonal Coupling in Cavity BPM with Slots," DIPAC'09, Basel, Switzerland, May 2009, MOPD07, pp. 44-46 (2009).

[27] H. Schmickler, et.al., "Submicron Mulit-Bunch BPM for CLIC," IPAC'10, Kyoto, Japan, May 2010, MOPE087, pp. 1185-87 (2010).

[28] C. Simon, et.al., "Status of the Re-entrant Cavity Beam Position Monitor for the European XFEL Project," BIW'10, Santa Fe, NM, USA, May 2010, TUPSM038, pp. 210-213 (2010).

[29] J. Y. Ryu, et.al., "Development of a Re-entrant Cavity L-Band Beam Position Monitor for ILC," to be published.

[30] S. Molloy, et.al., "High Precision Superconducting Cavity Diangostics with Higher Order Mode Measurements," Phys. Rev. ST Accel. Beams **9**, 112802 (2006).

[31] G. Vismara, "Signal Processing for Beam Position Monitors," BIW'00, Cambridge, MA, USA, May 2000, AIP Conf. Proc. **546** (2000), pp. 36-60.

[32] V. Schlott, et.al., "First Operational Experience with the Digital Beam Position Monitoring System for the Swiss Light Source," EPAC'00, Vienna, Austria, June 2000, pp. 1809-11.

[33] M. Wendt, et.al., "High Resolution BPMs with Integrated Gain Correction System," DIPAC'09, Basel, Switzerland, May 2009, MOPD19, pp. 89-91 (2009).

[34] Instrumentation Technologies, http://www.i-tech.si

[35] Analog Devices, AN-282, AN-501.

1.3   Further Reading II:

Pickups
P. Forck, JUAS Lecture Notes on Beam Instrumentation and Diagnostics

JUAS

Joint Universities Accelerator School

Lecture Notes on
Beam Instrumentation and Diagnostics

Peter Forck

Gesellschaft für Schwerionenforschung (GSI)
Darmstadt, Germany

e-mail: p.forck@gsi.de

Joint University Accelerator School

January – March 2011
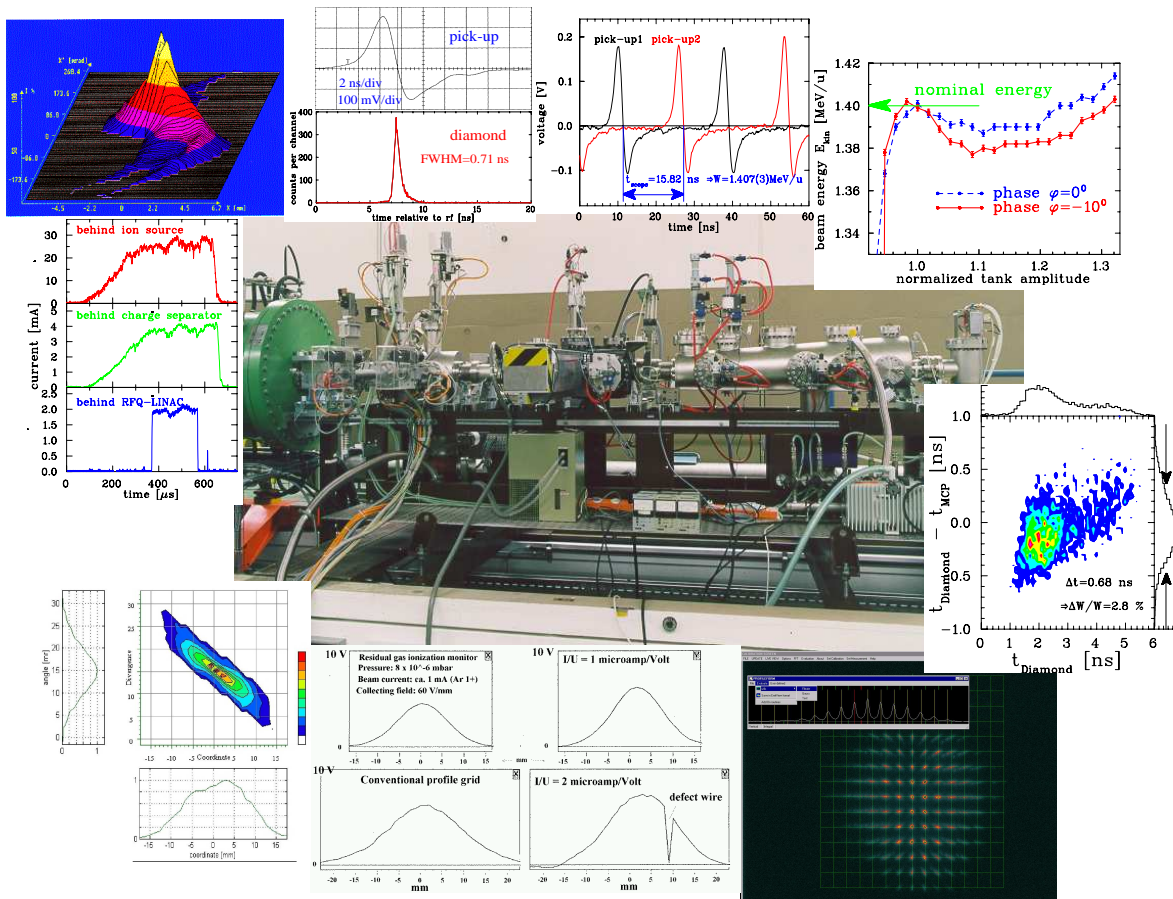
A picture of the mobile test bench including some measurements, as provided for the commissioning of the high current injector at GSI in 1999.

Chapter 5

Pick-ups for bunched beams

The longitudinal bunch shape as well as the position of a beam is usually determined with pick-up plates. The idea is to measure on an insulated metal plate the charges induced by the electric field of the beam particles, see Fig. 5.1. Because the electric field of a bunched beam is time dependent, an ac signal is seen on the plate and the coupling is done using rf technologies. The principle signal shape, as well as the most often used types of pick-ups are described. The application is the determination of the beam position (center-of-mass). To this end, four pick-up plates are installed and the difference of the signals yields the center-of-mass in both transverse axes. This installation is called a **B**eam **P**osition **M**onitor **BPM**. In a synchrotron, the closed orbit is determined by the BPMs. Measurements based on this position information are discussed, namely the determination of the tune and the lattice functions of a synchrotron.
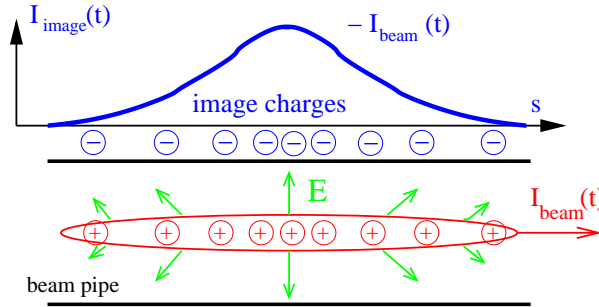
Figure 5.1: The beam current induces a wall current of the same magnitude but reversed polarity.

5.1 Signal treatment of capacitive pick-ups

As shown in Fig. 5.2, a capacitive pick-up consists of a plate or a ring inserted in the beam pipe. Here the induced image charge of the beam is coupled via an amplifier for further processing. The plate at a distance a from the beam center has an area of A and a length in longitudinal direction of l. The current I_{im} driven by the image charge Q_{im} is

$$I_{im}(t) \equiv \frac{dQ_{im}}{dt} = -\frac{A}{2\pi a l} \cdot \frac{dQ_{beam}(t)}{dt}.$$ (5.1)

Having a beam with velocity β we can write for the derivative of the beam charge $dQ_{beam}(t)/dt$

$$\frac{dQ_{beam}(t)}{dt} = \frac{l}{\beta c}\frac{dI_{beam}}{dt} = -\frac{l}{\beta c} \cdot i\omega I_{beam}(\omega)$$ (5.2)

78
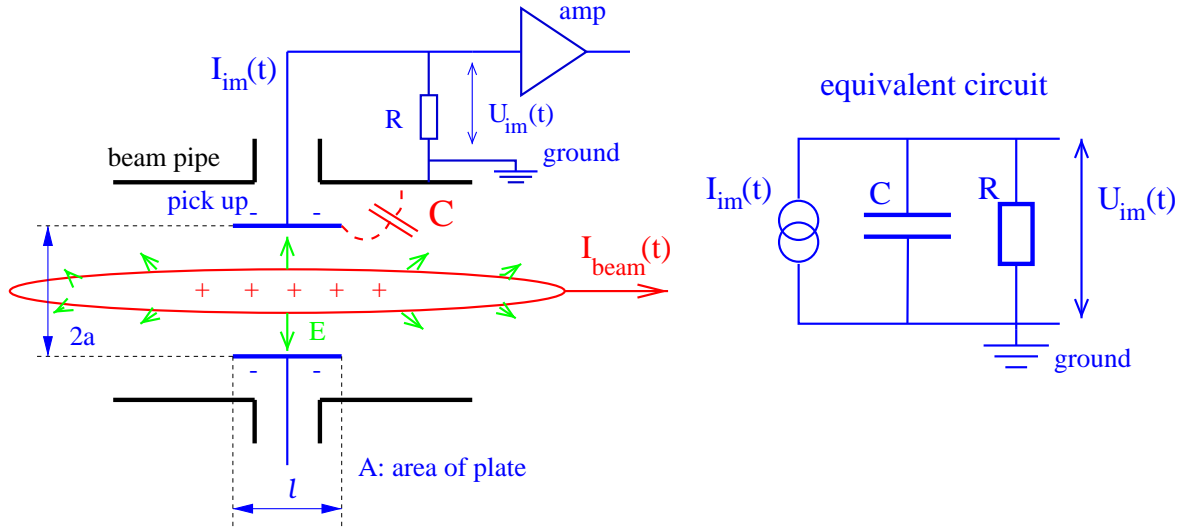
Figure 5.2: Scheme of a pick-up electrode and it's equivalent circuit.

where the beam current is expressed in frequency domain as $I_{beam} = I_0 e^{-i\omega t}$ [1]. As the signal we use the voltage drop at a resistor R

$$U_{im}(\omega) = R \cdot I_{im}(\omega) = Z_t(\omega, \beta) \cdot I_{beam}(\omega) \tag{5.3}$$

For all types of pick-up plates, the general quantity of longitudinal transfer impedance $Z_t(\omega, \beta)$ is defined in the frequency domain according to Ohm's law. For more detailed discussion see [72, 73, 74].It describes the effect of the beam on the pick-up voltage and it is dependent on frequency, on the velocity of the beam particles β and on geometrical factors. It is very helpful to make the description in the frequency domain, where the independent variable is the angular frequency ω, related to the time domain by Fourier transformation [2].

The capacitive pick-up of Fig. 5.2 has a certain capacitance C, which is determined by the distance of the plate with respect to the beam pipe and a capacitance contributed by the cable between the plate and the amplifier input. This amplifier has a input resistor R. Using a current source to model the beam and the parallel connection of the equivalent circuit we can write its impedance Z as

$$\frac{1}{Z} = \frac{1}{R} + i\omega C \quad \Longleftrightarrow \quad Z = \frac{R}{1 + i\omega RC} \tag{5.6}$$

Therefore the transfer function of the pick-up is

$$U_{im} = \frac{R}{1 + i\omega RC} \cdot I_{im} = \frac{1}{\beta c} \cdot \frac{1}{C} \cdot \frac{A}{2\pi a} \cdot \frac{i\omega RC}{1 + i\omega RC} \cdot I_{beam} \equiv Z_t(\omega, \beta) \cdot I_{beam}. \tag{5.7}$$

---

[1]More precisely: The derivative of a function df/dt can be expressed as a multiplication of its Fourier transformation $\tilde{f}(\omega)$ with $-i\omega$.

[2]The frequency domain function $\tilde{f}(\omega)$ is calculated from the time domain function $f(t)$ by Fourier transformation as

$$\tilde{f}(\omega) = \frac{1}{\sqrt{2\pi}} \int\limits_{-\infty}^{\infty} f(t) e^{-i\omega t} dt \quad . \tag{5.4}$$

By inverse transformation the time domain function can be recovered as

$$f(t) = \frac{1}{\sqrt{2\pi}} \int\limits_{-\infty}^{\infty} \tilde{f}(\omega) e^{i\omega t} d\omega \tag{5.5}$$

if the given integral for $\tilde{f}(\omega)$ exists. Normally the absolute value $|\tilde{f}(\omega)|$ and the phase $\tan\varphi = Re(\tilde{f})/Im(\tilde{f})$ of this complex (in mathematical sense) function is displayed.
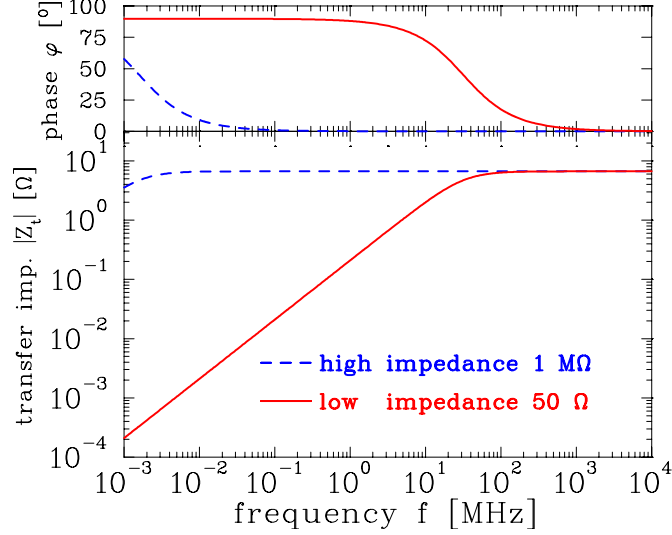
Figure 5.3: Absolute value and phase of the transfer impedance for a $l = 10$ cm long cylindrical pick-up with a capacitance of $C = 100$ pF and an ion velocity of $\beta = 50\%$ for high (1 MΩ) and low (50 Ω) input impedance of the amplifier. The parameters are typical for a proton/heavy ion synchrotron. The high-pass characteristic is clearly seen corresponding to a signal decreasing for low frequencies.
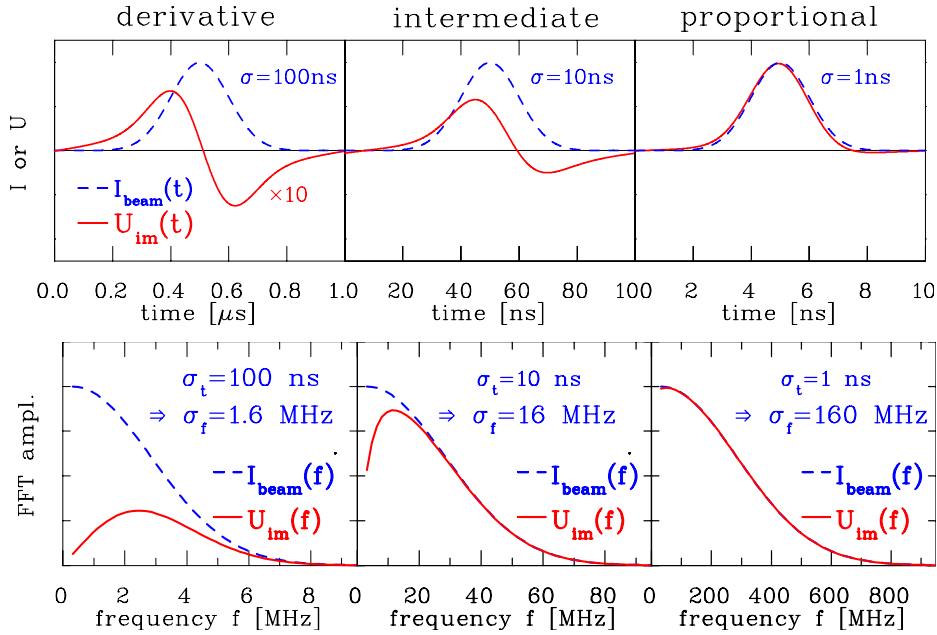
Figure 5.4: Simulation of the image voltage $U_{im}(t)$ for the values of the pick-up used in Fig. 5.3 terminated with $R = 50$ Ω for three different bunch lengths of Gaussian distribution with σ of 100 ns, 10 ns and 1 ns, respectively. The cut-off frequency f_{cut} is 32 MHz. Note the different time scales. (The bunch length in the last case is artificially short for a proton synchrotron.) The shape of U_{im} is generated by the following steps: Given $I_{beam}(t) \rightarrow$ FFT yields $\tilde{I}_{beam}(\omega)$ $\rightarrow$ multiplying by $Z_t(\omega)$ yields $\tilde{U}_{im}(\omega) = Z_t(\omega) \cdot \tilde{I}_{beam}(\omega) \rightarrow$ inverse FFT yields $U_{im}(t)$. The Fourier transformations are shown in the lower plots. Note, that a Gaussian function in time domain of width of σ_t has a Fourier transformation described by a Gaussian function of width $\sigma_f = 1/(2\pi\sigma_t)$ centered at $f = 0$.

80

This is a description of a first-order high-pass filter with a cut-off frequency $f_{cut} = \omega_{cut}/2\pi = (2\pi RC)^{-1}$. For the case of the so called linear cut pick-ups used at proton synchrotrons (see below), a typical value of the capacitance is $C = 100$ pF with a length of $l = 10$ cm. The high-pass characteristic is shown in Fig. 5.3 for a 50 Ω and a high impedance 1 MΩ amplifier input resistor. In the figure the absolute value

$$|Z_t| = \frac{1}{\beta c} \cdot \frac{1}{C} \cdot \frac{A}{2\pi a} \cdot \frac{\omega/\omega_{cut}}{\sqrt{1 + \omega^2/\omega_{cut}^2}} \quad \text{and the phase relation} \quad \varphi = \arctan\left(\omega_{cut}/\omega\right) \quad (5.8)$$

is shown. A pick-up has to match the interesting frequency range, which is given by the accelerating frequency and the bunch length. In a proton synchrotron typical values of the accelerating frequency are in the range from 1-10 MHz, while for LINACs and electron synchrotrons typically 100 MHz to 3 GHz are used. We can distinguish two different cases for the transfer impedance, namely:

- **high frequency range** $\omega \gg \omega_{cut}$: Here we have

$$Z_t \propto \frac{i\omega/\omega_{cut}}{1 + i\omega/\omega_{cut}} \longrightarrow 1. \quad (5.9)$$

  The resulting voltage drop at R is for this case

$$U_{im}(t) = \frac{1}{\beta c C} \cdot \frac{A}{2\pi a} \cdot I_{beam}(t). \quad (5.10)$$

  Therefore the pick-up signal is a direct image of the bunch time structure with no phase shift, i.e. $\varphi = 0$. To get a low cut-off frequency $\omega_{cut} = 1/RC$, high impedance input resistors are used to monitor long bunches, e.g. in the proton synchrotron. The calculated signal shape is shown in Fig. 5.4 (right). Note that in the figure a 50 Ω termination is considered, leading to a large value of the cut-off frequency $f_{cut} = 32$ MHz. In the application of a proton synchrotron, high impedance (~ 1 MΩ) termination yielding a much lower value of the cut-off frequency, $f_{cut} = 10$ kHz in this case. A typical signal from this circuit is given in Fig. 5.5.

- **low frequency range** $\omega \ll \omega_{cut}$: The transfer impedance is here

$$Z_t \propto \frac{i\omega/\omega_{cut}}{1 + i\omega/\omega_{cut}} \longrightarrow i\frac{\omega}{\omega_{cut}}. \quad (5.11)$$

  Therefore the voltage across R is in this case

$$U_{im}(t) = \frac{R}{\beta c} \cdot \frac{A}{2\pi a} \cdot i\omega I_{beam} = \frac{R}{\beta c} \cdot \frac{A}{2\pi a} \cdot \frac{dI_{beam}}{dt} \quad (5.12)$$

  using again the frequency domain relation $I_{beam} = I_0 e^{-i\omega t}$. We see that the measured voltage is proportional to the derivative of the beam current. This can also be seen from the phase relation of the high-pass filter in Fig. 5.3, where a phase shift of 90° corresponds to a derivative. The signal is bipolar, as shown in Fig. 5.4 (left). A measurement from the GSI-LINAC is shown in Fig. 5.6.

The signal at the amplifier output depends on the frequency range as compared to the cut-off frequency. Of course the bunches are not pure sine waves, and therefore it might be that a mixture of proportional and derivative components are present, see Fig. 5.4 (middle).

With respect to the different limits of the transfer impedance, two important applications are discussed:
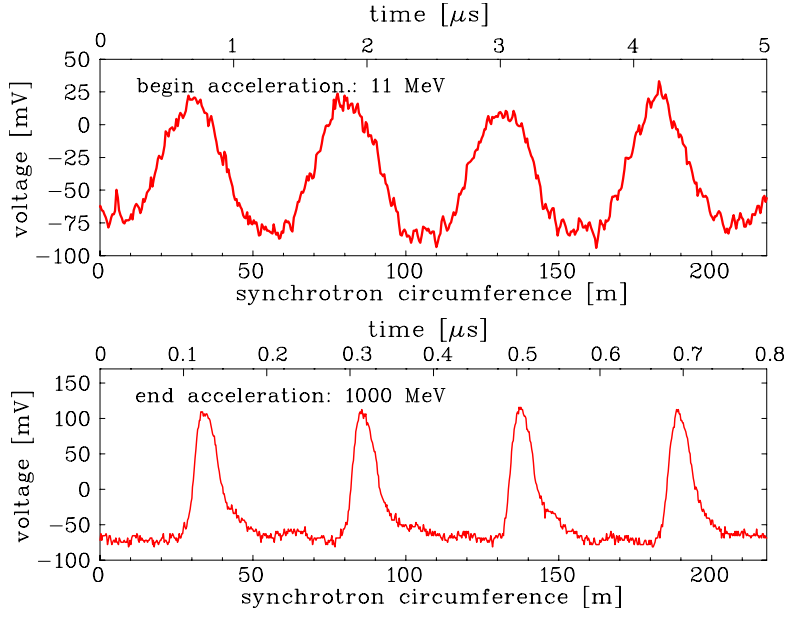
Figure 5.5: Bunch signals from a shoe-box pick-ups for 1 MΩ termination. The upper curve shows the bunches along the synchrotron circumference at the begin of the acceleration, the lower curve after reaching the final energy. Note the different time scales on top of the plots.
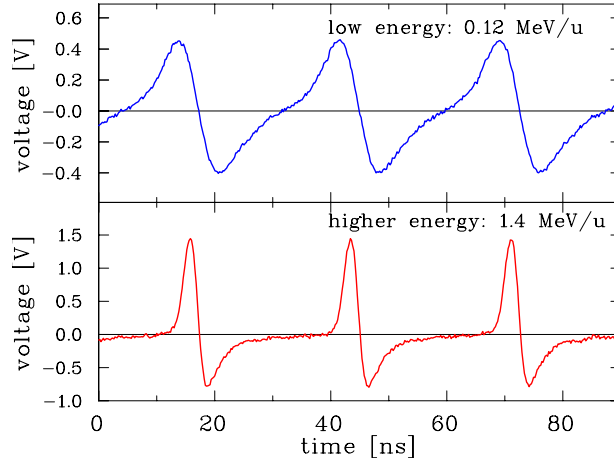
Figure 5.6: Bunch signal from a capacitive pick-up with 0.12 MeV/u (top) and 1.4 MeV/u (bottom) energy at the GSI-LINAC. The derivative behavior is caused by 50 Ω termination to achieve a large bandwidth of the amplifier. The accelerating frequency is 36 MHz.

- **Range $\omega \gg \omega_{cut}$ realized by a *low* ω_{cut} due to high impedance:**
  In a proton/heavy ion synchrotron a low frequency (1-10 MHz) is used for acceleration, resulting in bunches of several meters in length. In these machines, large apertures are necessary of more than $a = 10$ cm lowering the transfer impedance due to $Z_t \propto 1/a$. To get a larger sensitivity, the length of the pick-up in beam direction is increased, typically $l \sim 10$ cm due to $Z_t \propto l$. Note that the pick-up length is still much shorter than the bunch length. To have a flat curve of the sensitivity, i.e., a large bandwidth, a low $\omega_{cut} = 1/RC$ is used by feeding the signal into a high impedance FET transistor as the first step of the amplifier. A bandwidth of the amplifier circuit of 100 MHz can be reached, but it is very difficult to build them with larger bandwidth. To prevent for signal degeneration due to the limited amplifier bandwidth the application of high impedance amplifiers is restricted to proton/heavy ion

82

synchrotrons with less than ~ 10 MHz acceleration frequency. (The observation of the contribution in the bunch spectrum from the tenth harmonic is sufficient.) As stated above and shown in Fig. 5.5 a direct image of the bunch is seen in this case.

- **Range $\omega \ll \omega_{cut}$ realized by a high ω_{cut} due to 50 Ω impedance:**
  At LINACs, the bunches are short, in the mm range, due to the higher accelerating frequencies (100 MHz to 3 GHz). First, one does not gain signal strength by making the length l larger. Second, a 50 Ω termination is used to prevent reflections and to get smooth signal processing with a large bandwidth up to several GHz. The short l, and therefore a lower capacitance C, and the $R = 50$ Ω leads to a high ω_{cut} and the derivative of the bunches is seen as displayed in Fig. 5.6.

The foregoing discussion does not take into account the effect of the frequency response of the associated cables. See [73] for a more detailed discussion. Moreover, at the high frequencies the excitation of standing wave modes might be possible.

5.2 LINAC pick-up for longitudinal bunch observation
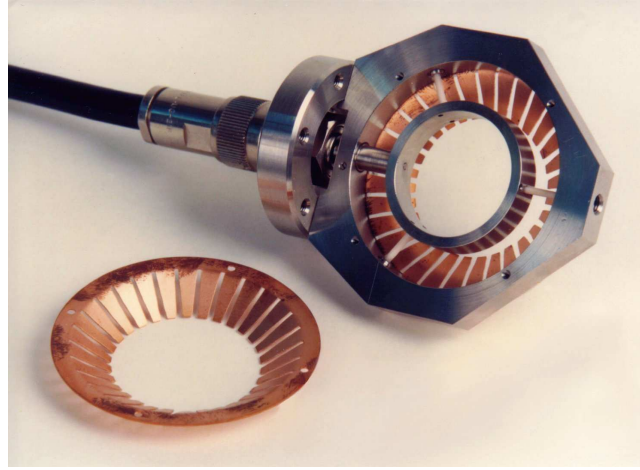
Figure 5.7: Capacitive pick-up in 50 Ω geometry as used for the longitudinal bunch observation at the 108 MHz GSI-LINAC. The inner diameter is 35 mm.

Figure 5.8: Calculation of the impedance of a ring pick-up as a function of the length in beam direction.

The observation of the bunches is an important parameter for the settings of a LINAC, to visualize the bunch shape, to setup the right phases between different accelerating structures

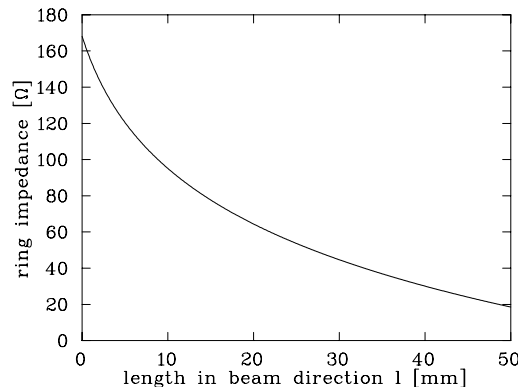and to measure the energy via time-of-flight in the case of proton/heavy ion LINACs; this is discussed in Chapter 6. Normally, 50 Ω is used as the input impedance of the amplifier, because a bandwidth of several GHz is needed [78]. A frequency of 1 GHz corresponds to a wavelengths of 30 cm in free space (TEM-mode), so the signal transit times can not be neglected. In case of the pick-up shown in Fig. 5.7 the 50 Ω is realized between the inner ring shaped electrode and the outer ring at ground potential. To calculate the impedance, one can take advantage of formulas given for the design of strip-lines. The capacitive pick-up is a strip-line bent around the beam pipe axis and its impedance Z_0 is given by

$$Z_0(l) = \frac{87}{\sqrt{\varepsilon_r + 1.4}} \ln \left(\frac{5.98h}{0.8l + d} \right) \qquad (5.13)$$

where ε_r is the relative permeability, h is the distance between inner and outer conductor, d is the thickness of the inner ring and l is the length of the inner ring in beam direction. The diagram of Fig. 5.8 holds for $\varepsilon_r = 1$, $d = 3\,\text{mm}$ and $h = 10\,\text{mm}$. The induced signal can travel along two ways to the output cable corresponding to a parallel circuit of two transmission lines. The pick-up ring shown in Fig. 5.7 is designed for an impedance of 100 Ω, to match the 50 Ω signal transmission via the coax-cable. A typical bunch signal measured with such a pick-up is shown in Fig. 5.6.

5.3   Position measurement with a capacitive pick-up
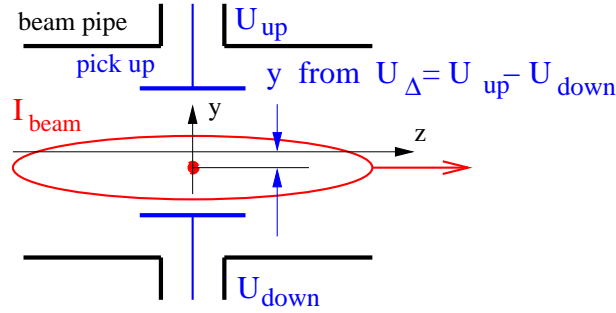
Figure 5.9: Schematics of a BPM for the vertical position reading using the proximity effect.

The deviation of the beam center with respect to the center of the vacuum chamber can be monitored using four isolated plates or buttons by determining the difference voltage $\Delta U_x = U_{right} - U_{left}$ or $\Delta U_y = U_{up} - U_{down}$ of opposite plates. The closer distance to one of the plates leads to a higher induced voltage. This is called the 'proximity effect' and schematically shown in Fig. 5.9. Normalizing to the total signal $\Sigma U_x = U_{right} + U_{left}$, the horizontal displacement x can be obtained via

$$x = \frac{1}{S_x} \cdot \frac{U_{right} - U_{left}}{U_{right} + U_{left}} = \frac{1}{S_x} \cdot \frac{\Delta U_x}{\Sigma U_x} \qquad \text{(horizontal)} \qquad (5.14)$$

which is independent of the beam intensity. For the vertical plane the position y is given by

$$y = \frac{1}{S_y} \cdot \frac{U_{up} - U_{down}}{U_{up} + U_{down}} = \frac{1}{S_y} \cdot \frac{\Delta U_y}{\Sigma U_y} \qquad \text{(vertical)}. \qquad (5.15)$$

This position measurement is the most frequent application of pick-ups, hence they are called **B**eam **P**osition **M**onitor **BPM**. The proportional constant S_x respectively S_y between the measured normalized voltage difference and the beam displacement is called **position sensitivity**

84
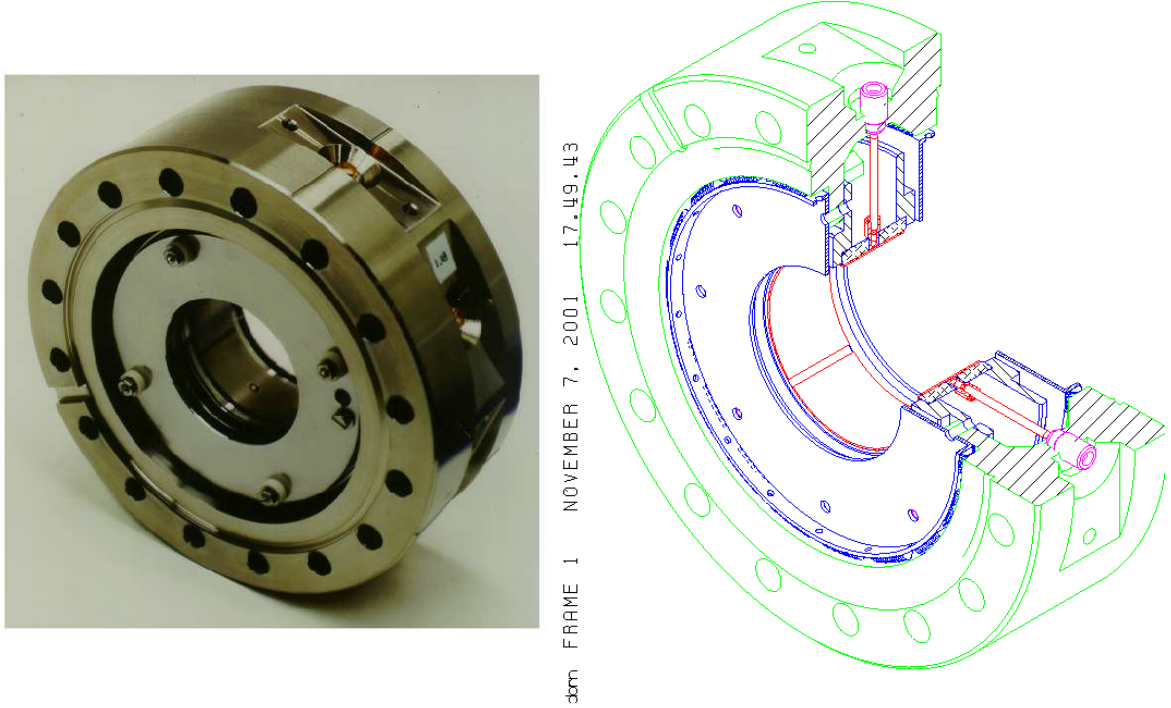
Figure 5.10: Photo and schematic drawing of a capacitive position sensitive pick-up at the GSI-LINAC. The aperture is 50 mm and the electrode length 20 mm.

and its unit is $S = [\%/mm]$. It is possible that the position sensitivity additionally depends on the beam position itself, corresponding to a non-linear voltage response for a large beam displacement. Moreover, S can also depends on the evaluation frequency.

Like in the case of longitudinal coupling, we can define the transverse transfer impedance $Z_\perp$ as

$$\Delta U_x = Z_\perp \cdot x I_{beam} \tag{5.16}$$

for an off-center position x and a beam current I_{beam}; the product $x I_{beam}$ is sometimes called the dipole moment of the beam. $Z_\perp$ can be written as a product of the longitudinal transfer impedance Z_t and a geometric non-linear function $g(x)$ as

$$Z_\perp = \frac{Z_t}{g(x)}. \tag{5.17}$$

An example of a capacitive pick-up used at the GSI-LINAC is shown in Fig. 5.10. The plates consist of (nearly) a quarter cylinder segment with radius a. For typical displacements up to $x < 1/2 \cdot a$ the function $g(x) = a$ is sufficiently constant. For larger displacements, the response is non-linear and a correction algorithm has to be applied to the digitized signals. For the device shown, the aperture is 50 mm and a relatively large length of $l = 20$ mm in the beam direction is used to attain a large signal strength.

5.4 Position measurement using button pick-ups

For a round arrangement of buttons, a simple 2-dimensional electro-static model can used to calculate the voltage difference as a function of beam displacement. According to Fig. 5.11 we assume a thin, 'pencil' beam of current I_{beam} which is located off-center by the amount r at an
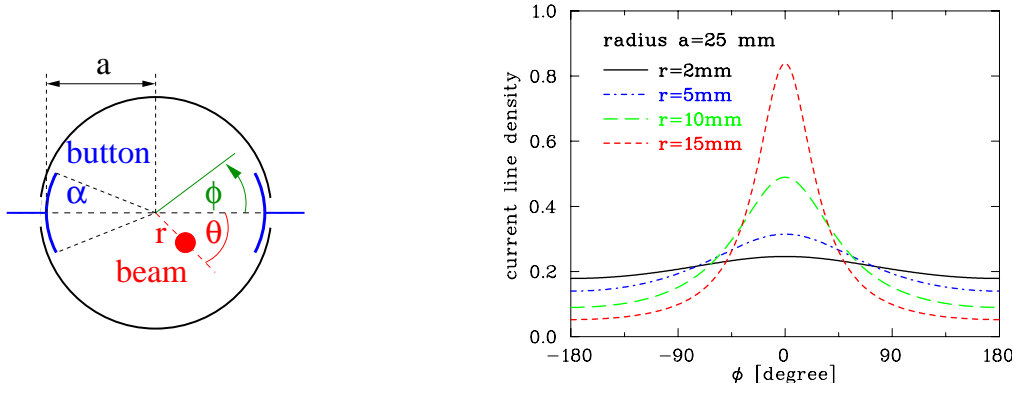
Figure 5.11: Schematics for a button BPM and the image current density generated by a 'pencil' beam at different displacements r for an azimuth $\theta = 0$.
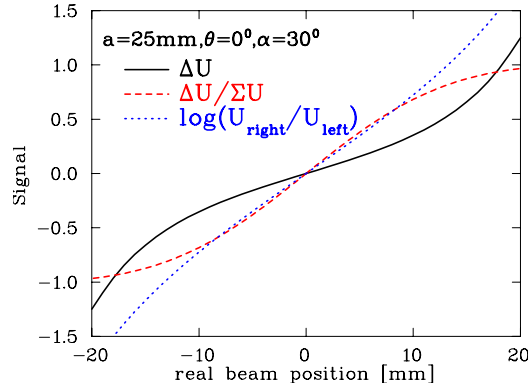
Figure 5.12: Difference voltage, normalized difference and logarithmic ratio for a button BPM arrangement of angular coverage $\alpha = 30^o$ as a function of horizontal beam displacement i.e. $\theta = 0$ for a beam pipe radius $a = 25$ mm.

angle θ. The wall current density j_{im} at the beam pipe of radius a is given as a function of the azimuthal angle ϕ as

$$j_{im}(\phi) = \frac{I_{beam}}{2\pi a} \cdot \left(\frac{a^2 - r^2}{a^2 + r^2 - 2ar \cdot \cos(\phi - \theta)} \right) \tag{5.18}$$

and is depicted in Fig. 5.11; see [79] for a derivation of this formula.

As discussed above, this represents the proximity effect, where the current density depends on the distance with respect to the beam center. The buttons covering an angle α and the image current I_{im} is recorded as given by:

$$I_{im} = a \int\limits_{-\alpha/2}^{+\alpha/2} j_{im}(\phi) d\phi \quad . \tag{5.19}$$

The resulting signal difference for opposite plates as a function of horizontal beam displacement (corresponding to $\theta = 0$) shows a significant non-linear behavior as displayed in Fig. 5.12. It can be seen, that for the normalized difference $\Delta U/\Sigma U$ the linear range continues to larger beam offsets. The non-linearity increases if the beam center moves outside the horizontal axis, which is depicted in Fig. 5.13 for different values of the azimuthal orientation θ as a function of horizontal displacement according to Eqs. 5.18 and 5.19. For an orientation along the diagonal line, a significant deviation from linearity starts for this case even at about 1/4 of the beam pipe

86

23
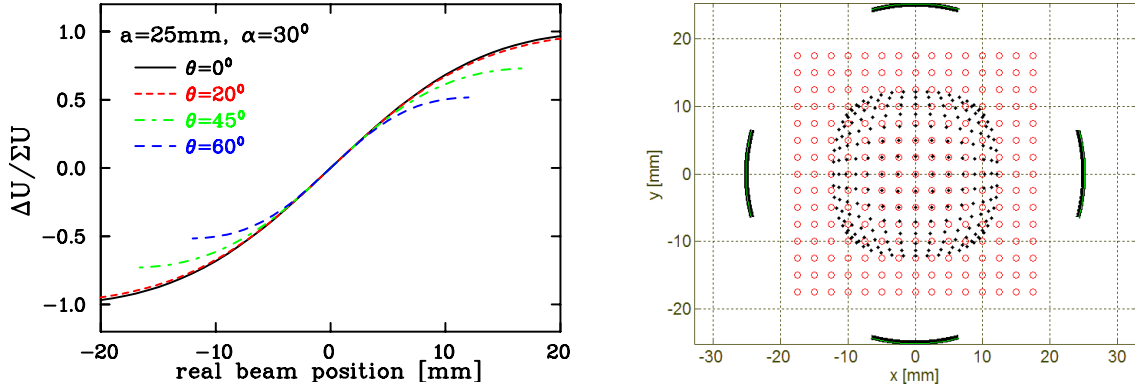
Figure 5.13: Left: Horizontal position calculation for different azimuthal beam orientation θ for the parameters of Fig. 5.12. Right: In the position map the open circles represent the real beam position and the dots are the results of the $1/S \cdot \Delta U / \Sigma U$ algorithm with $S = 7.4\ \%/mm$ for the central part.
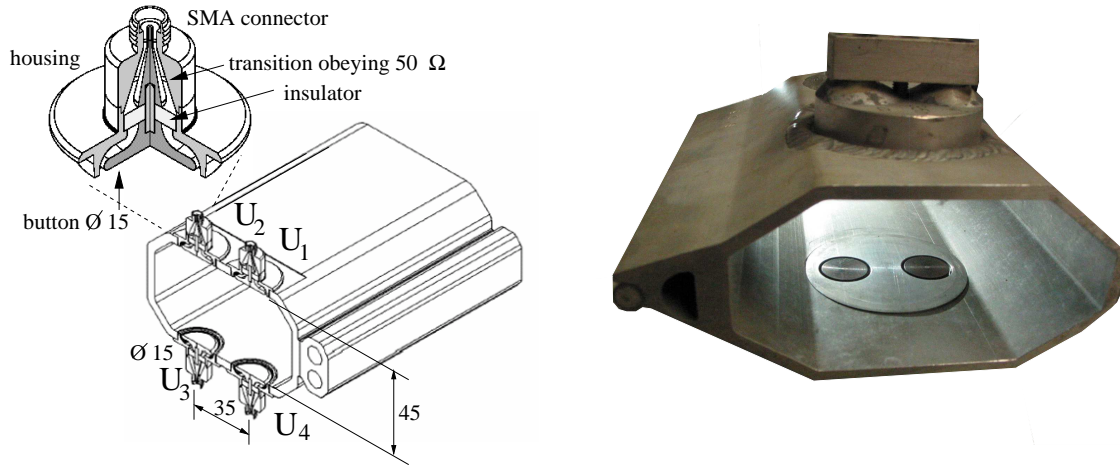
Figure 5.14: Right: Typical button BPM arrangement within a vacuum chamber at a synchrotron light source, from [83]. Right: Photo of the realization at HERA, DESY.

radius. However, in the central part the reading is nearly independent of the orientation leading to a universal position sensitivity S. The dependence between the horizontal and vertical plane is better depicted in the position map of Fig. 5.13, right: Here the real beam positions with equidistant steps are plotted as well as the results using $1/S \cdot \Delta U / \Sigma U$ calculations with S fitted at the central part.

Button pick-ups are the most popular devices for electron accelerators. They consist of a circular plate of typically 1 cm diameter mounted flush with the vacuum chamber as shown in Fig. 5.14. The cross section of the chamber is not changed by this insertion, to avoid excitation of wake fields by the beam. The button itself should have a short vacuum feed-through with a smooth transition to the 50 Ω cable, to avoid excitation of standing waves and to reach a bandwidth up to 10 GHz. Fig. 5.14 shows a typical setup used at electron accelerators, where the buttons are not mounted in the horizontal plane to avoid synchrotron light hitting the feed-through. According to Fig. 5.15 the position is calculated via

$$\text{horizontal:} \quad \frac{\Delta U_x}{\Sigma U_x} = \frac{(U_2 + U_4) - (U_1 + U_3)}{U_1 + U_2 + U_3 + U_4} \qquad \text{vertical:} \quad \frac{\Delta U_y}{\Sigma U_y} = \frac{(U_1 + U_2) - (U_3 + U_4)}{U_1 + U_2 + U_3 + U_4}$$
(5.20)

using all four pick-up voltages for the position determination. This geometry leads to a non-
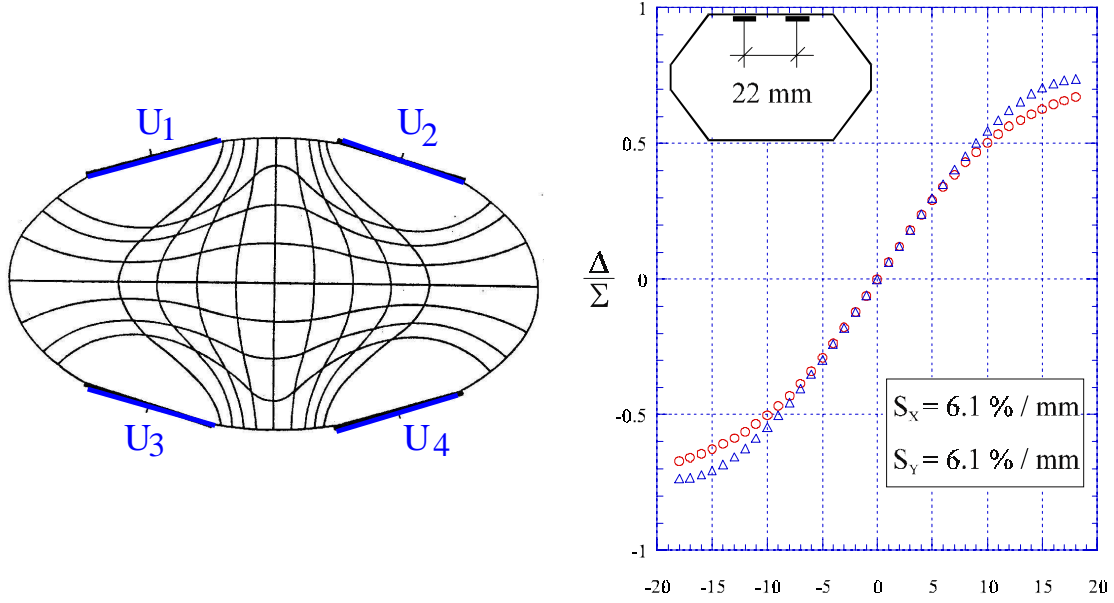
Figure 5.15: Iso-level curves for an arrangement of button pick-ups are shown on the left. On the right: The calculated accuracy for the difference voltage over the sum Δ/Σ as a function of beam displacement (horizontal o, vertical $\triangle$) for the displayed button arrangement [85].

linear position sensitivity (i.e. non linear $g(x)$ in Eq. 5.17). The iso-levels for this geometry are shown. A displacement of the beam center on one of these lines lead to the same reading in the difference voltage of the desired plane. A good location of the buttons for a linear sensitivity has to be calculated numerically (see e.g. [84, 85]). The optimized location depends on the size and distances of the pick-ups, as well as the chamber cross section. The result for such an optimized setting is shown in Fig. 5.15.

5.5 'Shoe box' pick-ups using the so-called linear cut

Due to the long bunches at proton/heavy ion synchrotrons, one can use long plates of typically 20 cm to enhance the signal strength. A box-like device is used normally, to get a precise linear dependence with respect to the beam displacement, see Fig. 5.16. For the previously discussed pick-up geometries, the signal of the plate closer to the beam's center-of-mass is larger than that
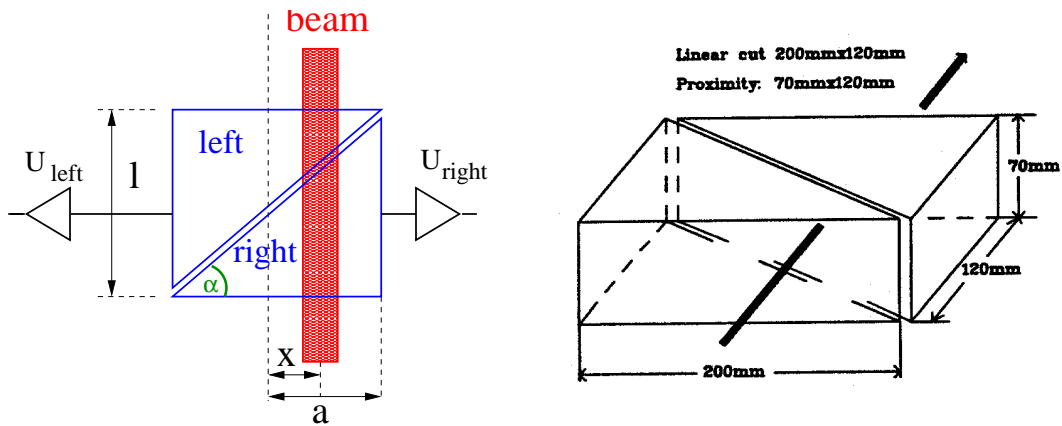
Figure 5.16: Scheme of the position measurement using the so-called linear cut and an example of an electrode arrangement for the horizontal plane.

88
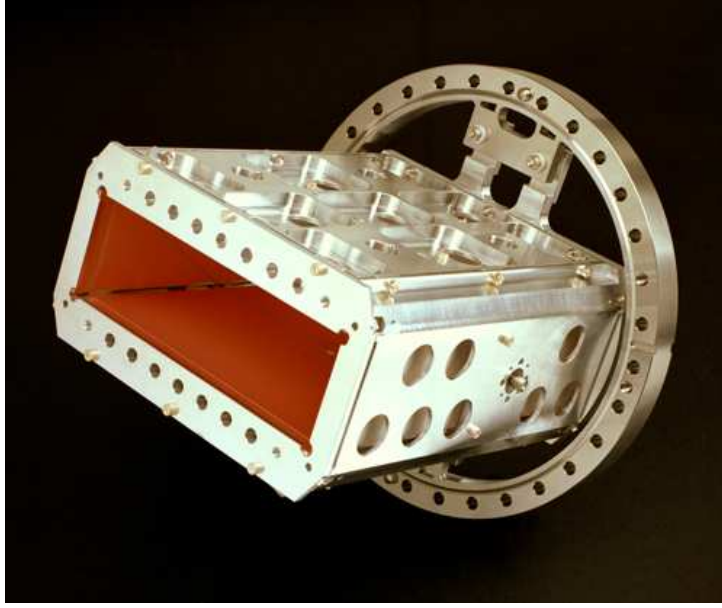
Figure 5.17: Linear cut position pick-up from the GSI synchrotron ring.

of the more distant plate; this is called the proximity effect. In contrary to that, the shoe-box pick-ups have another principle: The influenced signal is proportional to the actual plate length at the beam center position. For a given beam displacement x the electrode's image voltage U_{im} is proportional to the length l of the beam projected on the electrode surface as shown for the horizontal direction in Fig. 5.16, left. For triangle electrodes with half-aperture a one can write:

$$l_{right} = (a + x) \cdot \tan \alpha \quad \text{and} \quad l_{left} = (a - x) \cdot \tan \alpha \quad \Longrightarrow \quad x = a \cdot \frac{l_{right} - l_{left}}{l_{right} + l_{left}} \quad . \quad (5.21)$$

The position reading is linear and can be expressed by the image voltages as

$$x = a \cdot \frac{U_{right} - U_{left}}{U_{right} + U_{left}} \equiv \frac{1}{S_x} \cdot \frac{\Delta U_x}{\Sigma U_x} \quad \Longrightarrow \quad S_x = \frac{1}{a} \quad (5.22)$$

which shows that the position sensitivity for this ideal case is simply given by the inverse of the half-aperture. Compared to other types of pick-ups, the position sensitivity is constant for nearly the full range of displacements, i.e. nearly no corrections due to non-linearities have to be applied [86]. This is demonstrated in Fig. 5.18. The electrode arrangements is shown in Fig. 5.16 and the analog signal in Fig. 5.5.

5.6 Signal treatment of a stripline pick-up

When the bunch length becomes comparable to the length of a capacitive pick-up, the signal is distorted. In the discussion above, the pick-up was treated as a grounded prolongation of the beam pipe. Now we want to take the signal propagation via a transmission line into account. The stripline pick-up is used for short bunches with relativistic velocities. In a collider, the system offers the possibility of the signal suppression from one of the counter-moving beams, due to their directional characteristic (see below).

A stripline pick-up consists of a transmission line of several cm length l, having at both ends a feed-through with a impedance of R_1 and R_2, normally 50 Ω, see Fig. 5.19. The stripline is installed in a cylindrical chamber with radius r at a distance from the beam center a covering an angle of α. This line has a certain impedance Z_{strip} depending on the parameters r, a, α

89

Figure 5.18: Numerical calculation of the position reading $\Delta U/\Sigma U$ as a function of beam displacement for the horizontal plane. The plot also includes the calculations for a beam offset in the vertical direction and proves the decoupling of both planes [86]. It is performed for the pick-up shown right and in Fig 5.17 with a 200×70 mm^2 cross section and 350 mm length.

Figure 5.19: Scheme of a stripline pick-up.

Figure 5.20: Single shot signal from from a 30 cm stripline pick-up recorded at the ALS synchrotron light facility for a single bunch with 1 ns/div [75].

90
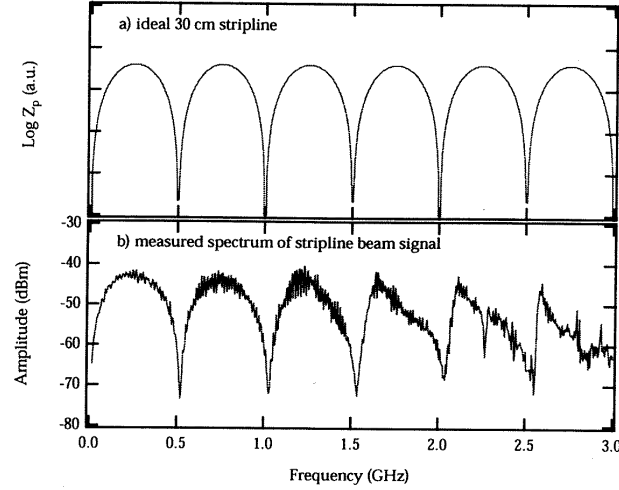
Figure 5.21: Calculated transfer impedance of an ideal 30 cm stripline (a) and and a measurement (b) with a spectrum analyzer for a single bunch signal [75]. The frequency range is 0 to 3 GHz.

[82]. The stripline is matched to the outer resistor $Z_{strip} = R_1 = R_2$. In the following, a beam velocity $\beta = 1$ and a bunch length much shorter than the stripline are assumed. When the beam enters the upstream port 1 of the stripline, a fraction of the image charge of the wall current acts as a current source. Due to the matching of the voltage divider $Z_{strip} = R_1$ half of this signal travels toward the feed-through 1 and half of it travels down the stripline. Assuming a TEM mode with a phase velocity c, this signal travels in phase with the beam. At the downstream port 2 the image charge leaves the stripline, generating an equal and opposite current source and it is split in half due to $Z_{strip} = R_2$. However, the image current is leaving the detector and has the opposite sign to that of the upstream port. Therefore, this half of the signal cancels the signal traveling with the beam created at the upstream port 1. The other half travels now back toward the upstream port and arrives there at the time $2l/c$. A signal recorded with this device is shown in Fig. 5.20.
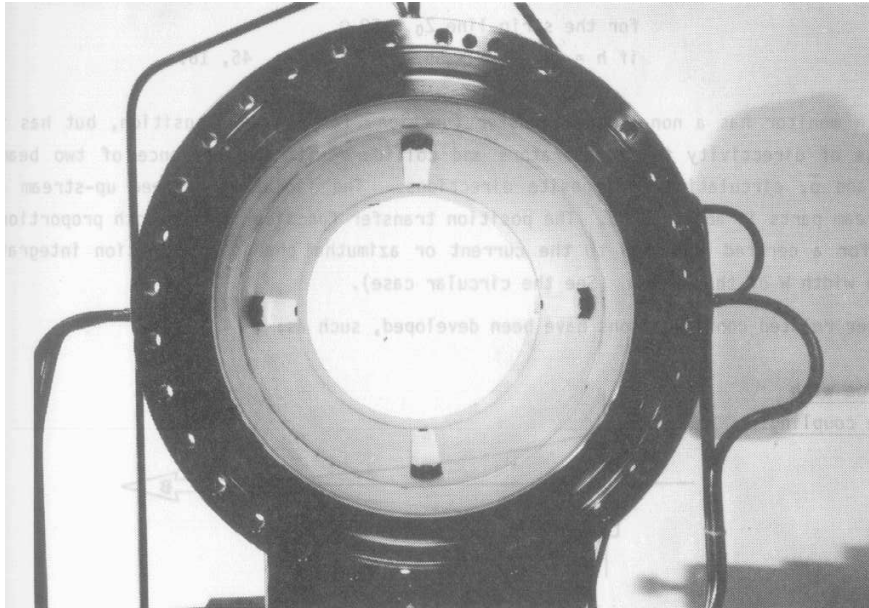
Figure 5.22: Photo of a stripline pick-up at the CERN SPS, from [82].

91

We can write the behavior at port 1 as

$$U_1(t) = \frac{1}{2} \cdot \frac{\alpha}{2\pi} \cdot R_1 \left(I_{beam}(t) - I_{beam}(t - 2l/c) \right) \ . \tag{5.23}$$

For very short bunches, i.e., $I_{beam}(t) \to \delta(t)$, it can be shown via Fourier transformation that the corresponding transfer impedance Z_t is [74, 77, 76]

$$Z_t(\omega) = Z_{strip} \cdot \frac{\alpha}{2\pi} \cdot \sin\left(\omega l/c\right) \cdot e^{i(\pi/2 - \omega l/c)} \tag{5.24}$$

The absolute value of Z_t compared to a measurement is shown in Fig. 5.21, as recorded for a 30 cm matched detector at the ALS synchrotron light facility [75].

The transfer impedance shows some interesting features:

- $|Z_t|$ shows a maximum for $l = c/4f = \lambda/4$, where λ is the wave length. Therefore it this called a quarter wave coupler.

- The length l is chosen to work close to the maximum sensitivity.

- The sensitivity is zero for $l = \lambda/2$. This means no signal is present when the spacing between bunches are equal to $2l$, because the interference between following bunches is destructive.

- The phase for Z_t are straight lines with a zero phase shift at the maximum sensitivity $l = \lambda/4$. For this frequency, the recorded signal is a direct image of the bunch.

- In contrast with capacitive pick-ups, short bunches can be monitored without signal deformation (working at the maximum sensitivity).

Matching the stripline with good accuracy is a difficult task, due to the high desired frequency range. To prevent reflections at the downstream port, ferrite absorbers can be used [81]. In colliders, the directional coupling can be very useful to distinguish between the position of the two counter-rotating beams within a common vacuum chamber. An example of a realization at CERN SPS is shown in Fig. 5.22.

For the position measurement other techniques are also used, including monitors measuring the magnetic field (so called inductive pick-ups) or the excitation of cavity modes. Further descriptions can be found in [82, 94, 95].

5.7 Electronic treatment for position determination

To get the position of the beam, the signals from the electrodes have to be compared. For this comparison, the signal shape (differentiation or proportional behavior) is of minor importance. The electronics used for this purpose are described only very briefly. A detailed review is given in [87]. For the position resolution, the signal-to-noise ratio is important. Beside the stray fields from the rf cavities, the broadband amplifier noise, as well as the electronic noise of the following devices contribute. Therefore a minimum bunch current is needed for a reliable position measurement. Two different principles are commonly used: the so called broadband and narrowband processing:

In the broadband case, as shown in Fig. 5.23, the signals from the individual plates are amplified (or even attenuated) to adapt the signal strength to the ADC input level. The sum and difference signal is then calculated from the digital values. For noise reduction and alias-product suppression, a lowpass filter is used matched to the sample rate of the ADC. In older installations fast sampling was not possible and an external trigger, as generated from the
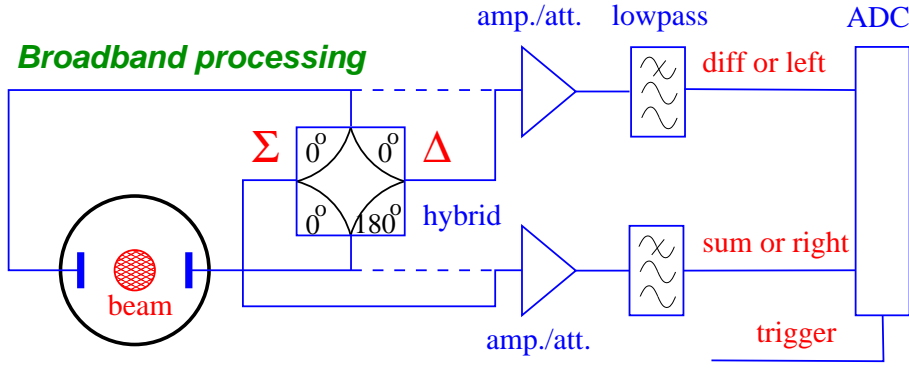
Figure 5.23: Scheme of a broadband signal processing. The plate signals are either fed directly to the amplifier (dashed line) or via a hybrid the sum and difference is generated in an analog manner (solid line).
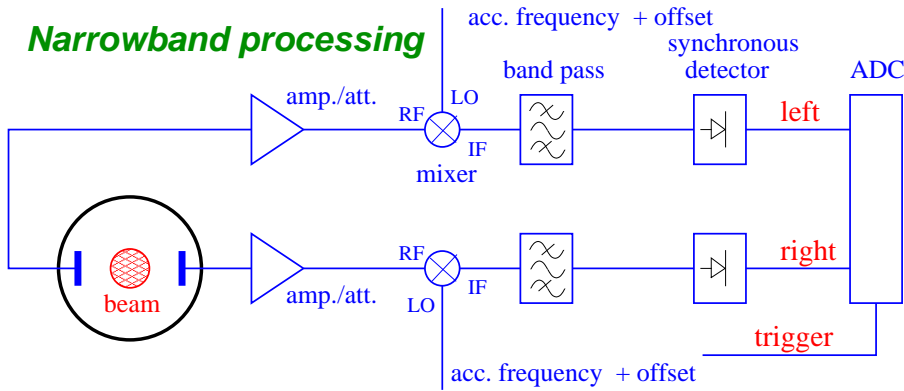
Figure 5.24: Schematic signal analysis for a narrowband treatment.

bunch passage in an analog manner forced the digitalization. In many applications the sum and difference voltages are analogously generated by a 180° hybrid or a differential transformer. Because they are pure passive devices, they can be mounted quite close to the BPM plates even in case of high radiation. The resulting sum and difference signals are then stored in the ADC. The difference signal, which is normally lower by at least a factor of 10, can be amplified by a higher amount than the sum signal to exploit the full ADC range. (An overview of standard rf components can be found in [88].) The analog electronics is required to match the signal shape to the properties of the ADCs and an appropriate trigger is used for the digitalization. Modern installations do not use these types of analog electronics, instead the signal is directly digitized by a fast ADCs or digital receivers, which are even commercially available [89]. With the help of high speed digital signal processing the bunch signal is than reduced to one value per bunch and the beam position is calculated from the sum and difference value [90, 91]. The precision of this method is lower as compared to the narrowband processing described below. For electron machines, with small beam size, a resolution of 100 μm can been achieved by this broadband processing. The advantage is the possibility to do a bunch-by-bunch analysis (i.e. measuring the position of always the same bunch rotating in a synchrotron) by using an appropriate trigger setting or precise digital signal processing.

The narrowband processing is used to get a higher precision of the position reading, attaining 1 μm in electron machines here. The better signal-to-noise ratio is achieved by reducing the bandwidth of the signal processing by several orders of magnitude. As an illustrative example the Fourier-Transformation of the signal form the GSI-LINAC pick-up is shown in Fig. 5.25. The spectral power of the signal is mainly available at the bunch repetition harmonics nf_0. The
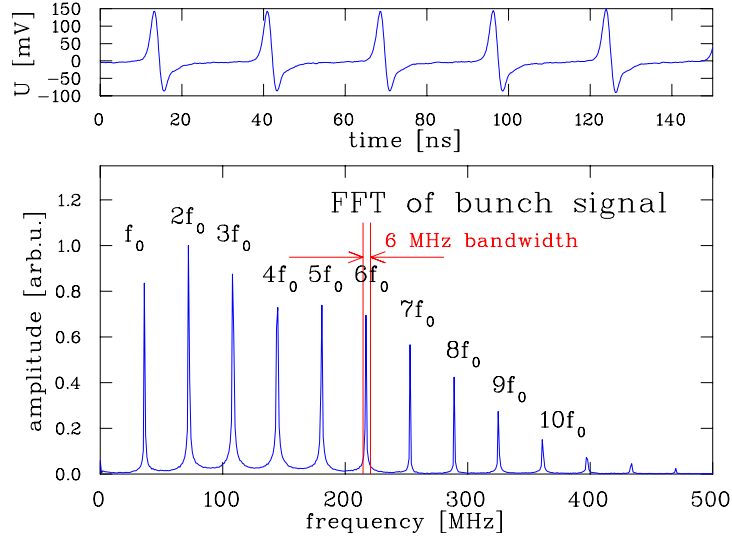
Figure 5.25: Bunch signal (top) and its Fourier transformation (bottom) at the GSI-LINAC of a 1.4 MeV/u beam. In the Fourier spectrum each line corresponds to the indicated harmonics of the 36 MHz accelerating frequency. The position evaluation is done at $6f_0 = 216.8$ MHz by a 6 MHz narrowband processing as indicated by the red lines.
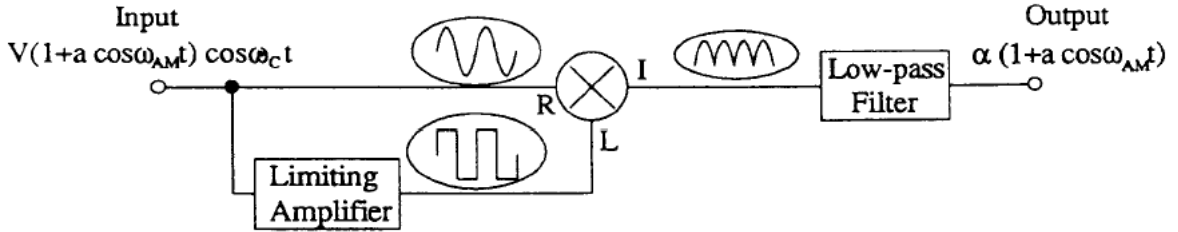
Figure 5.26: Scheme of a synchronous detector to rectify an rf signal: The rf signal is split and one branch is fed into a limiter amplifier driven into saturation, which transforms the signal to a bipolar rectangular pulse. This signal is mixed with the original signal to yield a unipolar waveform (corresponding to the square). It is passed through a low-pass filter and can then be digitized by a low sampling ADC.

position evaluation uses only this large signal power within the band of frequency span Δf, while the thermal noise is reduced as $U_{eff} \propto \sqrt{\Delta f}$. Technically, the pick-up signal is mixed with the accelerating frequency. A mixer is a passive rf-device multiplying the two waves at the port RF (for radio frequency) and LO (for local oscillator). The product is available at port IF (for intermediate frequency). From a mathematical point of view, the mixer multiplies the two waves at LO and RF and we get from a trigonometric theorem [3]

$$A_{IF}(t) = A_{RF} \cdot A_{LO} \cos \omega_{RF} t \cdot \cos \omega_{LO} t = \frac{1}{2} A_{RF} \cdot A_{LO} \left[\cos(\omega_{RF} - \omega_{LO})t + \cos(\omega_{RF} + \omega_{LO})t\right]. \tag{5.25}$$

Typically 10.7 MHz, or one of its harmonics (due to it's large use in telecommunication), is filtered out by a narrow bandpass filter. The signal is rectified by a so called synchronous detector, for which the schematics are shown in Fig. 5.26.The resulting quasi-dc signal is then digitized and the position is calculated via software. In general, this technique is called heterodyne mixing and the same principle is used in a spectrum analyzer. The mixing is equivalent to an average over many turns leading to much higher precision in the position reading. But this method does not allow a turn-by-turn observation. For a proton/heavy ion synchrotron at non-relativistic ve-

---

[3]$\cos x \cdot \cos y = 1/2 \cdot [\cos(x - y) + \cos(x + y)]$

Figure 5.27: Example of a position measurement done at the GSI synchrotron for a partly misaligned beam during the acceleration. The top plot shows the position around the ring at a certain time, the lower left is the position for one pick-up and the lower right is the sum signal power $\propto U_\Sigma^2$ during the ramp for the same single pick-up.

locities, this method can also be applied, because the varying accelerating frequency is changed in phase with the bunch signal, resulting in a constant intermediate frequency. Such a system is commercially available [92]. Modern systems use digital filtering and data reduction with a Digital Signal Processor [93]. Other, more complex techniques suited for large accelerators are described in [87].

5.8 Closed orbit measurement

In a synchrotron, several pick-ups for the determination of the closed orbit are installed. A good choice is to have four pick-ups per tune value separated approximately by about $\mu \simeq 90^o$ betatron phase advance. The pick-ups should be located at position with a large value of the betatron function to have a reasonable spatial resolution even for smaller average beam excursions. The closed orbit is the central beam path along the machine, taking the existing imperfections into account. The closed orbit might differ from the ideal path, defined by the center of the quadrupole magnets. Only for a good alignment the real beam behave as expected from beam optics calculations, e.g. no beam steering by the quadrupole magnets occurs. An example for the use of a position measurement is displayed in Fig. 5.27 during the acceleration in the SIS synchrotron.

The position reading of the pick-ups around the ring can be used as the input of a feedback loop to do an active beam correction, see e.g. [97]. Such a feedback system is installed in most synchrotrons, but a description is out of the scope of this lecture.

Frequently used abbreviations

ac	alternating current
ACCT	alternating current current transformer
ADC	analog-digital converter
amp	amplifier (electronic device)
BIF	beam induced fluorescence monitor
BLM	beam loss monitor
BSM	bunch shape monitor
BTF	beam transfer function
BW	band-width for electrical devices
CCD	charged coupled device for a camera
dc	direct current
DCCT	direct current current transformer
DTL	drift tube LINAC
DSO	digital signal oscilloscope
DSP	digital signal processor
FFT	fast Fourier transformation
FWHM	full width half maximum
Grid	identical with SEM-grid for profiles
Harp	identical with SEM-grid for profiles
HV	high voltage above ~ 1 kV
IC	ionization chamber
IF	intermediate frequency for a rf-mixer
IPM	ionization profile monitor, identical with RGM
IR	infra red light
LO	local oscillator for rf-mixer
MCP	micro channel plate
mw	micro waves with 1 GHz $< f <$ 100 GHz
MWPC	multi wire proportional chamber for profiles
NWA	network analyzer
op-amp	operational amplifier (electronic chip device)
OTR	optical transition radiation for profiles
PHD	pulse height distribution for particle detectors
PMT	photo-multiplier tube
pre-amp	first stage amplifier direct behind detector (fully equipped electronic device)
rf	radio frequency with 100 kHz $< f <$ 1 GHz
RFQ	radio frequency quadrupole LINAC
RGM	residual gas (profile) monitor, identical with IPM
SEEM	secondary electron emission monitor, identical with SEM
SEM	secondary electron (emission) monitor, identical with SEEM
SEM-grid	secondary electron emission grid for profiles, identical to harp
SLM	synchrotron light monitor
SPA	spectrum analyzer
SR	synchrotron radiation
SRM	synchrotron radiation monitor
TOF	time-of-flight
UV	ultra violet light
WCM	wall current monitor

145

Bibliography

[73] S.R. Smith, *Proc. Beam Instr. Workshop BIW 96,* Argonne AIP 390, p. 50 (1996).

[74] G.R. Lambertson, *Electromagnetic Detectors,* Proc. Anacapri, Lecture Notes in Physics 343, Springer-Verlag, p. 380 (1988).

[75] J.M. Byrd, Bunched Beam Signals in the time and frequency domain, in *Proceeding of the School on Beam measurement,* Montreux, p. 233 World Scientific Singapore (1999).

[76] L. Vos, *Proc. Diag. Instrum. Part. Acc. Conf. DIPAC 95,* Travemünde, DESY M9507, p. 20 (1995).

[77] .R. Lambertson, Dynamic devices-Pickups and Kickers, in *Proc. of SLAC and FERMILAB Summer School,* Stanford, AIP Conf. Proc. 153, p. 1413 (1985).

[78] J.F. Power et al., *Proc. Beam Instr. Workshop BIW 2000,* Cambridge AIP 546, p. 535 (2000).

[79] B.G. Pine, *CARE-ABI Workshop Lüneburg 2006,* see adweb.desy.de/mdi/CARE/Lueneburg/ABI-Lueneburg.htm (2006).

[80] T.J. Shea, R.L. Witkover, *Proc. Beam Instr. Workshop BIW 98,* Stanford AIP 451, p. 145 (1998).

[81] P.R. Cameron et al., *Proc. Part. Acc. Conf. PAC 95,* Dallas, p. 2458 (1995).

[82] J. Borer, R. Jung, *Proc. CERN Acc. School,* Geneva, CERN84-15, p.385 (1983).

[83] N. Kurita et al., *Proc. Part. Acc. Conf. PAC 95,* Dallas, p. 2512 (1995).

[84] C.K. Ng et al, *Proc. Part. Acc. Conf. PAC 95,* Dallas, p. 2485 (1995).

[85] A. Labrador et al., *Proc. Euro. Part. Acc. Conf. EPAC 98,* Stockholm, p. 1547 (1998).

[86] P. Kowina et al., *Proc. Diag. Instrum. Part. Acc. Conf. DIPAC 2005,,* Lyon, p. 114 (2005).

[87] G. Vismara, *Proc. Beam Instr. Workshop BIW 2000,* Cambridge AIP 546, p. 36 (2000) and G. Vismara, *Proc. Diag. Instrum. Part. Acc. Conf. DIPAC 99,* Chester, p. 11 (1999).

[88] R. Garoby, Low Level R.F. Building Blocks, in *CERN Acc. School,* CERN 93-03, p. 428 (1992), http://cas.web.cern.ch/cas/CAS_Proceedings.html.

[89] Company I-Tech, www.i-tech.si.

[90] J.M. Belleman, *Proc. Diag. Instrum. Part. Acc. Conf. DIPAC 05,* Lyon, p. 137 (2005).

[91] A. Galatis et al.,*Proc. Diag. Instrum. Part. Acc. Conf. DIPAC 07,* Venice, (2007).

[92] K. Unser, *Proc. Beam Instr. Workshop BIW 96,* Argonne AIP 390, p. 527 (1996) and www.bergoz.com.

[93] V. Schlott et al., *Proc. Euro. Part. Acc. Conf. EPAC 2000,* Vienna p. 1809 (2000) and www.i-tech.si.

[94] M. Wendt, J.R. Maidment, *Proc. Beam Instr. Workshop BIW 2000,* Cambridge AIP 546, p. 614 (2000).

[95] R. Lorenz, *Proc. Beam Instr. Workshop BIW 98,* Stanford AIP 451, p. 53 (1998).

[96] B. Dehning et al., *Proc. Euro. Part. Acc. Conf. EPAC 98,* Stockholm, p. 430 (1998).

[97] J.D. Fox, E. Kikuzani, Bunch feedback system and signal processing, in *Proceeding of the School on Beam measurement,* Montreux, p. 579 World Scientific Singapore (1999).

Chapter 2

Tune Measurement

2.1   Introduction

Diagnostics and Control
of the Time Evolution of Beam Parameters
H. Schmickler, Proceedings of Beam Instrumentation Workshop DIPAC, 1997

EUROPEAN ORGANIZATION FOR NUCLEAR RESEARCH

European Laboratory for Particle Physics

CERN - SL DIVISION

Diagnostics and Control of the
Time Evolution of Beam Parameters

Hermann Schmickler

Abstract

Measurement tools for the betatron tunes, chromaticity and coupling exists in every circular accelerator. This article reviews diagnostic tools for the time evolution of these beam parameters in view of potential online feedbacks on magnetic elements in the LHC. For chromaticity measurements a new development made at CERN based on the detection of the phase difference between head and tail betatron oscillations is presented.

Geneva, Switzerland
December, 1997

Diagnostics and Control of the
Time Evolution of Beam Parameters

Hermann Schmickler, CERN, CH-1211 Geneva 23, (Switzerland)

Abstract: Measurement tools for the betatron tunes, chromaticity and coupling exists in every circular accelerator. This article reviews diagnostic tools for the time evolution of these beam parameters in view of potential online feedbacks on magnetic elements in the LHC. For chromaticity measurements a new development made at CERN based on the detection of the phase difference between head and tail betatron oscillations is presented.

Introduction: The following work has been stimulated by the participation in a working group called "*Dynamic Effects Working Group*" at CERN. In this working group various aspects of time varying magnetic fields and their control are studied for the LHC [1]. In particular at the beginning of the acceleration large variations of the betatron tunes, the chromaticities and coupling over a few seconds can be anticipated.

The author has collected experience from FNAL (Tevatron) , DESY (HERA-P), from older proton machines at CERN (SPS, ISR, PS) and from LEP on the subjects of measurement tools and eventual online feedback loops.

1. TUNE MEASUREMENTS

1.1 Fourier Transform (FFT) of beam motion:

The most common method for tune measurements is the excitation of a beam motion (in most cases broad band excitation with white noise) and the computation of the power density spectrum in frequency domain. The betatron tunes are determined as the frequency with the highest amplitude peak. The frequency resolution Δf is inversely proportional to the number of oscillation samples (Nsamp). One can write: $\Delta f = 2/Nsamp$. So if for example one needs a tune resolution of 10^{-3}, at least 2000 samples have to be acquired. A modern computer can perform the time frequency transform (FFT) of 2048 samples in about 1 msec. For typical signal to noise ratios about a factor 4 can be gained in tune resolution by interpolation between the measured amplitude values [2]. If there is enough external excitation from other sources (ground motion, power supply ripple) or the beam is slightly unstable by itself the method also gives useful information without specific beam excitation. The signal to noise ratio can be improved by averaging several spectra into one measurement display.
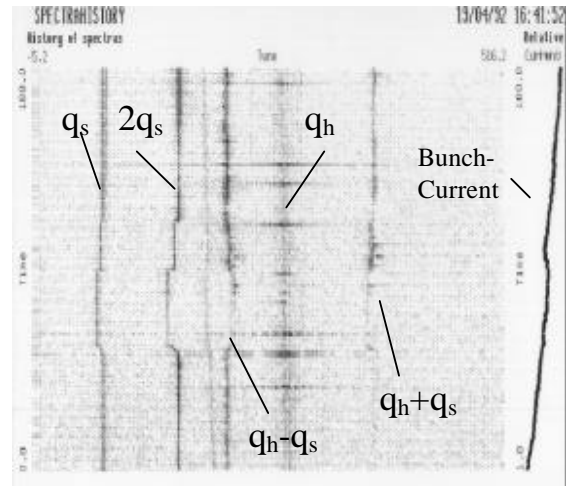
Fig.1: Accumulated spectra during LEP injection.

The time evolution of the tunes can be measured by accumulating many spectra and presenting them in a mountain range display. Figure 1 gives an example measured in LEP during injection. This figure nicely illustrates the diagnostic power of accumulated spectra. Apart from the horizontal tune multiples of the synchrotron tune and the synchrotron sidebands of the horizontal tune are visible. During a certain period two Rf-cavities had tripped (visible as shift in the synchrotron tunes). Such a tool is indispensable for machine set up and the study of many dynamic processes.

1.2 Chirp Excitation

As a variant of the previous method the beams are excited with a sine wave of time variable frequency. If one sends the excitation signal to a loudspeaker one gets the impression of a singing bird (at least at large machines!). For this reason the excitation is called "chirp" excitation. The chirp range is set around the expected betatron tunes and the length is taken corresponding to the requested time resolution and precision of the tune measurements. Data analysis of the resulting beam motion is either via sliding window Fourier transform or via a wavelet analysis [3]. The advantage of this method compared to noise excitation is that the phase information between excitation and beam motion is easier obtained and hence due to the better signal to noise ratio smaller excitation

amplitudes can be used. Figure 2 shows the result of a chirp measurement in the SPS. The sweep length is 20 msec and the repetition rate is 30 msec. In total 150 chirp measurements cover acceleration. More details can be found in [4].
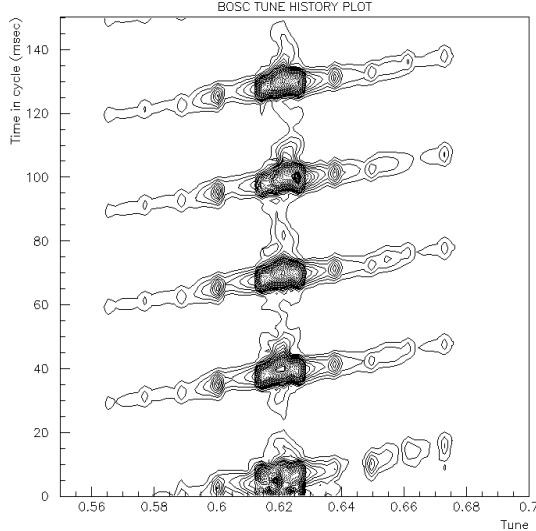
Fig. 2: Chirp tune measurement in the SPS. The horizontal scale is tune, the vertical scale is time (msec). The amplitude of the beam motion is encoded as grey scale.

1.3 Swept Frequency Analysis

For this method (often called "Network Analysis") the beams are excited with a steady sinusoidal wave. Amplitude and Phase of the resulting oscillation are precisely determined by means of harmonic analysis. Thereafter the excitation frequency is increased in steps until the range of interest is covered. This represents a very precise measurement yielding the full information of the beam transfer function. The disadvantage is the long measurement time, which renders the method of little use for the study of dynamic phenomena. Details can be found in [5].

1.4 Phase Locked Loop Tune Tracker (PLL)

Most tune measurements use the amplitude peak of the beam oscillation as signal for tune measurements. This is somewhat odd, since the amplitude information with "0-slope" at its maximum suffers much more from noise than the phase information, which has its maximum slope at the tune resonance. Phase Locked Loop Circuits instead make use of the phase slope. The beams are excited with a continuos sine wave. By changing the frequency of the exciting oscillator an analog or digital circuit assures that the phase difference between excitation and beam motion is 90^0. The tune measurement simply consists in a readout of the (filtered) frequency of the oscillator. In reality the design of such a PLL is more complicated, in particular the lock-in procedure and additional regulation circuits for constant amplitude of the beam oscillation. Many

details can be found in [6]. As the readout of the oscillator frequency can be made almost continuos a PLL circuit is the ideal tool for tracking the time evolution of the betatron tunes during machine transitions. Good measurement examples can be found in chapter 2.1 and 3.1 of this report.

1.5 Discussion

Common to all tune measurements is an exciter and an oscillation detector. The most natural approach is to implement the data treatment and the synthesis of the beam stimulus as a digital process of a system located "between" the monitor and the exciter. With the computing power of modern digital signal processors this should be a possible concept even for machines with revolution periods down to the microsecond. In that case the change in functionality is realised by a software reload.

The following functionalities are imported for the study of dynamic machine processes:

- Accumulated FFT spectra. Apart from the betatron tune lines other important spectral information is contained in the measurements. Beam excitation is done with random kicks or chirp signals.

- PLL tune tracking. In contrast to the previous method only the values of the betatron tunes are measured. With a good compromise in time resolution versus measurement noise a new tune reading is obtained every 100 machine turns.

The **Emittance Blowup** due to the beam excitation is of little importance for lepton machines, but this aspect is the key question for a proton machine. For machine studies and measurements during the setting up emittance blowup to a certain level can be tolerated, but on the operational beams for luminosity production one will only occasionally use a measurement with large (mm) oscillations. Accumulated or integrated spectra are very useful as they can be done without any excitation. In case the beams are quiet or kept quiet with a transverse feedback the use of chirp excitations can be considered, as the beam stimulus is centred around the region of interest. PLL tune tracking is on the first sight the worst one can do, as the beams are continuously excited on the resonance. On the other hand the very good signal to noise ratio of a PLL allows to work with sub micron beam oscillation amplitudes. Although not yet completely operational it has been shown at HERA-P that an online PLL tune measurement on two of the bunches of an operational beam was used for long periods without significant blowup [7].

2. Chromaticty Measurements

2.1 Variation of beam momentum

The commonly used method works by measuring directly the quantities involved in the definition of the chromaticity ξ. The definition is:

$$\Delta q = x \cdot \frac{\Delta p}{p} = x \cdot a \cdot \frac{\Delta f_{RF}}{f_{RF}} \qquad (1)$$

(α = momentum compaction factor)

i.e. one measures the tune dependence Δq on beam momentum (Δp/p), which is very often done by varying the Rf-frequency (Δf_{RF}/f_{RF}).
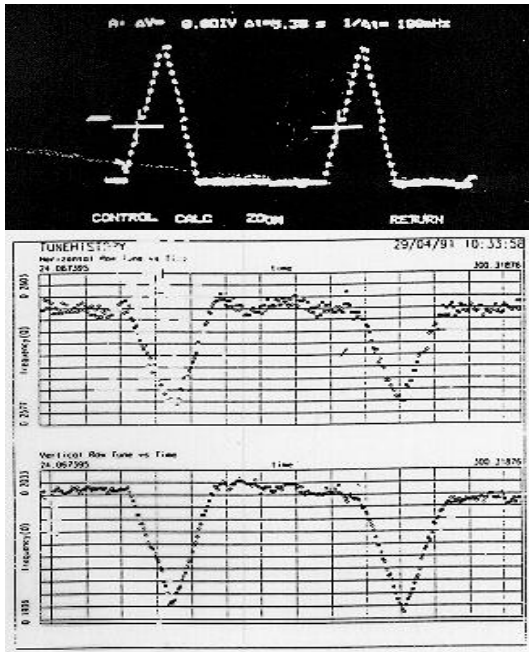
Fig. 3 Dynamic Chromaticty Measurement in LEP. Rf-frequency modulation measured on the tuning system (top trace) and tunes measured in PLL mode (bottom traces).

Figure 3 illustrates the measurement procedure implemented for LEP [8]. The tunes are measured in PLL mode (bottom traces) and the Rf-frequency is modulated in a three second long cycle with an asymmetric wave shape. The asymmetrie of the modulation is important, as it allows to identify the sign of the chromaticities from the tune measurements. This is nicely visible in figure 4, which shows a chromaticty meaurement during a beta squeeze of LEP. The top trace shows a diminishing horizontal chromaticity, which changes sign and then returns back to nominal sign and magnitude. The vertical chromaticity stays almost constant.
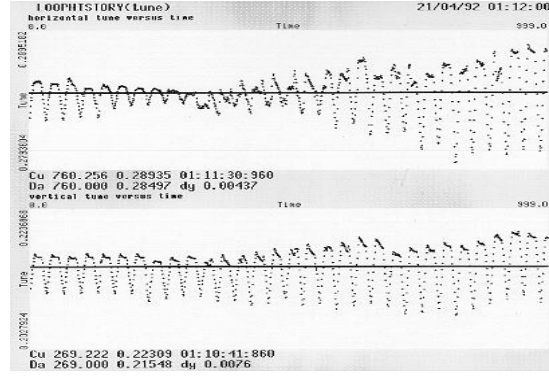
Fig.4: Horizontal (top trace) and vertical (bottom trace) chromaticity measurements during the beta squeeze in LEP.

2.2 Amplitude of Synchrotron Sidebands

The amplitude ratio of the betatron lines to their synchrotron side bands contains information on the chromaticty of the machine. This could well be used on accumulated tune spectra during machine transitions in order to get chromaticity information, but if the betatron tunes change a lot, it is not clear whether systematic lattice resonances influence the observed amplitude ratio. Studies have been made in LEP [9], but the issue has not been continued. In particular in proton machines the measurements are quite difficult, as the synchrotron tune is low and the signals of the side bands are often swamped in the spectral leakage of the main line.

2.3 Width of Tune Resonance

Using again equation (1) one can see that the momentum spread of the beam will result in a width of the betatron lines. Hence measuring the width of the resonance (best via swept frequency analysis (see chapter 1.3)) could be used as a measure of chromaticty. But there are other effects contributing to the line width (radiation damping, transverse feedbacks...), such that one normally looks only for variations in the width in order to deduce chromaticity changes. But in particular during acceleration this analysis is quite complicated, as the momentum spread changes during the measurement.

2.4 Frequency Shift in Bunch Spectrum

The longitudinal bunch profile generates a certain frequency spectrum in an electromagnetic coupler. If one excites betatron oscillations the longitudinal shape of the bunch changes depending on the chromaticty and hence will result in a different bunch spectrum. A detailed analysis yields that in frequency domain the measurable quantity is a shift in the peak of the bunch spectrum [10]. Experiments with this method are quite difficult and are at present not exploited for routine operation.

2.5 Phase of Head and Tail Betatron oscillations

This method is presently under development at CERN and has been stimulated by the ideas of the previous method. Rather than measuring in frequency domain the shift in bunch spectrum, the betatron oscillations of head and tail are individually sampled in time domain. The observable linked to the chromaticty is the phase difference between the head and tail oscillations. By the exciting kick this phase difference is initially forced to zero, evolving to a maximum after half a synchrotron period and then the oscillations rephase again after one complete synchrotron period. Figure 5 shows a computer simulation of the head tail motion for non zero chromaticty for illustration. The vertical axis is time (in [ns] along the longitudinal bunch profile), the horizontal axis is the revolution number after the kick stimulus and the amplitude of the betatron oscillation is encoded as grey scale. The head and tail oscillations are sampled in time slices indicated by the horizontal lines.
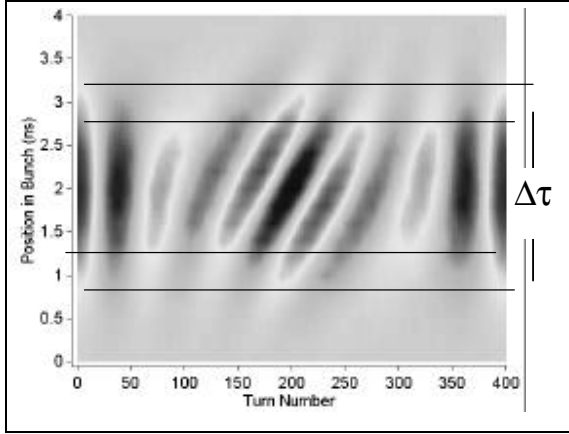
Fig. 5: Computer simulation of head-tail motion.

The chromaticity can be expressed as follows:

$$x = \frac{-h \cdot \Delta\Psi_i}{Q_0 w_0 \Delta t \left(\cos(2p \cdot i Q_s) - 1\right)} \qquad (2)$$

with: $\eta = 1/\gamma 2 - \alpha$; Qs = synchrotron tune, ω_0 = angular revolution frequency; $\Delta\Psi_i$ = head-tail phase difference, $\Delta\tau$ = sampling time interval (see figure 6), Q_0 = betatron tune and i turn index since initial kick

Practically the measured chromaticity does not depend on the betatron tune, as Q_0 in equation 2 is the total tune of the machine. A first series of measurements have been performed in the SPS in order to validate the basic idea. The results are very good. For instance an agreement within 15% of the chromaticty measured via momentum change and the new method could be found over a wide range of chromaticities. One dataset from these measurements is reported in figure 7. It shows the measured head-tail phase shift turn by turn for 3 different values of of the sampling time interval $\Delta\tau$. As expected from equation 2 the dependence is linear. Any explanation of experimental details would leave the scope of this paper, but can be found in [11]
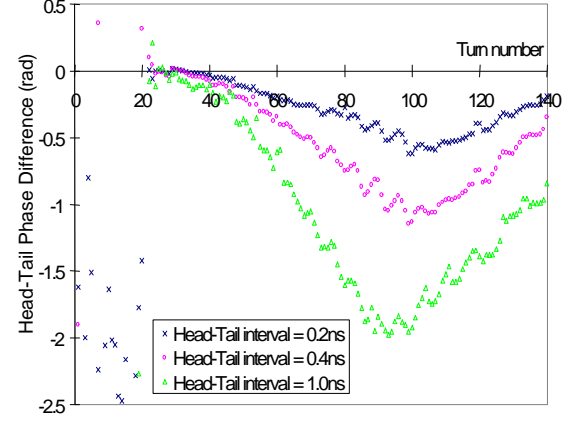
Fig. 6: Measured phase difference of head-tail betatron oscillations for 3 different sampling time intervals.

2.6 Discussion

By variation of the beam momentum and tune tracking a solid operational tool is available for dynamic chromaticity measurements. By extending the range of momentum variation even the non linear part of the chromaticty curve can be examined. But still the method has some limitations: The rate by which the beam momentum is changed can not made extremely short, for example in LEP the modulation cycle is limited to a 3 second interval. This is certainly too long for a chromaticity measurement during the start of acceleration, were a time resolution as short as 100 msec would be of interest. The LHC will require for the nominal beam currents tight control of the orbit, in particular in the collimation region. Periodic momentum changes and hence orbit changes in dispersive regions will be a problem. Secondly if one imagines the use of an online tune regulation loop a chromaticty measurement based on tune differences is very unfavourable. In that case the chromaticty would have to be deduced from the trims that the regulator has send to the quadrupoles in order to keep the tunes constant. With some sense for practical implementations one feels that this would not work!

For these reasons the development work on the head-tail sampling has been launched. The method provides a chromaticty reading independent of the betatron tunes and a measurement time of one synchrotron period (15 to 50 msec in case of the LHC). Further analysis will show the influence of octupolar fields, the limit in signal to noise ratio and consequently the amount of emittance growth that is linked with a single measurement.

3. Coupling Measurements

Coupling Measurements and Control are also important for the LHC. As the working point will be very close to the diagonal a bad compensation of betatron coupling will make tune and chromaticty measurements almost impossible. A very good and comprehensive summary of linear betatron coupling can be found in [12].

3.1 Closest Tune Approach

For this method both betatron tunes are measured during a linear power converter ramp, which crosses the values of the horizontal and vertical tunes. The remaining separation of the tune traces is a direct measure for the total coupling coefficent $|c|$. A measurement example from is shown in figure 7. In order to ensure that the PLL keeps tracking both tunes even when they approach each other the measurements are done on two different bunches.
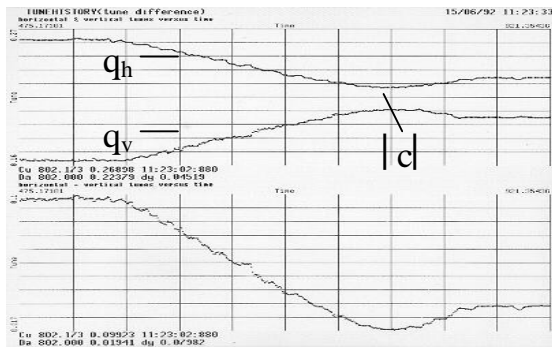
Fig. 7: PLL tune tracking during a swap of the tunes. The two top traces show the tunes, the bottom trace the tune difference reading.

3.2 Kick Method

The above method does not allow diagnostic during machine transitions. A better tool, although demanding quite large beam excitations for the measurement of small coupling coefficients, consists in applying a single kick in one plane and observing the time evolution of the betatron oscillations in both planes. The method is described in [12].

Summary

Comprehensive tools for tune, chromaticty and coupling measurements will be available for the diagnostic of dynamic phenomena in the LHC. The major development effort over the next years will be to improve the signal to noise ratio of the oscillation detectors for minimising the emittance blowup during the measurement. Control of the time evolution of these beam parameters will first of all be achieved by feed forward techniques, i.e. beam and magnetic measurements on one acceleration cycle and then incorporation of the necessary trims into the power converter functions.

In case the reproducibility of the machine is not good enough to comply with tight tolerances an online feedback on magnetic correction elements has to be implemented. It should be noted that none of the big present hadron storage rings make operationally use of an online feedback on tune, chromaticty or coupling. The implementation of online feedbacks demands an effort on two additional fronts: The design of the feedback itself taking into account the dynamic behaviour of all involved elements and secondly the design of reliable measurement systems, which deliver signals for the betatron tunes, chromaticities and eventually coupling, without the need of human interpretation of the results.

References:

[1] R. Bailey et al., "Dynamic Effects and their Control at the LHC", PAC97, Vancouver, 12-16 May 1997, LHC Project Report 124

[2] H. Schmickler, "Study of the Accuracy and Computation Time requirements for a FFT based Measurement of Betatron Oscillations in LEP", LEP/BI/Note 87-10

[3] - K.H. Mess, "Time and Frequency Domain Measurements", Presentation MOI2, this workshop.
- A. Stillman, "Wavelet Analysis and Accelerator Signals", Proc. of the BIW94, Vancouver (Canada)

[4] C. Boccard et al., "Tune Measurements in the SPS as Multicycling machine", Proc. of EPAC96, pp. 1600-1602, Sitges (Barcelona), 10-14 June 1996.

[5] I. Farago et al., "Performance of the LEP Q-Meter during Operation and Machine Studies", Proc. of EPAC90, Nice (France), June 12-16, 1990, CERN/SL/90-40(BI)

[6] K.D.Lohmann et al., "Design and Functionality of the LEP Q-Meter", Proc. of EPAC90, Nice (France), June 12-16, 1990, CERN/SL/90-32(BI)

[7] J. Klute, "A New Tune Measurement System for the HERA Proton Ring", Contribution TUP11, this workshop.

[8] G. Buur et al., "Dynamic Tune and Chromaticity Measurements in LEP", CERN SL/92-15(DI), paper presented at the 3rd EPAC, Berlin, 24 March 1992

[9] K. Cornelis et al., "Resonant behaviour of head-tail modes", SL-MD Note 145 (CERN).

[10] A. Hofmann, "Diagnostics and Cures for Beam Proc. of the 8th international conference on high energy accelerators, CERN 1971

[11] D Cocq, R. Jones and H. Schmickler, "Chromaticity Measurements from Head-Tail Phase-Shift", internal CERN publication in preparation and abstract submitted to EPAC98.

[12] P.J.Bryant, "A simple theory for weak betatron coupling", CERN accelerator school, CERN 89-03, pp 50ff.

2.2 Further Reading I:

High Sensitivity Tune Measurement by Direct Diode Detection
M.Gasior & R.Jones, Proceedings of Beam Instrumentation Workshop DIPAC, 2005

HIGH SENSITIVITY TUNE MEASUREMENT
BY DIRECT DIODE DETECTION

M. Gasior, R. Jones, CERN, Geneva, Switzerland

Abstract

The fractional part of the betatron tune for a circular accelerator can be measured by observing beam oscillations on a position pick-up. In frequency domain the betatron frequency is seen as sidebands on either side of the revolution harmonics. Usually beam signal pulses from the pick-up are very short with respect to the revolution period, resulting in a broadband spectrum.

Classical tune measurement systems filter out just one of the betatron sidebands. As a consequence, most of the betatron energy is lost and only a very small fraction remains for further processing. This paper describes a new method, referred to as Direct Diode Detection (3D). It is based on the idea of time stretching beam pulses from the pick-up in order to increase the betatron frequency content in the baseband. The 3D method was recently tested in the CERN SPS and PS, BNL RHIC and FNAL Tevatron machines. Results from all these machines [1, 2, 3, 4] show that this method can increase the betatron signal level by orders of magnitude as compared to classical systems, making it possible to observe tunes with no explicit excitation. Frequency resolution in the order of 10-5 and amplitude sensitivity in the order of 10 nm has been achieved with this very simple hardware.

HIGH SENSITIVITY TUNE MEASUREMENT
BY DIRECT DIODE DETECTION

M. Gasior, R. Jones, CERN, Geneva, Switzerland

Abstract

The fractional part of the betatron tune for a circular accelerator can be measured by observing beam oscillations on a position pick-up. In frequency domain the betatron frequency is seen as sidebands on either side of the revolution harmonics. Usually beam signal pulses from the pick-up are very short with respect to the revolution period, resulting in a broadband spectrum. Classical tune measurement systems filter out just one of the betatron sidebands. As a consequence, most of the betatron energy is lost and only a very small fraction remains for further processing. This paper describes a new method, referred to as Direct Diode Detection (3D). It is based on the idea of time stretching beam pulses from the pick-up in order to increase the betatron frequency content in the baseband. The 3D method was recently tested in the CERN SPS and PS, BNL RHIC and FNAL Tevatron machines. Results from all these machines [1, 2, 3, 4] show that this method can increase the betatron signal level by orders of magnitude as compared to classical systems, making it possible to observe tunes with no explicit excitation. Frequency resolution in the order of 10^{-5} and amplitude sensitivity in the order of 10 nm has been achieved with this very simple hardware.

3D PRINCIPLE AND THE HARDWARE

The crucial part of a 3D-based tune measurement system is the peak detector. Two such detectors connected to opposing electrodes of a beam position pick-up (PU) (see Fig. 1) yield the amplitude modulation envelope of the beam signals. Such signals, depicted in Fig. 2, are superimposed on a DC voltage related to the bunch amplitude (revolution frequency content). The signal difference, shown in Fig. 3 for single bunch in the machine, contains almost the whole bunch modulation amplitude, with a DC component related to the beam offset from the centre of the pick-up. Since the DC content can be easily suppressed by series capacitors, most of the corresponding revolution frequency (f_r) background can be removed by the peak detectors before the first amplifying stage. In Fig. 4 the f_r attenuation characteristic is shown assuming single bunch in the machine, which is the most difficult case to deal with. For a detector time constant $\tau = R_f C_f$, which is larger than the machine revolution period $T = 1/f_r$, the suppression of the revolution line goes as $4\tau/T$ [1]. This makes it possible to obtain f_r attenuation in the order of 50 dB for $\tau \approx 100$, which is easily achievable in practice.

The 3D circuit in Fig. 1 can be also understood as two sample-and-hold blocks, sampling bunch signals close to their maxima at the bunch repetition rate, downmixing the wideband bunch spectrum into the baseband.
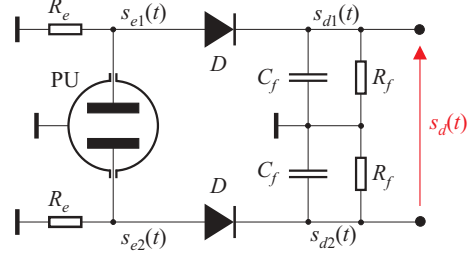

Figure 1: Direct Diode Detection principle.
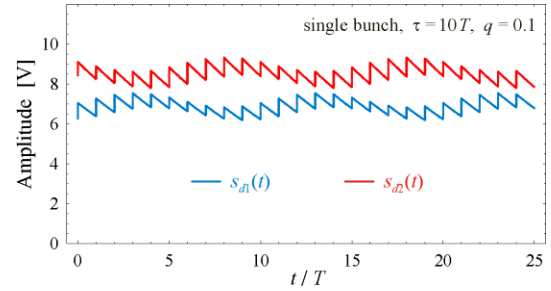
Figure 2: An example of peak detector voltages.
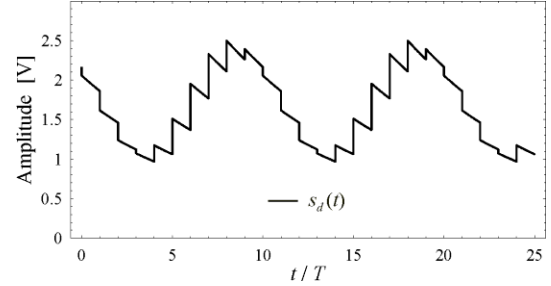
Figure 3: Difference of the signals in Fig. 2.
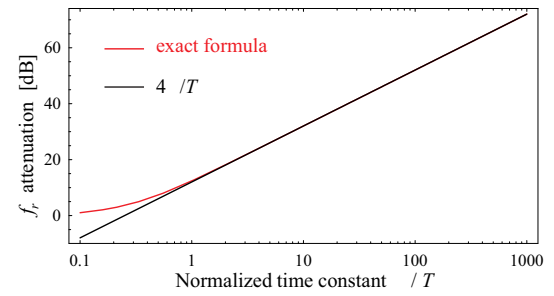
Figure 4: 3D circuitry revolution frequency attenuation.
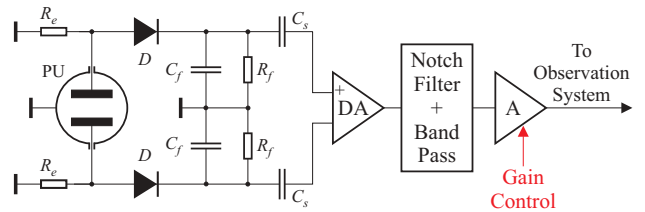
Figure 5: Block diagram of a 3D-BBQ system.

A block diagram of a 3D Base-Band Q (BBQ) measurement system is depicted in Fig. 5. The peak detector voltages with the DC content removed by the series capacitors are subtracted by the differential amplifier (DA), further increasing the suppression of f_r for beams close to the PU centre and improving the interference immunity. A notch filter attenuates f_r by another large factor, in the order of 100 dB [1]. The high cut-off frequency of the band pass filter is $0.5 f_r$, as for all possible tune values one betatron sideband is always present in the band $(0, f_r/2)$. The typical low cut-off is $0.1 f_r$, which means that the observation system only has to process frequencies between 0.1 and $0.5 f_r$. For large machines, therefore, the 3D-BBQ output signal can be digitised with a 24-bit audio ADC at the revolution frequency, requiring relatively little processing power to yield a signal spectrum through an FFT, or to build a tune tracker based on a digital phase-locked loop (PLL) [2].

Notice that a 3D-BBQ system is 'low frequency' only after the detectors, due to the 'time stretching' of the short beam pulses. Before the detectors the processed bandwidth can easily be as high as a few hundred MHz. In the detection process the spectral content from this wide bandwidth is converted to the baseband, resulting in a very high sensitivity.

3D-BBQ prototypes according to the block diagram of Fig. 5 have been installed on four machines, namely SPS ($f_r \approx 43$ kHz), PS ($f_r \approx 477$ kHz), RHIC ($f_r \approx 78$ kHz) and Tevatron ($f_r \approx 48$ kHz) (chronological order). All prototypes were based on very similar hardware, with only the notch and band-pass filters adjusted for the machine f_r.

A detailed comparison of the 3D and classical tune measurement methods are given in [1], together with a quantitative estimate of the signal to noise improvement given by the 3D method operated on a machine with a single bunch. This factor is in the order of 30 dB for the PS, 40 dB for RHIC and Tevatron, 50 dB for the SPS, and 60 dB for the LHC.

RESULTS

All installed prototypes were sensitive enough to observe betatron oscillations with no explicit beam excitation. Such oscillations, with amplitudes in the μm range, were seen to be almost always present in the beam.

Examples of such measurements made with the SPS BBQ prototype and no intentional beam excitation are shown in Fig. 6 and 7. Figure 6 shows the horizontal tune path for the lowest intensity SPS beam of $\approx 5 \cdot 10^9$ protons in a single bunch at 26 GeV, during a programmed tune change of $\approx 5 \cdot 10^{-3}$. Figure 7 shows the SPS horizontal tune variations induced by the jaws of an LHC collimator prototype as it was cycled between a fully opened position and a gap of 1.96 mm. This measurement was performed with a single bunch at 270 GeV and formed part of a series used to evaluate impedance-induced tune changes introduced by LHC collimators [5]. Tune variations as small as a few Hz could be resolved in this
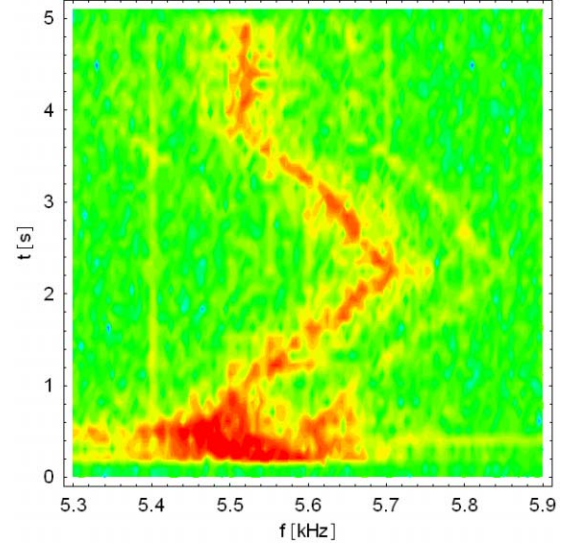
Figure 6: SPS, single bunch LHC pilot beam ($\approx 5 \cdot 10^9$ p$^+$).
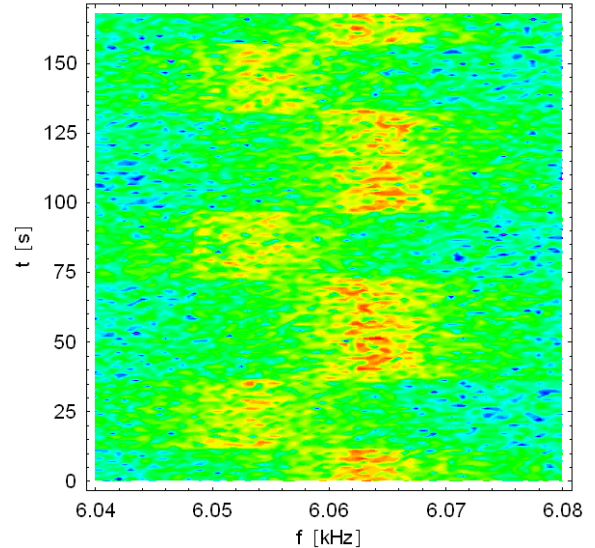
Figure 7: SPS, single bunch LHC beam ($\approx 10^{11}$ p$^+$).
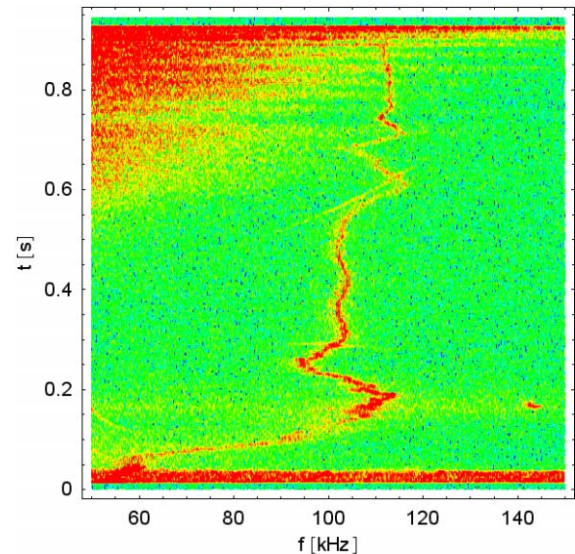
Figure 8: PS, AD beam (4 bunches, $\approx 4 \cdot 10^{12}$ p$^+$/b).

way, with the tune resolution in the order of 10^{-5}. These SPS measurements were acquired using a low cost 24-bit PC sound card followed by off-line spectral analysis.

Figure 8 shows the horizontal tune evolution measured by the PS BBQ prototype with no explicit excitation for a beam destined for the Antiproton Decelerator (AD), and accelerated from 1.4 to 26 GeV. The noise-like components appearing from the middle of the record onwards result from the RF beam gymnastics performed for this type of PS beam.

Figure 9 shows a vertical plane time record from the RHIC 3D-BBQ prototype, with the corresponding frequency spectra shown in Figure 10. The largest amplitude signals correspond to beam oscillations caused by high voltage sweeps, related to the operation of an Ionization Profile Monitor (IPM). Each excitation consists of a burst of a hundred pulses, applied every 100th revolution. If either of the tunes happen to be a multiple of $f_r/100$, then these kicks resonantly excite the beam, as seen in the spectra for frequencies around 17.1 kHz ($0.22 f_r$, close to the horizontal tune) and 17.9 kHz ($0.23 f_r$, vicinity of the vertical tune).

Mains harmonics are clearly visible around the betatron tune paths throughout the RHIC acceleration cycle. These lines increase considerably once the main ramping power supplies are turned on around 26 s from the beginning of the record. The corresponding increase in the time domain signal can be seen in Figure 9. The presence of mains harmonics in the beam spectrum is reported in detail in [3] and is thought to be caused by magnetic field ripple in the main RHIC dipoles. Similar phenomenon was observed with the 3D-BBQs on the SPS, PS and Tevatron.

A comparison at RHIC between spectra from calibrated, million turn BPM data and that of the 3D-BBQ data has quantified the noise floor of the RHIC BBQ prototype at less than 10 nm. This is an order of magnitude better than most existing tune measurement systems.

CONCLUSIONS

This paper has introduced the principle of tune measurement using Direct Diode Detection. It has been shown to be highly sensitive while using simple, cheap and robust hardware. Prototypes recently installed on four machines, namely the CERN SPS and PS, BNL RHIC and FNAL Tevatron, have given very good results and are in the process of being converted into fully operational systems. Due to the many advantages of this method, 3D baseband tune measurement systems will be gradually introduced on all circular machines at CERN. This includes the LHC, where it is hoped to use the 3D-BBQ as part of a PLL tune tracking system, for the measurement of tune, chromaticity and coupling [5], with the ultimate aim of providing reliable tune feedback.

The 3D method is still under development and its full potential has probably not yet been fully realised. Extensive studies will therefore continue on this technique.
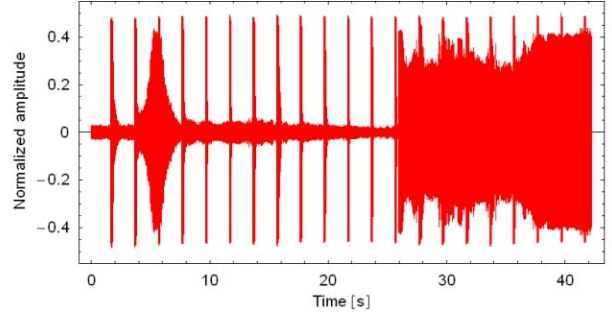
Figure 9: RHIC, a 3D-BBQ signal sound card record.
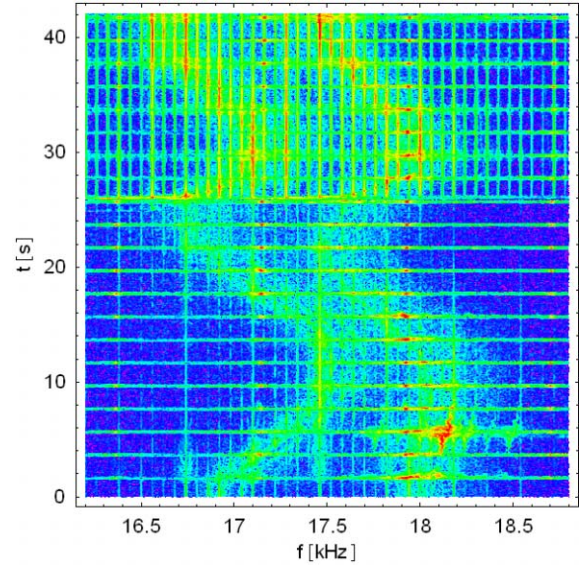
Figure 10: RHIC, spectra of the signal in Fig. 9.

ACKNOWLEDGMENTS

REFERENCES

[1] M. Gasior, R. Jones, "The Principle and First Results of Betatron Tune Measurement by Direct Diode Detection", CERN-LHC-Project-Report-8XX.

[2] P. Cameron et al., "Advances Towards the Measurement and Control of LHC Tune, Chromaticity, and Coupling", these proceedings.

[3] P. Cameron, M. Gasior, R. Jones, C.-Y. Tan, "The Effects and Possible Origins of Mains Ripple in the Vicinity of the Betatron Spectrum", this proceedings.

[4] C.-Y. Tan, "Novel Tune Diagnostics for the Tevatron", PAC 2005.

[5] H. Burkhardt et al., "Measurements of the LHC Collimator Impedance with Beam in the SPS", PAC 2005.

[6] P. Cameron, M. Gasior, R. Jones, Y. Luo , "Towards a Robust Phase Locked Loop Tune Feedback System - The Continuous Measurement of Global Betatron Coupling Using a Phase Locked Loop Tune Measurement System", these proceedings.

Chapter 3

Profile and Emittance Measurement

3.1   Introduction

Introduction to the Diagnostics of Transverse Beam Motion
Extracted from the CAS Proceedings, Trondheim, Norway, 2013

Introduction to the Diagnostics of Transverse Beam Motion

(Extracted from the Advanced CAS Proceedings, Trondheim, Norway, 2013 [1])

M. Gasior, R. Jones, T. Lefevre, H. Schmickler
CERN, Geneva, Switzerland

K. Wittenburg
DESY, Hamburg, Germany

EMITTANCE MEASUREMENT

The ultimate luminosity of any collider is inversely proportional to the transverse emittance of the colliding beams. Preservation of emittance and hence emittance measurements are therefore of particular importance in the long chain of accelerators and storage rings of big hadron colliders, as the emittance of a hadron bunch is not appreciably reduced through mechanisms such as the radiation damping associated with lepton machines.

In lepton machines, achieving the smallest possible vertical emittance is a common goal for damping rings for linear colliders, for particle factories based on the crab-waist collision scheme, and for light-source storage rings providing photon beams of highest brightness. The measurement of such small emittance beams is therefore very important and is one of the main challenges for modern day beam instrumentalists.

Good explanations of emittance can be found in Refs. [1, 2]. The emittance, which includes about 98% of the beam-particles, can be defined as

$$\varepsilon(98\%) = \frac{beamwidth^2 - \left(\frac{\Delta P}{P} \cdot D_m\right)^2}{\beta_m} = \frac{FWHM^2 - \left(\frac{\Delta P}{P} \cdot D_m\right)^2}{\beta_m} \qquad (4.1)$$

where FWHM is the measured full width at half height (2.35σ) of the beam, $\Delta P/P$ the FWHM of the momentum spread, D_m the value of the dispersion-function and β_m the value of the beta-function at the monitor position. From this equation one can immediately see that the measurement of emittance depends on many parameters. This limits the accuracy to which emittance can be calculated, which is generally with a precision no better than around 10%. A number of instruments are capable of measuring the beam profile quite precisely, but in calculating the emittance one also relies on knowledge of the beam optical parameters at the place of the instrument and these are often fraught with considerable uncertainties.

The remainder of this section is devoted to the measurement of beam size, from which the emittance is then calculated.

Scintillator and Optical Transition Radiation Screens

Scintillator screens have been used for nearly a century and are the simplest and most convincing device when one has to thread a beam through a transfer line and into and around an accelerator. The modern version consists of a doped alumina screen which is inserted into the beam and can stand high intensities and large amounts of integrated charge. In its simplest form a graticuled screen is observed using a TV-camera. It can deliver a wealth of information to the eye of an experienced observer, but only in a semi-quantitative way. Much can be done about that with modern means of rapid image treatment, but questions concerning the linearity of these screens at high beam densities remain.

Optical Transition Radiation (OTR) screens are a cheap substitute for scintillator screens. OTR radiation is generated when a charged-particle beam transits the interface of two media with different dielectric constants (e.g. vacuum to metal or vice versa) [3]. Since this is a surface phenomenon, the screens can be made of very thin foils which reduces beam scattering and minimises heat deposition. The radiation produced is emitted in two cones around the angle of reflection for backward (vacuum to

metal) OTR so that if the foil is placed at 45° to the beam direction, the radiation produced is at 90° to the beam direction. In addition two cones of forward OTR (metal to vacuum) are produced around the beam direction (see Fig. 1). The angular distribution of the emitted radiation has a central hole and a peak located at $1/\gamma$. The higher the value of γ the sharper the peaks and the more light can be collected, which is why OTR is generally suited to lepton or high energy hadron machines. However, the experience from modern, Linac-based, fourth-generation light sources (free electron lasers (FELs)) shows that OTR diagnostics fail because of coherence effects in the OTR emission process. As a consequence such machines have reverted to the use of scintillating screen monitors for transverse beam profile measurements, with additional effort to reach high-resolution imaging [4].

(a)   (b)
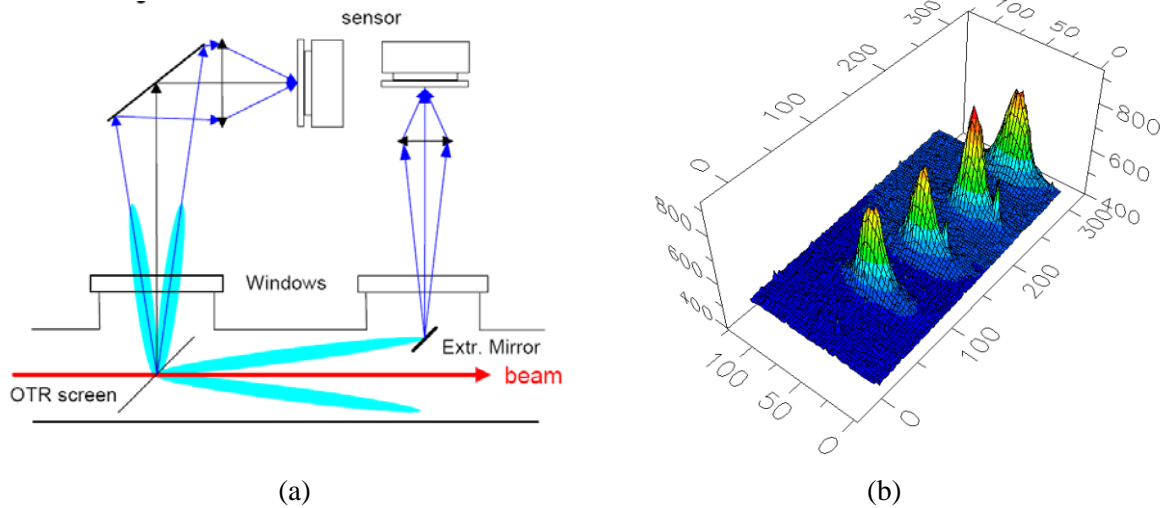
Fig. 1   (a) Backward and forward OTR patterns with their imaging schemes.
(b) Example of 2D OTR images taken every four turns at injection in the CERN-SPS.

SEM-Grids

Secondary Emission (SEM) Grids, also known as harps, consist of ribbons or wires which are placed in the beam. As the beam intercepts the grid, secondary emission occurs leading to a current in each strip which is proportional to the beam intensity at that location. By measuring this current for all strips a beam profile is obtained. SEM-grids are the most widely used means to measure the density profile of beams in transfer lines. In addition, sets of three, properly spaced (i.e. with the right phase advance between monitors), allow a determination of the emittance ellipse. What makes them popular is their simple and robust construction, the fact that there is little doubt about the measured distribution, and their high sensitivity, in particular at low energies and for ions. At higher energies they can be considered semi-transparent. Amongst their drawbacks are the limited spatial resolution (difficult to get the wire spacing much below 0.25mm) and the rather high cost for the mechanisms and electronics.

Wire Scanners

Of all the instruments used for measuring the emittance of circulating beams, wire-scanners are considered to be the most trustworthy. They come in two different types; rotative and linear. Rotative wire scanners consist of a thin wire (some tens of microns in diameter) mounted on a fork which is attached to a rotating motor (see Fig. 2), while linear scanners use motors which push/pull the wire across the beam. There are two ways of obtaining a beam profile with wire scanners; by measuring the secondary emission current as a function of wire position (similar to the SEM-grid acquisition mentioned above) or by measuring the flux of secondary particles created as the beam interacts with the wire. This latter technique is often used for high intensities, where the heating of the wire produces thermal emission which falsifies the secondary emission results. It relies on the use of radiation

detectors, typically scintillators followed by photo-multipliers, placed downstream of the wire scanner to detect the γ-radiation and secondary particles produced when the wire intercepts the beam. To make the flux collected independent of the wire position may require the summation of the signals from two or more detectors positioned around the beam chamber.

Fast wire scanners are nearly non-destructive over a wide range of energies. Their spatial resolution can reach the micrometer range and, with fast gated electronics, the profiles of individual bunches can be observed. Their great sensitivity also allows them to be used for the study of beam halos.
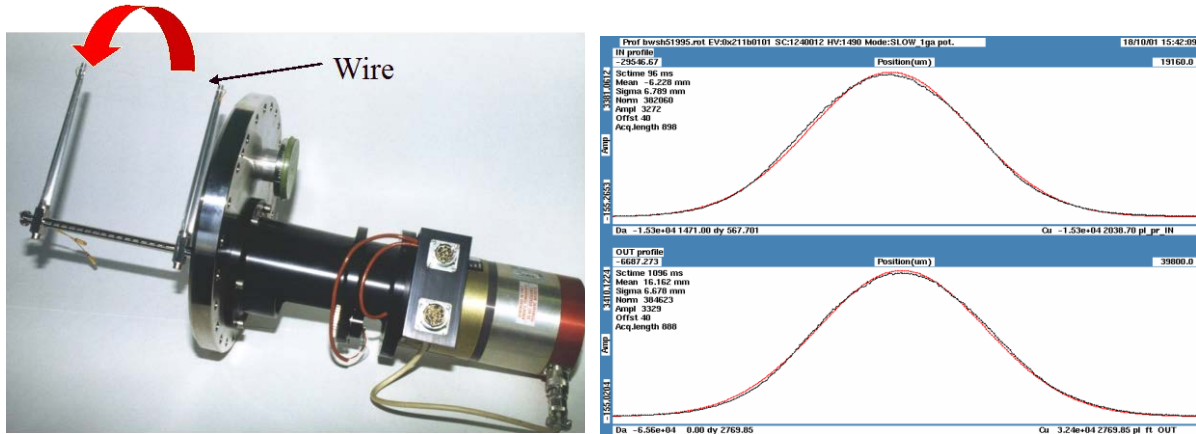
Fig. 2 Rotative wire scanner and an example of a wire scanner profile measurement.

Residual Gas Monitors

Ionization Profile Monitors

Ionization profile monitors are used in many high-energy accelerators in order to reconstruct transverse beam distributions (see e.g. Ref. [5]). The signal results from the collection of either the ions or the electrons produced by the beam ionizing the small amount of residual gas in the vacuum chamber. These ions or electrons are accelerated using a bias voltage of several kilovolts and collected on a micro channel plate (MCP). The avalanche of electrons produced by the MCP then either hits a phosphor screen, giving an image of the beam profile that can be monitored using a charge-coupled device (CCD) camera (see Fig. 3), or impinges on a strip detector that can be read-out to give a profile. Due to their rigidity, ions are less sensitive to the distorting effects of the space charge from the circulating beam, but their slow drift time, even with high bias voltages, means that they spend a long time in this beam field, making it difficult to analyse rms beam dimensions smaller than one millimetre. In order to use electrons to produce an image, a transverse magnetic field needs to be added, around which the electrons spiral on their way to the MCP. This eliminates, to a large extent, the space charge effects of the beam and allows sharper images to be produced than with ions. This additional magnetic field, however, is also seen by the beam and has to be compensated by corrector magnets either side of the ionization profile monitor.
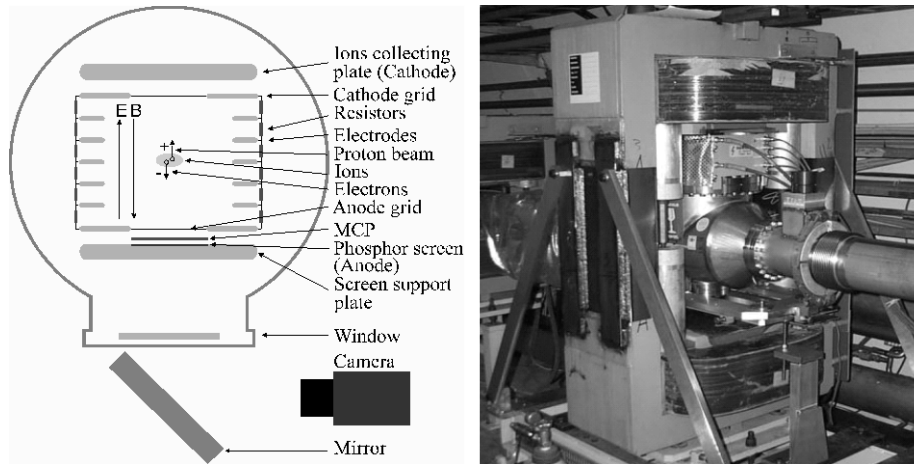
Fig. 3 Principle of a residual gas ionisation profile monitor and an example from the CERN-SPS.

Luminescence Monitors

Luminescence monitors (see e.g. Ref. [6]) also rely on the interaction of the beam with a gas in the vacuum chamber. The traversing beam excites electrons in the gas molecules from the ground state to a higher energy level. Once the beam has passed the electrons return to the ground state and emit photons of a precise wavelength. In the case of nitrogen the dominant photon wavelength is 391.3 nm, corresponding to light at the lower end of the visible range, for which many detectors are available. In general, the residual gas alone does not produce enough photons for accurate imaging and hence a local pressure bump is usually created by injecting a small amount of gas to enhance the photon production. The principle of luminescence monitoring and a schematic layout of such an instrument are shown in Fig. 4.

Fig. 4: Principle of luminescence monitoring and an example set-up

Most users consider both the residual gas ionisation and luminescence profile monitors to be semi-quantitative and not be relied upon for absolute emittance measurements, even after calibration against some other instrument such as a wire scanner. Their virtual transparency for the beam, however, makes them useful for the continuous on-line tracking of beam size.

Synchrotron Radiation Monitors

Synchrotron radiation monitors are limited to highly relativistic particles and offer a completely nondestructive and continuous measurement of the two-dimensional density distribution of the beam. These monitors make use of the light produced when highly relativistic particles are deflected by a magnetic field. They are therefore usually positioned to make use of parasitic light produced by a

dipole magnet in the machine or behind a purpose-built 'wiggler' or 'undulator' magnet in which the beam is deflected several times to enhance photon emission.

The most common way of measuring the beam size with synchrotron radiation is to directly image the extracted light using traditional optics and a camera. The spatial resolution of such systems is usually limited by diffraction and depth-of-field effects. If the beam is sufficiently relativistic then the photon emission extends into the hard X-ray region of the spectrum and X-ray detectors can be used, for which diffraction effects can be almost disregarded. High-brilliance third-generation synchrotron light sources use special X-ray optics (e.g. pinhole, compound refractive lens, coded aperture, Fresnel zone plate, etc.) to achieve the required resolution (≈ 1 μm) for their small beam sizes. A way to overcome the resolution limits in the optical range is to use interferometry or point spread function analysis of the π-polarization of the visible synchrotron light [7, 8].

REFERENCES

[1] E. Wilson, Transverse beam dynamics, CAS, CERN 85-19, Vol. 1 (1985).

[2] J. Buon, Beam phase space and emittance, CAS, CERN 91-04 (1991).

[3] J. Bosser *et al*., Optical transition radiation proton beam profile monitor, CERN/SPS 84-17 (1984).

[4] Ch. Wiebers *et al*., Scintillating screen monitors for transverse electron beam profile diagnostics at the European XFEL, Proc. IBIC2013, Oxford, 2013.

[5] T. Giacomini, P. Forck *et al*., Ionization profile monitors—IPM @ GSI, Proc. DIPAC2011, Hamburg, 2011.

[6] F. Becker, Beam induced fluorescence monitors, Proc. DIPAC2011, Hamburg, Germany, 16–18 May, 2011.

[7] S. Takano, Beam diagnostics with synchrotron radiation in light sources, Proc. IPAC'10, Kyoto, 2010.

[8] A.S. Hernandez *et al*., The new SLS beam size monitor, first results, Proc. 4th IPAC2013, Shanghai, 2013.

Profile and Emittance Measurement using Synchrotron Light

3.2 Introduction to Synchrotron Light Monitors

Synchrotron Light Monitors
K. Wittenburg

Synchrotron light profile monitor

In electron accelerators the effect of synchrotron radiation (SR) can be used for beam size measurements. In this course we will focus on profile determination, but SR can also be used for bunch length measurements with e.g. streak cameras with a resolution of < 1 ps.

From classical electrodynamics the radiated power is given for a momentum change dp/dt and a particle with mass m_0 and charge e:

$$P_{SR} = \frac{e^2 c}{6\pi\varepsilon_0 (m_0 c^2)} \left[\frac{dp}{dt} \right]^2$$

For linear accelerators dp/dt = dW/dx. For typical values of dW/dx = 10 - 20 MeV/m the SR is negligible. In circular machines an acceleration perpendicular to the velocity exists mainly in the dipole magnets (field B) with a bending radius $\rho = \beta\gamma m_0 c/(eB)$. The total power of N circulating particles with $\gamma = E/m_0 c^2$ is than

$$P_{tot} = \frac{e^2 c \gamma^4}{6\pi\varepsilon_0 \rho^2} N$$

This expression is also valid for a ring having all magnets of the same strength and field-free sections in between.

The critical wavelength λ_c divides the Spectrum of SR in two parts of equal power:

$$\lambda_c = \frac{4\pi\rho}{3\gamma^3}$$
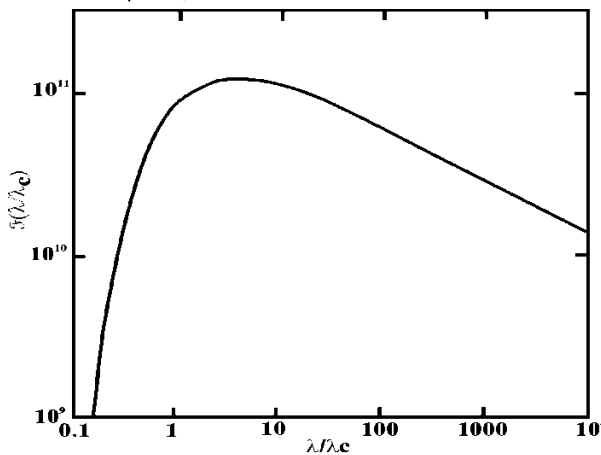
flux integrated over all ψ (Krinsky *et al.* 1983).

The opening angle Ψ of the SR (1/2 of cone!) for $\lambda \gg \lambda_c$:

$$\Psi = \frac{1}{\gamma} \left(\frac{\lambda}{\lambda_c} \right)^{1/3} = \left(\frac{3\lambda}{4\pi\rho} \right)^{1/3}$$

Path length s:

s = $\rho\theta$

ρ = Bending radius of Dipole

$$\delta\rho \approx 1.22 \frac{\lambda}{\theta}$$

$$\Delta\rho = \frac{\rho\theta^2}{8}$$

Synchrotron Radiation

$$\Psi = \frac{1}{\gamma}\left(\frac{E_c}{E}\right)^{\frac{1}{3}}$$

l_s

ρ

θ

θ

D

THE ELECTROMAGNETIC SPECTRUM

| Wavelength (in meters) | 10^3 | 10^2 | 10^1 | 1 | 10^{-1} | 10^{-2} | 10^{-3} | 10^{-4} | 10^{-5} | 10^{-6} | 10^{-7} | 10^{-8} | 10^{-9} | 10^{-10} | 10^{-11} | 10^{-12} |

longer ← Size of a wavelength → shorter

Soccer Field   House   Baseball   This Period   Cell   Bacteria   Virus   Protein   Water Molecule

Common name of wave

RADIO WAVES   INFRARED   VISIBLE   ULTRAVIOLET   "HARD" X RAYS

MICROWAVES   "SOFT" X RAYS   GAMMA RAYS

Sources

AM Radio   FM Radio   Microwave Oven   Radar   People   Light Bulb   Advanced Light Source   X-Ray Machines   Radioactive Elements

| Frequency (waves per second) | 10^6 | 10^7 | 10^8 | 10^9 | 10^{10} | 10^{11} | 10^{12} | 10^{13} | 10^{14} | 10^{15} | 10^{16} | 10^{17} | 10^{18} | 10^{19} | 10^{20} |

lower ← → higher

| Energy of one photon (electron volts) | 10^{-9} | 10^{-8} | 10^{-7} | 10^{-6} | 10^{-5} | 10^{-4} | 10^{-3} | 10^{-2} | 10^{-1} | 1 | 10^1 | 10^2 | 10^3 | 10^4 | 10^5 | 10^6 |

An Example: HERAe

Synchrotron radiation profile monitor in HERAe

R = ρ = 604814.3 mm
G = O-L = 6485.5 mm
B = L-Z = 1182.3 mm
O-S1 = 6216 mm
L = O_a-O_i = 1035 mm
opening angle (horizontal): tanθ/2 = d/2/6216 => θ/2 = arc tan d/2/6216 = <u>0.85 mrad</u>
opening angle (vertikal): Ψ(λ) = 1/γ (λ/$λ_c$)$^{1/3}$
with
γ = E/$m_0$$c^2$ = E [MeV]/0.511 = 23483 at 12 GeV and 52838 at 27 GeV
and

$$\lambda_c = \frac{4\pi\rho}{3\gamma^3} = 0.017 \, nm << \lambda \approx 500 \, nm$$

References attached

A Review of Optical Diagnostics Techniques for Beam Profile Measurements.
J A Clarke
EPAC94
http://accelconf.web.cern.ch/AccelConf/e94/PDF/EPAC1994_1643.PDF

Further readings:

Characteristics of synchrotron radiation/ Hofmann, A ;
In: CAS - CERN Accelerator School : Synchrotron Radiation and Free Electron Lasers,
Grenoble, France, 22 - 27 Apr 1996 - CERN, Geneva, 1998. [CERN-98-04]
http://doc.cern.ch/archive/cernrep//1998/98-04/p303.pdf

DIAGNOSTICS FOR ULTRA-LOW EMITTANCE BEAMS
J.W. Flanagan, KEK, Tsukuba, 305-0801 Japan
IPAC2011
http://accelconf.web.cern.ch/AccelConf/IPAC2011/papers/weyb01.pdf

Optical resolution of beam cross-section measurements by means of synchrotron radiation,
A. Hofmann, F. Meot, Nucl. Instr. Meth. 203 (1982) 483

Accurate and Efficient Computation of Synchrotron Radiation in the Near Field Region
O. Chubar, P. Elleaume, ESRF, Grenoble, France
Proc. EPAC 1998 Stockholm, Sweden
http://accelconf.web.cern.ch/AccelConf/e98/PAPERS/THP01G.PDF

Synchrotron Radiation Profile Monitor for HERA Positron Beam
G. Kube, Rainer Fischer, Kay Wittenburg - Deutsches Elektronen Synchrotron DESY
11th Beam Instrumentation Workshop, May 3-6 2004, Knoxville, Tennessee, USA
http://adweb.desy.de/mdi/downloads/Kube BIW04.pdf

Detailed Resolution Studies of the Synchrotron Radiation Profile Monitor for HERAe
Gero Kube, Rainer Fischer, Kay Wittenburg (DESY, Hamburg)
Proc. DIPAC 2005 Lyon
http://accelconf.web.cern.ch/AccelConf/d05/PAPERS/POT025.PDF

Interferometer:

SPATIAL COHERENCY OF THE SYNCHROTRON RADIATION AT THE VISIBLE LIGHT REGION AND ITS APPLICATION FOR THE ELECTRON BEAM PROFILE MEASUREMENT.
By T. Mitsuhashi (KEK, Tsukuba). KEK-PREPRINT-97-56, May 1997. 4pp. Talk given at 17th IEEE Particle Accelerator Conference (PAC 97): Accelerator Science, Technology and Applications, Vancouver, Canada, 12-16 May 1997.
http://accelconf.web.cern.ch/accelconf/pac97/papers/pdf/3V016.PDF

Intensity Interferometer and its application to Beam Diagnostics,
Elfim Gluskin, ANL,
PAC 1991 San Francisco
http://accelconf.web.cern.ch/AccelConf/p91/PDF/PAC1991_1169.PDF

MEASUREMENT OF SMALL TRANSVERSE BEAM SIZE USING INTERFEROMETRY
T. Mitsuhashi
High Energy Accelerator Research Organisation, Oho, Tsukuba, Ibaraki, 305-0801 Japan
DIPAC 2001 Proceedings - ESRF, Grenoble
http://accelconf.web.cern.ch/AccelConf/d01/papers/IT06.pdf

Recent Progress in SR Interferometer
Authors: T.M. Mitsuhashi [KEK, Ibaraki, Japan]
IBIC2012
http://accelconf.web.cern.ch/AccelConf/IBIC2012/papers/weic02.pdf

3.3 Further Reading I:

A Review of Optical Diagnostics Techniques for Beam Profile Measurements

J A Clarke, Proceedings of European Particle Accelerator Conference EPAC94, 1994

A Review of Optical Diagnostics Techniques for Beam Profile Measurements.

J A Clarke

DRAL Daresbury Laboratory, Daresbury, Warrington WA4 4AD, UK

Abstract

The measurement of beam profiles using optical detectors is widespread. This paper reviews the various optical techniques employed in the community and points out the advantages and disadvantages for each one, illustrated by practical examples including experience with systems at the Daresbury SRS. Fundamental imaging limitations will be discussed together with calibration methods.

1. INTRODUCTION

In every particle accelerator the beam profile is an important parameter. Many methods exist for determining the beam profile, including several destructive techniques. This paper deals only with methods which rely on emitted visible synchrotron radiation from bending magnets as the diagnostic means. A review of the imaging resolution is given, followed by a discussion of optical detectors in use in the accelerator community. Possible calibration methods are also highlighted.

2. IMAGING RESOLUTION

The resolution of profile measurements by synchrotron radiation (SR) is strictly limited by fundamental effects. It is important that these effects are minimised so that the best resolution is obtained for the profile measurement. The horizontal and vertical cases are not the same; they are dealt with separately below.

2.1 Horizontal Case

2.1.1 Chromatic Error

In precise optical imaging of SR it is necessary to monochromate the light. This is most easily achieved with a bandpass filter. Typically a filter with a 500 nm centre wavelength and 30 nm bandwidth is used. However, as will be shown later, shorter wavelengths will improve the resolution.

2.1.2 Depth of Field Error

By its very nature the electron beam is a long source of light. This means that the imaging of the SR will produce a significant depth of field error, dependent upon the acceptance angle. For the simple case, illustrated in figure 1, the depth of field error is given by:

$$\sigma_{df} = \frac{L}{2}\theta \tag{1}$$

where L is the length of the source and θ is the half-acceptance angle. Note that L is given by:

$$L = 2R(\theta + \sigma_{SR}) \tag{2}$$

where R is the electron orbit radius and σ_{SR}, the natural opening angle of the photon beam, is given by:

$$\sigma_{SR} = \left(\frac{3\lambda}{4\pi R}\right)^{1/3} \tag{3}$$

for the case where λ, the wavelength of the light, is much longer than the critical wavelength. This is usually the case for visible wavelengths. Note that σ_{SR} is the same in both planes.

Figure 1. Depth of field error sketch.

2.1.3 Diffraction Error

Any imaging problem that involves apertures will inevitably have a diffraction error. Contrary to the depth of field error in the previous section, this error increases as the aperture is decreased. It is usual to restrict the aperture with either a circular iris or a vertical slit. The formulae for the diffraction resolution for these two cases are given below [1]. For an iris,

$$\sigma_{diff} = 0.61\frac{\lambda}{\theta} \tag{4}$$

and for a slit,

$$\sigma_{diff} = 0.5\frac{\lambda}{\theta}. \tag{5}$$

Clearly, a vertical slit will give the better resolution.

2.1.4 Curvature Error

Due to the nature of the source, the curvature of the electron beam also contributes an error term that limits the horizontal resolution. From the geometry shown in figure 2 it is straightforward to derive the apparent width of the source as:

$$\sigma_{curv} = \frac{R\theta^2}{2}. \tag{6}$$
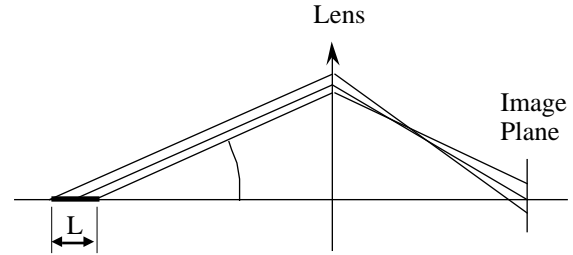
So, for a particular wavelength, the best resolution is found by minimising the sum of the squares of the three error terms described in equations (1), (5) and (6). For the SRS with R = 5.5 m, σ_{SR} = 2.8 mrad and λ = 500 nm, the optimum value of θ is 2.6 mrad, defined by a vertical slit. This gives a combined value of 125 μm for the apparent width of a negligible cross-section beam.
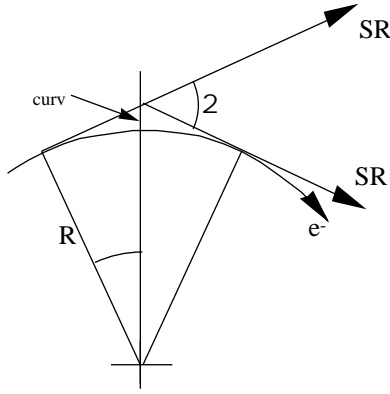
Figure 2. Curvature error sketch.

2.2 Vertical Case

For the vertical case the chromatic and depth of field errors are as for the horizontal. However, in the horizontal case the relevant diffraction effect and the depth of field error were both in the same plane. This is not true for the vertical case. Here the depth of field is again determined by the horizontal acceptance, but the diffraction is now only of consequence in the vertical plane. This means that the horizontal acceptance must be set to limit the depth of field and that any vertical acceptance limit will introduce unnecessary broadening due to diffraction. Therefore, in the vertical plane it is most advantageous to use a vertical slit instead of a circular iris. The minimum diffraction error is determined by the natural opening angle of the source. The diffraction limited resolution in the vertical plane can be estimated by replacing   by $_{SR}$ in equation (5). The difference between using a slit and an iris is illustrated in figure 3 for the SRS.
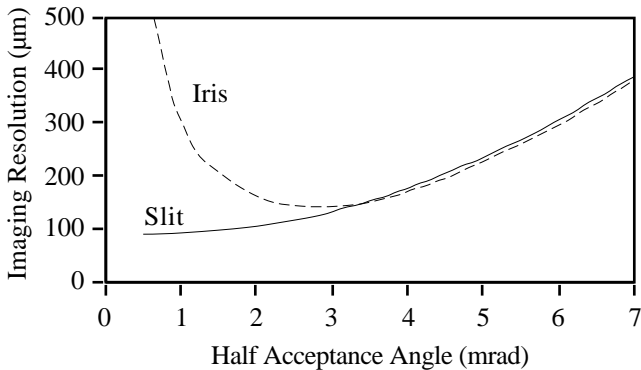
Figure 3. Apparent vertical width of a beam of narrow cross-section vs half acceptance angle for a slit and a circular iris.

Clearly the best vertical resolution is found by using a narrow vertical slit. However, since it is common to measure the profile of both planes with the same detector (eg a CCD camera) this is not always practical. Generally a compromise must be found between the resolution of the two planes in setting the horizontal acceptance, but since the vertical source size is usually much smaller than the horizontal it is normal to sacrifice some horizontal resolution in favour of the vertical. In fact, in modern 3rd generation light sources the vertical beam size may be significantly less than the diffraction limited resolution. In this case accurate profile measurements can best be made with light of a significantly shorter wavelength.

3. CHARGE COUPLED DEVICES

The most common detector used for measuring beam profiles is the Charge Coupled Device (CCD). Such a device is a solid state detector that essentially consists of an array of discrete potential wells (known as pixels) that store accumulated charge. The charge, induced by incident photons, is read out sequentially. A complete description of CCDs is given in ref [2]. The CCD chip has a well defined geometry, which makes them ideal for metrology, with typical pixel sizes of 20 μm x 20 μm. Each chip will contain something like 512 x 512 pixels.

CCDs can have two geometries, Frame Transfer and Inter-Line Transfer (figure 4). Both of these can be used for profile measurements. The difference between the two types relates to the method used for reading out the accumulated charge. Each CCD has a memory area that is light insensitive to which all of the stored charges are transferred after a fixed integration time. The Frame Transfer type has a better horizontal spatial resolution but the Inter-Line type has a faster image to memory shift [3].
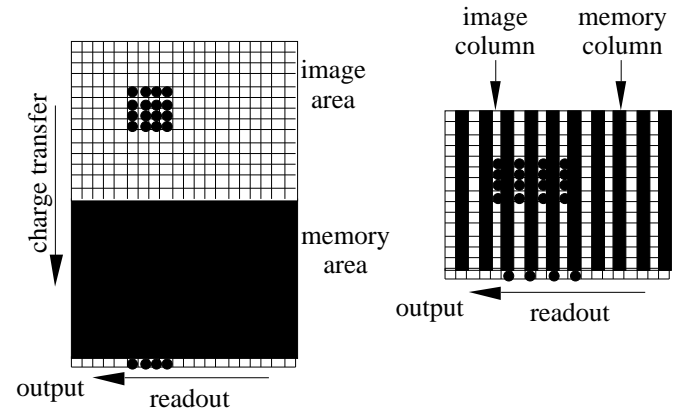
Figure 4. The two types of CCD detector. Frame Transfer on the left and Inter-Line Transfer on the right.

In order to use these devices for profile measurements it is necessary to connect the CCD camera to a framegrabber. A framegrabber is a device that interrogates the CCD and stores the reading for each pixel in buffer memory. It essentially consists of an Analogue to Digital Converter and some RAM (eg for an 8 bit ADC and 512 x 512 pixel array, 256 kbytes are required).

The CCD and framegrabber each have their own internal clocks for controlling timing functions. To achieve the best resolution it is necessary to synchronise these internal clocks [4] although for most applications this would only prevent a small error.

The framegrabber is usually a plug-in computer card. The values in the framegrabber memory can be manipulated by the computer to find the beam profiles. Although the framegrabber generally comes with some commercial software, this is not normally sufficient. It is not uncommon to have to write software for controlling the framegrabber and for determining the beam profiles. This software will have to determine the

centre of the beam using some peak detection algorithm, and then select the appropriate pixels for each plane. This is not straightforward and may need to be optimised for each particular application. For example, at Elettra this has been resolved by averaging and smoothing [5].

It is important to remember when using CCD cameras that the output is not necessarily linear with light intensity. It is common for camera manufacturers to apply a so-called 'gamma correction' to the CCD output to compensate for the fact that TV monitors have a non-linear response. Although the optical detector itself is inherently linear, the electronics in most cameras applies a logarithmic scaling to the output. If this correction factor is not removed either by adjusting the camera hardware or software then the CCD will not give accurate beam profile measurements [6].

It is often desirable to measure several beam profiles rapidly, over a few ms say, to investigate beam damping or instability. Unfortunately CCDs are relatively slow, running at TV refresh rate speeds. By screening off 90% of the optical detector (Frame Transfer type) and using it as a memory area it has been shown that it is possible to measure a short burst of profiles at around 10 kHz [7].

It is also useful to be able to monitor beam profiles from linacs or synchrotrons at their repetition rates of typically 50Hz. This can best be achieved by using fast shutters locked to the beam cycle. Mechanical shutters are possible but electro-optical ones are preferred. These are a sandwich of a photocathode, micro-channel plate and phosphor screen. The shutter is controlled by gating the accelerating potential across the micro-channel plate. Such a shutter has been used to monitor profiles stroboscopically turn-by-turn in the SLC damping rings [8].

4. PHOTODIODE ARRAYS

An alternative detector that can be used for measuring profiles is the Photodiode Array (PDA) [9]. This is a one dimensional strip of photodiodes (typically 25 μm long) that have an output that is linearly dependent upon the light intensity. This is a purely analogue device, unlike the CCD and framegrabber. The photodiodes are read sequentially and the output can be observed on a scope.

Of course, since the arrays are one dimensional the profile of only one plane can be observed. Therefore two arrays are required to measure both horizontal and vertical profiles simultaneously. This does however have the advantage of allowing the optical system to be optimised for each plane unlike the two dimensional CCD. The other advantage of the one dimensional array is that the need to find the centre of gravity of the beam is removed, greatly simplifying the measurement procedure.

Unlike the CCD the PDA does not lend itself easily to computer control. One method of overcoming this is to control the scope observing the PDA output. This has been successfully demonstrated at Daresbury where the scope is controlled over the GPIB interface [10]. Here, the scope trace is captured by the computer and the profile determined.

Typical integration times for PDAs are 25 ms, so like the CCD they are not ideally suited to rapid profile measurements.

However the fast shutter that was mentioned in the previous section could equally well be applied to the PDA.

5. CALIBRATION

An important requirement that must not be overlooked is proper calibration of the detector. In many cases the accuracy of the final measurement is limited by calibration error rather than by imaging resolution. Calibration here refers to the determination of the magnification of the optical system employed and so relates the measured profile width in the laboratory to the actual width in the storage ring.

Of course, if the focal lengths of the lenses used is well known then a theoretical calibration can be predicted. However it is always desirable to check this by experiment. This can best be achieved by moving the electron beam by a known amount and measuring how far the focussed image moves. The electron beam can be moved with local bumps or by varying the RF frequency, so long as the change in position of the beam is accurately known.

6. SUMMARY

Measurement of beam profiles with synchrotron radiation is now commonplace. A review has been given of the points that need to be considered when deciding upon a particular technique. The simplest method to use is based upon a photodiode array detector. However, the most common method employed is with a CCD camera and framegrabber. This may take longer to commission because of software requirements but the final product has greater potential.

7. REFERENCES

[1] A. Hofmann and F. Meot, "Optical Resolution of Beam Cross-Section Measurements by means of Synchrotron Radiation", Nucl. Inst. Meth., 203 (1982), pp 483 - 493.

[2] J.A. Hall, "Arrays and Charge-Coupled Devices", in Applied Optics and Optical Engineering, Academic Press, 1980, pp 349 - 400.

[3] R. Jung, "Image Acquisition and Processing for Beam Observation", Proceedings of the First European Workshop on Beam Diagnostics and Instrumentation for Particle Accelerators, Montreux, Switzerland, May 1993, pp 54 - 63.

[4] J.M. Raynor and P. Seitz, "The Technology and Practical Problems of Pixel-Synchronous CCD Data Acquisition for Optical Metrology Applications", SPIE vol. 1395, pp 96 - 103.

[5] G.R. Aiello and F. Cavazzoni, "The Beam Profile Monitors for Elettra", Proceedings of the European Particle Accelerator Conference, Nice, France, June 1990, pp 747 - 749.

[6] Y. Hashimoto et al, "Beam Profile Monitor using Alumina Screen and CCD Camera", Eighth Symposium on Accelerator Science and Technology, Japan, November 1991.

[7] C. Bovet et al, "The LEP Synchrotron Light Monitors", Proceedings of the IEEE Particle Accelerator Conference, San Francisco, USA, May 1991, pp 1160 - 1162.

[8] M. Minty et al, "Using a Fast-Gated Camera for Measurements of Transverse Beam Distributions and Damping Times", Proceedings of the 1992 Accelerator Instrumentation Workshop, Berkeley, USA, October 1992.

[9] R.J. Nawrocky et al, "A Beam Profile Monitor for the NSLS VUV Ring Employing Linear Photodiode Arrays", IEEE Trans. Nucl. Sci., NS-32, 1985, pp 1893 - 1895.

[10] J.A. Clarke and P.A. McIntosh, "The Application of LabVIEW for Data Acquisition at an Accelerator Laboratory", these proceedings.

Profile and Emittance Measurement using Wire Scanners

3.4   References:

References attached:

**High Resolution Measurements of Lepton Beam Transverse Distributions
with the LEP Wire Scanners.**
J. Camas, G. Crockford, G. Ferioli. C. Fischer, J.J. Gras, R. Jung, J. Koopman. J. Mann
CERN CH-1211 Geneva 23,Switzerland
PAC93
http://accelconf.web.cern.ch/AccelConf/p93/PDF/PAC1993_2504.PDF

Design of a High-precision Fast Wire Scanner for the SPS at CERN
R. Veness, N. Chritin, B. Dehning, J. Emery, J.F. Herranz Alvarez, M. Koujili, S.
Samuelsson, J.L. Sirvent Blasco; CERN, Geneva, Switzerland
International Beam Instrumentation Conference, IBIC2012, Tsukuba, Japan, Oct 1-4,
2012
http://ibic12.kek.jp/prepress/papers/mopb79.pdf

Further readings

Conventional Wire Scanners at TESLA
K.Wittenburg
Tesla Report 2000-18
http://adweb.desy.de/mdi/downloads/conventional wire at tesla.pdf

SNS LINAC WIRE SCANNER SYSTEM, Signal Levels and Accuracy;
M. A. Plum, et al,
LINAC2002
http://cern.ch/AccelConf/l02/PAPERS/MO458.PDF

**Analysis of the Influence of Fibre Diameter on Wirescanner Beam Profile
Measurements**
Q. King; SPS-ABM-TM/Note/8802 (1988))
http://adweb.desy.de/mdi/documentation/wire_scanner_at/ttf_new/analysis.pdf

OBSERVATION OF THERMAL EFFECTS ON THE LEP WIRE SCANNERS.
J. Camas, C. Fischer, J.J. Gras, R. Jung, J. Koopman (CERN). CERN-SL-95-20-BI,
May 1995. 4pp. Presented at the 16th Particle Accelerator Conference - PAC 95,
Dallas, TX, USA, 1 - 5 May 1995. Published in IEEE PAC 1995:2649-2651)
http://accelconf.web.cern.ch/AccelConf/p95/ARTICLES/TPC/TPC21.PDF

**CAVITY MODE RELATED WIRE BREAKING OF THE SPS WIRE
SCANNERS AND LOSS MEASUREMENTS OF WIRE MATERIALS**
F. Caspers, B. Dehning, E.Jensen, J. Koopman, J.F. Malo, CERN, Geneva, Switzerland
F. Roncarolo, CERN/University of Lausanne, Switzerland; DIPAC03)
http://accelconf.web.cern.ch/AccelConf/d03/papers/PM12.pdf

QUARTZ WIRES VERSUS CARBON FIBERS FOR IMPROVED BEAM HANDLING CAPACITY OF THE LEP WIRE SCANNERS.
By C. Fischer, R. Jung, J. Koopman (CERN). CERN-SL-96-09-BI, May 1996. 8pp. Talk given at 7th Beam Instrumentation Workshop (BIW 96), Argonne, IL, 6-9 May 1996.

Thermal Load on Wirescanners
Lars Fröhlich
37th ICFA Advanced Beam Dynamics Workshop on Future Light Sources; May 15-19, 2006 in Hamburg, Germany
http://www.desy.de/~ahluwali/technicalnotes/2006_02.pdf

Operational Limits of Wire Scanners on LHC Beam
Mariusz Sapinski, Tom Kroyer (CERN, Geneva)
2008 Beam Instrumentation Workshop (BIW08) held on May 4-8, 2008 at the Granlibakken Conference Center and Lodge in Tahoe City, CA, USA, pp.383-388
http://www.als.lbl.gov/biw08/papers-final/TUPTPF066.pdf

Carbon Fiber Damage in Accelerator Beam
CERN-BE-2009-028
DIPAC09
Sapinski, M ; Dehning, B ; Guerrero, A ; Koopman, J ; Métral, E ; DIPAC09, Basel
http://dipac09.web.psi.ch/ppp/papers/tupd40.pdf

Beam Interaction with Thin Materials: Heat Deposition, Cooling Phenomena and Damage Limits
M. Sapinski,
2012 Beam Instrumentation Workshop (BIW12), April 15-19, 2012, Newport News, USA

3.5   Further Reading I:

High Resolution Measurements of Lepton Beam Transverse Distributions with the LEP Wire Scanners

J. Camas et al., Proceedings of Particle Accelerator Conference PAC93, 1993

High Resolution Measurements of Lepton Beam Transverse Distributions with the LEP Wire Scanners.

J. Camas, G. Crockford, G. Ferioli, C. Fischer, J.J. Gras, R. Jung, J. Koopman, J. Mann
CERN CH-1211 Geneva 23,Switzerland

Abstract

A large number of improvements were carried-out on the LEP Wire-Scanners in preparation for the 1992 running period. They include modifications of the monitors mechanics to decrease the vibrations and the heating of the wire by the beam generated electromagnetic fields, improvements of the detector chain and a software re-organization at the various levels for better noise rejection, improved user interface and "off-line" data analysis capabilities. It is now also possible to acquire the profiles of each of the sixteen circulating bunches, electrons and positrons, during the same sweep. As a consequence of these actions the quality of the collected data is much improved. The results are presented and discussed.

I. INTRODUCTION

Four wire-scanners are installed in LEP straight section 1 [1] to provide transverse distributions in both horizontal and vertical planes. Figure 1 gives the lay-out of the monitors together with their associated detectors.
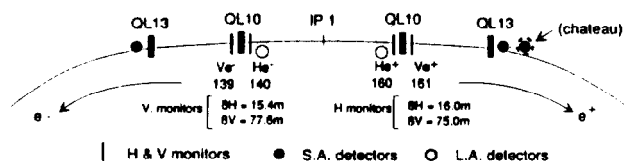
Fig 1:The LEP Wire-Scanners arrangement and Optics Parameters

One horizontal and one vertical monitor are symmetrically installed and are each associated with two detectors:

    -a scintillator located behind a thin window, 75 meters downstream of the wire, receives the Bremsstrahlung resulting from the beam-wire interaction emitted at small angles (S.A.). It acquires the scan of the associated beam (i.e. e- profile from the monitors located on the e- injection side).

    -a scintillator installed against the vacuum chamber near to the horizontal monitor collects the emission at large angles (L.A.) during the passage of the counter-rotating beam.

The signal received by the S.A. scintillators [1] is attenuated by 4 orders of magnitude before transmission to a photo-multiplier which has a gain 100 times smaller than that of the L.A. detectors.

II. THERMAL AND MECHANICAL OBSERVATIONS

Fourteen wires have been destroyed from 1989 to 1992, most of them in 1989 and 1990. With the exception of two 50 μm Beryllium wires, they were 36 μm thick carbon wires. The Be wires showed clearly [1] that the wire had melted over its full length, excluding beam energy deposition as the only destruction mechanism. This is confirmed by previous measurements at the SPS where the wires survived higher intensities at comparable speeds. Moreover, permanent wire average temperature monitoring has shown several interesting features(Figure 2):
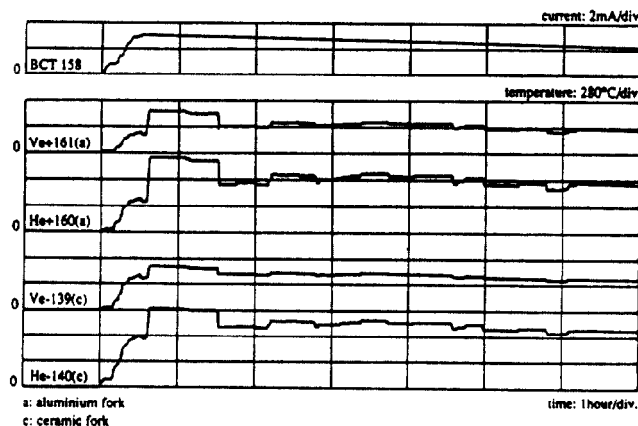
Fig. 2: Long term recording of wire resistance (temperature) and beam current with wires retracted in the parking position

The temperature of the wires increase with the stored current and the vertical wires temperature increases less than that of the horizontal ones. This indicates that the heating is of electromagnetic origin, due to the wake fields generated in the wire scanner tanks. The vertical wires heat up less because they are retracted in a rectangular tube functioning as a waveguide below cut-off. The second evidence in favour of electromagnetic heating is the fact that the wire temperature changes when beam manipulations modifying the bunch length take place at constant circulating beam intensity. Finally wire temperature recordings during scans provide other evidence of heating by electromagnetic coupling (Figure 3).
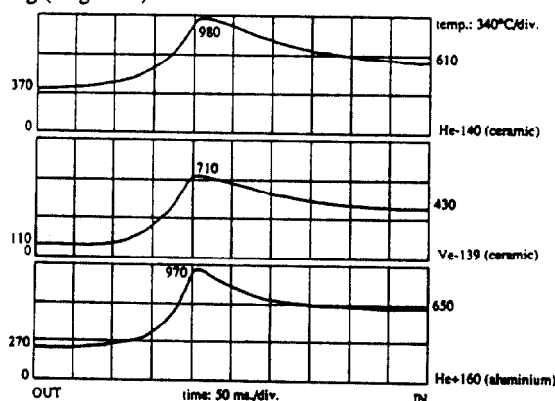
Fig. 3: Wire resistance change during scans of 300 μA on 300 μA circulating beams. Calculated temperatures are indicated.

As the wire approaches the beam, a temperature increase starts at approximately 40 mm from the beam centre, mainly due to coupling to the electric field. A steady state temperature is reached again when the wire is far from the beam. This results mainly from the magnetic field created by the beam passing in the loop formed by the wire and the supporting fork. The temperature increase of the

horizontal and vertical wires is inconsistent, the latter being too low compared to the former. Laboratory tests have shown that thermoemission starts at around 1000°C and shifts the resistance measurement towards lower equivalent temperatures. Electromagnetic heating of the wire being established, the fork construction was analysed for possible improvements. A coupling capacitance of a few pF was found between the wire and the fork; this was created between the aluminium arm, the wire supporting aluminium piece and the ceramic insulator (Figure 4). Two different types of supporting forks were installed in early 1991. The first design had a modified wire support piece and ceramic transition pieces to decrease the coupling capacitance (Figure 4).
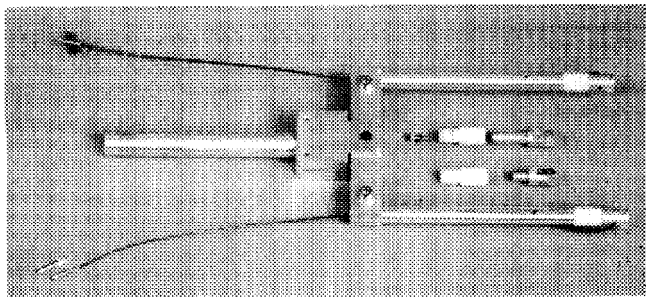
Fig. 4: Wire supporting fork with original (top) and modified (bottom) wire holding and ceramic isolating pieces.

A second design was implemented with the whole supporting tubes made of ceramic. In 1992, the wire length of the combined aluminium/ceramic forks was reduced from 55 to 29 mm. The vertical wire with this design broke twice in 1992. The temperature recording of the first incident showed that it happened at a circulating current of 2.8 mA; the temperature reached was 1280°C, uncorrected for thermoemission. For 1993, a 30 μm quartz wire has been installed in place of the broken wire. The quartz wire will definitely break any current loop leading to heating but it may experience high voltage breakthroughs when passing through the beam. Since 1991, no wires with full ceramic arms were broken.

Scans taken in 1991 and 1992 are affected by a shift of the beam centre of charge between the IN and OUT directions of the order of 100 μm. Laboratory tests have shown that it is due to an inertia induced movement of the driving screw [1]. This effect could be reduced in the laboratory from 70 to 10 μm by using a counter-pin pushing on the free end of the driving shaft. This modification could not be implemented for the 1993 LEP start-up.

III. LOW LEVEL AND APPLICATION SOFTWARE

The basic software design used in 1992 was unchanged from 1991. Amongst the various data structures exchanged between the local equipment server and the application, the PROFILE structures (one per profile) hold all the signals relative to a given bunch received from the photo-multiplier. If their initial analysis (sigma processing within the server) is successful, these data are trimmed to +/- 4 sigmas; otherwise the entire profile is stored for more detailed "off-line" analysis. An analysis failure usually occurs when all signals are hidden within the noise. However, even with a good signal level the fit results (mainly the standard deviation) are noise dependent. In order to cope with this, two different methods have been tested :

- a simple rms calculation over the whole profile followed by a second iteration over a limited window
- a more refined gaussian fit providing a chi-squared minimization on all data above 10% of the maximum amplitude.

The later technique is less noise sensitive but is also less accurate when the distribution is not gaussian. For the future runs the results of both the rms processing and the gaussian fit will be forwarded to the application for systematic comparisons.

The application interface has also been upgraded for 1993 owing to the availability of more powerful graphic tools. It will be possible to display simultaneously up to eight circulating bunch profiles (of the same beam or of the two e+/e- beams) and to display IN and OUT profiles relative to a given scan on the same plot. These modifications added to better "off-line" analysis facilities will ease the interpretation of results.

IV. RESULTS AND DISCUSSION

A scan is systematically performed in the IN(beam) and OUT(of beam) directions. As a result, two profiles are measured and can be compared each time a sweep is triggered in a given plane. The wire position (x axis) is in millimeters whereas the y scale unit is arbitrary and depends on the monitor gain setting.
HORIZONTAL PLANE:
In this plane the signal received by the S.A. detectors is excellent and provides good gaussian fits of the bunch profiles. This is illustrated on Figure 5 in the case of a positron bunch analysed with the monitor located on the positron side. Standard deviations from both scan directions are in agreement within +/- 1.3%.

	IN	OUT
<x>(mm)	3.660	3.649
sigma (mm)	.475	.463

Fig 5: IN and OUT profiles and fit results of a positron bunch scanned with the He+ monitor and analysed with the S.A. detector at the window

Another S.A. detector (chateau) located fifteen meters downstream from the Bremsstrahlung radiation extraction window was also used in order to investigate eventual acceptance problems and effects of background close to the vacuum chamber. This detector was shifted radially which gave better shielding. Its response is given on Figure 6 for the same bunch .

	IN	OUT
<x>(mm)	3.696	3.670
sigma(mm)	.499	.479
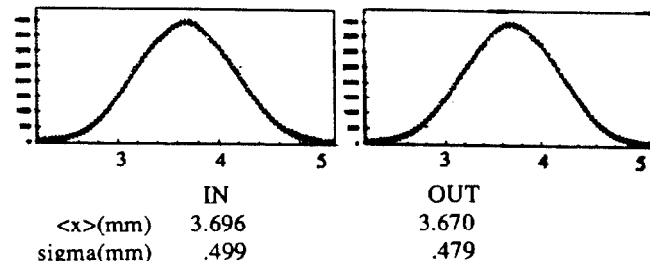
Fig 6: IN and OUT profiles and fit results of the same bunch from the S.A. detector located 15 meters downstream from the window

Between the IN and OUT directions the agreement is +/-2% and both S.A. detectors give the same standard deviation within +/-2.1%

The response of the L.A. detectors is less good. The signal to noise ratio at large angle is less favourable and a compromise must be found between the shielding depth protecting the scintillator from background and the signal level to be analysed. In order to reduce the background noise 10 mm of Lead was necessary. However some saturation then started to affect the photo-multiplier in the peak region (Figure 7)

	IN	OUT
<x>(mm)	1.716	1.729
sigma(mm)	.506	.503

Fig 7: IN and OUT profiles and fit results of the same bunch scanned with the He- monitor and analysed with the L.A. detector.

The fit results provided by both directions agree very well but lead to standard deviations 5% higher than the S.A. detectors. The different average positions indicate that the beam trajectory is different at the e+ and at the e- monitors.

VERTICAL PLANE :

Typical profiles performed using the vertical monitors are shown on Figure 8 for the S.A. detectors.

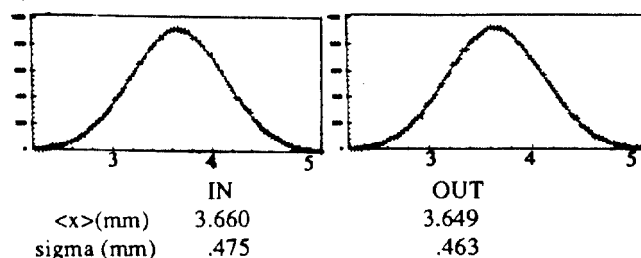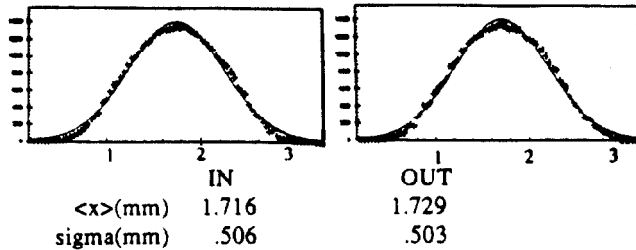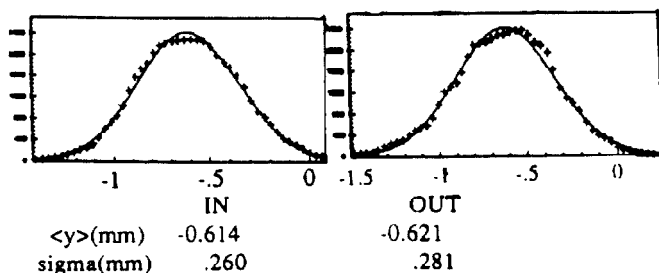|	IN	OUT
<y>(mm)	-0.614	-0.621
sigma(mm)	.260	.281

Fig 8: IN and OUT profiles and fit results of an electron bunch scanned with the Ve- monitor and analysed with the S.A. detector at the window.

Vertical profiles are usually affected by blow-up effects resulting from Coulomb Scattering of the beam through the wire. Taking the emittance ratio in LEP and the present monitor performances these effects can now be neglected in the horizontal plane at 46 GeV. They dilute mainly the second half of the vertical scan (positive and negative sides for respectively the IN and OUT directions) as can be seen on Figure 8. Hence, a direct gaussian fit provides a too pessimistic result. By modelling this effect and analysing the non-perturbed halves of the IN and OUT profiles [1], it is possible to reconstruct the initial distribution. An example of the results is given on Figure 9. A reduction of the rms value by 10% to 20% is then observed with respect to the fit of the entire measured distribution. However this method still suffers from the random mechanical effects (section II) and from timing imprecisions. Therefore it cannot be used systematically.

The L.A. detectors suffer from a lack of signal in the case of vertical profiles as they are located near to the H monitors (Figure1) five meters downstream from the vertical ones.

H scan(no blow-up)   V scan
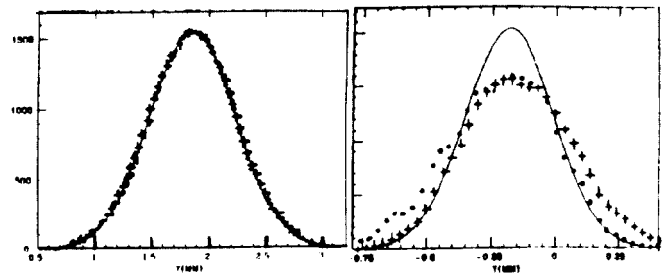
Fig 9: Initial distributions from IN and OUT profile analysis :
+: IN direction , •: OUT direction , ———: fitted profile .

The gaussian fits of profiles from the S.A. detectors provide emittance values of 0.9nm to 1 nm in the vertical plane and 14nm to 15 nm horizontally. The precision achieved is a few per cent in the horizontal plane. Vertically the results are not so accurate as long as blow-up effects are not properly eliminated.

V. COMPARISON WITH S.R. MONITORS

These figures, can be used to calibrate the U.V. telescopes [2].The agreement between the two devices is disturbed by parasitic effects which must be considered; they are at locations in the machine where the optics are not the same and where beam dynamical effects are different (for example coupling). This can account for discrepancies of around 20%. Some 50Hz noise also disturbs the two devices differently as they have different modes of acquisition

VI. FUTURE UPGRADES AND CONCLUSION

Several steps will be taken to improve wire-scanner performances in addition to the ones discussed in section II. The mechanics will be modified to reduce the shift between the two directions. It has also been considered to add to each monitor a wire rotated by 45 degrees. This will allow a better evaluation of the tilt effects. The electric noise level will be reduced in the wire scanners environment by installing filters on adjacent motorised devices.These improvements are foreseen for the 1994 runs. Both the S.A. and L.A. detectors have been modified. The former will have a better acceptance in particular close to the vacuum chamber whereas the shape of the later has been reconsidered to increase its acceptance and hence have better signal to noise ratio.

Several software modifications will be implemented apart from the availability of the new application (section III). An interlock will prevent any scans above a given circulating beam current and temperatures will be systematically recorded during wire sweeps. The timing will be upgraded so as to lower the uncertainty in the absolute position reference between IN and OUT scans from 50 μm down to 10 μm (rms).The wire status will also be monitored in permanence.

Resulting from these modifications we expect to have the same level of performance in both the horizontal and vertical planes.

VIII. REFERENCES

[1] B.Bouchet et al., "Wire-Scanners at LEP", Proc. of the 1991 IEEE Part. Accel. Conf., San-Francisco, 6-9 May 1991 .

[2] G. Burtin et al., "Performance and Operational Experience of the LEP Synchrotron Light Telescopes", these proceedings.

3.6   Further Reading II:

Design of a High-precision Fast Wire Scanner for the SPS at CERN

R. Veness et al., Proceedings of International Beam Instrumentation Conference IBIC, 2012

DESIGN OF A HIGH-PRECISION FAST WIRE SCANNER FOR THE SPS AT CERN

R. Veness, N. Chritin, B. Dehning, J. Emery, J. Herranz Alvarez, M. Koujili, S. Samuelsson,
J.L. Sirvent, CERN, Geneva, Switzerland

Abstract

Studies are going on of a new wire scanner concept. All moving parts are inside the beam vacuum and it is specified for use in all the machines across the CERN accelerator complex. Key components have been developed and tested. Work is now focussing on the installation of a prototype for test in the Super Proton Synchrotron (SPS) accelerator.

This article presents the specification of the device and constraints on the design for integration in the different accelerators at CERN. The design issues of the mechanical components are discussed and optimisation work shown. Finally, the prototype design, integrating the several components into the vacuum tank is presented.

INTRODUCTION

Wire scanners are installed in the LHC and all circular machines in the injector chain as a means to measure the transverse beam profile and hence emittance. The motivation for the development of a new scanner design has been described in a previous article [1], along with the concept with the rotor of the motor and wire position measurement system inside the beam vacuum [see Figure 1]. Development of key components, in particular the motor and control system, are well advanced [2]. Work is now focussing on the integration of all the required components with the aim of producing a scanner capable of 20 ms^{-1} scanning speed combined with 2 µm position precision.

A number of mechanical components require careful optimisation. These include the motor housing, shaft, bearings, fork and wire. In addition, the design concept includes an in-vacuum optical position encoder in order to reach the required precision. Development of these components is described in the following sections.
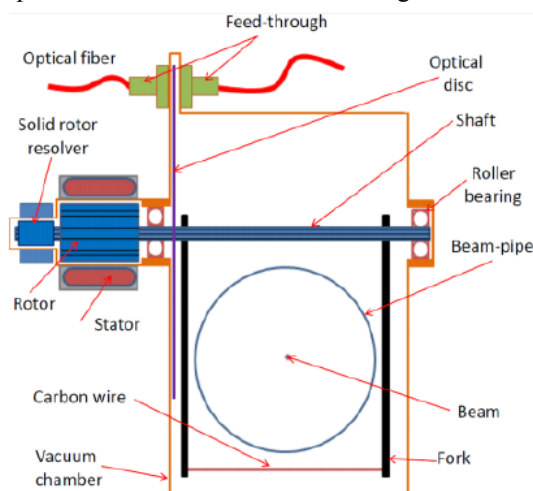
Figure 1: Fast Wire Scanner concept.

INTEGRATION CONSTRAINTS

Wire scanners are currently installed in the PS, Booster, SPS and LHC at CERN. It would greatly simplify operation and maintenance if the same basic design could be implemented for all of these machines. To this end, the main constraints in terms of machine physics, operation and environment have been analysed for each machine. These are summarised in Table 1.

Table 1: Summary of Integration Constraints from the CERN Accelerator Complex

Machine	Scan aperture (mm)	RF Screen	Bakeout	Space Constraint
PS Booster	146x70	N	N	Axial, Transverse
PS	146x70	N	N	Axial
SPS	152x83	Y	N	-
LHC	65x65	Y	Y	Transverse

The scan aperture is the horizontal and vertical space that must be cleared by the wire. RF screens are required in some machines to minimise impedance and RF heating effects. Integration of new scanners into existing machines must take into account machine geometries and equipment. Axial space constraints occur in machines with a tight lattice whereas transverse constraints are seen with parallel equipment on the beamline (eg, the cryogenic distribution line in the LHC). It can be seen from table 1 that each of the machines brings constraints to the design. A solution has been adopted where the main components can be integrated into designs for the PS, SPS and LHC. Each machine will require a different fork geometry and a different flange interface, but other main components and principles will be common. The layout of the Booster with 4 rings in very close proximity mean that it has not yet been possible to integrate the design into this machine.

Combining these constraints leads to a design with aperture range up to 152 by 152, with the option to include RF screen and to be bakeable to 200°C in order to activate a low emission yield getter coating used in the LHC vacuum system.

DESIGN OF COMPONENTS

Motor Housing

The motor housing has the function of separating the rotor in-vacuum and stator on the atmospheric side of the

electric motor. The housing needs to be thin to fit in the relatively small air gap (approximately 0.8 mm) between the rotor and stator. The required wall thickness of the housing has been determined using finite element method (FEM) analysis. The analysis shows that elastic instability is the critical failure mode. The stability of the structure increases strongly with wall thickness. The dependence of stability on the length of the structure is weaker, where a shorter structure increases the stability. Furthermore, a thicker housing (within the limits of this problem) is easier to manufacture. When all the above mentioned considerations are put together, the optimum wall thickness of the motor housing is determined to be 0.4 mm.
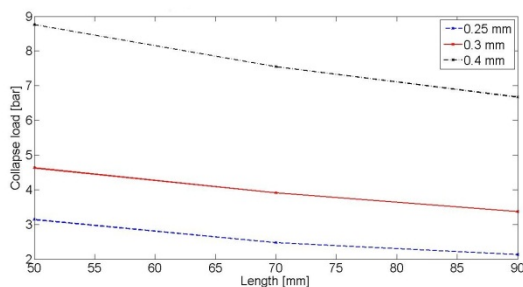
Figure 2: Graph of motor housing collapse load for different lengths and wall thicknesses.

Shaft and Bearings

One principal of this design is to support forks and position measurement system on one rigid structure to maximise precision. The shaft forms the core of the mechanical structure. It is driven by the motor and supports the rotor, forks and optical disc. The main constraint on the shaft is its deformation in torsion. The torsional deformation appears due to the acceleration of the shaft and the inertias of the components mounted on the shaft. This deformation must be kept small to ensure accuracy of the measurements. Although the shaft is not accelerating when the wire passes through the beam, the shaft will vibrate with a maximum amplitude corresponding to the torsional deformation due to the acceleration. The shaft needs to be hollow to be able to pass cables through it. Analysis of the shaft, using analytical calculations and FEM simulations, show that using a larger outer diameter has a strong effect on the stiffness. It is also shown that the stress in the shaft is low and the inertia of the shaft is of little importance compared to the inertias of the components mounted on the shaft. This means that the strength of the material is not critical and that a stiff, relatively heavy stainless steel is a better material choice compared to lighter, more flexible alternatives such as aluminium or titanium. The analysis also shows that it is the optical disc and the disc holder which give the largest contribution to the shaft twist. This is because they are mounted on the shaft end opposite to the motor. Therefore effort should be put into minimising the mass of these components. Figure 3 showsthe offset of the wire position relative to the

encoder which the shaft vibrations give rise to. The calculations show that an outer diameter of 35 mm is needed to keep the deformation below the tolerated limit of 5 μm.
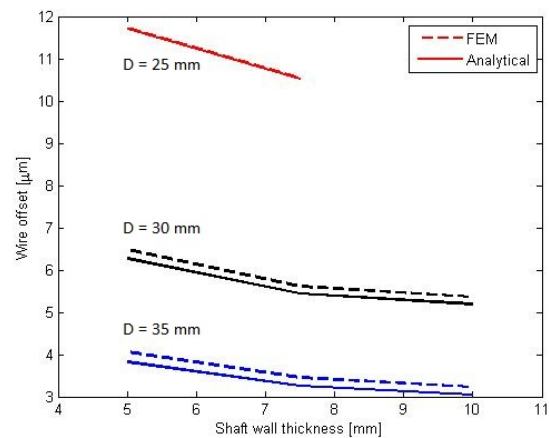
Figure 3: Graph of relative offset of wire vs. encoder for different shaft diameters and thicknesses.

The bearings need to assure high precision in terms of radial runout and the materials used must be UHV compatible and radiation and bake out resistant. This means that traditional lubricants such as oil and grease cannot be used [3]. Instead one must rely on running the bearings without any lubricant or possibly using solid lubricants (such as molybdenum disulphide or tungsten disulphide coatings). It is also recommendable to use different materials for the races and the rolling elements in the bearing, to avoid cold welding. One available alternative for this is hybrid bearings which use steel races and ceramic rolling elements.

Optical Disc and Support

The principle selected for the high precision determination of the beam size is an optical system based on a glass disc with a photo-lithographed μm pattern made of high reflectivity chrome, placed inside the vacuum chamber and fixed on the scanner shaft. This incremental angle encoder uses single-mode optical fibre and UHV fibre optic feedthrough (9/125μm) to drive 1310 nm laser light on a 1:1 lens system in-vacuum that focuses the light on the disc surface with a 10 μm light spot size. Using the reflectivity of the chrome pattern, the reflected light is coupled back into the same fibre, and through an optical circulator directed to the photodiode. The laser diode, circulator, photodiode and subsequent electronics will be located in the surface building and only one optical fibre will go down to the accelerator tunnel (250 m). The performance of this single fibre angular position sensor has been tested and validated on the bench shown in Fig 4.
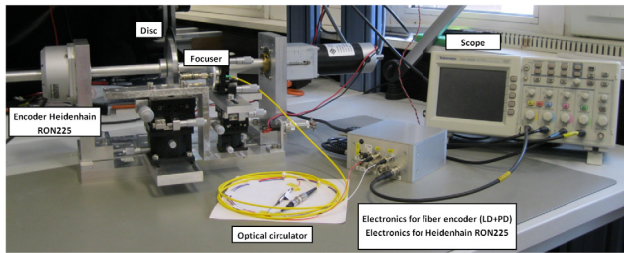
Figure 4: Test bench for the optical position sensor.

This fibre encoder provides a resolution of 157 µRad with a track of 10 µm slits, and two position references using only one channel. An accuracy of ±25 µRad is reached by angular calibration with a commercial encoder Heidenhain RON225 (Fig. 5). With this calibration, eccentricity errors, and partly grating errors can be minimized.
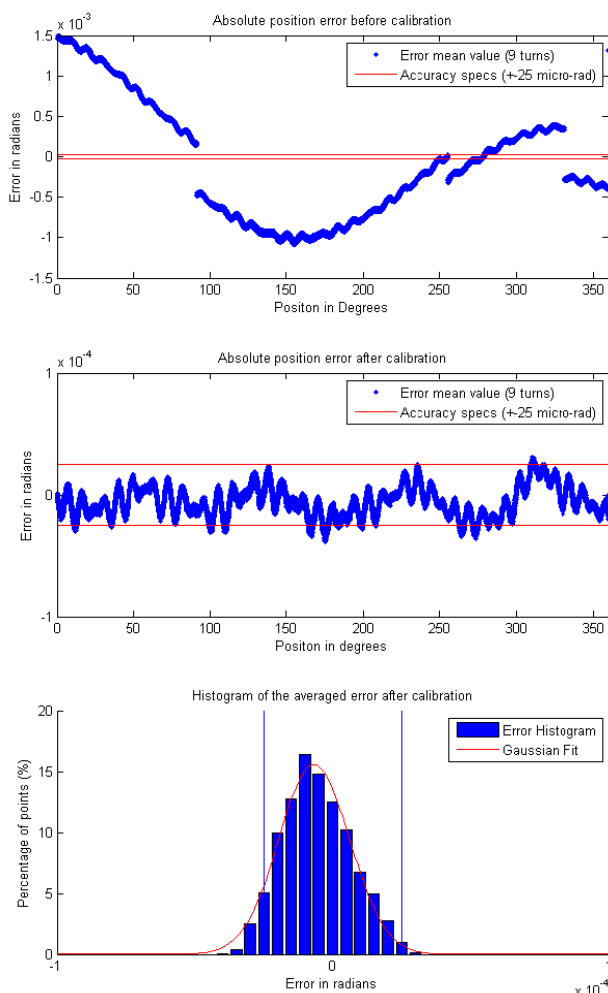
Figure 5: Error before calibration (top), calibration applied (center) and error histogram (bottom). Calibration made with Heidenhein RON225 angular position sensor.

The final system is UHV compatible with EMI immunity, works with temperatures up to 200ºC, and it is radiation tolerant due the special fibre used. Studies are on-going to verify the use of a 5 µm track to reach better mechanical resolutions (around 70 µRad), and the incorporation of other calibration methods on the scanner working axis to perform a more reliable calibration procedure.

Magnetic Restraint System

The design will integrate a magnetic restraint in order to prevent unplanned movements of the fork during transportation or installation and also during operation in case of power or control system failure.

Uncontrolled movement of the wire within the beam aperture could cause the melting of the wire and quenching of superconducting magnets (in the case of the LHC). This effect is enhanced as the wire speed due to its own unbalanced weight would be much slower than the nominal speed required for safe operation of the scanner.

The conceptual design of the restraint system consists of a magnetic circuit in two parts: One part outside of the vacuum has a permanent magnet and electrical coil; the other part inside the vacuum consists of a ferromagnetic piece fixed to the shaft. This has two poles that, when aligned with the external magnetic circuit, define an equilibrium position corresponding to the 'parked' fork positions. When the electric coil is energized it cancels the field of the permanent magnet allowing the shaft to rotate freely. This concept can be seen in Figure 6.
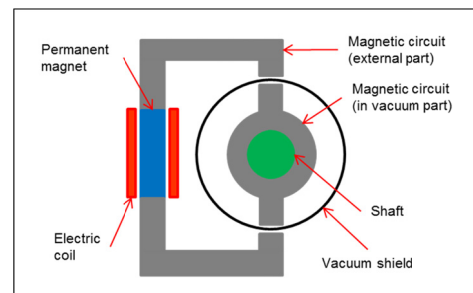
Figure 6: Conceptual design for the magnetic restraint system.

Forks

The two forks which support the wire need to be carefully optimised. They need to be stiff enough to maintain the wire under tension and prevent excessive deformation and vibration during wire acceleration. However the forks are also a major component of the inertial load on the shaft and motor, so the mass and mass distribution need to be optimised. From the manufacturing viewpoint, there will be different designs for each machine due to the different apertures, so quantities will be small.

Considering all of these factors, it is logical to consider making these components using metal additive manufacturing [4] (also referred to as 3D printing). This method will allow complex geometries to be optimised using FEM, and produced directly in small quantities from 3D CAD models allowing for forms that cannot be produced with conventional machining.

Studies of the wire are on-going and will be presented separately.

STATUS AND NEXT STEPS

All major components have been integrated into a 3D model with an envelope which would allow installation into the PS, SPS or LHC. Figure 7 shows a section through this model. The scanner is assembled as one self-contained 'cartridge' that will be inserted into the accelerator vacuum chamber. This will protect the wire from damage during insertion – a common problem with existing designs. A prototype will be constructed and tested in the coming months to verify the operation of the scanner assembly and performance. It is then planned to produce a first production model for test in the SPS accelerator. This will be installed in the forthcoming 'Long Shutdown 1' of all CERN accelerators in 2013-14. The plan is then to produce a series of scanners for installation in the second Long Shutdown scheduled for 2018-19.
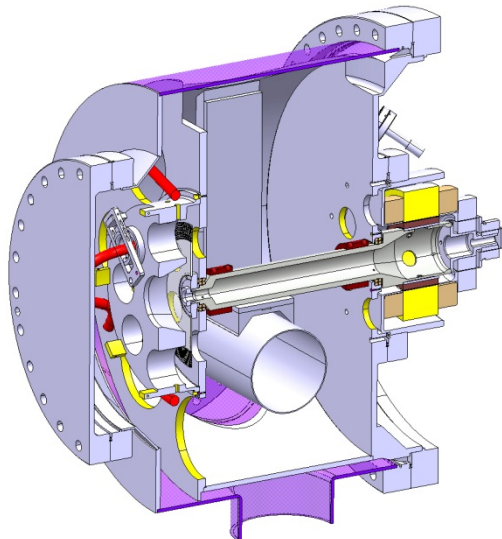
Figure 7: 3-D model section through the scanner.

REFERENCES

[1] M.Koujili et al. 'Fast and High Accuracy Wire Scanner' DIPAC'09 Conference – 25-27 May 2009 /Basel-CH

[2] B.Dehning et al. 'Vacuum Actuator and Controller Design for a Fast Wire Scanner' Proceedings of BIW2012, Newport News, Virginia, USA

[3] D. Ramos 'Bibliographic search on bearing technology for ultra-high vacuum applications' Internal communication (2008).

[4] L.E. Murr et al. 'Metal Fabrication by Additive Manufacturing Using Laser and Electron Beam Melting Technologies' J. Mater. Sci. Technol., 2012, 28(1), 1-14.

Emittance Measurement

3.7   Introduction to Emittance

S.Y. Lee, from Accelerator Physics, World Scientific, pp 54-55
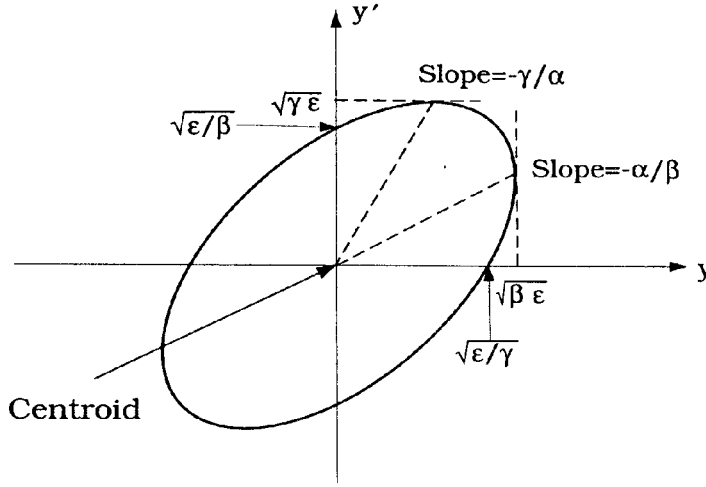
Figure 2.8: The Courant–Snyder invariant ellipse. The area enclosed by the ellipse is equal to $\pi\epsilon$, where ϵ is twice the betatron action; α, β and γ are betatron amplitude functions.

A. The emittance of a beam

A beam is usually composed of particles distributed in the phase space. Depending on the initial beam preparation, we approximate a realistic beam distribution function by some simple analytic formula. Neglecting dissipation and diffusion processes, each particle in the distribution function has its invariant Courant–Snyder ellipse.

Given a normalized distribution function $\rho(y, y')$ with $\int \rho(y, y') dy dy' = 1$, the moments of the beam distribution are

$$\langle y \rangle = \int y \rho(y, y') dy dy', \quad \langle y' \rangle = \int y' \rho(y, y') dy dy', \tag{2.94}$$

$$\sigma_y^2 = \int (y - \langle y \rangle)^2 \rho(y, y') dy dy', \quad \sigma_{y'}^2 = \int (y' - \langle y' \rangle)^2 \rho(y, y') dy dy', \tag{2.95}$$

$$\sigma_{yy'} = \int (y - \langle y \rangle)(y' - \langle y' \rangle) \rho(y, y') dy dy' = r \sigma_y \sigma_{y'}, \tag{2.96}$$

where σ_y and $\sigma_{y'}$ are the rms beam widths, $\sigma_{yy'}$ is the correlation, and r is the correlation coefficient. The rms beam emittance is then defined as

$$\epsilon_{\rm rms} = \sqrt{\sigma_y^2 \sigma_{y'}^2 - \sigma_{yy'}^2} = \sigma_y \sigma_{y'} \sqrt{1 - r^2}. \tag{2.97}$$

If the accelerator is composed of linear elements such as dipoles and quadrupoles, the emittance defined in Eq. (2.97) is invariant. The rms emittance is equal to the phase-space area enclosed by the Courant–Snyder ellipse of the rms particle (see Exercise 2.2.16).

Although incorrect, the term "emittance" is often loosely used as twice the action variable of betatron oscillations. The betatron oscillations of "a particle" with an "emittance" ϵ is

$$y(s) = \sqrt{\frac{\beta \epsilon}{\pi}} \cos[\nu\phi(s) + \delta]. \tag{2.98}$$

Figure 2.8 shows a Courant–Snyder invariant ellipse for a given emittance of a beam. For a beam with rms emittance ϵ, the rms beam width is $\sqrt{\beta(s)\epsilon}$, and the beam rms divergence y' is $\sqrt{\gamma(s)\epsilon}$. Since $\gamma = (1 + \alpha^2)/\beta$, the transverse beam divergence is smaller at a location with a large $\beta(s)$ value, i.e. all particles travel in parallel paths. In accelerator design, a proper $\beta(s)$ value is therefore important for achieving many desirable properties.

B. The σ-matrix

The σ-matrix of a beam distribution is defined as

$$\sigma = \begin{pmatrix} \sigma_{11} & \sigma_{12} \\ \sigma_{12} & \sigma_{22} \end{pmatrix} = \begin{pmatrix} \sigma_y^2 & \sigma_{yy'} \\ \sigma_{yy'} & \sigma_{y'}^2 \end{pmatrix} = \langle (\mathbf{y} - \langle \mathbf{y} \rangle)(\mathbf{y} - \langle \mathbf{y} \rangle)^\dagger \rangle, \tag{2.99}$$

where $\mathbf{y}$ is the betatron state matrix of Eq. (2.36), $\mathbf{y}^\dagger = (y, y')$ is the transpose of $\mathbf{y}$, and $\langle \mathbf{y} \rangle$ is the first moment. The rms emittance becomes (see also Exercise 2.2.14)

$$\epsilon_{\rm rms} = \sqrt{\det \sigma} = \sqrt{\sigma_{11}\sigma_{22} - \sigma_{12}^2}. \tag{2.97}$$

Using the transfer matrix, we obtain

$$\sigma_2 = M_{21}\sigma_1 M_{21}^\dagger. \tag{2.100}$$

It is easy to verify that $\mathbf{y}^\dagger \sigma^{-1} \mathbf{y}$ is invariant under linear betatron motion, thus the beam distribution is

$$\rho(y, y') = \rho(\mathbf{y}^\dagger \sigma^{-1} \mathbf{y}). \tag{2.101}$$

C. Emittance measurement

The emittance can be obtained by measuring the σ-matrix. The beam profile of protons and ions is usually measured by using wire scanners or ionization profile monitors. Synchrotron light monitors are commonly used in electron storage rings. More recently, laser light has been used to measure electron beam size in the sub-micron range. Using the rms beam size and Courant-Snyder parameters, we can deduce the emittance of the beam.

References

Attached:

S.Y. Lee,
Accelerator Physics, Chapter 2, Transverse Motion, B. Sigma Matrix
World Scientific, pp 54-55

Further readings:

Emittance Measurements at the Bates Linac,
K.D. Jacobs, J.B. Flanz, T. Russ
http://accelconf.web.cern.ch/accelconf/p89/PDF/PAC1989_1529.PDF,

Basic accelerator course,
like Schmüser and Rossbach in previous CAS CERN 94-01 v 1;
http://doc.cern.ch/cgi-bin/tiff2pdf?/archive/cernrep/1994/94-01/p17.tif.

Beam-line instruments
Raich, U ;
Joint US-CERN-Japan-Russia Particle Accelerators School on Beam Measurement,
Montreux, Switzerland, 11-20 May 1998
World Sci., Singapore, 1999. - pp.263-276

3.8   Further Reading I:

Amplitude Function Mismatch

M. Syphers et al., Proceedings of Particle Accelerator Conference PAC93, 1993

Amplitude Function Mismatch

M.J. Syphers, T. Sen
Superconducting Super Collider Laboratory*
2550 Beckleymeade Ave., Dallas, TX 75237
and
D. A. Edwards
DESY/Fermilab
P. O. Box 500, Batavia, IL 60510

Abstract

We develop the general equation of motion of an amplitude function mismatch in an accelerator lattice and look at its solution for some interesting cases. For a free β-wave oscillation the amplitude of the mismatch is written in terms of the determinant of a single matrix made up of the difference between the new Courant-Snyder parameters and their ideal values. Using this result, once one calculates the mismatch of the amplitude function and its slope at one point in the lattice (at the end of a *nearly* matched insertion, for example), then the maximum mismatch downstream can be easily computed. The formalism is also used to describe emittance growth in a hadron synchrotron caused by amplitude function mismatches at injection.

While most of the content of this paper is not new to the accelerator physics community, we thought it would be useful to place this important, basic information all in one place. Besides the classic work of Courant and Snyder, our sources include other papers, internal reports, and numerous discussions with our colleagues. More details may be found in a related paper.[1]

I. A STARTING POINT

The general solution for linear betatron oscillations in one transverse degree of freedom can be written as[2] $x(s) = A\sqrt{\beta(s)}\cos[\psi(s) + \delta]$ where A and δ are constants given by the particle's initial conditions. The phase advance $\psi(s)$ and the amplitude function $\beta(s)$ satisfy the differential equations $\psi' = \frac{1}{\beta}$, $2\beta\beta'' - \beta'^2 + 4\beta^2 K = 4$, where $K = e(\partial B_y/\partial x)/p$, with e = charge, p = momentum, $\partial B_y/\partial x$ = magnetic field gradient, and $\beta' = d\beta/ds$, etc. When one considers the periodic solution of the amplitude function, the motion through a single repeat period can be described in terms of the Courant-Snyder parameters $\beta(s)$, $\alpha(s) \equiv -(d\beta(s)/ds)/2$, and $\gamma(s) \equiv (1 + \alpha^2)/\beta$, using the matrix

$$\begin{pmatrix} \cos\psi_C + \alpha\sin\psi_C & \beta\sin\psi_C \\ -\gamma\sin\psi_C & \cos\psi_C - \alpha\sin\psi_C \end{pmatrix} \quad (1)$$

which operates on the state vector X, with $X = (x, x')^T$. Here, the phase advance is $\psi_C = 2\pi\nu = \int_{s_0}^{s_0+C} \frac{ds}{\beta(s)}$, where

C is the repeat distance of the hardware, which may be the circumference of the accelerator, and ν is the *tune* of the synchrotron.

The matrix of Equation 1 is often written in compact form as $M = I\cos\psi_C + J\sin\psi_C$ where

$$J \equiv \begin{pmatrix} \alpha & \beta \\ -\gamma & -\alpha \end{pmatrix}. \quad (2)$$

The amplitude function and its slope propagate through an accelerator section according to

$$J_2 = M(s_1 \to s_2)J_1 M(s_1 \to s_2)^{-1}, \quad (3)$$

where J_1 and J_2 contain Courant-Snyder parameters corresponding to points 1 and 2, and $M(s_1 \to s_2)$ is the transport matrix between these two points.

II. PROPAGATION OF A THIN GRADIENT ERROR

We wish to see how the amplitude function downstream of a thin gradient error is altered. If $J_0(s_0)$ is the matrix of unperturbed Courant-Snyder parameters at the location of the error and $J_0(s)$ contains the unperturbed parameters at a point downstream, then, using Equation 3,

$$\Delta J(s) = M(s_0 \to s)\Delta J(s_0)M(s_0 \to s)^{-1}, \quad (4)$$

where

$$\Delta J(s) = J(s) - J_0(s) = \begin{pmatrix} \alpha - \alpha_0 & \beta - \beta_0 \\ -(\gamma - \gamma_0) & -(\alpha - \alpha_0) \end{pmatrix}; \quad (5)$$

β is the new value of the amplitude function at s, β_0 is the unperturbed value, etc. Through a thin quad, $\Delta\alpha = q\beta_0$, $\Delta\beta = 0$, and $\Delta\gamma = 2\alpha q + \beta q^2$ and so

$$\frac{\Delta\beta(s)}{\beta_0(s)} = -(\beta_i q)\sin 2\psi_0(s - s_0)$$
$$+ \frac{1}{2}(\beta_i q)^2 [1 - \cos 2\psi_0(s - s_0)] \quad (6)$$

where $\psi_0(s - s_0)$ is the unperturbed phase advance between points s_0 and s and $\beta_i \equiv \beta_0(s_0)$. The amplitude function perturbation oscillates at twice the betatron frequency and for $(\beta_i q)$ sufficiently small, the perturbation describes simple harmonic motion. The change in α also propagates at

twice the betatron frequency, it being given by

$$\Delta\alpha(s) = \beta_i q\left[\cos 2\psi_0(s-s_0) - \alpha_0(s)\sin 2\psi_0(s-s_0)\right]$$
$$-\frac{1}{2}(\beta_i q)^2[\sin 2\psi_0(s-s_0)$$
$$-\alpha_0(s)(1 - \cos 2\psi_0(s-s_0))] \quad . \qquad (7)$$

Introducing this quad error also changes the phase advance across the lattice. The new phase advance $\psi(s-s_0)$ across this section may be calculated using $\sin\psi(s-s_0) = \bar{M}(s_0 \rightarrow s)_{12}/\sqrt{\beta_i\beta(s)}$ where $\bar{M}(s_0 \rightarrow s)_{12}$ is the (1,2) element of the new ring matrix and $\beta(s)$ is the new amplitude function at s. Using Equation 6, we obtain

$$\sin\psi(s-s_0) = [1 - \beta_i q \sin 2\psi_0(s-s_0)$$
$$+ (\beta_i q)^2 \sin^2\psi_0(s-s_0)]^{-1/2}\sin\psi_0(s-s_0) \quad . \qquad (8)$$

An explicit result for the change in the phase advance may be obtained perturbatively in orders of the quad error q from the above exact expression. To second order in q, we find that the change $\Delta\psi \equiv \psi(s-s_0) - \psi_0(s-s_0)$ is

$$\Delta\psi = \beta_i q \sin^2\psi_0(s-s_0)$$
$$- (\beta_i q)^2 \sin 2\psi_0(s-s_0)\sin^2\psi_0(s-s_0) + O(q^3) \quad . \qquad (9)$$

To first order in q, at a point $\pi/2$ away from the location of the error, there is no change in the β function while the change in phase advance is at its maximum value of $\beta_i q$.

III. EQUATION OF MOTION OF β-WAVE

The equation of motion for an amplitude function mismatch is nonlinear when s is taken as the independent variable. A more congenial equation can be developed by using the the reduced phase $\phi \equiv \psi/\nu$ as the independent variable. For betatron oscillations the Floquet transformation, where the other variable is $\zeta = x/\sqrt{\beta}$, produces the equation of motion $\frac{d^2\zeta}{d\phi^2} + \nu^2\zeta = 0$ which is pure simple harmonic motion with frequency (tune) ν. For the amplitude function mismatch, we need to define the reduced phase in terms of the unperturbed functions. That is, let $\phi \equiv \psi_0/\nu_0$, where $d\psi_0/ds = 1/\beta_0$, and ν_0 is the unperturbed tune. The equation of motion for $[\beta(\phi) - \beta_0(\phi)]/\beta_0(\phi) \equiv \Delta\beta/\beta_0$ in the absence of gradient errors is then

$$\frac{d^2}{d\phi^2}\frac{\Delta\beta}{\beta_0} + (2\nu_0)^2\frac{\Delta\beta}{\beta_0} = -2\nu_0^2 \det\Delta J$$
$$= 2\nu_0^2[\Delta\alpha^2 - \Delta\beta\Delta\gamma] \quad (10)$$

where $\Delta\alpha = \alpha(\phi) - \alpha_0(\phi)$, etc. The quantity $\det\Delta J$ is an invariant in portions of the lattice without gradient perturbations as can be seen with the aid of Equation 3.

So, the free amplitude function distortion oscillates with twice the betatron tune and with a constant offset given by the determinant of the ΔJ matrix at any point. This offset must be there since $\beta > 0$ and hence $\Delta\beta/\beta$ must always be greater than -1.

Rewritten in terms of the Courant-Snyder parameters,

$$\det\Delta J = -\frac{\left(\frac{\Delta\beta}{\beta_0}\right)^2 + \left(\Delta\alpha - \alpha_0\frac{\Delta\beta}{\beta_0}\right)^2}{1 + \Delta\beta/\beta_0} < 0. \qquad (11)$$

Thus, $|\det\Delta J|^{1/2}$ can be interpreted as the amplitude of the β mismatch for small perturbations.

The solution to Equation 10 is just simple harmonic motion with a constant term added:

$$\frac{\Delta\beta}{\beta_0}(\phi) = A\cos 2\nu_0\phi + B\sin 2\nu_0\phi + \frac{1}{2}|\det\Delta J|. \qquad (12)$$

The constants A and B are found from the initial conditions:

$$A = \frac{\Delta\beta}{\beta_0}(0) - \frac{1}{2}|\det\Delta J|, \qquad (13)$$

$$B = \alpha_0\frac{\Delta\beta}{\beta_0}(0) - \Delta\alpha(0). \qquad (14)$$

Thus, the maximum value of $\Delta\beta/\beta_0$ downstream of our starting point $\phi = 0$ is given by

$$\left(\frac{\Delta\beta}{\beta_0}\right)_{max} = \sqrt{A^2 + B^2} + \frac{1}{2}|\det\Delta J|$$
$$= \frac{|\det\Delta J|}{2} + \sqrt{|\det\Delta J| + \left(\frac{|\det\Delta J|}{2}\right)^2}(15)$$

where use has been made of Equation 11. The maxima occur at phases where

$$\tan 2\nu_0\phi = \left(\frac{\alpha_0\frac{\Delta\beta}{\beta_0} - \Delta\alpha}{\frac{\Delta\beta}{\beta_0} - |\det\Delta J|/2}\right)_0 \quad . \qquad (16)$$

The usefulness of the above result is, of course, that once one calculates the mismatch of the amplitude function and its slope at one point in the lattice (at the end of a *nearly* matched insertion, for example), then the maximum mismatch downstream can be computed immediately.

If we look once again at the perturbation downstream of a thin quadrupole error, we see that just after the quad,

$$\det\Delta J = \begin{vmatrix} q\beta_i & 0 \\ -\Delta\gamma & -q\beta_i \end{vmatrix} = -(q\beta_i)^2 \qquad (17)$$

where $\beta_i = \beta_0$ at the location of the quadrupole. Then,

$$\left(\frac{\Delta\beta}{\beta_0}\right)_{max} = q\beta_i\sqrt{1 + (q\beta_i)^2/4} + \frac{1}{2}(q\beta_i)^2 \qquad (18)$$
$$\approx q\beta_i = \sqrt{|\det\Delta J|} \qquad (19)$$

where the last line is valid for small perturbations.

IV. GENERAL EQUATION OF MOTION

To include the driving terms due to gradient errors in the equation of motion for $\Delta\beta/\beta_0$, we let β_0 satisfy the differential equation $K\beta_0 = \gamma_0 + \alpha'_0$, and let β satisfy $(K + k)\beta = \gamma + \alpha'$, where $\beta = \beta_0 + \Delta\beta$, etc. Then, the relative β error satisfies

$$\frac{d^2}{d\phi^2}\frac{\Delta\beta}{\beta_0}(\phi) + (2\nu_0)^2\frac{\Delta\beta}{\beta_0}(\phi)$$

$$= -2\nu_0^2\left[\beta_0^2(\phi)\,k(\phi)\left(1 + \frac{\Delta\beta}{\beta_0}(\phi)\right) + \det\Delta J(\phi)\right]. \quad (20)$$

Here, in general, $\det\Delta J(\phi)$ is not invariant as it is altered by gradient perturbations:

$$\frac{d}{d\phi}\det\Delta J(\phi) = \beta_0^2 k\frac{d}{d\phi}\frac{\Delta\beta}{\beta_0} \quad (21)$$

For small perturbations we can drop quantities which are second order in the small quantities, e.g. $k\Delta\beta$. This reduces Equation 20 to

$$\frac{d^2}{d\phi^2}\frac{\Delta\beta}{\beta_0}(\phi) + (2\nu_0)^2\frac{\Delta\beta}{\beta_0}(\phi) = -2\nu_0^2\,\beta_0^2\,k(\phi) \quad (22)$$

as appears in Courant and Snyder.[2]

Noting that $\Delta\alpha - \alpha_0(\Delta\beta/\beta_0) = -(1/2\nu_0)d(\Delta\beta/\beta_0)/d\phi$, one can easily exhibit Equation 20 entirely in terms of $\Delta\beta/\beta_0$ and its derivatives with respect to ϕ. Differentiating this resulting equation one obtains a *linear* differential equation for $\Delta\beta/\beta_0$:

$$\frac{d^3}{d\phi^3}\frac{\Delta\beta}{\beta_0} + (2\nu_0)^2(1 + \beta_0^2 k)\frac{d}{d\phi}\frac{\Delta\beta}{\beta_0}$$

$$+ 2\nu_0^2\frac{d}{d\phi}[\beta_0^2 k](1 + \frac{\Delta\beta}{\beta_0}) = 0. \quad (23)$$

V. INJECTION MISMATCH

It is also of interest to look at the effects of mismatches of amplitude functions upon entrance to an accelerator. The treatment below may be followed in more detail in [3] and [4]. A beam which is described by Courant-Snyder parameters that are not the periodic parameters of the accelerator into which it is injected will tend to filament due to nonlinearities and hence have its emittance increased. Suppose β and α are the Courant-Snyder parameters as delivered by the beamline to a particular point in an accelerator, and β_o, α_o are the periodic lattice functions of the ring at that point. A particle with trajectory (x, x') can be viewed in the $(x, \beta x' + \alpha x) \equiv (x, \eta)$ phase space corresponding to the beamline functions, or in the $(x, \beta_0 x' + \alpha_0 x) \equiv (x, \eta_0)$ phase space corresponding to the lattice functions of the ring. If the phase space motion lies on a circle in the beamline view, then the phase space motion will lie on an ellipse in the ring view. The equation of the ellipse in the "ring" system will be

$$\frac{(1 + \Delta\alpha_r^2)}{\beta_r}x^2 + 2\Delta\alpha_r\,x\eta_0 + \beta_r\eta_0^2 = \beta_0 A^2. \quad (24)$$

where $\beta_r \equiv \beta/\beta_0$ and $\Delta\alpha_r \equiv \alpha - \alpha_0(\beta/\beta_0)$.

If the phase space coordinate system were rotated so that the cross-term in the equation of the ellipse were eliminated, the ellipse would have the form $x_e^2/b_r + b_r\eta_{oe}^2 = \beta_0 A^2$ where $b_r \equiv F + \sqrt{F^2 - 1}$ and F is given by

$$F \equiv \frac{1}{2}[\beta_0\gamma + \gamma_0\beta - 2\alpha_0\alpha]. \quad (25)$$

Note that if $\Delta\alpha_r = 0$, then $b_r = \beta_r$.

There is a physical significance to the quantity b_r; it is the ratio of the areas of two circumscribed ellipses which have shapes and orientations given by the two sets of Courant-Snyder parameters found in the matrices J and J_0. This might suggest that a beam contained within the smaller ellipse upon injection into the synchrotron (whose periodic functions give ellipses similar to the larger one) will have its emittance increased by a factor b_r. However, this would be an over-estimate of the increase of the average of the emittances of all the particles.

If in the beamline view the new phase space trajectory is $x^2 + \eta^2 = b_r R^2$, then in the synchrotron view, the equation of the ellipse would be $\frac{x^2}{b_r R^2} + \frac{\eta_0^2}{R^2/b_r} = 1$. A particle with initial phase space coordinates x_i and η_{oi} will commence describing a circular trajectory of radius a in phase space upon subsequent revolutions about the ring. The equilibrium distribution will have variance in the x coordinate

$$\sigma^2 = \langle x^2\rangle = \frac{\langle a^2\rangle}{2} = \frac{b_r^2 + 1}{2b_r}\sigma_0^2 = F\,\sigma_0^2, \quad (26)$$

where σ_0^2 is the variance in the absence of a mismatch. This expression can be rewritten in terms of $\det\Delta J$ which we found in Section III.:

$$\frac{\sigma^2}{\sigma_0^2} = 1 + \frac{1}{2}\left|\det(\Delta J)\right|. \quad (27)$$

For the case where the slope of the amplitude function is matched and equal to zero, we have

$$\frac{\sigma^2}{\sigma_0^2} = 1 + \frac{1}{2}\left(\frac{\Delta\beta/\beta_0}{\sqrt{1 + \Delta\beta/\beta_0}}\right)^2. \quad (28)$$

This says that a 20% β mismatch at injection, for example, would cause only a 2% increase in the rms emittance.

VI. REFERENCES

[1] T. Sen, M. J. Syphers, "Notes on Amplitude Function Mismatch," SSC Report SSCL-604, October 1992.

[2] E.D. Courant and H.S. Snyder, "Theory of the Alternating-Gradient Synchrotron," Annals of Physics, vol. 3, No. 1, p.26 (1958).

[3] M. J. Syphers, "Injection Mismatch and Phase Space Dilution," Fermilab FN-458, June 1987.

[4] D. A. Edwards and M. J. Syphers, *An Introduction to the Physics of High Energy Accelerators*, John Wiley, and Sons, New York, 1993.

Chapter 4

Beam Loss Monitoring

4.1 Introduction

Beam Loss Detection

K. Wittenburg, Proceedings of European Workshop on Beam Diagnostics and Instrumentation for Particle Accelerators, Montreux, Switzerland, 1993, CERN PS/93-35 (BD)

Beam Loss Detection

K. Wittenburg

Deutsches Elektronen Synchrotron, DESY; Hamburg

1 Abstract

A review of Beam Loss Monitor Systems (BLM systems) used in accelerators since about 1960 is given, with emphasis on systems suitable for measuring and localizing beam losses over an entire accelerator. Techniques presented include: Long and Short Ionization Chambers, Scintillation Counters, Electron Multipliers, Cryogenic Calorimeters and PIN Photodiodes.

2 Introduction

2.1 Uses of BLM systems

The usual goal of particle accelerators is to deliver high luminosity to experiments. The information from BLMs helps in the tuning of the machines for the high beam currents and long lifetimes necessary for improved luminosity.

Beam loss may result in damage to accelerator components or the experimental detectors. A task of the BLM system is to avoid such damage; in some accelerators it is an integral part of the protection system, signaling a beam abort system to fire if a certain loss rate is exceed (Ref. 1, 2, 3). This is of vital importance to the Generation of superconducting accelerators, for which beam losses in the superconducting components may lead to a quench, resulting in a shut-down of accelerator operation during the quench recovery procedure, as well as possible damage to the components. Another task of BLM systems is to identify of the position (and time) of unacceptable losses. This often indicates the source of the problem in the machine. A BLM system provides a fast way to determine the position of aperture restrictions and semitransparent obstacles in the accelerator, and helps to keep the radiation level in the accelerator and its surroundings as low as possible.

2.2 Principles of loss detection

In case of a beam loss, the BLM system has to establish the number of lost particles in a certain position and time interval[1]. All BLM systems discussed here are mounted outside of the vacuum chamber, so that the detector normally observes the shower caused by the lost particles interacting in the vacuum chamber walls or in the material of the magnets. The number of detected particles (amount of radiation, dose) and the signal from the BLM should be proportional to the number of lost particles. This proportionality depends on the position of the BLM in respect to the beam, type of the lost particles and the intervening material, but also on the momentum of the lost particles, which may vary by a large ratio during the acceleration cycle. Together with the specification for acceptable beam losses as a function of beam momentum, this defines a minimum required sensitivity and dynamic range for BLMs. Additional sensitivity combined with a larger dynamic range extend the utility of the system for diagnostic work.

One has to distinguish between two types of losses:

FAST LOSSES:

Total beam loss during one or very few turns. In most cases there is no need of a BLM system to localize the error in the machine. Often it is a easily detectable error like a closed vacuum valve, a broken power supply, a

---

[1] I exclude from my talk beam current monitors, which give the amount of losses but not the position

fired (or not fired) kicker, etc. Nevertheless it could be dangerous for accelerator components (especially superconducting components) and a BLM system may warn if an intolerable dose occurs.

SLOW LOSSES:

Partial beam loss over a time (circular machines) or distance (LINAC, transport lines) interval. In storage-rings, the lifetime is defined by slow losses. There are many reasons for these losses and a BLM system is very helpful for finding out what is happening in the machine. In superconducting accelerators a BLM system may prevent from beam loss induced quenches caused by slow losses.

In addition measurements of injection-, ejection- or collimator- efficiencies can be performed using BLMs (e.g. Ref. 4), as well as background measurements in the detectors (e.g. Ref. 27, 28). This survey concentrates on BLM systems which cover the entire accelerator.

3 Long Ionization-Chambers

In 1963, Panowsky (Ref. 5) proposed for SLAC a BLM system consisting of one long (3.5 km) hollow coaxial cable. It is an industrial RG-319/U cable with a diameter of 4.1 cm, filled with Ar (95%) + CO_2 (5%) and used as an ionization-chamber (Panowski's long ionisation chamber, PLIC). It is mounted on the ceiling along the LINAC, about 2 m from the beam.
Position sensitivity is achieved by reading out at one end the time delay between the direct pulse and the reflected pulse from the other end. The time resolution is about 30 ns ($\approx$ 8 m), for shorter PLICs about 5 ns are achieved. This BLM system has been working for more than 20 years and was upgraded for the SLC (Ref. 6). Nearly the entire SLC is covered with a few PLICs
This principle of space resolution works for one-shot (-turn) accelerators (and transport lines) with a bunch train much shorter than the machine and with relativistic particles. For particles travelling significantly slower than the signal in the cable ($\approx$0.92c) the resolution of multiple hits in the cable becomes difficult. In this case and for circular machines it is necessary to split the cable. Each segment has to be read out separately, with spatial resolution approximately equal to the length of the unit. This was done in the BNL 200 MeV LINAC, where 30 cables, each 7-9 m long, are used (Ref. 7). They are installed at 1.5 - 3 m from the beam.
In the AGS ring, Booster and transport lines about 200 monitors with a length of about 5 m are installed (Ref. 8, 9). To improve the sensitivity of the BLM system in the AGS ring for ion acceleration the cables were moved from a position below the magnets to the median plane on the open side of the magnets (Ref. 10). The dynamic range of the BLMs is about 10^3.
In the KEK-PS 56 air-filled cables with a length of about 6 m are installed. Using amplifiers with a variable gain, a dynamic range of 10^4 is archived (Ref. 11).

4 Short Ionisation Chambers

Short ionization chambers are used in many accelerators. They are more or less equally spaced along the accelerator with additional units at special positions such as aperture restrictions, targets, collimators, etc. An early example of an Air filled Ionisation Chamber is the AIC proposed in 1966 in Ref. 12 (Fig. 1). 100 AICs were installed in the CERN-PS. Each chamber had a volume of about 8000 cm^3 and used a multi-electrode layout to reduce the drift path, and hence the recombination probability, of the ions and electrons, with the goal of improved linearity. A dynamic range of 10^3 was obtained.
The idea of AIC was renewed in 1992 in Ref. 14. The authors propose an AIC with a 2π geometry around the beam pipe. The goal is to measure the loss in the vacuum wall independent of azimuth angle and with high sensitivity.
The TEVATRON relies on 216 Argon filled glass sealed coaxial ionization chambers to protect the superconducting magnets from beam loss induced quenches (Ref. 1). The volume of each chamber is 190 cm^3 (Fig. 2). Most are positioned adjacent to each superconducting quadrupole. An Ar-filled chamber has the advantage of a better linearity because of a lower recombination rate than in AICs. A dynamic range of 10^4 has been reached.

A new idea is proposed in Ref. 15 for the UNK superconducting magnets. The ionization chamber is an integral part of the magnet and uses the liquid Helium as an ionization medium. A 2π geometry close to the beam pipe is foreseen, with predicted dynamic range of 10^5, but additional investigations are necessary to determine the linearity in this range, which may be restricted by the recombination rate.

5 Scintillation counters

In case of losses in a machine without a, BLM system, a temporary installation of plastic scintillator with photomultiplier readout is often made. This counters have a well known behavior but the strong radiation damage of the plastic scintillator restricts their long term use. Liquid scintillators avoid this damage and were installed in some accelerators, e.g. Ref. 16, 17. Fig. 3 shows the device at LAMPF with a dimension of 500 cm^3. A photomultiplier (PM) inside a oil filled paint can detects the scintillation light from the oil. This BLM is very fast, the pulse rise time is about 10 ns and a dynamic range of 10^5 was obtained. The gain of the photomultipliers varies within a factor of 10. Therefore a careful intercalibration of the BLM sensitivities was necessary by adjusting the high voltage (HV). The drift of the gain is a well known behavior of PMs. A stabilized HV-source and continuous monitoring of the photomultiplier gain over the run period keep the calibration error small.

6 Aluminum Cathode Electron Multipliers

An enhanced sensitivity of photomultipliers to ionized radiation is archived by replacing the photocathode by an aluminum foil. This foil works as secondary electron emitter when irradiated. A BLM system consisting of this Aluminum Cathode Electron Multipliers (ACEM) was proposed in Ref. 18 and installed in the CERN-PS (100 units) and in the PS-Booster (48 units). They are located on top of the magnets behind each straight section plus 32 additional positions for specific applications (PS).The dimensions of the tube are 4 cm in diameter and 9 cm length plus the adjacent HV-divider (Fig. 4). This BLM is very fast; the rise time of the signal is about 10 ns. For the dynamic range a value of 10^6 was exceeded by adjusting the HV. An careful selection of the ACEMs had led to gain variations of 10 %, but intercalibration and gain monitoring was performed nevertheless. This BLM system is rather expensive because the ACEM is not a standard tube of PM-suppliers (Ref. 20).

7 Cryogenic Microcalorimeters

A new system called the Cryogenic Microcalorimeter was proposed and tested in 1992 for LEP (Ref. 21). It is designed to detect beam loss induced quenches in the superconducting quadrupoles of LEP. This detector is different from all the other BLMs presented here because it does not make use of the charge created by the lost particles. A carbon resistor thermometer measures the temperature rise of the liquid Helium in the cryostat produced by beam losses. It is a very small device with dimensions of about 3 x 3 x 1.5 mm (see Fig. 5). Its position is restricted to the cryostat of superconducting magnets.
No values for the linearity and the dynamic range are available up to now but first measurements indicate an easily detectable signal with a rise time of about 20 ms in case of a beam induced quench. The signal occurs well before the quench and it should give enough time for the quench protection system to take action. The dynamic range is limited by the critical (quench-) temperature of the liquid Helium and by the noise of the monitor. One can expect that, with a known correlation between losses and temperature, this detector will work in a BLM system for superconducting accelerators. For quantitative loss measurements the temperature increase due to synchrotron radiation has to taken into account.

8 PIN Photodiodes

Most of the existing BLM systems are installed in hadron accelerators or in Linacs. Circular electron accelerators emit hard synchrotron - radiation (SR). The radiation interacts with the BLMs and a separation between SR-background and the beam loss distributions using the traditional BLM techniques is practically impossible. HERA is an accelerator with an electron and a proton ring in the same tunnel, operating at the same time. Protection of the superconducting proton magnets from beam loss induced quenches must rely on a BLM

system which sees only the proton beam losses and not the SR-background. The (hadronic) shower created by beam losses includes a large number of charged particles, in contrast to the photons of the SR. The HERA BLM system consists of two PIN Photodiodes, mounted close together (face to face) and read out in coincidence (Ref. 22). Thus charged particles crossing through the diodes give a coincidence signal, while photons interact in only one diode do not.

In contrast to the charge detection of most other BLM systems, coincidences are counted, with the count rate is proportional to the loss rate so long as the number of overlapping coincidences is small.

The Photodiodes (2 x 2.5 x 2.5 mm^3) and the preamplifier (5 x 5 x 5 cm^3) are shielded by a hat of 3 cm of lead (Fig. 6). The overall reduction of SR signals is about 10^4, resulting in a count rate of ≈ 1 Hz with 25 mA current at 30 GeV/c in the electron ring (Ref. 23). The system has very low noise, with a dark count rate of less than 0.01 Hz. The pulse length is adapted to the 96 ns bunch spacing in HERA, so that the maximum count rate is 10.4 MHz. Therefore a. dynamic range of more than 10^9 is available.

The radiation resistance of the BLMs is adequate for long term use in HERA. A dose of 5 x 10^5 rad leads to a small and tolerable reduction in gain (Ref. 24, 25), while the dose reaching the monitor below the lead shield will be about 10^4 rads/year. BLMs are mounted on top of each of the superconducting quadrupoles. At this position the showering of the lost protons give a count rate which is independent of the radial position of the loss, and, within 5 m, also of the longitudinal position (Ref. 23). Additional BLMs are mounted on collimators, and on some of the warm quadrupole magnets, for a total of 250 units.

   The BLM system has been operating since the 1992 running period and their good performance is indicated by some measurements:

   1) The loss rotes calculated from lifetime and measured by the BLMs agree to within 25 % (Ref. 26)[2].

   2) The counts are integrated over a time period of 5.2 ms to match the cryogenic time constant of the superconducting magnets (>20 ms). The predicted coincidence rate corresponding to the critical loss rate for a quench at 820 GeV/c is about 860 counts/5.2 ms. The only beam induced quench of a HERA quadrupole in 1992 showed a count rate of 1258 counts/5.2 ms for the quenched quadrupole. A nearby quadrupole which did not quench showed a rate of 893 counts/5.2 ms. The critical rate must be somewhere in between and is not far away from the predicted one. The critical rate was detected about 100 ms before the magnet quenched.

   3) A lifetime problem in the HERA electron ring was solved using the BLMs. All monitors were moved from the proton ring to the electron ring to find the problematic section. A high count rate, inversely proportional to the beam lifetime, was measured in one of the straight sections. The problem vanished after a part of the vacuum-chamber in this section was replaced. This result demonstrates that the BLM system is also useful in high energy electron rings. It is planned to install about 250 additional monitors in the HERA electron ring.

9 Summary

   Some Beam Loss Monitors techniques for measuring losses along an entire accelerator have been presented.

   A long ionization chambers using a single coaxial cable works well for one-shot accelerators or transport lines. To achieve spatial resolution of losses along an entire accelerator two conditions must be fulfilled: 1) The machine must be much longer than the bunch train, and 2), the particles must be relativistic.

   The most common BLM now in use is a short ionization chamber. Whether a simple air filled chamber is adequate, or an Argon or Helium filled chamber, with superior higher dynamic range, must be used, depends on the conditions of the particular accelerator. Ionisation chambers are radiation resistant but respond to synchrotron radiation.

   A very sensitive system for measuring beam losses is an electron multiplier in combination with a photocathode and scintillator or with an Aluminum cathode acting as secondary electron emitter. Because of the adjustable gain the dynamic range can be large, but the calibration of each device must be adjusted and monitored over time. These systems are also sensitive to synchrotron radiation and relatively expensive.

   The Cryogenic microcalorimeter measures the temperature rise of the liquid Helium in superconducting magnets resulting from beam loss. The temperature rise corresponding to beam loss sufficient to cause a quench

---

[2] Please note that the efficiency of the BLM to charged particles is about 20 time higher than previously assumed (Ref. 27). Correct the loss-rate in Ref. 26 by 1/20.

is readily observed. Some additional investigations must be made of the dynamic range and the linearity of this device but first measurements indicate its suitability for quench prevention and loss measurements. The temperature rise due to synchrotron radiation must be taken into account when using Cryogenic Microcalorimeters for loss diagnostics in electron machines. The application of the calorimeter is limited to superconducting magnets.

The combination of two PIN-Photodiodes in a coincidence counting results in a detector with very large dynamic range and extremely effective rejection of synchrotron radiation. The small dimensions permit simple shielding and easy installation at any position. The measured radiation resistance permits long term use also in high energy electron machines with a high radiation background. The monitor with its simple accompanying electronic is inexpensive, which may be of great importance in very big machines with a large number of loss monitors. A (present) limitation is the inability to distinguish overlapping counts, so that the response is linear only for losses for which there is significantly less than one count per coincidence interval.

Acknowledgements

10 References

Ref. 1: R.E. Shafer et al.; The TEVATRON Beam Position and Beam Loss Monitoring System.
Int. Conf. on High Energy Accelerators, Fermilab, (1983)

Ref. 2: M. Fishman, D. Reagan; The SLAC Long Ion Chamber System for Machine Protection.
IEEE Trans. on Nucl. Science Vol. 14 (1967), p.1096 - 1098

Ref. 3: SSC Central Design Group; Conceptual Design of the Superconducting Super Coillider. SSC-SR-2020, (1986)

Ref. 4: F. Hornstra; The System for precise Measurement of Accelerator Extraction Efficiency.
Nucl. Instr. & Methods 128, (1975), p. 435 - 440

Ref. 5: W.K.H. Panofsky; SLAC Internal Report TN-63-57, (1963)

Ref. 6: J. Rolfe et al.; Long Ion Chamber System for the SLC.
SLAC-PUB-4925, (1989)

Ref. 7: J. Balsamo et al.; Long Radiation Detector System for Beam Loss Monitoring.
IEEE Trans. on Nucl. Science Vol.NS-24, No. 3, (1977), p. 1807-1809

Ref. 8: R.L. Witkover; Microprocessor Based Beam Loss Monitor System for the AGS.
IEEE Trans. on Nucl. Science, Vol. NS-26, No. 3, (1979), p. 3313-3315

Ref. 9: E.R. Beadle et al.; The AGS Beam Loss Monitor System.
Proc. Part. Accel. Conf., San Francisco, (1991), p. 1231-1233

Ref. 10: G.W. Bennett et al.; The Upgraded Ring Loss Radiation Monitoring System at the AGS.
Proc. Part. Accel. Conf., Chicago, (1989); BNL-41824

Ref. 11: N. Nahagawa et al.; Beam Loss Monitoring System with Free - Air Ionisation Chambers.
Nucl, Instr. & Meth. 174, (1980), p. 401 - 409

Ref. 12: V. Agoritsas; Air Ionisation Chamber as Detector of the Beam Losses in the CPS Ring.
Internal Report CERN MPS/Int.CO 66-23, (1966)

Ref. 13: J.J. Merminod; Le System d'Obversation des Pertes du Fraisceau Interne du PS.
CERN MPS/Int. CO 68-6, (1968)

Ref. 14: S.N. Lapitsky et al.; The Concept of Beam Loss Monitors Design and their Implementation at IHEP.
Proc. 15th Int. Conf. on high Energy Accel., Hamburg, (1992), p.242-244

Ref. 15: I.A. Kurochkin et al.; Beam Loss Monitor for Superconducting Accelerators.
IHEP 91-168, (1991), Protvino

Ref. 16: J.R. Parker et al.; A Beam-Spill Monitor for LAMPF.
IEEE Trans. on Nucl. Science Vol. 18 No. 3, (1971), p. 825-826

Ref. 17: R.A. Lundy and D.F. Sutter; A System for Monitoring Proton Losses from the NAL Main Accelerator.
IEEE Trans. on Nucl. Science Vol. 20 No. 3, (1973), p. 596-598

Ref. 18: V. Agoritsas and C. Johnson; EMI Aluminum Cathode Electron Multipliers: CERN TESTS.
CERN MPS/CO Note 71-51, (1971)

Ref. 19: V. Agoritsas et al.; A Microprocessor-Based System for Continuous Monitoring of Radiation Levels
around the CERN PS and PSB Accelerators.
CERN PS/ 85-60 (CO), (1985)

Ref. 20: Thorn EMI, Technical Data sheet; Nuclear Radiation Detector Type 9841 (Aluminum Cathode Electron
Multiplier), (1989)

Ref. 21: Ph. Lebrun et al.; Cryogenic Microcalorimeters for Measurement of Energy Deposition by Beam Losses
in Superconducting Accelerator Magnets.
15th Int. Conf. on high Energy Accel., Hamburg, (1992), p. 592-595

Ref. 22: K. Wittenburg; Strahlverlustmonitore für den HERA Protonen-Ring.
DESY HERA 89-23, (1989)

Ref. 23: S. Schlögl; Einsatz von PIN-Photodioden als Protonen-Strahlverlustmonitore bei HERA.
DESY HERA 92-03, (1992)

Ref. 24: K. Wittenburg; Radiation Damage in PIN - Photodiodes.
Nucl. Instr. & Meth. A270, (1988), p. 56 - 61

Ref. 25: K. Wittenburg; Strahlenschäden am Photodioden Verstärker.
Interner Bericht, PKTR note No. 9, (1987)

Ref. 26: S. Schlögl and K. Wittenburg; A Beam Loss Monitor System for HERA.
Proc. 15th Int. Conf. on high Energy Accel., Hamburg, (1992), p. 254-256

Ref. 27: E. Morre; Ein Untergrundmonitor für das ZEUS-Experiment.
Diploma Thesis, (1992), University Hamburg

Ref. 28: J. Wear; The ALEPH Rapid Beam Loss Interlock- System.
This proceedings

11   Figures
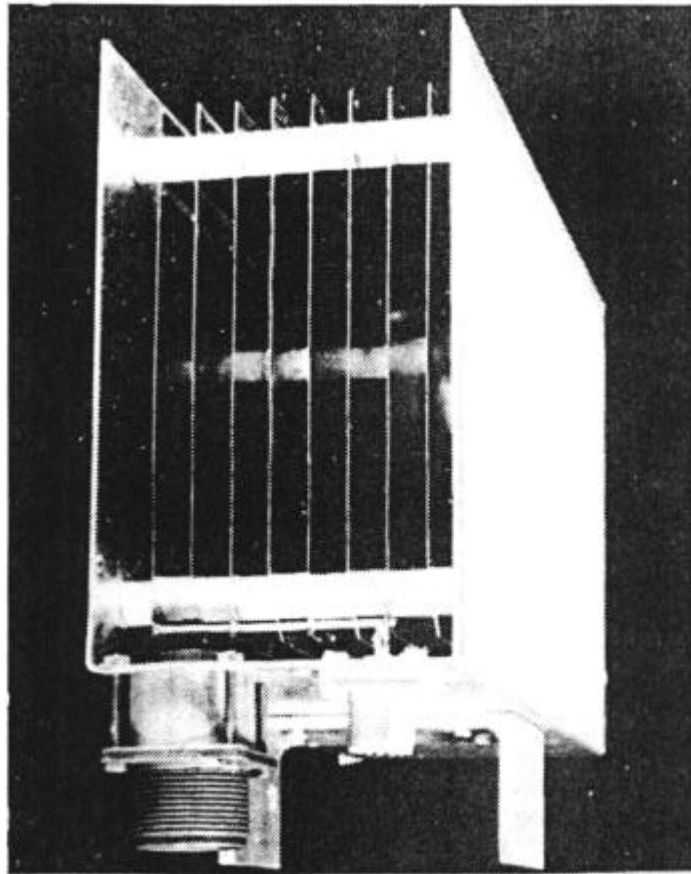
Figure 1: Air Ionisation Chamber at the PS (1968). The cover is removed (from Ref. 13).

Figure 2: The TEVATRON Argon filled Ionization Chamber (1983)

RCA 4552 DEV. TYPE C31028 DEVELOPED FOR CBS LABS EVR

I PINT PAINT CAN (FRICTION LID CAN) INVERTED

INSULATORS PILLAR 1/4 DIA. x 3/4 LG.

RESISTOR STRING 100K EACH

LID
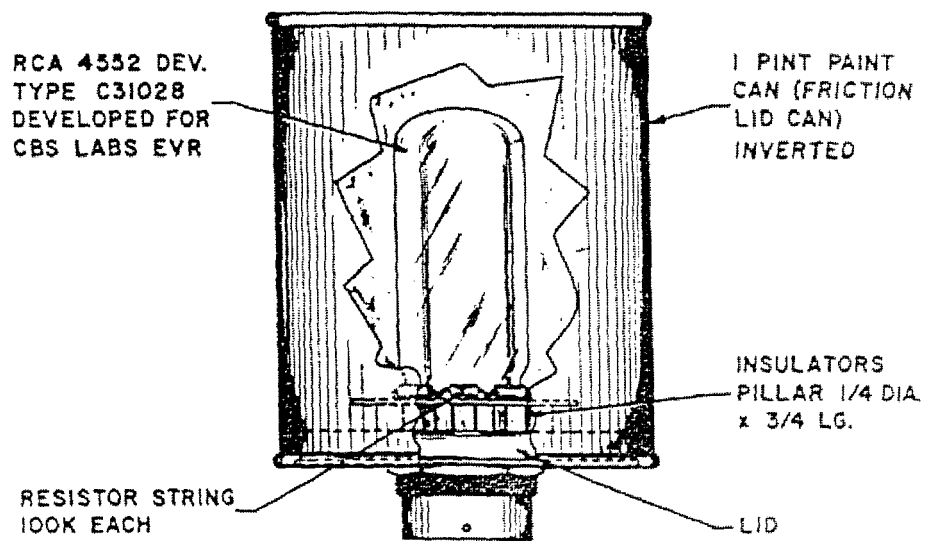
Figure 3: The Liquid Scintillator BLM at LAMPF (1971), (from Ref. 16)
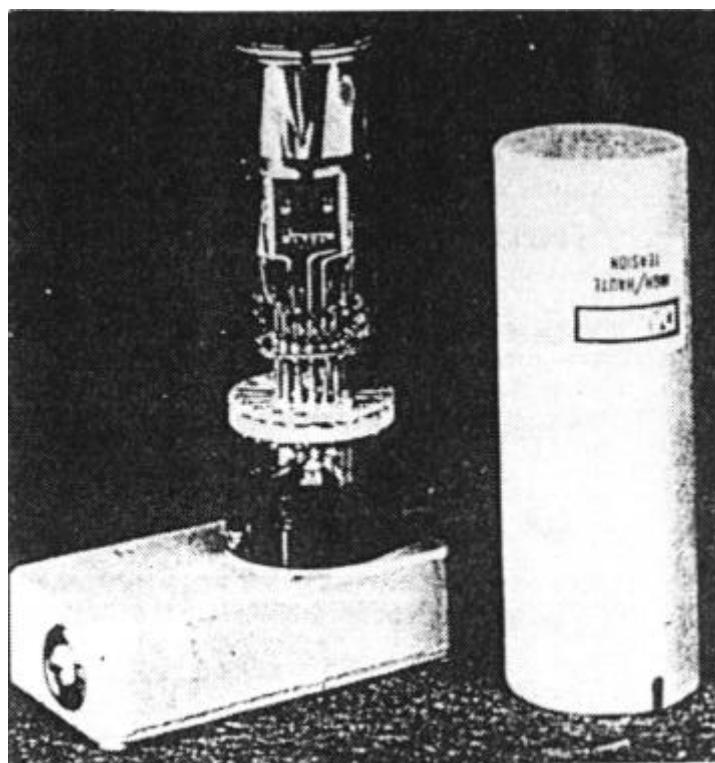
Figure 4: The Aluminum Electron Multiplier at CERN PS (1985), (from Ref. 19).

/1: cover / 2: body /
3,4: thermometer sleeve / 5: stud cover / 6: plug /
7: support stud / 8: carbon resistor thermometer.
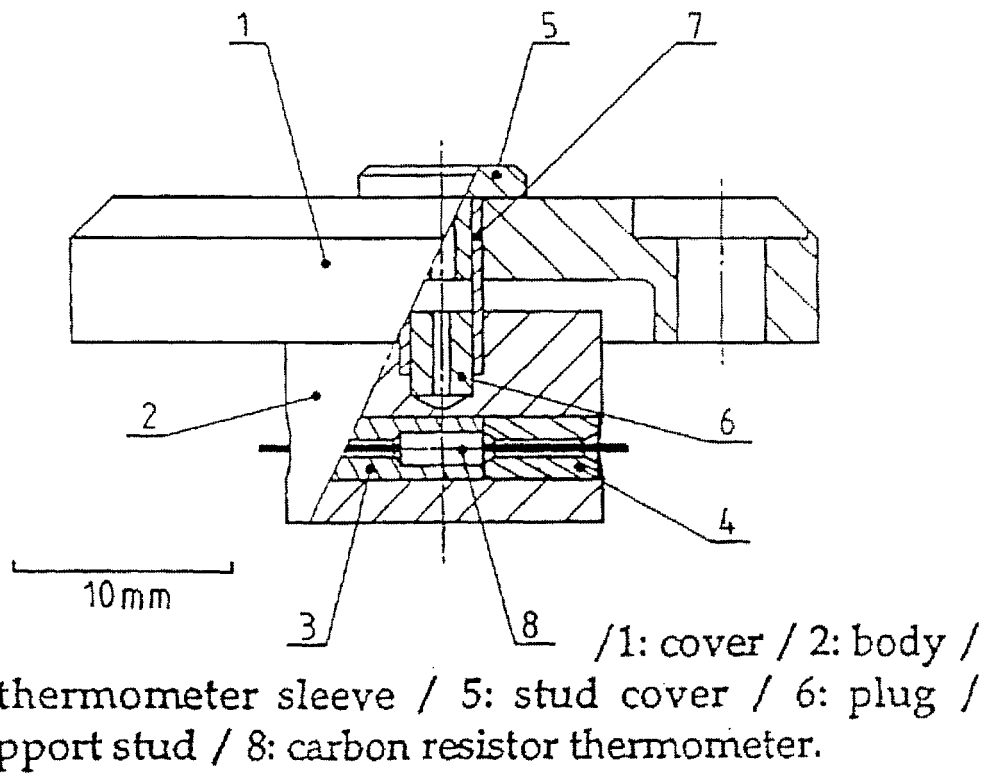
Figure 5: Cut-away view of the microcalorimeter (1992), (from Ref. 21).
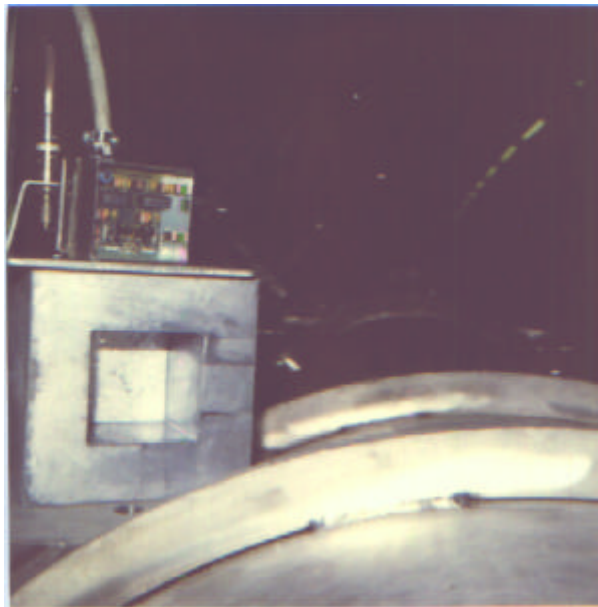
Figure 6: The PIN Photodiode BLM on top of a HERA magnet (1991). The lead hat is removed
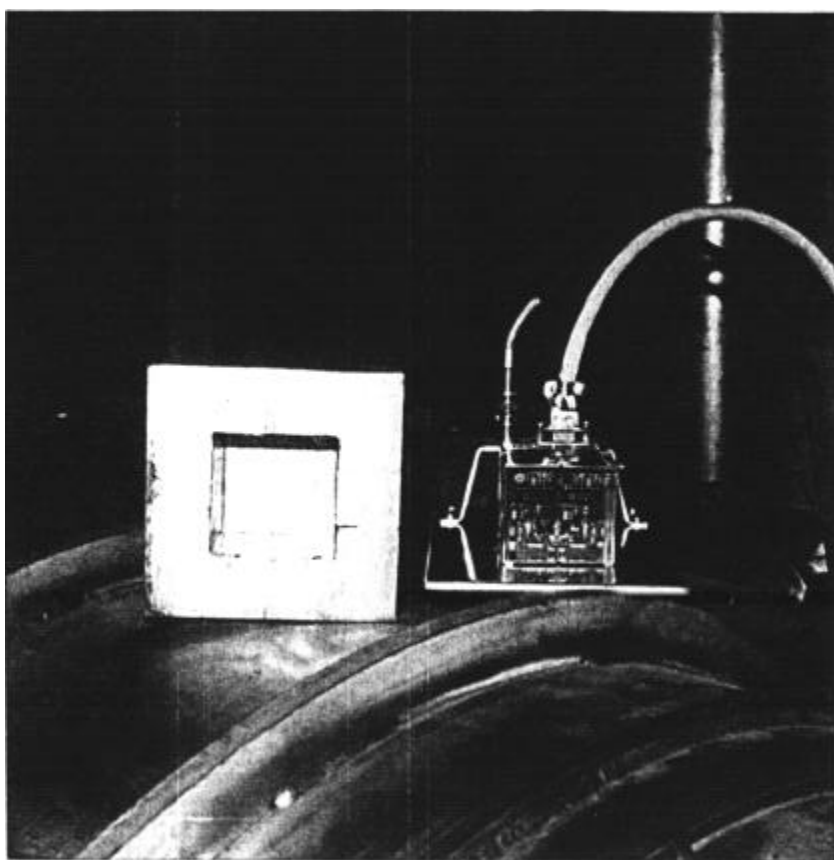
References attached:

Beam Loss Detection
K. Wittenburg
Deutsches Elektronen Synchrotron, DESY
Proc. 1st European Workshop on Beam Diagnostics and Instrumentation for Particle
Accelerators, Montreux, Switzerland, 3-5.5.1993,
CERN PS/93-35 (BD)
http://adweb.desy.de/mdi/downloads/BLM-DET.pdf

Beam Loss Monitoring and Control
Kay Wittenburg,
Deutsches Elektronen Synchrotron DESY, Hamburg, Germany
Proc. Eighth European Particle Accelerator Conference, La Villette – PARIS, 3 - 7 June 2002
http://accelconf.web.cern.ch/AccelConf/e02/PAPERS/THYGB001.pdf

References to download:

K. Wittenburg
Beam loss monitors
CERN Accelerator School 2008 Specialised Beam Diagnostics School in Dourdan, France,
CERN-2009-005; pp 249 ff.; http://cdsweb.cern.ch/record/1071486/files/cern-2009-005.pdf
Abstract
This lesson discusses the fundamental aspects of measuring beam losses including their use for beam diagnostic
and safety issues. Also the detailed functionality and detection principle of various common beam loss monitors
are presented, with a focus on their intrinsic sensitivity.

R.E. Shafer
A Tutorial on Beam Loss Monitoring
Proc. 10th Beam Instrumentation Workshop
Brookhaven National Laboratory, Upton, NY
May 6 - 9, 2002
http://ab-div-bdi-bl-blm.web.cern.ch/ab-div-bdi-bl-
blm/Beam_loss_detectors/Literature/schaefer_biw02_tutorial.pdf
Abstract. The beam loss monitoring system is one of the two most widely distributed beam
diagnostic systems at most particle accelerator facilities. This tutorial reviews the characteristics
of the ionizing radiation from beam losses, and the properties of beam loss radiation detectors.

E.B. Holzer et al.,
Beam loss monitoring system for the LHC.,
CERN-AB-2006-009, Feb 2006. 2005 IEEE Nuclear Science Symposium and Medical
Imaging Conference, El Conquistador Resort, Puerto Rico, 23-29 Oct 2005. , IEEE, Volume
2:1052 – 1056, http://weblib.cern.ch/abstract?CERN-AB-2006-009

L. Fröhlich,
Beam Loss Monitors,
ERL Instrumentation Workshop, Cornell University, 2-3 June 2008
http://tesla.desy.de/~lfroehli/download/ERL_instrumentation_ws_2008_BLMs.pdf

4.2   Further Reading I:

Beam Loss Monitoring and Control
*K. Wittenburg, Proceedings of European Particle Accelerator Conference
EPAC02, 2002*

BEAM LOSS MONITORING AND CONTROL

Kay Wittenburg, Deutsches Elektronen Synchrotron DESY, Hamburg, Germany

Abstract

The use of Beam Loss Monitors (BLMs) as sensitive tools for various beam diagnostic applications will be discussed as well as their tasks in machine protection and loss location detection. Examples will illustrate that an appropriate design of a BLM-system and a proper understanding of loss events can improve machine performance.

1 INTROCUCTION

"You do not need a BLM-System as long as you have a perfect machine without <u>any</u> problems. However, you probably do not have such a nice machine, therefore you better install one."

Beam loss monitor systems are designed for measuring beam losses around an accelerator or storage ring. A detailed understanding of the loss mechanism, together with an appropriate design of the BLM-System and an appropriate location of the monitors enable a wide field of very useful beam diagnostics and machine protection possibilities.

Beam losses can be divided into two different classes:

1) **Irregular losses**, sometimes called "fast or uncontrolled losses": These losses may be distributed around the accelerator and not obviously on a collimation system. They are very often a result of a misaligned beam or a fault condition, e.g. operation failure, trip of the HF-system or of a magnet power supply. Losses should be avoided and should be kept to low levels

- to keep activation low enough for hands-on maintenance, personal safety and environmental protection,
- to protect machine parts from beam related (radiation) damage. This includes quench protection of superconducting magnets and acceleration structures and protection of detector components,
- to achieve long beam lifetimes or an efficient beam transport to get high integrated luminosity for the related experiments.

Sometimes such losses have to be tolerated even at a high level at low repetition rates during machine studies. However, a beam loss monitor system should define the allowed level of those losses. The better protection there is against these losses, the less likely is down time due to damage of components. A post mortem event analysis is most helpful to understand and analyse the faulty condition.

Some examples of such a functionality of beam loss monitor systems will be given in this paper.

2) **Regular losses**, sometimes called "slow" or "controlled" losses: Those losses are typically not avoidable and are localized on the collimator system or on other (hopefully known) aperture limits. They might occur continuously during operational running and correspond to the lifetime/transport efficiency of the beam in the accelerator. The lowest possible loss rate is defined by the theoretical beam lifetime limitation due to various effects, like residual gas, Touschek effect, etc.

Some examples will be discussed, where, with the help of a beam loss monitor system, the measurement of losses can be used for machine diagnostic purposes.

<u>It is clearly advantageous to design a BLM-System which is able to deal with both loss modes.</u>

2 SOME COMMON ASPECTS

There are some common aspects, which are valid for every beam loss monitor system:
a) Type of loss monitor
b) Positioning of the loss monitor

2.1 Type of Loss Monitor

Typical beam loss monitors detect beam losses by measurement of ionising radiation produced by lost beam in real-time and with a certain position resolution. Other systems, like differential beam current measurements, have a very rough position resolution, or have a very long time constant (e.g. dose measurements or activation) and are not the subject of this talk.

The produced radiation consists mainly of electromagnetic particles (electron-, positron- and gamma- shower), while the loss of a hadron (proton, ion) produces some hadronic particles (protons, neutrons), too. However, the signal source of beam loss monitors is mainly the ionizing capability of the charged shower particles.

Different types of such loss monitors exist and detailed descriptions of most types can be found in [1, 2]. Options for beam loss monitors might be: long and short Ion chambers, Photomultipliers with scintillators (incl. Optical Fibers), PIN Diodes, Secondary Emission Multiplier-Tubes, Microcalorimeters, Compton Diodes, etc. A nice list of "considerations in selecting a beam loss monitor" is discussed in [2]:

- Sensitivity
- Type of output (current or pulse)
- Ease of calibration (online)
- System end-to-end online tests
- Uniformity of calibration (unit to unit)
- Calibration drift due to aging, radiation damage, outgassing, etc.
- Radiation hardness (material)

- Reliability, Availability, Maintainability, Inspect ability, Robustness
- Cost (incl. Electronics)
- Shieldability from unwanted radiation (Synchrotron Radiation)
- Physical size
- Spatial uniformity of coverage (e.g. in long tunnel, directionality)
- Dynamic range (rads/sec and rads)
- Bandwidth (temporal resolution)
- Response to low duty cycle (pulsed) radiation
- Instantaneous dynamic range (vs. switched gain dynamic range)
- Response to excessively high radiation levels (graceful degradation)

Consideration of these parameters gives a good guide to find (or design) the best monitor type for a particular beam loss application.

2.2 Positioning of the Loss Monitor

The loss of a high-energy particle in the wall of a beam pipe results in a shower of particles, which leak out of the pipe (Low energy beam particles, which do not create a shower leakage outside the vacuum pipe wall, will be hardly detectable by a loss monitor system). The signal of a loss detector will be highest, if it is located at the maximum of the shower. Refs. [3, 4, 5] are using Monte Carlo simulations to find the optimum locations for the monitors, as well as to calibrate the monitors in terms of 'lost particles/signal'. The length of the shower depends on the energy of the lost particle and ranges from some meters for very high proton energies [4] to a few cm for medium electron energies [5]. Therefore the expected location of lost particles has to be studied in advance to locate the monitors at the right location, especially at electron accelerators. But this means, that an understanding of the loss mechanism and dynamics in the accelerator is necessary to predict the typical positions of losses. For example, Refs [5, 6] had done detailed particle tracking studies to follow the trajectory of an electron in the accelerator after an energy loss due to scattering on a residual gas molecule or on a microparticle.

There are many different reasons for beam losses and a complete beam loss system has to be carefully designed for a detection of a specific loss mechanism.

In the following, some examples for different loss mechanisms, their detection and their use for beam control and diagnoses will be presented.

3 SOME EXAMPLES FOR IRREGULAR, UNCONTROLLED LOSSES

3.1 Radiation Damage

A serious problem for high current and high brilliance accelerators is the high power density of the beam. A misaligned beam is able to destroy the beam pipe or collimators and may break the vacuum. This fact makes the BLM-System one of the primary diagnostic tools for beam tuning and equipment protection in these machines. Such a system must have enough sensitivity and dynamic range to measure low-level losses at low current (test-) beams, as well as high local losses of short duration. Together with well-designed collimation and machine interlock systems, the BLM-System should prevent harmful accidents by switching off the beam in time in case that the loss rate exceeds a certain threshold at any position. But it should also serve as a sensitive diagnostic tool during the set-up periods of the accelerator to prevent high losses at nominal currents [7, 8]. This will help to prevent excessive activation of the environment and equipment damage. Especially for high-current proton and ion accelerators, this became a very important for hands-on maintenance as well as for ground water and air activation [9].

3.2 Obstructions

The set-up periods of a new accelerator or after a reconstruction of an existing machine are always associated with beam losses, before the machine goes into normal operation. Unexpected losses can be caused by a various number of reasons, and a BLM-System may help to find them. A 'beautiful' example is discussed in [10], where an RF-finger pointing in the beam line prevented the beam from circulating in Rhic. The loss pattern showed an apparent obstacle in the ring at a certain location. The losses there went away as the beam was steered locally around an obstacle after which the beam began circulating for thousands of turns.

Other obstacle-like obstructions are vacuum-crashes and trapped microparticles [11]. They caused in more or less sudden drops in the lifetime due to scattering of the electrons on the additional particles in the beam pipe. The lifetime is reduced because beam particles lose energy by bremsstrahlung both in the field of the atomic nuclei and in the macroscopic field of the highly charged microparticle or 'dust'. The deviation of the electron orbit from the nominal orbit depends on the dispersion function in the accelerator and on the energy loss. Therefore the electrons may be lost behind the following bending magnet on the <u>inside</u> wall of the vacuum chamber. Beam loss monitors located at this location are sensitive to these effects and therefore can measure the vacuum-distribution, vacuum leaks (Fig. 1) and the existence, location and even the movement of microparticles [6, 12].

3.3 Quench Protection

Superconducting accelerators need a dedicated BLM-system to prevent beam loss induced quenches. Such a system has to detect losses fast enough before they lead to a high energy deposition in the superconducting material. A time constant of a few ms is adequate for the main loss system. HERA has shown, that the BLM-system is very often the last chance to recognize a doomed beam and to dump it before it is lost uncontrollably, possibly quenching magnets [3, 13]. Care has to be taken, to set-up
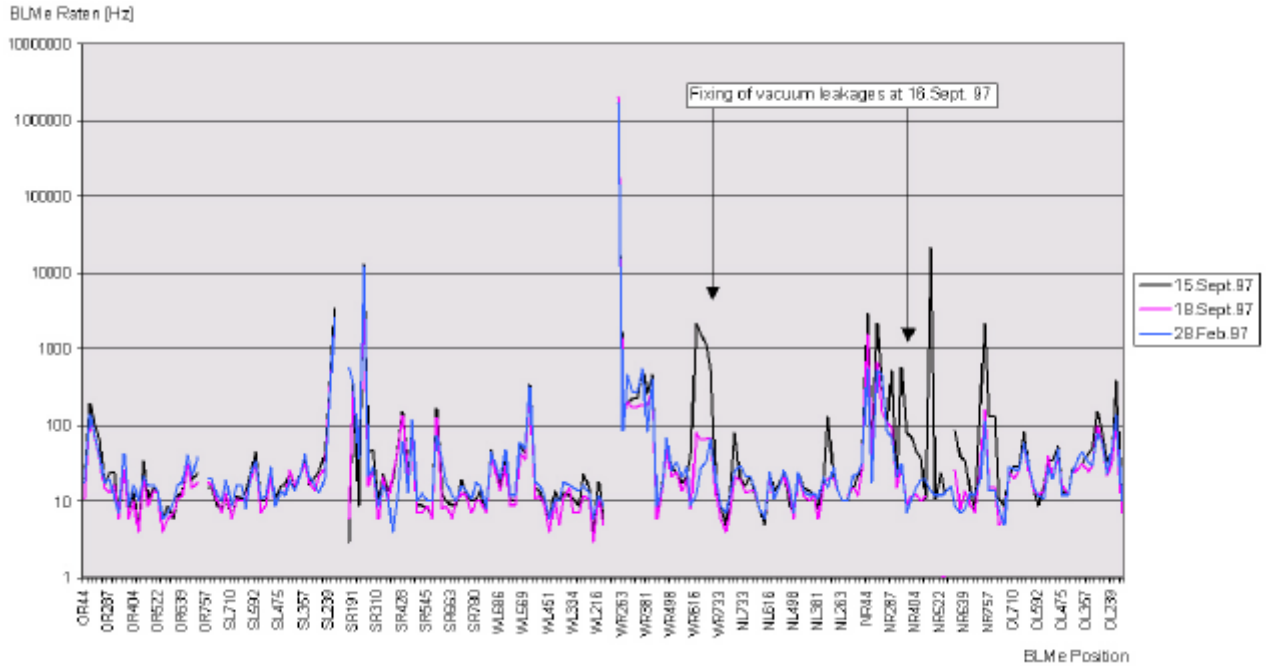
Figure 1: Beam loss monitor signals versus their location along HERAe at different dates during 1997. The two vacuum leaks on the 15.Sept. are clearly visible, as well as their reparation on the next day. Note the reproducibility of the rates.

such a system properly, so that it is not overly active (dumping too often) and also not too relaxed, allowing dangerous loss rates. Typical locations for the protection system monitors are the quadrupoles of the accelerator, were the beam has its largest dimensions. The quadrupoles act as local aperture limits and therefore the chance for a loss is larger there. It might turn out, that some special locations are more sensitive to losses than others, e.g. global aperture limits and collimators. For such locations a special treatment of the alarm-threshold, timing constant (faster) and sensitivity is applicable. Even an additional type of monitor might be the right choice.

In all cases of fast beam losses, an event archive is most helpful for a post mortem analysis of the data, to find out the reason for the loss. Certainly this will improve the operational efficiency of the accelerator.

4 SOME EXAMPLES FOR REGULAR, CONTROLLED LOSSES

4.1 Injection Studies

The injection of beam into the next accelerator of a chain should work with the highest possible efficiency. Keeping the loss rate of adjacent BLMs as low as possible is a very simple way of tuning the injection schema. BLMs measure the loss directly and with better sensitivity and resolution than the differential beam current measurement. This became important, if low injection (test-) currents are required as a result of radiation safety issues. Additional, a distributed BLM-system shows the areas of losses during the injection process as well as the loss timing behaviour (Fig. 2). By placing BLMs at

betatron and dispersion aperture limits, one can distinguish between transversal mismatch (betatron oscillations) and energy mismatch (dispersion) at injection [15].
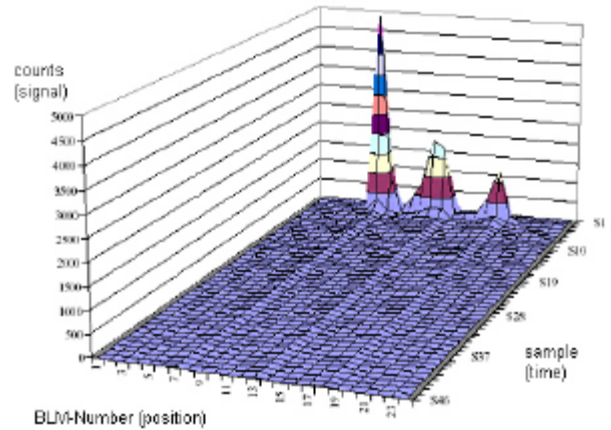
Figure 2: Surface plot of beam loss at injection and afterwards (from [14]).

4.2 Lifetime Limitations

Beside of unwanted conditions, there are unavoidable effects which limit the beam lifetime in an accelerator, e.g. vacuum lifetime (Coulomb scattering), Touschek effect, quantum lifetime, etc.:

Touschek Effect: Particles inside a bunch perform transverse oscillations around the closed orbit. If two particles scatter, they can transform their transverse momenta into longitudinal momenta. If the new momenta are outside the momentum aperture the particles are lost.

Good locations for the detection of Touschek scattered particles are in high dispersion sections following sections where a high particle density is reached. Since the two colliding particles lose and gain an equal amount of momentum, they will hit the in- <u>and outside</u> walls of the vacuum chamber. In principle the selectivity of the detection to Touschek events can be improved by counting losses at these locations in coincidence.

<u>Coulomb Scattering etc.:</u> Particles scatter elastically or inelastically with residual gas atoms or photons (Compton) or emit a high energy synchrotron radiation photon (Quantum). This leads to betatron or synchrotron oscillations and increases the population of the tails of the beam. If the amplitudes are outside the aperture the particles are lost. Losses from elastic scattering occur at aperture limits (small gap insertions, septum magnet, mechanical scrapers and other obstructions). If the energy carried away by the emitted photon is too large, the particle gets lost after the following bending magnet on the <u>inside</u> wall of the vacuum chamber.

A BLM-System with good selectivity to the different loss mechanisms is a very useful tool for various kinds of beam diagnostics, especially in Touschek limited (electron-) accelerators: The Touschek loss rate depends on the 3-dimensional electron density and on the spin of the scattering particles. Therefore any change of one or more of these parameters has an influence on the loss rates at the selected monitors. The BLM-System at BESSY was used to determine the (desired) vertical beam blow up due to a resonant head-tail mode excitation [16]. At ESRF the BLM-System was used to study the beam coupling between the transversal planes [17]. At ALS and BESSY the BLM-System was used to calibrate precisely the beam energy and observing its variation in time by using resonant depolarization of the beam [16, 18].
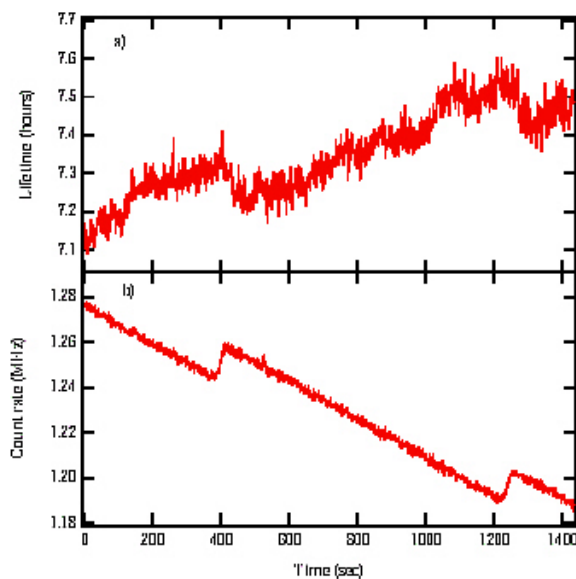

Figure 3: Beam lifetime derived from current monitor and count rate from beam loss monitor showing two partial spin depolarizations over a 25 minute period (from [18]). Note the much clearer signal from the BLM.

One useful applications of the energy measurement is the precise determination of the momentum compaction factor [18].

4.3 Tail Scans

Non-Gaussian tails in the transverse and longitudinal beam distribution produce lower beam lifetimes and background in experimental detectors. With beam profile monitoring, these tails are difficult to detect because of their small population in respect to the core of the beam. A combination of scrapers and BLMs is a good choice to measure the tail population and to get rid of it. Transverse tails are best measured at scraper positions with a large β-function and with no dispersion, while for longitudinal tail scraping scraper positions at small β-function and large dispersion are best. The measurement and scraping can be done by moving the scraper in small steps closer to the beam core measuring at each step the response of the adjacent BLM. This procedure does not affect the lifetime because the particles in the tails will get lost anyhow (as long as the scraper doesn't reach the beam core). Coulomb or Touschek scattering are the dominant processes for creating tails in lower energy electron rings, while at the very high energy ring LEP the dominant processes are Compton scattering on thermal photons (horizontal) and beam-beam bremsstrahlung (vertical) [19].

In the high-energy proton accelerator HERAp, the lifetime limitation arises from proton diffusion due to beam-beam interaction and tune modulation due to ground motion. The ground motion frequencies can be measured with BLMs at the scrapers [20, 21]. The loss spectrum of a very stable machine corresponds very well with the ground motion spectrum. The diffusion parameters at different tune modulation settings are measured by retracting the scraper from the beam tail and observing the time constants of the adjacent loss rate decrease and slow increase afterwards [20].

4.4 Tune Scans

Any change of the 3-dimansional phase space of a particle beam will effect the loss rates. By observing these losses as a function of the tune, the phase space area of the lattice can be investigated, as well as the influence of insertion devices that may cause non-linearities [16, 22]. The examination of the tune area might be somewhat lengthy, when only measuring the small changes of the beam lifetime. With the help a BLM-System, this procedure can be done very fast because the change of the loss rate can be measured immediately. [23] had shown, that a combination of a collimator and a BLM is a very sensitive tool to make fast tune scans of the area around the working point even at very long lifetimes and very small lifetime-changes.

5 CONCUSIONS

It has been shown, that a beam loss monitor system is a multi-faceted beam instrumentation tool, which opens a

wide field of applications. A precondition is a proper understanding of the physics of the beam loss to place the monitors at their adequate positions.

BLM-systems are frequently used to minimise irregular, uncontrolled losses to protect the environment and equipment of the accelerator from radiation damage; in superconducting accelerators also from beam loss induced quenches. They also serve as a sensitive tool to localise and study any kind of physical obstruction in the accelerator, from abominably RF-fingers down to different vacuum problems. Also a BLM-system helps to study and optimise the injection scheme of an accelerator. BLM-systems play an important role in investigating and optimising the beam lifetime, which is defined by different, but regular losses. A BLM-System with a good selectivity to the different loss mechanisms is a very useful tool for various kinds of beam diagnostics and beam control, e.g. controlled beam blow-up, coupling studies and tune scans. Even a precise energy calibration of the beam can be done with signals from a BLM-system. The combination of a scraper and a BLM offers additional useful applications for lifetime studies, e.g. ground motion observation, beam diffusion measurements and tail scans.

6 REFERENCES

[1] K. Wittenburg, "Beam Loss Detection**,** 1st European Workshop on Beam Diagnostics and Instrumentation for Particle Accelerators, Montreux, Switzerland, 3-5.5.1993, CERN PS/93-35 (BD)

[2] R. E. Shafer, "A tutorial on Beam Loss Monitoring," 10th Beam Instrumentation Workshop 2002, Brookhaven, Mai 2002.

 [3] K. Wittenburg, "The PIN-Diode Beam Loss Monitor System At HERA" Beam Instrumentation Workshop 2000, Boston, USA, Mai 2000

[4] A. Arauzo et al., "LHC Beam Loss Monitors", DIPAC2001, Grenoble

[5] L. Yuxion et al., "The beam loss monitoring system for the HLS storage ring", Nucl. Instr. & Meth. A467-468, 2001

[6] F. Ridoutt, K. Wittenburg, "Experience with the Electron and Proton Beam Loss monitor System at HERA", EPAC 1996, Stiges

[7] D. Gassner et al., "Spallation Neutron Source Beam Loss Monitor System"; 9th Beam Instrumentation Workshop, Boston, USA; May 2000

[8] M. C. Ross, D. McCormick, "A Coaxial Cable Beam Loss Monitor Ion Chamber System for High Power Multi-Bunch Beams", 19th International Linear Accelerator Conference (Linac 98), Chicago, IL, Aug 1998.

[9] O. E. Krivosheev, N. V. Mokhov, "Tolerable Beam Loss at High-Intensity Proton Machines", Proce ICFA Beam Halo and Scraping Workshop, Lake Como, WI, 1999

[10] P. Thompson et al., "RHIC Beam Loss Monitor System Commissioning in RHIC Year 00 Run", 9th Beam Instrumentation Workshop (BIW 2000), Cambridge, Massachusetts, May 2000. and:
http://www.rhichome.bnl.gov/RHIC/YearZero/early_beam.html

[11] Zimmermann, F. et al., "Trapped macroparticles in electron storage rings", 16th Particle Accelerator Conference : PAC '95, Dallas, TX, USA, May 1995

[12] B. Joly, U. Weinrich, G. A. Naylor, "Beam Loss Monitors at the ESRF", 4th DIPAC, 1999, Chester, UK, May 1999.

[13] M. Lomperski: "Beam losses at HERA - is everything understood?", 11th Chamonix workshop 2001
http://cern.web.cern.ch/CERN/Divisions/SL/publications/chamx2001/PAPERS/8-2-ml.pdf

[14] J. Hinkson, "ALS Beam Instrumentation, Beam Loss Monitoring", not published, Feb. 1999

[15] A. Pietryla, W. Berg, "A Cerenkov Radiation Detection System for the Advanced Photon Source Storage Ring", PAC 2001, Chicago, USA, 2001

[16] P. Kuske "Accelerator Physics Experiments with Beam Loss Monitors at BESSY", 5th DIPAC2001, Grenoble, 2001

[17] Weinrich, Udo, "Mastering beam losses on small gap vacuum chambers in synchrotron light sources", ESRF 1999, Dortmund, Univ., thesis, 2000

[18] C. Steier, J. Byrd, P. Kuske, "Energy Calibration of the Electron Beam of the ALS Using Resonant Depolarisation", EPAC2000, Vienna, Austria, 2000

[19] H. Burkhardt, I. Reichel, G. Roy, "Transverse Beam Tails due to Inelastic Scattering", Phys. Rev. Spec. Top. Accel. Beams : 3 (2000)

 [20] Brüning, O ; Mess, K H ; Seidel, M ; Willeke, F , "Measuring the effect of an external tune modulation on the particle diffusion in the proton storage ring of HERA"DESY-HERA-94-01,DESY, Jan 1994.

[21] K.H. Mess, M. Seidel, "Measurement of Proton Beam Oscillations at low Frequencies", EPAC 94, Vol. 2, London 1994

[22] K.T. Hsu et al. "Real-Time Beam Loss Monitoring and its Applications in SRRC" Particle Accelerator Conference, Vancouver, B.C., Canada, May 1997

[23] O. Kaul, B. Sarau, K. Wittenburg , "Fast Measurement of Lifetime Changes and Beam Losses in DORIS by the use of Bremsstrahlung from a Collimator", DIPAC 97, Frascati, Italy, 1997

Chapter 5

Bunch Length Measurement

5.1   Introduction

T. Lefevre

Lectures on Bunch Length Measurements

by T. Lefevre, CERN

Abstract

This lecture gives an introduction to the main techniques used to measure the longitudinal structure of particle beams. It is composed of two distinct parts. The first is a short introduction to the production of particle bunches, like we can observe them in most accelerators. The second part reviews the different techniques classically used to measure bunch length and presents their performances and limitations.

More ..

In accelerators, the time structure of the beam is governed by the characteristic of the accelerating field. On one side of the present technology, electrostatic accelerators produce DC particle beams that have no variation in time. On the opposite side, Radio-Frequency (RF) accelerators generate beams with a time microstructure extremely well defined. The sinusoidal time behavior of the RF field only provides stable conditions for acceleration during a time that is small compared to the electric field period, noted T. Therefore, a typical beam accelerated in an RF cavity is composed of a succession of particle bunches, spaced by a time equal to T with a duration, called bunch length, equivalent to a fraction of T (Typically, T/200). Nowadays RF accelerators may have operating frequency up to tens of Gigahertzs, which means that particle bunches can naturally be as short as few picoseconds. For some applications, like in Free Electron Lasers [1,2] or TeV Linear Colliders [3,4], the bunch length is even shorter, typically 10-100 femtoseconds long. In order to produce particle bunches as short, they have to be compressed. Two techniques, based on RF manipulations, have been developed, namely ballistic bunching [5] and magnetic compression [6]. Moreover, since the late 90's, the development of ultra-short intense laser pulses has contributed to the development of innovative acceleration schemes, i.e. Laser Plasma Wakefield Acceleration (LPWA) [7]. Here the accelerating field is generated by the interaction of a laser beam with a gas cell. The resulting plasma wave has a very high electric field that may oscillate at frequency up to Terahertzs. The corresponding bunch length is of the order of femtoseconds.

In order to measure the longitudinal behavior of the particle beams, a lot of instruments have been developed during the last three decades. They can be regrouped in different categories: Direct Beam Observation, Detection of Coherent Radiation, Radio-Frequency Manipulation and Sampling Techniques.

Direct Beam Observation means that the longitudinal structure of the beam is directly measured by means of fast detectors. For example, the beam current can be measured using Wall Current Monitors [8] and then digitalized using a fast oscilloscope. Wall Current Monitors have already proven their performances up to 10GHz and state of the art oscilloscopes are improving their specifications every year with sampling rate as high as 20-50GSa/s. Another very popular method since 20years relies on the use of

Streak Cameras [9]. In this case an optical repliqua of the beam longitudinal distribution is first generated using an adequate technique like Synchrotron Radiation [9], Transition Radiation [9], Diffraction Radiation [10], Cherenkov Radiation [11], ... This light pulse is then analyzed by the Streak Camera, with time resolution down to 200fs.

The observation of Coherent Radiation can also provide information on the bunch length [12]. Let's consider a bunch, consisting of many particles, classically 10^9 to 10^{11}, that radiates light through one of the effect listed in the previous paragraph. For wavelength shorter than the bunch length, the particles radiate incoherently, not being affected by the radiation of the neighbors. And the power emitted is proportional to the number of particles. For wavelength longer or equal to the bunch length, every particle emits radiation in phase, in a coherent way and the emitted power scales with the number of particles squared. In this condition, the bunch length can be obtained by measuring the power spectrum of the beam radiation. This technique, applicable to any kind of radiation has in theory no resolution limit. In practice, the method is relatively simple to implement and has already demonstrated its performances for the measurement of extremely short bunches. One limitation resides in the fact that it cannot directly provide a profile but just an estimate of the bunch length.

In order to measure the longitudinal profile of the bunch, physicists have also conceived beam diagnostics based on Radio-Frequency manipulation. Here the main idea is to encode, using RF devices, longitudinal structure of the beam into spatial information, which is easier to measure. For example, one can use an RF deflecting cavity [13] that will kick the head of the bunch in one direction and the tail of the bunch in the opposite direction. By measuring the transverse beam size downstream, one can reconstruct the longitudinal bunch profile. A similar technique exists if using an RF accelerating structure combined with a profile monitor in a dispersive region. RF deflectors become a standard instrument for femtosecond bunches [14] with the only disadvantage that this is a destructive and expensive method.

The last category of instruments presented here are basing on sampling with very short laser pulses. Electro-optic sampling [15] is the most developed technique. It is based on the conversion of the coulomb field of the bunch into an optical intensity variation. An electro-optic crystal is placed close to the beam. The field of the particle induces a polarization change of the laser beam passing through the crystal at the same time. Other sampling techniques have been tested using different processes, like Compton scattering [16] or Laser photo-neutralization [17]. Whatever is the process involved, sampling techniques always need laser pulses shorter than the particle bunch length and extremely precise laser-beam synchronization.

Since few years, single shot electro-optic techniques have been proposed and tested and are becoming the reference for non-destructive short bunch length monitoring [18].

---

[1] http://xfel.desy.de/

[2] http://lcls.slac.stanford.edu/

[3] http://www.linearcollider.org/cms/

[4] http://clic-study.web.cern.ch/CLIC-Study/

[5] B. Beutner *et al*, *"Velocity Bunching at FLASH"*, EPAC conference, Genoa, (2008), 113

6 M. Borland, *"Design and Performance simulations of the bunch compressor for the Advanced Photon Source Low-Energy Undulator Test Line Free-Electron Laser"*, Physical Review Special Topics – Accelerators and Beams, 4 (2001), 074201

7 W. Leemans *et al*, *"Laser-driven plasma based accelerators: Wakefield excitation, channel guiding and laser triggeres particle injection"*, Physics of Plasma, 5 (1998), 1615

8 P. Odier, *"A New Wide Band Wall Current Monitor"*, Proceeding of DIPAC 2003, Mainz, Germany, pp.216

9 C. Welsch *et al*, *"Longitudinal Beam Profile Measurements at CTF3 Using a Streak Camera"*, Journal of Instrumentation, 1, (2006), P09002

10 P. Karatev *et al*, " Beam-Size Measurement with Optical Diffraction Radiation at KEK ATF", Physical Review Letters, 93, 244802 (2004)

11 J. Bähr *et al*, *"Silica Aerogel Radiators for Bunch Length Measurements"*, Nuclear Instruments and Methods in Phys. Res. A, 538 (2005), 597

12 O. Grimm, *"Coherent Radiation Diagnostics for Short Bunches"*, Particle Accelerator Conference (PAC 07), Albuquerque, New Mexico, (2007) p.2653

13 P. Emma *et al*, *"A Transverse RF Deflecting Structure for Bunch Length and Phase Space Diagnostics"*, LCLS-TN-00-12, (2000)

14 M. Huening *et al*, *"Observation of Femtosecond Bunch Length Using a Transverse Deflecting Structure"*, Free Electron Laser Conference, Stanford, California,(2005) p.538

15 S.P. Jamison *et al*, "*Femtosecond Resolution Bunch Profile Measurement*", EPAC Conference, Edinburgh (2006), 915

16 W.P. Leemans *et al*, "*X-ray Based subpicosecond Electron Bunch Characterization using 90° Thomson Scattering*", Physical Review Letters 77, (1996), 4182

17 R. Connolly *et al*, "*A Transverse Phase-Space Measurement Technique for High Brightness H- Beams*", Nuclear Instruments and Methods in Phys. Res A 312, (1992), 415

18 B. Steffen *et al*, "*Electro-Optic Time Profile Monitors for Femtosecond Electron Bunches at the soft X-ray Free Electron Laser FLASH*", Physical Review Special Topics – Accelerators and Beams 12 032802 (2009)

5.2   Further Reading I:

Silica Aerogel Radiators for Bunch Length Measurements
J. Bähr et al, Nuclear Instruments and Methods in Phys. Res. A, 538 (2005), 597

Silica aerogel radiators for bunch length measurements ☆

J. Bähr[a], V. Djordjadze[a], D. Lipka[a],*, A. Onuchin[b], F. Stephan[a]

[a]*DESY Zeuthen, Platanenallee 6, 15738 Zeuthen, Germany*
[b]*Budker Institut of Nuclear Physics, Novosibirsk 630090, Russia*

Abstract

Cherenkov radiators based on silica aerogel are used to measure the electron bunch length at the photo injector test facility at DESY Zeuthen (PITZ). The energy range of those electrons is 4–5 MeV. In this paper, the time resolution defined by the usage of aerogel is calculated analytically and Monte Carlo simulations are performed. It is shown that silica aerogel gives the possibility to reach a time resolution of about 0.1 ps for high photon intensities and a time resolution of about 0.02 ps can be obtained for thin silica aerogel radiators.
© 2004 Elsevier B.V. All rights reserved.

1. Introduction

Successful optimization of the photo injector test facility at DESY Zeuthen (PITZ) requires beam diagnostics, allowing to measure electron beam properties with high resolution. To measure the temporal properties at electron energies of 4–5 MeV by optical means a radiation process is needed at which a photon bunch is produced with the same time properties as the electron bunch.

Optical transition radiation which is widely used for accelerator diagnostics produces a low number of photons per electron. In addition, those photons are produced with a wide angular distribution at these energies. Using Cherenkov radiation a significantly larger number of photons is obtained. In order to produce these photons in a Cherenkov cone with small opening angle, a material with small index of refraction is required. Therefore, silica aerogel is studied as alternative in this paper. For convenience of writing, only the short form aerogel is mainly used hereafter.

In the following section the basic properties of aerogels are summarized. In Section 3 analytical calculations on the expected degradation of the

time resolution are presented. In Section 4 GEANT 4 simulations are compared with the analytical calculations. Finally, the results are summarized.

2. Aerogel radiators

2.1. Optical properties

The main optical properties of aerogel [1–8] are characterized by three parameters:

(1) Index of refraction n.
   It is determined by the density ρ. The correct dependence [1] is $n = \sqrt{1 + \alpha\rho}$ where $\alpha = (0.438 \pm 0.001)\ (\text{g/cm}^3)^{-1}$ for a wavelength $\lambda = 400$ nm. For low densities it is possible to use $n \approx 1 + k\rho$, where $k \approx 0.21\ (\text{g/cm}^3)^{-1}$. The chemical composition of aerogel is SiO_2, therefore the aerogel dispersion can be calculated from the quartz dispersion. Aerogels are produced in a range of index of refraction of 1.006–1.13 [1–3].
(2) Light scattering length L_{sc}.
   This quantity is defined as the path length after which a fraction $1/e$ of the photons is not scattered. This effect is caused by Rayleigh scattering, for which $L_{sc} \sim \lambda^4$. Usually L_{sc} is cited at $\lambda = 400$ nm. For good aerogels the scattering length is $L_{sc} = 1-2$ cm, for best aerogels $L_{sc} = 4-5$ cm. The dependence of L_{sc} on the refractive index n is weak [1,4].
(3) Light absorption length L_{ab}.
   The light absorption length is defined as the path length after which a fraction $1/e$ of photons is not absorbed. It mainly depends on an admixture contained in the aerogel. The L_{ab} dependence on λ is a complicated relation [1,5]. For good aerogels $L_{ab} = 1$ m at $\lambda = 400$ nm and for best aerogels it reaches a value of 10 m.

2.2. Maximum thickness of aerogel

The maximum thickness of an aerogel sample is mainly limited by the scattering length L_{sc}. Let us

denote the number of Cherenkov photons per unit length of the electron path by $N_{ph,1}$. The number of photons, which do not suffer from Rayleigh scattering, in dependence on the aerogel thickness, has the form

$$N_{ph} = N_{ph,1} L_{sc}(1 - e^{-l/L_{sc}}). \qquad (1)$$

The maximum number of photons $N_{phmax} = N_{ph,1} L_{sc}$ is reached at $l \gg L_{sc}$. A good choice of aerogel thickness is $0.5 L_{sc}$. In that case about 80% of the produced photons will be collected and 20% will be scattered. The ratio of the background to the effect is around 0.25. Therefore, the maximum thickness used in this paper is $l_{max} \approx 2$ cm.

2.3. Number of photoelectrons

It is convenient to express the number of Cherenkov photons per unit length of the particle path and per unit wavelength interval in the following form [9]

$$\frac{d^2 N_{ph}}{dl\, d\lambda} = 2\pi\alpha \frac{1}{\lambda^2}\left(1 - \frac{1}{n^2\beta^2}\right), \qquad (2)$$

where $\alpha = \frac{1}{137}$ and $\beta = v/c$.

Let us express the quantum efficiency of the photon detector in a form $Q(\lambda) = Q_0 f(\lambda)$, where Q_0 is the quantum efficiency at the maximum of the spectral distribution. Let us denote the collection efficiency of the Cherenkov photons on the photo cathode of the detector by $G(\lambda)$. Then the photo electron number can be written as

$$N_{pe} = \left(1 - \frac{1}{n^2\beta^2}\right)Q_0 l 2\pi\alpha \int \frac{1}{\lambda^2} f(\lambda) G(\lambda)\, d\lambda$$
$$= \left(1 - \frac{1}{n^2\beta^2}\right)Q_0 l B(\lambda), \qquad (3)$$

where $B(\lambda) = 2\pi\alpha \int \frac{1}{\lambda^2} f(\lambda) G(\lambda)\, d\lambda$.

Taking $f(\lambda)$ for a borosilicate glass window and a bialkali photo cathode [10] with $Q_0 = 20\%$ and $G = 1$, particles with $\beta = 1$ in matter with $n = 1.5$ gives $N_{pe} = l65$ photo electrons, where l is the path length in cm. In Table 1, the corresponding data are presented for electrons with $pc = 4.0$ MeV ($\beta = 0.9919$) and $pc = 4.5$ MeV ($\beta = 0.9936$).

2.4. Multiple scattering

The mean squared angle of the electron multiple scattering can be calculated using the Rossi formula including a correction [11]:

$$\theta_{MS} = \sqrt{\bar{\theta^2}} = \frac{21\,\text{MeV}}{p\beta c} \sqrt{\frac{l}{X_0}} \left(1.0 + 0.038 \ln \frac{l}{X_0}\right). \tag{4}$$

Aerogel is SiO_2, therefore $X_0 = 27\,\text{g/cm}^2$, the same as for quartz [2,11]. For refractive indices of $n = 1.01$, $n = 1.03$ and $n = 1.05$ the corresponding radiation length is $X_0 = 570\,\text{cm}$, $X_0 = 190\,\text{cm}$ and $X_0 = 115\,\text{cm}$, respectively.

In Table 2, the data for Cherenkov angle θ_C, radius of the Cherenkov cone at the exit of the aerogel plate $r_C = l \tan \theta_C$ and the multiple

Table 1
Number of photo electrons per 1 cm path length of electrons with $p = 4.0\,\text{MeV}/c$ and $p = 4.5\,\text{MeV}/c$ in materials with different index of refraction

n	$p = 4.0\,\text{MeV}/c$	$p = 4.5\,\text{MeV}/c$
1.008	0.034	0.36
1.01	0.53	0.82
1.03	5.3	5.3
1.05	9.5	9.5
1.5	65	65

A bialkali photo cathode with $Q_0 = 20\%$ and a light collection efficiency of $G = 1$ was assumed.

scattering angle θ_{MS} are presented for different aerogels.

3. Time resolution

3.1. Reference plane

At PITZ, the Cherenkov light will be transmitted over 26 m to the entrance slit of the streak camera by an optical transmission line. In general, the optical system will have an influence on the time dispersion. This effect is not considered in this article. To analyze the influence of the radiator itself, the streak camera entrance slit is considered to be virtually back imaged near to the exit plane of the aerogel radiator.

In this article, we assume that this reference plane (RP) is located parallel to the exit plane of the aerogel (see Fig. 1). All the questions concerning the resolution discussed in this article are only considered up to this RP.

3.2. Thickness of aerogel

Besides the refractive index n also the thickness of the aerogel l is an important parameter for the time resolution. The optimal thickness in a real experiment has to be chosen as a compromise between two contradictory requirements. To improve the signal-to-noise ratio of the Cherenkov light detection taking into account light losses along the optical transmission line, the radiator

Table 2
The parameters Cherenkov angle θ_C, Cherenkov cone radius r_C, angle of multiple scattering θ_{MS}, time difference because of path length differences Δ_{pl}, σ_{pl} of time difference, the time difference caused by multiple scattering $\Delta_{MS}(\delta)$ and the corresponding $\sigma_{MS}(\delta)$ for three aerogel radiators with $n = 1.01$, $n = 1.03$ and $n = 1.05$ and for two incident electron momenta at different thickness l

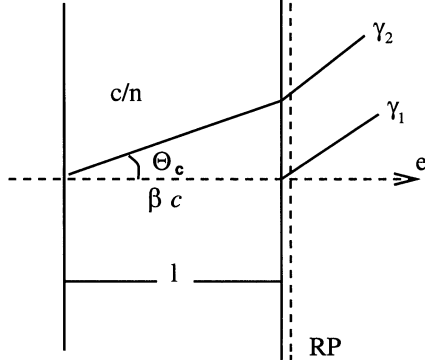| n	1.01	1.01	1.03	1.03	1.05	1.05	1.01	1.01
l (mm)	20	20	2	2	1	1	2	2
p (MeV/c)	4.0	4.5	4.0	4.5	4.0	4.5	4.0	4.5
θ_C (dg)	3.5	4.8	11.8	12.3	16.2	16.6	3.5	4.8
r_C (mm)	1.22	1.69	0.42	0.44	0.29	0.30	0.12	0.17
θ_{MS} (dg)	14.1	12.5	7.3	6.5	6.6	5.8	4.0	3.5
Δ_{pl} (ps)	0.25	0.48	0.30	0.32	0.29	0.30	0.025	0.048
σ_{pl} (ps)	0.072	0.14	0.085	0.092	0.082	0.086	0.0072	0.014
$\Delta_{MS}(\delta)$ (ps)	1.5	1.8	0.42	0.43	0.37	0.37	0.047	0.072
$\sigma_{MS}(\delta)$ (ps)	0.45	0.51	0.12	0.13	0.11	0.11	0.014	0.021

Fig. 1. Schematic view of the Cherenkov radiator system and the reference plane (RP, dashed line). The reference plane is meant to coincide with the downstream boundary of the Cherenkov radiator.

thickness has to be increased to produce more photons. But for improving the time resolution the radiator thickness is preferred to be small, as it will be shown in the next paragraphs. Two cases are considered:

(A) Large thickness: for comparison of aerogel samples with different n, the thickness will be chosen such that the number of Cherenkov photons is equal. It means that

$$l\left(1 - \frac{1}{n^2\beta^2}\right) = \text{const.} \qquad (5)$$

Aerogels with $n = 1.01$, $n = 1.03$, $n = 1.05$ will be considered. For $n = 1.01$ the optimal thickness is chosen to be about $l = 20$ mm (see Section 2.2). According to Eq. (5) the rounded thickness for the other radiators was chosen accordingly: for $n = 1.03$ $l = 2$ mm and for $n = 1.05$ $l = 1$ mm.

(B) Small thickness (for comparison): calculations for aerogel with $n = 1.01$ and $l = 2$ mm will be performed. The number of Cherenkov photons will be 10 times smaller in this case compared to case (A).

Modern technology allows to produce aerogel of such thicknesses.

3.3. Particle and light velocity

In Fig. 1 the electrons move perpendicular to the aerogel plate. The RP coincides with the second boundary of the aerogel. The time interval between the arrival of the Cherenkov photons on the RP is

$$\Delta_{pl} = \frac{ln}{c\cos\theta_C} - \frac{l}{\beta c} = \frac{n^2\beta}{c}\left(1 - \frac{1}{n^2\beta^2}\right)l. \qquad (6)$$

This effect is caused by the time difference of the particle and light arrival at the RP plane.

For $n = \text{const}$ Δ_{pl} is proportional to l. This means that one can improve the time resolution by decreasing the thickness.

The time distribution of the Cherenkov photon bunch has a rectangular shape (see Fig. 2, where $t_1 = l/\beta c$ and $t_2 = ln/c\cos\theta_C$), therefore the mean squared dispersion in time is $\sigma_{pl} = \Delta_{pl}/\sqrt{12}$.

The numerical values of the Δ_{pl} and σ_{pl} are summarized in Table 2.

3.4. Dispersion of refractive index

To study the dependence of the time resolution on the wavelength, it is convenient to write Eq. (6) in the form

$$\Delta_{pl} = \frac{\beta l}{c}\left(n^2 - \frac{1}{\beta^2}\right). \qquad (7)$$

The relative change for two different wavelengths is given by

$$\delta(\lambda_1, \lambda_2) = \frac{\Delta_{pl}(\lambda_1) - \Delta_{pl}(\lambda_2)}{\Delta_{pl}(\lambda_1)} = \frac{n^2(\lambda_1) - n^2(\lambda_2)}{n^2(\lambda_1) - (1/\beta^2)}. \qquad (8)$$

One can see that $\delta(\lambda_1, \lambda_2)$ does not depend on l. Some results of the calculation for aerogel with
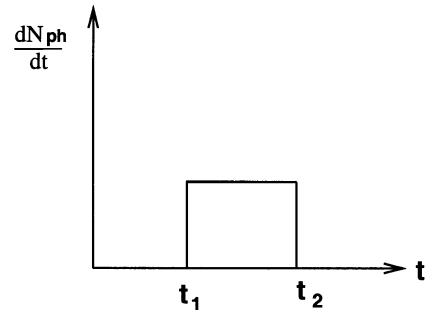

Fig. 2. Schematic view of the Cherenkov photon time distribution.

Table 3
$\delta(\lambda_1, \lambda_2)$ in % is the relative change of Δ_{pl} as a result of the dispersion of n

λ_1 (nm)	λ_2 (nm)	β	n		
			1.05	1.03	1.01
300	550	1	7	7	7
		0.9936^a	8	9	18
		0.9919^b	8	9	30
200	700	1	20	20	20
		0.9936^a	23	25	40
		0.9919^b	23	26	50

^{a}For $p = 4.5\,\text{MeV}/c$.
^{b}For $p = 4.0\,\text{MeV}/c$.

Eq. (8) are presented in Table 3 basing on quartz data from [12]. If one works far from the threshold for Cherenkov radiation $\beta \gg 1/n$ and one uses

$$n^2 = 1 + \alpha\rho \qquad (9)$$

one will obtain

$$\delta(\lambda_1, \lambda_2) = \frac{\alpha(\lambda_1) - \alpha(\lambda_2)}{\alpha(\lambda_1)}. \qquad (10)$$

In this case one can see that $\delta(\lambda_1, \lambda_2)$ does not depend on n and l.

The region $\lambda = 300-550\,\text{nm}$ is the sensitive region of a bialkali photo cathode with borosilicate glass. It is seen that the dispersion is small enough for $n = 1.05$ and $n = 1.03$ but is 30% for $n = 1.01$, $p = 4.0\,\text{MeV}/c$.

The region of 200–700 nm is presented for a dispersion estimation as an example for a photon detector with a wider sensitivity region.

3.5. Transverse dimensions and angular distribution of the electron beam

The arrival time of light on the chosen plane RP does not depend on the transverse coordinates of the electron, that is why there is no dispersion connected to the transverse size of the electron beam.

Two electrons e_1 and e_2 cross simultaneously the plane 1 (see Fig. 3). The electron e_1 is moving perpendicular to the aerogel plate and electron e_2 is moving at an angle α to it. In this case the time
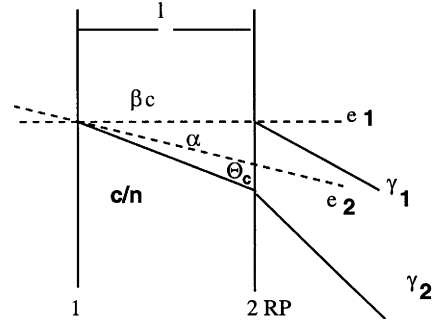

Fig. 3. Schematic view of the Cherenkov photon emission with different incident angles of the incoming electrons.

interval of the Cherenkov photons on the RP plane increases to

$$\Delta_\alpha = \frac{l}{c}\left(\frac{n}{\cos(\alpha + \theta_C)} - \frac{1}{\beta}\right). \qquad (11)$$

A typical value of α at the position where the Cherenkov radiator will be used at PITZ is $0.1°$. The resulting contribution of α to the time resolution is negligibly small because $\alpha \ll \theta_C$.

3.6. Multiple scattering

Multiple scattering in aerogel creates an angular spread of the electron beam, therefore it leads to a time dispersion as given by the Eq. (11). The analytical calculation of this effect is complicated. One could put $\alpha = \theta_{MS}$ in Eq. (11). In this case, one will do an overestimation of the multiple scattering influence, because the angle θ_{MS} refers only to the electrons at the exit of the aerogel. The photons produced in the first part inside of the aerogel will have more narrow distribution than the photons produced in the last part.

The mean squared value of the trajectory shift is $r_{MS} = \frac{1}{\sqrt{3}}\theta_{MS}l$ [11] (see Fig. 4). Let us introduce an angle δ, so that $tg\delta = r_{MS}/l = \frac{1}{\sqrt{3}}\theta_{MS}$ and let us assume that $\alpha = \delta$. The value of $\Delta_{MS}(\delta) = l/c((n/\cos(\delta + \theta_C)) - (1/\beta))$ is presented in Table 2. It is seen that thin aerogel radiators and the use of aerogel with high index of refraction is preferred.

In Table 2 an estimation of $\sigma_{MS}(\delta)$ which is defined as $\sigma_{MS}(\delta) \approx \Delta_{MS}(\delta)/\sqrt{12}$ is included. For
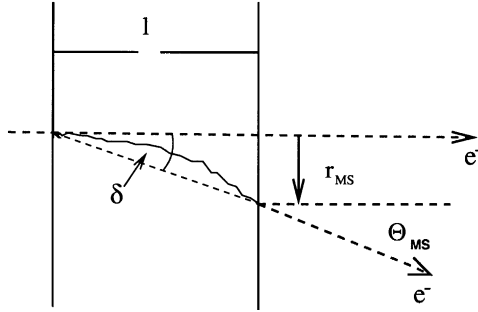
Fig. 4. Schematic view of the electron angular spread and shift due to multiple scattering.

$n = 1.05$, $n = 1.03$, and $n = 1.01$ with $l = 2\,\text{mm}$ the influence of multiple scattering is small, therefore the shape of the time spectrum is approximately rectangular. For $n = 1.01$ with $l = 20\,\text{mm}$ it is a rough estimation.

The data from Table 2 shows, that aerogel with $n = 1.01$, $l = 2\,\text{mm}$ gives the possibility to reach a time resolution $\sigma_{\text{MS}}(\delta) = 0.02\,\text{ps}$. Aerogel with $n = 1.05$, $l = 1\,\text{mm}$ gives 10 times more photons and $\sigma_{\text{MS}}(\delta) = 0.1\,\text{ps}$, whereas aerogel with $n = 1.05$, $l = 10\,\text{mm}$ would give 100 times more photons and $\sigma_{\text{MS}}(\delta) = 2\,\text{ps}$.

3.7. Other effects

Rayleigh scattering of Cherenkov photons inside aerogel is not considered. The scattered photons would have a wide angular distribution and only a small part of them would be within the acceptance of an optical transmission line.

The effect of energy loss due to ionization and Bremsstrahlung is negligibly small. Compton scattering of Cherenkov photons is much smaller than Rayleigh scattering, therefore this effect gives a negligible contribution to the time resolution. Scattering of photons at the boundary of aerogel is not considered because the index of refraction is small.

In addition to the effects on the time resolution of the aerogel radiator itself, other important sources contribute to the time resolution of a bunch length measurement system which are not considered in this article, e.g. dispersion of the optical transport system, streak camera resolution and time jitter of the facility.

4. Time resolution: Monte Carlo results

4.1. Simulation conditions

Simulations of the electron beam passage through aerogel for the PITZ set-up were performed using the GEANT 4 [13] code. The simulation setup consists of a vacuum tube with the electron beam, an aluminium entrance window, the aerogel piece and the corresponding RP (see Fig. 5). The thickness of the aerogel plate l is chosen as it is described in Section 3.2. Aerogel materials (SiO_2) with index of refraction of 1.01, 1.03 and 1.05 are investigated. In front of the aerogel a $20\,\mu\text{m}$ thick aluminium window can be positioned. This window will be used in the experiment to protect the rest of the PITZ vacuum system from outgasing particles from aerogel. An ideal photon detector is placed behind the aerogel at the reference plane as described above (see Section 3.1).

Electrons produce Cherenkov photons inside the aerogel in a wavelength range of 350–800 nm. The GEANT program was configured to perform a Cherenkov light simulation without wavelength dependence of the refractive index and assuming a photon detection efficiency of 100 percent. The physical processes include Cherenkov effect, Rayleigh scattering, multiple scattering, ionization and Bremsstrahlung. These processes are switched on one after another. No absorption and reflection of
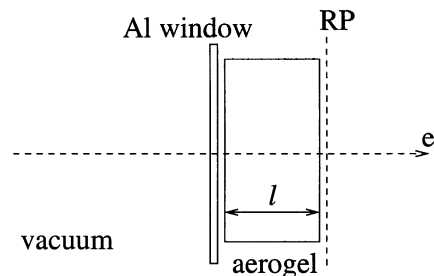

Fig. 5. Schematic view of the geometry of the GEANT 4 input.

the Cherenkov light at the boundaries of the aerogel were considered.

4.2. Acceptance model of the optical transmission line

To estimate the needed acceptance of the optical transmission line behind the aerogel plate, the transverse distribution of the photon emission points from the aerogel backplane and the angular distribution of the emitted photons are calculated for different processes. Both distributions are calculated with respect to the incident electron position and direction.

Fig. 6 shows the distribution of the photon output angle with respect to the incident electron direction for two examples: $n = 1.01$ and thickness $l = 20$ mm (figure top) and $n = 1.05$ and $l = 1$ mm (figure bottom) for an electron momentum of 4.5 MeV/c. The processes described above are applied one after another. The Cherenkov effect alone results in an angle θ_C equally to that shown in Table 2. By adding Rayleigh scattering an almost constant background is produced, the peak at θ_C is still very clear. The electron scattering in the aerogel and the aluminium window causes smearing of the distribution and a strong increase of the tail of the distribution. The behavior is similar for aerogel of different refractive indices and thicknesses except that the Cherenkov angle peak occurs at different angles.

Fig. 7 shows the distribution of the photon output radius r with respect to the incident electron position for $n = 1.01$ and thickness $l = 20$ mm (upper figure) and $n = 1.05$ and $l = 1$ mm (lower figure) for an electron momentum of 4.5 MeV/c. r is the distance between the exit point of photons in the aerogel exit plane relative to the incident electron beam position. In these figures different processes were added one after another. For the Cherenkov effect alone a radiation intensity edge occurs corresponding to r_C as shown in Table 2. Rayleigh scattering results in photons with larger radii but small intensities. By adding multiple scattering and the aluminium window the probability for larger radii increases and for smaller radii decreases. The effect of multiple

Fig. 6. Distribution of the Cherenkov photon bunches output angle with respect to the incident electron direction for $n = 1.01$ and thickness $l = 20$ mm (upper figure) and $n = 1.05$ and $l = 1$ mm (lower figure) for an electron momentum of 4.5 MeV/c. + Ray means just considering the Cherenkov effect and Rayleigh scattering. + MS means the inclusion of multiple scattering and + Al that of the aluminium window. Here the processes are added one after another.

scattering is much stronger for aerogel with low index of refraction.

For a realistic experimental design an acceptance angle for the optical transmission line between radiator and streak camera has to be chosen. Adding θ_C and θ_{MS} for the first three cases in Table 2 leads to a choice of an acceptance angle of about $20°$. In addition, all photons inside of a 5 mm radius around the initial electron direction are accepted, because the typical electron beam size at PITZ is smaller than this transverse size. This choice of cuts in angle and radius includes the peaks and edges seen in the Figs. 6 and 7, therefore most photons are collected. The following simulations are shown assuming these acceptance cuts.

Fig. 8. Time distribution of Cherenkov photon bunches produced by electron bunches of 4.5 MeV/c momentum, fixed electron direction and point-like source, no consideration of Rayleigh scattering, multiple scattering and aluminium window. The thickness of the aerogel samples is 20 mm for $n = 1.01$ and 1 mm for $n = 1.05$.
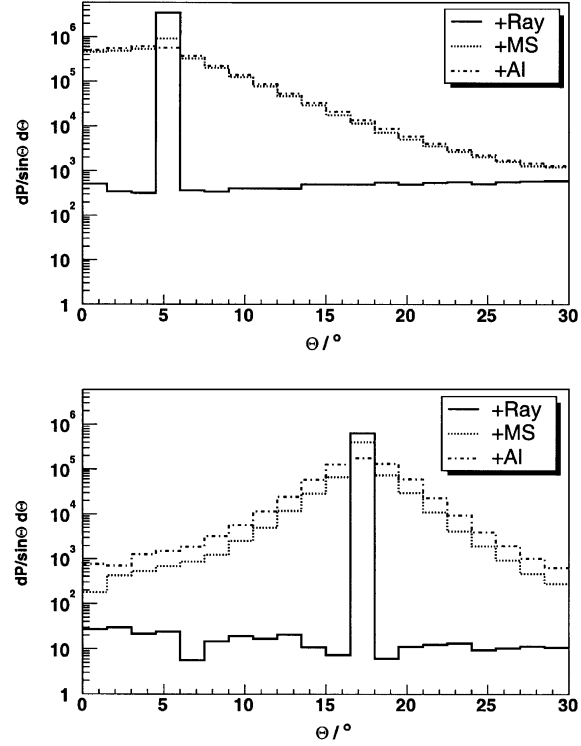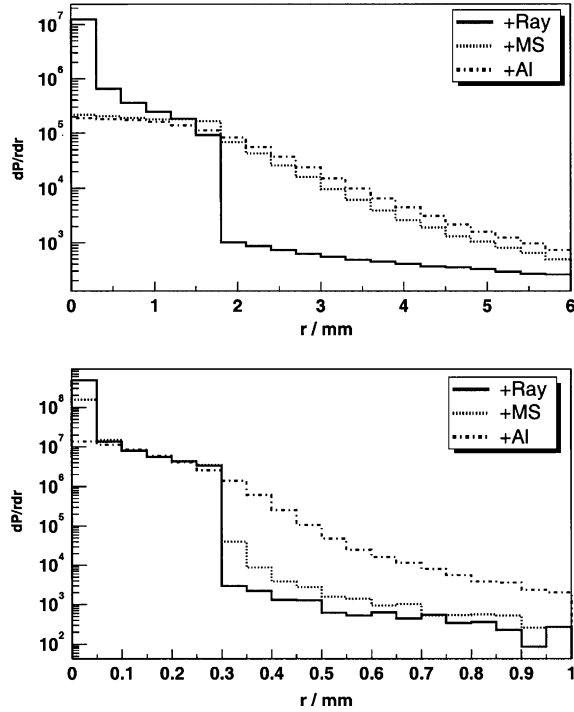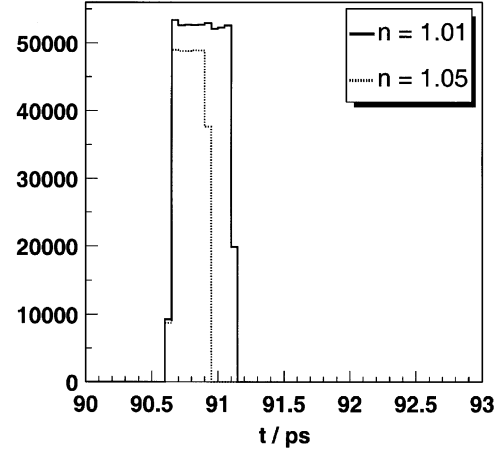
Fig. 7. Distribution of the Cherenkov photon bunches output radius with respect to the incident electron position for $n = 1.01$ and thickness $l = 20$ mm (upper figure) and $n = 1.05$ and $l = 1$ mm (lower figure) for an electron momentum of 4.5 MeV/c. Here the processes are added one after another. $+$Ray means the inclusion of Rayleigh scattering, $+$MS the inclusion of multiple scattering and $+$Al that of the aluminium window. The calculated values of r_C for pure Cherenkov effect are $r_C = 1.69$ mm and $r_C = 0.30$ mm respectively.

4.3. Particle and light velocity

To study the influence of different effects on the time resolution, simulations were performed step by step adding new phenomena to be considered in the simulation. The simplest case is when the bunch length is set to be zero and all electrons are assumed to have the same momentum, no aluminium window is in front of the aerogel and neglecting all electron interactions except the Cherenkov radiation. The electron incident angle is perpendicular to the aerogel plate.

Fig. 8 shows the time distribution of Cherenkov photons produced by electron bunches of 4.5 MeV/c momentum and arriving at the photon receiver plane for aerogels with $n = 1.01$ and $n = 1.05$ within the acceptance angle. The simulation time clock starts when the electrons start to move and ends when the photons, produced by the electrons, reach the photon receiver. This time distribution has a rectangular shape as expected from Fig. 2. The FWHM of these distributions is in agreement with the theoretical calculation of Δ_{pl} (see Table 2.). The simulated Cherenkov angle θ_C and cone radius r_C coincide with the expected values (see Figs. 6 and 7).

The integral of the distribution shown in Fig. 8 is proportional to the amount of emitted Cherenkov photons. These integrals are not equal for both distributions because the thickness was optimized for a momentum of 4 MeV/c.

4.4. Rayleigh scattering

To study the influence of Rayleigh scattering on the time resolution, a scattering length of 40 mm at 400 nm wavelength is assumed, using the proportionality mentioned in Section 2.1 (2). The resulting time distributions for an electron momentum of 4.5 MeV/c are shown in Fig. 9. The FWHM does not change compared to Fig. 8. A small
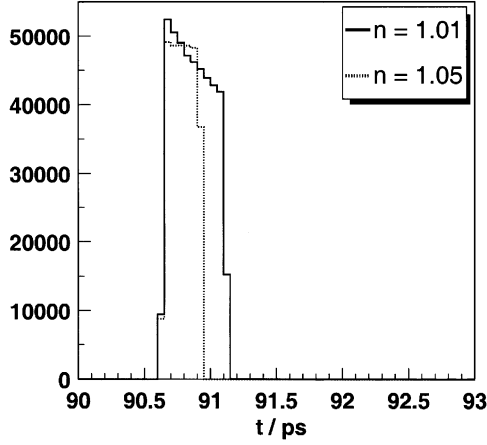
Fig. 9. Time distribution of Cherenkov photon bunches considering Rayleigh scattering produced by an electron bunch of 4.5 MeV/c momentum, without multiple scattering and aluminium window. The thickness of the aerogel samples is 20 mm for $n = 1.01$ and 1 mm for $n = 1.05$.

Fig. 10. Time distribution of Cherenkov photon bunches produced by electron bunches with a zero electron bunch length. Rayleigh and multiple scattering, ionization and Bremsstrahlung in aerogel are considered. No aluminium window is used, the momentum is 4.5 MeV/c. The thickness of the aerogel samples is 20 mm for $n = 1.01$ and 1 mm for $n = 1.05$.

decrease of intensity with time can be observed because of a longer way of the photons inside of the aerogel compared to photons which are produced near to the RP. The scattered photons have a large angle and radius (see Figs. 6 and 7) and therefore are mainly outside of the acceptance range.

4.5. Multiple scattering

To study the influence of multiple scattering, this process was included in the simulation. The processes ionization and Bremsstrahlung are added, too. Fig. 10 shows the time distributions of photons reaching the photon receiver for an electron momentum of 4.5 MeV/c. For a refractive index of $n = 1.01$ the shape of the distribution is changed completely compared to Fig. 9, it now has a long tail. The shape for $n = 1.05$ is mainly conserved, only for a logarithmic scale a small tail can be observed too. The reduction of the photon intensity at the beginning of the distribution compared to Fig. 9 is explained by the fact that due to multiple scattering the electron direction is changed. This results in a wider angular distribution of the emitted photons yielding longer path length.

4.6. Aluminium window

An aluminium window of 20 μm thickness is placed in front of the aerogel. This causes scattering of the electrons before they enter the aerogel. Fig. 11 shows the resulting time distributions for an electron momentum of 4.5 MeV/c. The tails are increased and longer. This is significant for $n = 1.01$. For $n = 1.05$ the tail is smaller by a factor of 10^3. Therefore it is not visible in this linear plot.

4.7. Resolution

The described time distributions are calculated assuming a point-like electron source. The RMS time duration is a measure of the RMS time resolution of the system. These values are shown in Table 4. The RMS values are increased and decreased with adding one effect after another. The reason is that some photons can be scattered away out of the acceptance cone and give no contribution to the RMS value. The last line of Table 4 is comparable with $\sigma_{MS}(\delta)$ of Table 2.

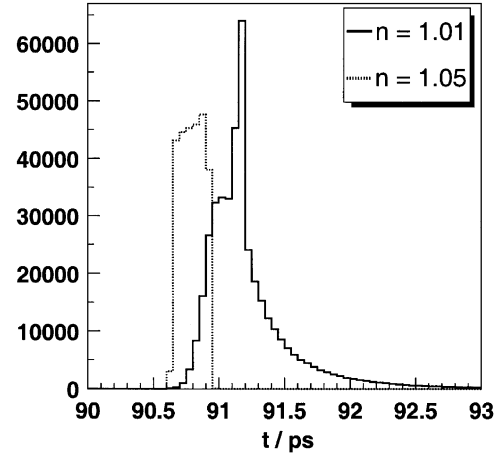The refractive index 1.01 is preferred for a small acceptance angle of an optical transmission line,
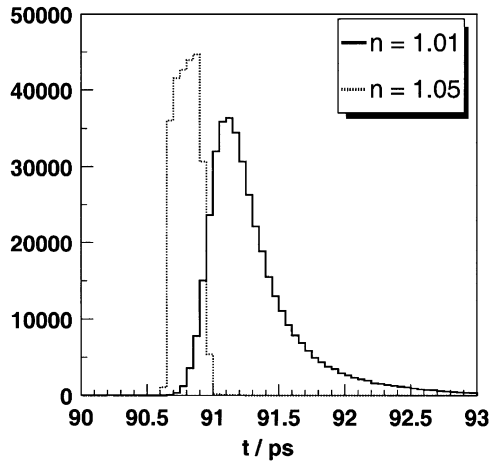
Fig. 11. Time distribution of Cherenkov photon bunches produced by electron bunches with zero electron bunch length. Rayleigh and multiple scattering, ionization and Bremsstrahlung and a 20 μm thick aluminium window are considered for an electron momentum of 4.5 MeV/c. The thickness of the aerogel samples is 20 mm for $n = 1.01$ and 1 mm for $n = 1.05$.

Fig. 12. Time distribution of Cherenkov photon bunches produced by electron bunches in aerogel with refractive index of 1.01 for a momentum of 4.5 MeV/c for different effects, the effects are added after another. The thickness of the aerogel sample is 2 mm.

Table 4
RMS time resolution in ps for different refractive indices and different thicknesses of aerogel samples for an electron momentum of 4.5 MeV/c

l (mm)	$n = 1.01$	$n = 1.03$	$n = 1.05$	$n = 1.01$
	20	2	1	2
Cherenkov	0.14	0.092	0.086	0.014
+ Ray	0.60	0.104	0.090	0.014
+ MS	0.80	0.094	0.084	0.012
+ Al	0.58	0.110	0.091	0.017

From top to bottom the processes are added to each other.

but due to the large thickness of 20 mm to obtain the same photon yield a worse time resolution is caused by multiple scattering. By using a smaller thickness, as it is described in Section 3.2(B), the number of photons is decreased by a factor of 10. Fig. 12 shows the time distribution for different processes, the time range is much smaller than for the thicker aerogel with $n = 1.01$. The corresponding time resolutions are also shown in Table 4. One can see that aerogel gives the possibility to reach a time resolution of 0.02 ps. This time resolution can

be reached if the detector is able to detect the weak signal.

To determine how the proposed system will measure the bunch length distribution, an electron beam simulated with ASTRA [14] is used as input for the GEANT 4 simulation. The beam has a transverse size of $RMS_{x,y} = 2.3$ mm and an angle distribution of $RMS_{x',y'} = 1.6$ mrad with a mean momentum of 4.54 MeV/c and a momentum spread of 1.4%.

The example shown in Fig. 13 is for the worst case of time resolution for $n = 1.01$ and thickness $l = 20$ mm. The thick solid line represents the time distribution of the electron beam, the thin line shows the time distribution produced by Cherenkov photons in aerogel. Only small differences can be seen. The distributions for the other considered aerogels match even better the electron beam time distribution.

5. Summary

The time resolution of aerogel radiators used for the measurement of the electron bunch length at the PITZ facility is analytically calculated and simulated with GEANT 4. It was shown, that for
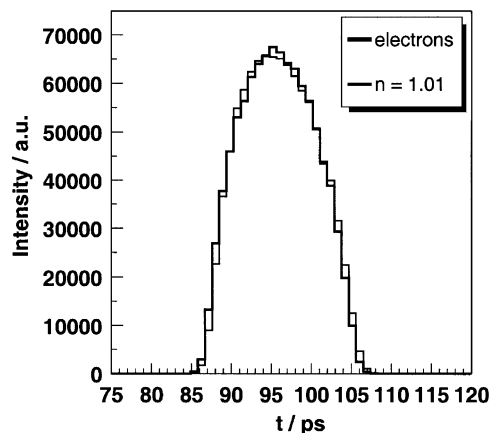
Fig. 13. Time distribution of a simulated electron beam and its corresponding Cherenkov photon beam produced in aerogel (refractive index $n = 1.01$, thickness 20 mm). The distributions are normalized to their areas.

aerogel of refraction index $n = 1.05$, 1 mm thickness and an aluminium window of 20 μm thickness, the time system response has a rectangular shape with the RMS resolution of ~ 0.1 ps. The tails are at the level of 10^{-3}. Such a radiator will allow to study the bunch structure of electrons. In addition, it is shown that with aerogel of $n = 1.01$ and 2 mm thickness a time resolution of ~ 0.02 ps could be reached if photon detectors with a corresponding time resolution and sensitivity would be available.

References

[1] A.F. Danyliuk, et al., Nucl. Instr. and Meth. A 494 (2002) 491.
[2] A.R. Buzykaev, et al., Nucl. Instr. and Meth. A 433 (1999) 396.
[3] T. Iijima, et al., Nucl. Instr. and Meth. A 453 (2000) 321.
[4] A.R. Buzykaev, et al., Nucl. Instr. and Meth. A 379 (1996) 465.
[5] M.Yu. Barnyakov, et al., Nucl. Instr. and Meth. A 453 (2000) 326.
[6] A.F. Danyliuk, et al., Nucl. Instr. and Meth. A 433 (1999) 406.
[7] M.Yu. Barnyakov, et al., Nucl. Instr. and Meth. A 494 (2002) 424.
[8] T. Iijima, et al., Nucl. Instr. and Meth. A 502 (2003) 231.
[9] I.M. Frank, I.E. Tamm, Dokl. Akad. Nauk, SSSR 14 (3) (1937) 109.
[10] Photomultiplier Tubes, Catalog TPM0003E02, Hamamatsu, October 1998.
[11] K. Hagiwara, et al., Particle data group, Phys. Rev. D 66 (2002) 010001.
[12] F. Kohlrausch, Teubner Verlag, ISBN 3-519-23000-3, 1996.
[13] GEANT 4, http://wwwasd.web.cern.ch/wwwasd/geant4/geant4.html.
[14] K. Flöttmann, A space charge tracking algorithm, http://www.desy.de/~mpyflo/Astra_dokumentation.

5.3   Further Reading II:

Coherent Radiation Diagnostics for Short Bunches
O. Grimm, Proceedings of Particle Accelerator Conference PAC07, 2007

COHERENT RADIATION DIAGNOSTICS FOR SHORT BUNCHES

O. Grimm[*], University of Hamburg, Germany

Abstract

Investigating the longitudinal charge distribution of electron bunches using coherent radiation has become an important diagnostic technique at many accelerators. The principle of the method and some example applications from the FLASH free-electron laser in Hamburg will be described in this article.

INTRODUCTION

The longitudinal charge distribution in an electron bunch is an important characteristic for many particle accelerators and storage rings: the gain length of a free-electron laser (FEL) depends on the peak current of the bunch, and thus, for a given charge, on the bunch length (a typical value is $15\,\mu$m$/50\,$fs); the slicing-technique for producing ultra-short x-ray pulses at third-generation light sources relies on producing and controlling a very short longitudinal structure in the bunch through interaction with a laser ($90\,\mu$m$/300\,$fs); high-energy physics machines need to achieve a sufficiently short bunch to avoid luminosity degradation due to the hourglass-effect ($600\,\mu$m$/2\,$ps).

Manipulating the bunch to get a desirable and short charge distribution is a complicated procedure and typically requires, for an FEL, several bunch compression steps involving complex longitudinal dynamics. Stable lasing is only achieved for a well-tuned machine. Measuring the longitudinal profiles, and thus guiding the tuning, is a very important ingredient for efficient machine running, as is the preservation of a once-found good machine setup using feedbacks.

Time-domain methods for measuring the longitudinal structure with resolutions in the 50 fs range exist, though typically require involved set-ups, for example high-power transverse deflecting cavities (that need special optics to attain maximum resolution and are thus are not parasitic to normal machine operation), or techniques based on electro-optic principles. Coherent radiation diagnostics (CRD) allows a different approach to this measurement task by working in the frequency domain. No individual technique is currently giving all the information that is needed, and therefore several approaches to longitudinal diagnostics are often employed in parallel.

The notion that the bunch charge distribution affects the emission spectrum is known for a long time, though only starting around 1990 the application for beam diagnostics

has been investigated.[1] See [2] for further references on original works.

This article will give a brief introduction to the principle of the diagnostic technique, followed by an overview of some of the experimental arrangements that are currently employed. By no means a complete coverage is intended or possible. The focus will be on studies and results from the FLASH free-electron laser at DESY, Hamburg.

PRINCIPLE OF CRD

The basic relation of coherent radiation diagnostics connects the radiation emission spectrum of a bunch of electrons, $\mathrm{d}U/\mathrm{d}\lambda$, to that of a single-electron, $(\mathrm{d}U/\mathrm{d}\lambda)_1$, by

$$\frac{\mathrm{d}U}{\mathrm{d}\lambda} = \left(\frac{\mathrm{d}U}{\mathrm{d}\lambda}\right)_1 \left(N + N(N-1)\,|F(\lambda)|^2\right). \quad (1)$$

N is the number of electrons in the bunch, $F(\lambda)$, the *form factor*, the Fourier transform of the normalized bunch charge distribution $S(z)$,

$$F(\lambda) = \int_{-\infty}^{\infty} S(z)e^{-2\pi\mathrm{i}z/\lambda}\,\mathrm{d}z. \quad (2)$$

Here, charge distribution and form factor are considered only for a line charge. A non-vanishing transverse extend influences the emission spectrum, although only weakly due to the strong collimation of the radiation for highly relativistic particles, unless the transverse extend is very large with respect to the wavelength. Transverse effects are studied in [3, 4].

The effect of coherent enhancement is illustrated in Fig. 1. For wavelengths comparable to the bunch length or larger, the spectral intensity is strongly amplified, as a large part of the bunch electrons emits coherently. The enhancement of the spectrum extends to shorter wavelengths for shorter bunches, and the shape of the spectrum depends on the shape of the charge distribution. Coherent radiation diagnostics uses this effect to deduce information about the bunch length or bunch shape. The derivations of the basic relations are given in detail in [5].

EXPERIMENTAL BASICS

Any setup that uses coherent radiation as a diagnostic tool includes as a minimum a source of some kind, some

---

[1]The first description of coherent effects is made, to the authors knowledge, in an originally unpublished paper in 1945 by Schwinger within the context of synchrotron radiation, including also a discussion on shielding. The paper has been reissued in [1].

[*] oliver.grimm@desy.de

06 Instrumentation, Controls, Feedback & Operational Aspects

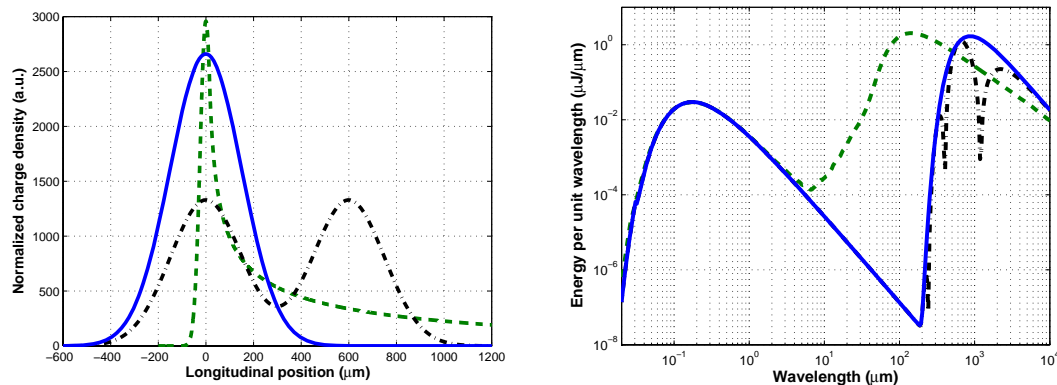T03 Beam Diagnostics and Instrumentation

Figure 1: Example for coherent enhancement. On the left, three different bunch shapes are shown, on the right the effect on the emission spectrum after Eq. 1 for 1 nC bunch charge. As single-electron spectrum, synchrotron radiation for circular motion is taken.

beam line to transport the radiation, and a detector. Additional components for a more detailed analysis of the radiation, like spectrometers, are often added, some of which are mentioned in subsequent sections.

Radiation sources

All processes that result in the emission of radiation from an electron are in principle suitable for the purpose of CRD. At FLASH, for example, synchrotron, transition and diffraction radiation are used so far, and a dedicated tunable electromagnetic infrared undulator is currently being installed [6]. The choice of source depends very much on the desired application, as the spectral characteristics and the influence on accelerator operation vary.

A fully parasitic source, not influencing accelerator operation at all, is synchrotron radiation if taken from an existing bunch compressor or bending magnet. This source covers a wide wavelength range. The emission spectrum, especially at long wavelengths, is complicated, as the usual spectrum derived for circular motion in free space is not valid for the comparatively short bending magnets in a bunch compressor (edge effect) and the typically flat vacuum chambers (cut-off) [7, 8]. Also the coherent enhancement can be affected if a bunch only moves on an arc instead of a circle [9].

Transition radiation is significantly more intensive and can be reasonably well calculated for realistic geometries [10]. It is, however, destructive (even for a thin radiator, the emittance is degraded strongly). A fast kicker is used at FLASH to extract a single bunch for beam diagnostics with transition radiation, allowing quasi-parasitic operation if longer bunch trains are used.

Diffraction radiation is parasitic if the gap in the radiator is sufficiently wide to prevent wake fields from disturbing subsequent bunches. Due to the gap, however, short wavelengths are strongly suppressed [10], and this source is thus not suitable for investigations of short bunch structures.

Smith-Purcell radiation essentially combines the source

with a spectrometer [11], as the emitted frequency depends on the observation angle. It requires, similar to diffraction radiation, a radiator close by the beam, rising the question of wake fields and the emission of short wavelengths.

Undulator radiation is a narrow-band, high-intensity source, in principle rendering a spectrometer for analysing the radiation obsolete. Attention has to be paid to higher harmonics if a wiggler-like spectrum is obtained from a high-K device.

Radiation transport

The emitted radiation has inevitably to be coupled out from the accelerator vacuum into a measurement setup, requiring some form of radiation transport beam line. To avoid absorption from water vapour that is prominent in the infrared, evacuation of the whole setup is desirable, though only a fore vacuum on the order of 0.1 mbar is needed for distances up to several 10 m. A window then has to separate the fore-vacuum from the ultra-high accelerator vacuum. Thin foils of polyethylene have a good wide-band transparency, though often are considered to be too fragile from a machine safety point-of-view. Other plastic materials, like for example TPX that has the advantage of being transparent in the visible, have also been used. Crystalline quartz (cut perpendicular to its optical axis to avoid birefringence) is frequently used, but its useful transmission range extends only down to 80 μm. The only fully satisfactory material with almost constant transmission of 70% from the visible up to at least millimeter waves is diamond. It is also a strong material, so that 0.5 mm thick windows of 20 mm aperture withstand atmospheric pressure. To avoid etalon interference, such a window is typically wedged with a angle of up to 1°.

As the design of the beam line usually requires full attention to diffraction effects, Fourier optics codes (for example ZEMAX) are used. Although the application and working of such a code is in principle straightforward, care must be taken to implement the source correctly.

06 Instrumentation, Controls, Feedback & Operational Aspects

T03 Beam Diagnostics and Instrumentation

Detectors

Broad-band infrared detectors are bolometric, that is their primary detection mechanism is heating due to absorption of radiation. A subsequent effect then converts the temperature change into an electric signal.

Widespread use is made of pyroelectric detectors that use a change of polarization of certain materials like $LiTaO_3$ with temperature. Such a detector is essentially a capacitor of a few square millimeter area and a thickness between $30\,\mu m$ and $100\,\mu m$. Radiation enters through the transparent top electrode, is absorbed, and the resulting surface charge or voltage from the polarization change is detected. Etalon interferences due to the relatively weak absorption in the far infrared are pronounced, as shown in a measurement in Fig. 2. Wedged crystals could overcome this problem, but have so far not been made.
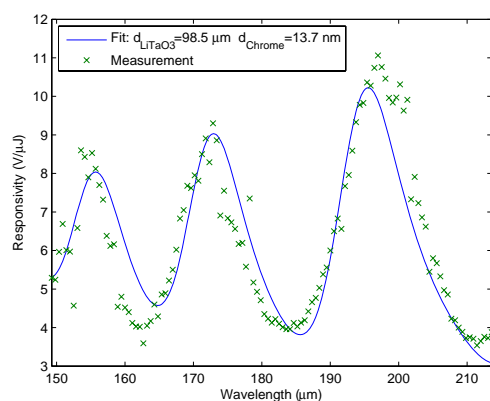

Figure 2: Response of a pyroelectric detector. The fit describes absorption in a stack of a thin Chrome top electrode, a $LiTaO_3$ crystal and a thick gold back electrode. The optical constant of $LiTaO_3$ are not known precisely, limiting the quality of the fit.

Pyroelectric detectors are intrinsically fast, and are used at FLASH with suitable read-out electronics to measure infrared radiation in long trains of up to 600 bunches with $1\,MHz$ repetition rate. Response speeds exceeding $1\,ns$ have been demonstrated elsewhere [12]. Since all pyroelectric crystals are also piezoelectric, mechanical vibrations excited by the absorption of short, intense infrared pulses result in ringing, typically at frequencies of several $100\,kHz$, depending on crystal geometry [12].

Another broad-band, room-temperature detector that is used frequently is the Golay cell, an opto-acoustic detector. The heating of a closed gas volume and subsequent pressure increase is detected optically via the flexing of a thin membrane. It is expected to have a much flatter response, showing no resonance structures like a pyroelectric detector, as the Golay cell has some similarity to a black body cavity. Measurements similar to those from Fig. 2 support this for the wavelength range $100\,\mu m$ to $160\,\mu m$, though indicate non-uniform response around $3\,mm$ [13].

06 Instrumentation, Controls, Feedback & Operational Aspects

Orders of magnitude more sensitivity are possible with cooled bolometers, essentially due to the decreased heat capacity of materials at low temperatures (liquid Helium) and the fast change of resistivity with temperature in the transition region from normal to superconducting state. A superconducting hot-electron bolometer was shown in [14] to have a time constant faster than $25\,ps$. Wide bandwidth operation of such a detector into the mid-infrared is usually not possible due to the steeply increasing heat load from room-temperature black body radiation. Cold filters are employed to limit thermal radiation from reaching the detecting element.

BUNCH COMPRESSION MONITOR

The simplest application of coherent radiation diagnostics uses the frequency-integrated intensity as a relative measure of bunch length. An example from FLASH is shown in Fig. 3: Transition or diffraction radiation from a screen is coupled out through a crystalline quartz window and transported to a pyroelectric detector.
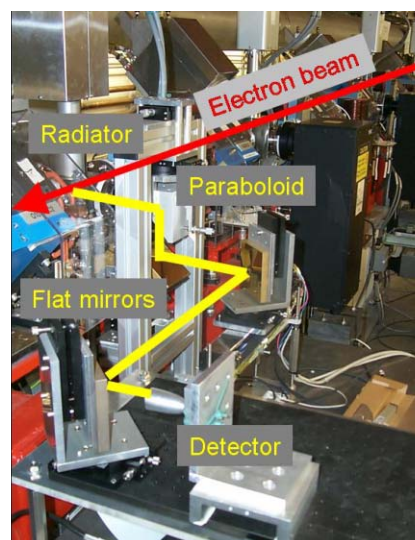
Figure 3: Bunch compression monitor setup at FLASH.

This compression monitor is installed after the first magnetic bunch compressor of FLASH. According to Fig. 1, the total radiation intensity increases with shorter bunches. The degree of bunch compression is adjusted by changing the acceleration phase of the acceleration module in front of the bunch compressor. A scan of this phase versus the intensity registered by the pyroelectric detector is shown in Fig. 4. Note that the curves obtained with synchrotron radiation from the last bunch compressor dipole magnet and with diffraction radiation from the set-up Fig. 3 are very similar except for the amplitude. Different pyroelectric detectors, different optics and only a simple alignment have been used, indicating the robustness of the method for determining maximum compression.

Such a scan, especially the deduced maximum compression phase, is used routinely at FLASH to establish the

T03 Beam Diagnostics and Instrumentation

Figure 4: Phase scan with two bunch compression monitors at FLASH. The varied phase is that of the accelerating module in front of the bunch compressor.

per se arbitrary setpoint phase scale. A typical phase for SASE operation is several degrees away from maximum compression, thus allowing a simple feedback a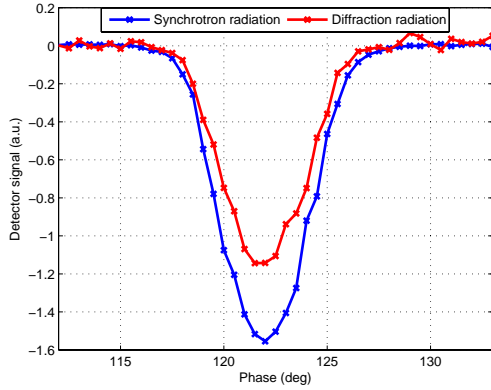lgorithm to stabilize the compression by regulating the module phase. This is an indispensable tool at FLASH to counteract drifts on the time-scale of some 10 seconds or longer. Despite the restricted wavelength range due to a crystalline quartz window, the phase found for maximum compression agrees well with the value expected from simulations.

A compression monitor based on using a ceramic gap as radiation source and diode detectors working up to several hundred GHz is proposed for the first bunch compressor of LCLS [15].

BUNCH SHAPE RECONSTRUCTION

By using the full spectral information instead of the frequency-integrated intensity, a more complete determination of the bunch profile is possible. Through knowledge of the single-electron spectrum and the bunch charge, at first the magnitude of the form factor $|F(\lambda)|$ can be deduced from (1). Inverting the Fourier transformation (2) to get the charge distribution is then possible if both amplitude and phase of the complex form factor are available. Although a strict solution of this phase-reconstruction problem is not possible, the Kramers-Kronig relation gives a handle to solve the problem from a practical point of view satisfactorily [2, 5, 16]. If the complex form factor is expressed as $F(\nu) = |F(\nu)| \exp(i\Theta(\nu))$, then

$$\Theta(\nu) = \frac{2\nu}{\pi} \int_0^\infty \frac{\ln(|F(\nu')|/|F(\nu)|)}{\nu^2 - \nu'^2} \, d\nu' \qquad (3)$$

yields a phase, the so-called *minimal phase*, that is compatible with the measured form factor amplitude. Although this solution is not necessarily unique, in practice the requirement to extrapolate the measured data to zero and infinite frequency, and the measurement errors are a more

serious problem of the reconstruction process than the non-rigorous mathematics.

It is usually difficult to assess the single-electron spectrum precisely. It requires detailed knowledge of not only the radiation generation process in the actual experimental setup, but also of the distortions of the spectrum by the beam line and by the response of the instrument used to measure the spectrum. In some cases it has been possible to measure the incoherent spectrum over a certain wavelength range by assuring that the bunch is long enough to suppress coherent effects [17], but otherwise it is necessary to resort to simulations.

An example for a bunch shape reconstruction at FLASH is given in Fig. 5, taken from [18]. Here, synchrotron radiation from the first bunch compressor was transported to an experimental station outside of the accelerator tunnel, and the spectrum measured with a Martin-Puplett interferometer. The result is compared to a streak camera measurement using the visible part of the synchrotron radiation spectrum at the same beam line.
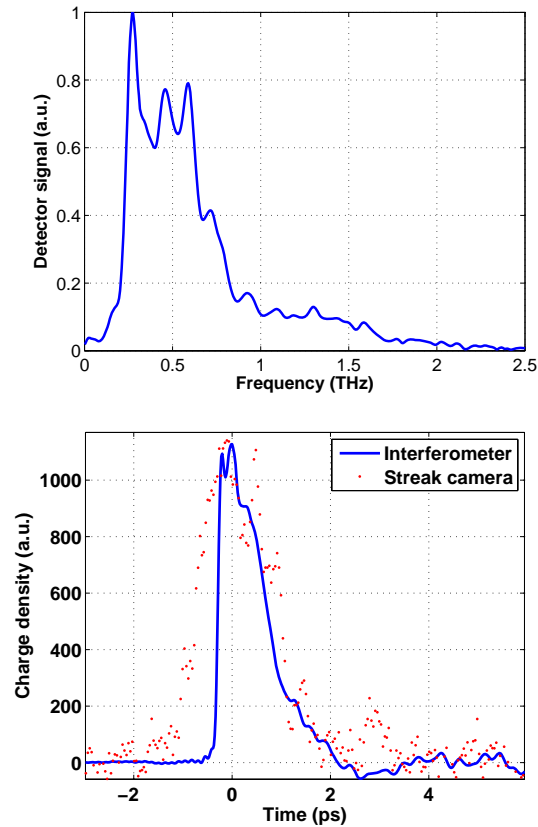
Figure 5: Example for a bunch shape reconstruction at FLASH. On top a measured synchrotron radiation spectrum, below the reconstructed charge distribution. The streak camera measurement has been made at the same synchrotron radiation beam line using visible light.

The streak camera resolution is limited to about 500 fs, the frequency-domain method mainly by the presence of a crystalline quartz window. Although an acceptable agree-

06 Instrumentation, Controls, Feedback & Operational Aspects

T03 Beam Diagnostics and Instrumentation

ment is found, the amount of work in correcting the measured spectrum and finding suitable extrapolations was significant, clearly indicating that full bunch shape reconstruction is still an experimental and not fully independent technique.

Another experimental result for full bunch reconstruction can be found in [19].

SINGLE-SHOT SPECTROMETER

A high variability of the SASE intensity on a shot-to-shot basis is found at FLASH. A thorough investigation using coherent radiation diagnostics requires thus equally fast spectral information, ruling out a scanning interferometer for this tasks. A single-shot spectrometer based on staged blazed gratings was developed at FLASH, allowing a wide wavelength coverage from $4\,\mu m$ up to some $500\,\mu m$. The details of the instrument are described in [20].

Measurements have been carried out at the FLASH transition radiation beamline which is located after the final bunch compression stage and equipped with a diamond window [21]. A phase scan with this instrument is reproduced in Fig. 6. Compared to the frequency-integrating scan from Fig. 4, it shows a much more complex behaviour, and especially a much stronger phase dependency (note that the phase scale in Fig. 4 has an arbitrary offset).
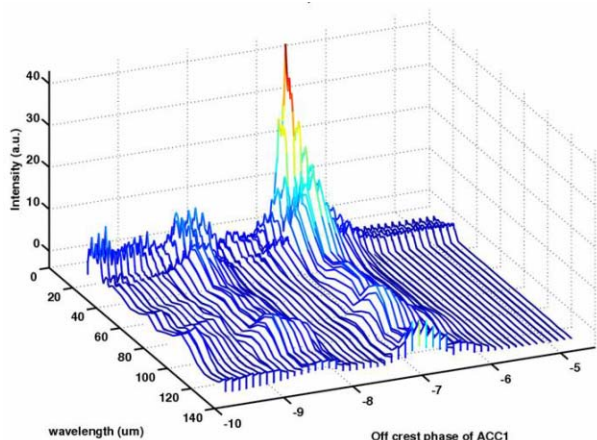

Figure 6: Phase scan with the single-shot spectrometer.

The narrow phase-band that shows high intensity at wavelengths around $30\,\mu m$ is typically also a good starting point for further machine optimization. SASE performance of FLASH is influenced by many parameters, thus no optimum setting can be suggested by such a measurement alone, but tuning has in several occasions been significantly shortened and improved by using CRD for the initial set-up.

CONCLUSION

Longitudinal bunch shape investigations using coherent radiation are by now a standard tool for nearly all machines operating with short bunches or short bunch features. The tools employed in routine machine operation are, however, invariably non-calibrated, thus giving only relative or empirical information to help setting up a machine. Full longitudinal charge profile reconstruction is still a specialist application, and typically requires significant, dedicated work.

From the experience gained at FLASH, there is a clear benefit from having a wide wavelength coverage with a single-shot resolving spectrometer, especially at the experimental level. With increased understanding of the measured spectra and their dependence on machine parameters, it will likely be possible to restrict the wavelength coverage at a later stage. The benefit, however, comes at the price of a significantly higher hardware complexity, requiring evacuated setups, diamond windows, and well designed optics.

ACKNOWLEDGMENTS

REFERENCES

[1] J. Schwinger, LBNL-39088 (1996)

[2] R. Lai, A.J. Sievers, Nucl. Instr. Meth. A397(1997) 221

[3] Y. Shibata et al., Phys. Rev. E50, 1479 (1994)

[4] A.H. Lumpkin, Phys. Rev. Lett 88, 234801 (2002)

[5] O. Grimm, P. Schmüser, TESLA FEL 2006-03 (2006)

[6] O. Grimm et al., Proceedings of FEL 2005, p. 183

[7] R.A. Bosch, Nucl. Instr. Meth. A482, 789 (2002)

[8] A. Paech et al., Proceedings of EPAC 2006, p. 1031

[9] E.L. Saldin et al., Nucl. Instr. Meth. A398, 373 (1997)

[10] S. Casalbuoni, B. Schmidt, P. Schmüser, TESLA 2005-15 (2005)

[11] G. Doucas et al., Proceedings of EPAC 2006, p. 1100

[12] C.B. Roundy, SPIE Vol. 62, 191 (1975) Infrared Technology

[13] E. Chiadroni, TESLA-FEL 2006-09 (2006)

[14] K. S. Il'in et al., Appl. Phys. Lett. 76, 2752 (2000)

[15] J. Frisch, SLAC, private communication

[16] J.S. Toll, Phys. Rev. 104, 1760 (1956)

[17] M. Abo-Bakr et al., Phys. Rev. Lett. 90, 094801 (2003)

[18] L. Fröhlich, DESY-THESIS 2005-011 (April 2005)

[19] G. Schneider et al., Nucl. Instr. Meth. A396, 283 (1997)

[20] H. Delsim-Hashemi, PhD thesis University of Hamburg, to be published

[21] S. Casalbuoni et al., TESLA 2006-04 (2006)

06 Instrumentation, Controls, Feedback & Operational Aspects

T03 Beam Diagnostics and Instrumentation

5.4   Further Reading III:

Observation of Femtosecond Bunch Length Using a Transverse Deflecting Structure

M. Huening et al., Proceedings of Free Electron Laser Conference FEL05, 2005

OBSERVATION OF FEMTOSECOND BUNCH LENGTH USING A TRANSVERSE DEFLECTING STRUCTURE

Markus Hüning*, Andy Bolzmann, Holger Schlarb (DESY, Hamburg),
Josef Frisch, Douglas McCormick, Marc Ross, Tonee Smith (SLAC, Menlo Park, California),
Jörg Rossbach (Universität Hamburg, Hamburg)

Abstract

The design of the VUV-FEL at DESY demands bunch lengths in the order of 50 fs and below. For the diagnostic of such very short bunches a transverse deflecting RF structure (LOLA) has been installed which streaks the beam according to the longitudinal distribution. Tests in the VUV-FEL yielded a rich substructure of the bunches. The most pronounced peak in the has a rms length of approximately 50 fs during FEL operation and below 20 fs FWHM at maximum compression. Depending on the transverse focusing a resolution well below 50 fs was achieved.

INTRODUCTION

To obtain enough gain for the SASE process it is necessary to produce peak currents in the order of 4 kA. With the present setup of the machine this can only be accomplished by compressing part of the bunch to 50 fs. Diagnosing such a short pulse poses a challenge to the beam instrumentation. Therefore a transversely deflecting structure is used to streak the beam.

For this purpose a structure formerly used for particle separation in secondary beams is utilized. It has been used before at SLAC under the name LOLA IV [1]. It is an S-band structure operating at a frequency of 2.856 GHz. Operating the structure close to the zero crossing of the field the bunches acquire no net deflection but are streaked vertically. Using a horizontally deflecting kicker one bunch per pulse is steered onto an OTR-screen. This way it is possible to diagnose parasitically one bunch out of a train of several hundred bunches. At SLAC this structure has been used for the same purpose [2,3,4]

SETUP

The setup of the VUV-FEL is depicted in figure 1. The electron bunches are created in an RF-gun and then accelerated in 5 superconducting modules up to presently 450 MeV. Behind the first and the third module there are two bunch compressors used to shape the longitudinal profile of the bunches. The initial bunch length is 7 ps (RMS) which is already long enough to probe the nonlinear rf curvature of the 1.3 GHz L-band cavities. This results in an incomplete compression in the first bunch compressor. The out coming bunch then has two main parts: A very short spike in the head and a tail which resembles the original distribution. The tail however still has an energy correlation imprinted in the first module and reshaped in the bunch compressor. Part of the tail is then compressed in the second bunch compressor to form a short spike with high peak current and good emittance. Depending on the exact phases in the modules #1-#3 the two bunch compressors produce a single or double spike at the exit of the linac. At the end of the acceleration sections, before the collimator system of the undulators, there is the transversely deflecting structure LOLA installed.

The structure is an S-band travelling wave structure. It operates in TE-TM-hybrid mode, so that a combination of electric and magnetic field produces a transverse kick. The maximum equivalent deflecting voltage is 20 MV over a structure length of 3.6 m. The fill-time is 680 ns, so that in a 1 MHz bunch train only one bunch is affected. A downstream OTR screen is utilized to analyse the streak. It is displaced from the centre of the beam pipe so that the beam can pass through. A kicker is used to steer only the bunch in question onto the screen.

To allow for a better synchronization with the master clock, LOLA is tuned to a frequency of 2.856059 GHz, which is an integer multiple of 1/11 of the master clock frequency of 9.027775 MHz. By means of an additional synchronization circuit it is guaranteed that the machine triggers always with a fixed phase relation to this reference [5]. At 9 MHz bunch rate this frequency offset
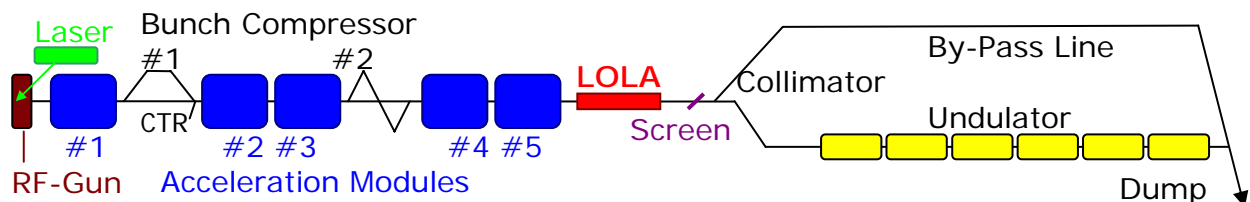

Figure 1: Schematic drawing of the VUV-FEL beam line. At the end of the accelerating section there is the transversely deflecting structure LOLA. It streaks the beam vertically so that on a downstream viewscreen the longitudinal profile of the bunches can be studied.

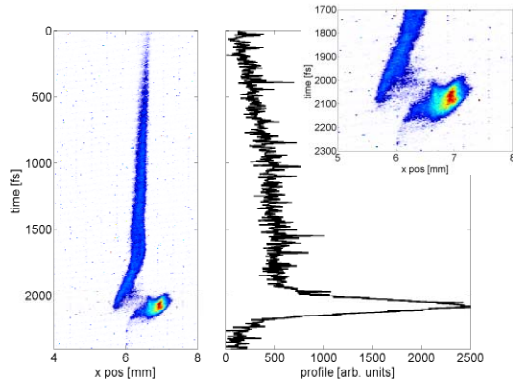*Corresponding author: markus.huening@desy.de

Figure 2: Image of the streaked bunch; inset: zoom on the spike at the head. The streak was approximately 4 fs/px.

results in a phase shift of 36° between neighbouring bunches. This way these bunches would miss the screen and not disturb the measurement.

Because an absolute calibration of the streak based on pure RF measurements did not seem precise enough, one power level was calibrated using the deflection of the beam. The calibration of the other power levels was then scaled according to the relative change of RF power. Relative power levels can be measured much more precisely than absolute levels, so that this method appeared accurate enough. For the calibration a relatively low power level was chosen, allowing for a phase shift of ~7° before the bunch misses the screen. In this way the influence of phase jitter on the calibration is reduced. A streak of 74 pixel/degree or 13.2 fs/pixel was measured. One pixel of the CCD corresponds to 26 μm. A maximum possible streak of 1.8 fs/pixel can be achieved. The optical setup allows for a better resolution than 26 μm.

The beam size at this location is larger, however. The standard beam optics foresee 200 μm spot size (RMS), which would then correspond to a resolution of approximately 15 fs. Unfortunately the spike is also the region of the largest energy spread in the bunch. An energy spread of ~1 MeV (RMS) is not uncommon. In

such a case each millimetre of vertical dispersion would contribute with 0.3 fs to above resolution.

RESULTS

The transverse deflecting structure LOLA has been used to measure the longitudinal bunch profile while the machine was setup for SASE operation. Two examples are given in the figures 2 and 3. While the performance of the FEL was quite similar in the two cases (approximately 1 μJ photon pulse), the two profiles differ considerably. Both setups were started from a standard setting defined as follows: The acceleration in the first module was adjusted 6 degrees from the maximum compression phase, which is defined by the maximum of the coherent diffraction radiation at a station closely behind the first bunch compressor (see figure 1). The second and third module are adjusted for on-crest operation so that they do not add considerably to the longitudinal energy distribution. The second bunch compressor then creates the spike necessary for the high peak current at low emittance.

In the first case (figure 2) the module 1 phase was subsequently tuned for less compression, so that no strong peak was produced in the first bunch compressor but only in the second. This would also explain the relatively weak sub-structure of the bunch, because CSR would play a big role only after the second compression stage when it can not influence the longitudinal profile very much.

In the second case (figure 3) the phase was tuned to stronger compression in the first bunch compressor, so that both bunch compressors produce a spike. This results in the double peak structure that can be observed. At the same time there is even more structure to the bunch. This is probably due to wakefield and CSR effects in the first bunch compressor, which can then be translated into a longitudinal modulation in the second compressor stage.

In both cases the width of the peak in the projected profile is measured to be in the order of 120 fs (FWHM). This result however has to be considered preliminary because not all detrimental effects have been considered thoroughly yet. The true width will be smaller than that.
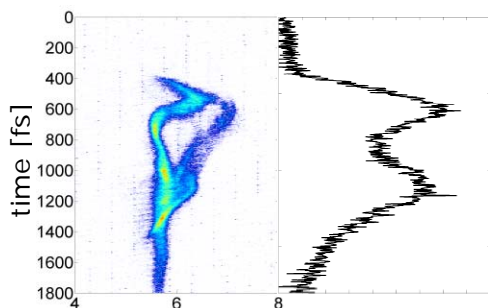

Figure 3: Bunch head with a double peak structure. There is a rich sub-structure of the bunch which shows not only longitudinally but transversely. Note that the streak is opposite to figure 2.
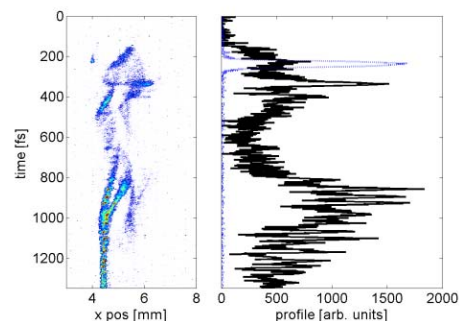

Figure 4: Bunch head with faster streak (2 fs/px) and optimized focusing. The dotted line in the right plot indicates the unstreaked beam size.

For the example in figure 4 the streak was increased and the unstreaked spot optimized for minimum vertical size. Consequently there was no lasing at that time, but the settings were somewhat close to the ones in figure 3. Exact consistency can not be guaranteed, particularly the compression might have been stronger. There is much more structure to be seen than in the previous cases. This appears in part enhanced by a lower intensity of the image which causes darker parts to vanish completely.

The effects that concern the most are the entanglement of the vertical and longitudinal structure of the bunch and the vertical dispersion. As can be seen from the figures 2 through 4 there is a strong variation of the horizontal profile along the bunch. This presumably has to be attributed to the two bunch compressors, which deflect horizontally. Nevertheless it can not be excluded that similar effects show vertically. Since the spike carries only a small fraction of the total bunch charge this can not be checked with the un-streaked beam. In this case the charge contained in the tail outshines the head.

A remedy to this problem might be a tomography in the z-y-plane. For this the voltage in the structure would have to be scanned while the change in profile would be recorded. This procedure is in preparation but is not finished yet. Likewise has the dispersion not been measured nor compensated yet.

The LOLA structure can also be used to monitor the jitter of the beam arrival time. This information is of special importance to pump-probe experiments to be
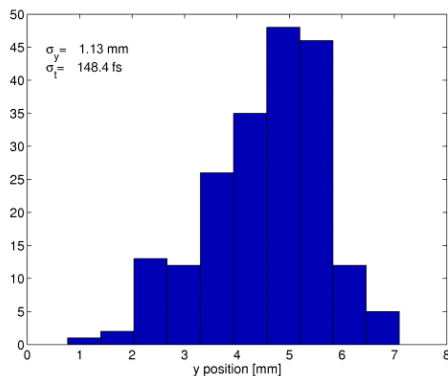

Figure 5: Phase jitter of the beam with respect to LOLA. The jitter due to the high power RF in LOLA is approx. 70 fs.

performed with external lasers synchronized to the master clock. The figure 5 shows the shot-by-shot jitter of the bunches measured with a BPM close to the viewscreen.

An RMS jitter of 145 fs (RMS) was measured. Note that this is the jitter of the beam with respect to the LOLA RF which can have a jitter by itself. The largest contribution will be the stability of the klystron, which was found to be in the order of 70 fs (RMS). A similar result for the beam jitter was found with electro-optical

sampling (EOS) at a nearby diagnostic station [6]. The main contribution to this timing jitter is expected to be the energy jitter in the first bunch compressor. Evaluation of this jitter delivered compatible results.

CONCLUSION AND OUTLOOK

A transversely deflecting structure has been successfully applied to the beam in the VUV-FEL at DESY. Although some important contributions to the measurement error are not fully controlled yet, the achieved resolution surpasses most other methods already and it can be used in normal operation of the accelerator.

There are plans to exploit more capabilities of this measurement method as well as measurements of slice-emittances. A first attempt has already been made [7], but for best results tomographic measurements are foreseen.

In view of higher bunch repetition rates at later times and in future projects, shorter structures with a shorter fill-time are being envisioned.

REFERENCES

[1] O. H. Altenmueller, R. R. Larsen, and G. A. Loew, *Investigations of Traveling-Wave Separators for the Stanford Two-Mile Linear Accelerator*, The Review of Scientific Instruments, Vol. 35, Number 4, April 1964.

[2] R. Akre, L. Bentson, P. Emma, P. Krejcik, *A Transverse RF Deflecting Structure for Bunch Length and Phase Space Diagnostics*, proceedings PAC 2001, p. 2353.

[3] R. Akre et al, *Bunch Length Measurements Using a Transverse Deflecting Structure in the SLAC Linac*, EPAC'02, Paris, France, June 2002.

[4] P. Krejcik et al, *Commissioning of the SPPS Linac Bunch Compressor*, proceedings PAC 2003, Portland, Oregon

[5] A. Bolzmann, *Diploma Thesis*, Universität Würzburg

[6] Bernd Steffen, Sara Casalbuoni, Ernst-Axel Knabbe, Bernhard Schmidt, Peter Schmüser, Axel Winter, *Spectral Decoding Electro Optic Bunch Length and Arrival Time Jitter Measurements at the DESY VUV-FEL*, this proceedings

[7] Michael Roehrs, Markus Huening, Holger Schlarb, *Measurement of Slice-Emmittance using a Transverse Deflecting Structure,* this proceedings

5.5   Further Reading IV:

Femtosecond Resolution Bunch Profile Measurement
S.P. Jamison et al, Proceedings of European Particle Accelerator Conference EPAC06, 2006

FEMTOSECOND RESOLUTION BUNCH PROFILE MEASUREMENTS

S.P. Jamison / ASTeC, Daresbury

G. Berden / FELIX, Nieuwegein, The Netherlands

A.M. MacLeod / University of Abertay Dundee, Dundee, UK

B. Steffen / DESY, Hamburg, Germany

P. J. Phillips, W.A. Gillespie / University of Dundee, Dundee, UK

Abstract

The measurement of ultrashort longitudinal bunch profiles is of growing importance to accelerator development and operation. With requirements of ~10fs time resolution, and a desire for non-destructive and real time diagnostics, the challenges for diagnostic development are significant. Alongside more established transverse deflecting cavity and CTR measurement techniques, new approaches arriving from the field of ultrafast lasers offer significant potential; Ultrafast electro-optic detection has now been demonstrated on several accelerators, and in many distinct forms, although challenges remain in getting to the desired time resolution. Proposed schemes combining ultrafast laser diagnostics with FEL interactions, such as the"optical replica" scheme also have considerable potential. Here, we discuss some of the recent developments in longitudinal diagnostics.

INTRODUCTION

Many different approaches to ultrafast characterization of electron bunches have been explored experimentally, and with the growing importance of such diagnostics to light source machines, more schemes are proposed to be tested in the near future. Here we discuss some of the leading longitudinal diagnostics techniques, with an emphasis on recent demonstrations of their sub-picosecond capabilities; this discussion is not intended to be an exhaustive review of the all the latest developments, but rather an examination of some of the experimental issues and challenges facing sub-ps longitudinal profile diagnostics. Furthermore, the longitudinal profile diagnostics are seen as distinct from approaches that aim to provide an empirical 'bunch-length' monitor, which only aims to inform on the first moments of the bunch profile, or on the presence of structure on a particular time scale of interest.

We discuss techniques through a sub-classification of i) spectral techniques, where the bunch profile is inferred from the spectral intensity of a radiated field, ii) electro-optic (EO) techniques where a Coulomb or radiated field is determined through sampling (possibly single shot) with an ultrafast laser, iii) direct electron bunch techniques, where an active change to the electron bunch properties is made in such a manner that the original longitudinal profile can be inferred from the bunch. Here we restrict ourselves to a brief discussion of transverse deflecting cavities, and proposed demonstrations of the 'optical replica' scheme.

SPECTRAL TECHNIQUES

Within spectral techniques we include the spectral measurements of coherent transition, diffraction and synchrotron radiation, and Smith-Purcell radiation (CTR, CDR , CSR and S-P, respectively). Such techniques have been applied to longitudinal bunch diagnostics in a considerable number of laboratories, and here we give selective examples to demonstrate the practical issues of their implementation and interpretation. These spectral techniques rely on causing the Coulomb field of the electron bunch to radiate in a controlled manner, and subsequently inferring the bunch profile from the emitted radiation spectrum. For femtosecond diagnostics it is important to address the temporal distinction in the Coulomb field and the electron bunch itself. At large distances from the bunch ($r \gg \sigma_z/\gamma$) the field will have a spreading angle of $\theta \sim 2/\gamma$, which corresponds to a temporal spreading in the field of $t \sim 2r/c\gamma$. Furthermore, the field strength will fall as $1/r$ at short distances from the electron bunch, and as $1/r^2$ at large distances. It therefore follows that the position of the radiating structure must be sufficiently close to the electron bunch both to retain the fast time structure and to ensure that the radiated field is sufficiently large for detection. As an example, for a $\gamma \sim 1000$ it follows that any measurements that wish to probe the bunch structure with a 10 fs resolution must be able to access the field distribution within a < 2 mm radius of the bunch (this requirement is also present in electro-optic techniques). For low energy machines this may be a deciding factor in the applicability of CDR or Smith-Purcell radiation techniques. A demonstration of the relative signal strength of CTR and CDR has been given by Delsim-Hashemi et al. [1, 2]. For a CTR or CDR screen inserted into the compressed bunch of FLASH, with $\gamma \sim 900$, the CDR energy is approximately two orders of magnitude reduced in power density with respect to the CTR radiation. The CDR screen is intercepting the Coulomb field at a radius of 5 mm from the bunch. They also observe a cut-off in the short wavelength emission for the diffraction radiation at $\lambda \approx 200\,\mu$m, while the transition radiation has a cutoff at the much shorter wavelength of $\lambda \approx 50\,\mu$m. In separate experiments, with a diffraction grating spectrometer they were able to observe CTR at wavelengths at short as $5\,\mu$m, thus identifying the presence of extremely short time structure in the bunch [3]. At SLAC, CTR has also been used to characterize the extremely short bunches available at the FFTB

facility [4]. Using a Michelson-Morely interferometer the autocorrelation of the CTR radiation was measured, from which the power spectrum of the CTR radiation is determined. In that work, Muggli et al. comment that limitations in the accuracy of the diagnostic arise from the difficulties of transporting and detecting the full spectral range of the far-infrared radiation; these effects limited the ability to infer an actual bunch profile, although bunch lengths of 210fs FWHM were however able to be determined. At the Advanced Photon Source (APS), CTR and CSR diagnostics have been demonstrated for profile reconstruction of sub-picosecond 150 MeV bunches [5, 6]. The spectrum of the CTR/CSR was obtained from a Michelson-Morely interferometer. To determine the profile of the bunch, the phase of the radiation was retrieved from the intensity spectrum from applying a "minimal phase approximation", a numerical process that is based on Kramers-Kronig relations. For the CTR measurements [5] the retrieved bunch profiles displayed FWHM durations as short as 290fs for leading spikes of the profile.

For Smith-Purcell radiation, the radiator is a periodic structure running parallel to the beamline. In such a structure the radiated power at a specific wavelength can be enhanced in proportion to the number of periods to the structure. It also has the property of acting as a wavelength dispersing element. Korby et al. [7] have determined bunch lengths using S-P radiation of a 15 MeV beam. Their S-P gratings had periods of either 6 mm or 10 mm, and a grating length of 100 mm. Through a moveable mirror directing the S-P radiation out of the beamline, they were able to determine the angular, and hence spectral, intensity of the radiation. Separately, Blakemore and Doucas [8, 9] have undertaken S-P experiments at the FELIX FEL facility in the Netherlands. In their experiments an array of 11 detectors arranged opposite the radiator were able to simultaneously collect the S-P radiation over a large angular range. They collect radiation in the range of $\lambda = 500\,\mu$m-3 mm, and determine a sub-ps bunch length. In both the above examples of S-P radiation, the bunch shape was not explicitly determined from the data; instead the experimental spectra were compared to calculated spectra based on trial bunch profiles.

In determining the bunch profile from the spectral content a number of issues must be accounted for. These issues can be summarized as i) the Coulomb field temporal profile at the radiator; ii) the propagation of the radiation to the detectors (Absorption, dispersion and diffraction); iii) the detector response, which may include the dispersive characteristics of the spectrometer. Finally, the net result is a power density measurement, and it therefore does not explicitly include information about the phase of the radiation (measurements of CTR or CSR by electro-optic techniques, which do measure the radiation phase, will be discussed separately below).

The propagation issue is one of the significant experimental challenges for spectral techniques. The long wavelength radiation is significantly affected by diffraction, and

there is always some long wavelength cutoff present. The design of transfer lines will usually be specific to the particular experimental conditions (e.g. transport distance from the beamline, available window aperture at the beamline, and the beam properties themselves). These issues, and the analysis of far-infrared (FIR) beamline propagation have been described in detail by Casalbuoni et al [10]; while focused particularly on the the CTR radiation transfer line at the 140m point of FLASH at DESY, the methods and many general results are equally applicable to other experimental situations.

Of a different character is the problem of missing phase information for the field. Lia and Sievers [11] have shown that the phase of the field can be determined from the field amplitude (i.e. the power spectrum) using Kramers-Kronig relation (KK). The KK relations relate the imaginary components of an analytic function through an integral function of the real components, with an integration range extending over the full spectral range of the signal. In the context of bunch diagnostics, a fundamental issue arises as to the validity of the KK phase retrieval in the absence of some spectral amplitude information. Grimm et al. [12] have discussed this issue with examples of sub-ps bunch profiles retrieved with different levels of missing data. Specifically, they show the importance of the long wavelength data in obtaining a faithful retrieval of the bunch shape. Earlier, Lai et al. also addressed this question of retrieval validity, and noted (as do Grimm et al.) that for some bunch profiles the underlying assumption of minimal phase employed in the retrieval may not always be appropriate; an example of a truncated Lorentzian with failed retrieval is given. The conclusion of Lai, Grimm, and others, however is that for "reasonable" bunch profiles, and with sufficient extent to the data, a meaningful bunch profile can indeed be obtained.

ELECTRO-OPTIC TECHNIQUES

Electro-optic techniques enable the ultrafast characterization of far-infrared (FIR) pulses directly in the time domain, and as such avoid the possible ambiguities associated with spectral techniques. In electron-bunch diagnostics, through carrying out the EO detection within the electron beamline, it is possible to measure the Coulomb field directly, avoiding the step of first causing the field to radiate; alternatively, the emitted CTR/CDR or CSR radiation can be measured with the EO detection outside the beamline. Unless otherwise stated, we will be referring to intra beamline measurements of the Coulomb field.

It is usual to describe the EO modulation as resulting from an electric field induced refractive index change within an EO material (such as appropriately orientated ZnTe or GaP crystals). This refractive index change can then be probed by optical means; the polarization components of a linearly polarised laser will experience a differing delay in propagating through the crystal, with the emerging pulse therefore becoming elliptically polarized.

This ellipticity can subsequently be converted into an intensity modulation by a suitable arrangement of polarisers. The net result is an intensity change in the optical probe as a function of the FIR field which is dependent on the particular arrangement of polarizers. In the two most commonly used arrangements, which we call "balanced detection" and "crossed polariser detection", the intensity change is proportional to field or field squared, respectively.

An alternative perspective for describing the EO process has been derived by Jamison et al [13]; the ellipticity induced in the optical pulse is the result of sum and difference frequency mixing of the FIR and optical field. This is a rigorous description, and has the advantage of being a more appropriate formalism for describing the interaction with long duration (few ps) chirped optical pulses such as used in single shot EO techniques. In essence, they have shown that the optical field spectrum exiting the EO crystal, for a given polarisation component, is given by

$$\tilde{E}_{\text{out}}^{\text{opt}}(\omega) = \tilde{E}_{\text{in}}^{\text{opt}}(\omega) + i\omega a \tilde{E}_{\text{in}}^{\text{opt}}(\omega) * \left[\tilde{E}^{\text{Coul}}(\omega) \tilde{R}(\omega) \right] \tag{1}$$

where the coefficient a is dependent on the polarization geometry. $\tilde{R}(\omega)$ describes the material response due to the nonlinear coefficient and phase-matching. From Eqn. 1 it can be said that the far infrared spectrum of the Coulomb field is now 'upconverted' into the optical region. A FIR bandwidth of $\sim$100% (if that can be assigned any rigorous meaning) is exchanged for an experimentally easier optical bandwidth of $\sim$5%. Importantly, if the EO frequency conversion is done directly on the Coulomb field within the beamline, the shift to optical frequencies allows the information from the DC component to propagate and be detected. Simple Fourier transformation of Equation 1 gives the equivalent expression for the optical field in the time domain,

$$E_{\text{out}}^{\text{opt}}(t) = E_{\text{in}}^{\text{opt}}(t) + a \left[E^{\text{Coul}}(t) * R(t) \right] \frac{\mathrm{d}}{\mathrm{d}t} E_{\text{in}}^{\text{opt}}(t) \tag{2}$$

We therefore see that the EO interaction has created a new optical pulse with pulse envelope described by the Coulomb field; in borrowing terminology from a quite distinct technique, we have created an "optical-replica" of the Coulomb field.

An important factor in the ultimate time resolution of EO techniques is the bandwidth of the response function, and the degree to which it is known. Fortunately, materials are available for which the response is approximately constant over the spectral region of interest. For the most commonly used crystal, ZnTe, $\tilde{R}(\omega)$ has an approximately flat spectrum from 0-2.5 THz. Sufficiently thin GaP crystals may have a cutoff as high as 8 THz ($\lambda \sim 37\mu m$). Other EO materials with even broader response functions are known, although to date they have not been used in electron-bunch diagnostic experiments. In using materials with such a flat spectral response, time resolutions of < 150 fs can potentially be obtained without the need for explicit calibration of the response; this assertion has recently been examined

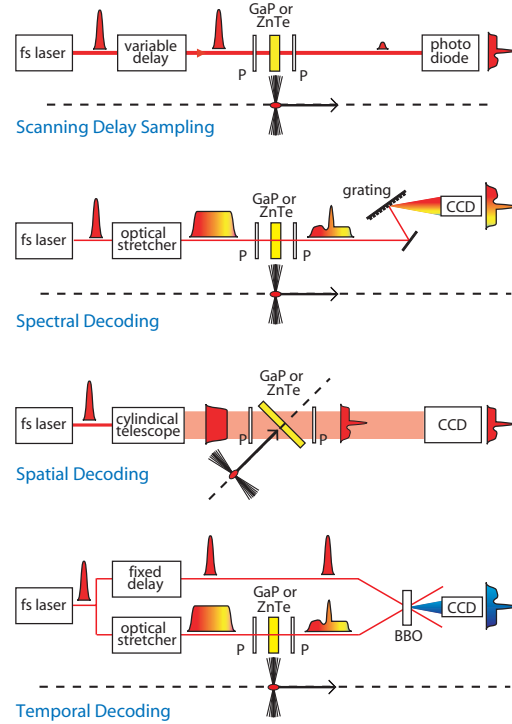through EO benchmarking experiments (as discussed below).

Figure 1: Schematic representations of the four EO detection techniques that have been demonstrated for detection of the bunch Coulomb field.

The above discussion describes the encoding of the Coulomb (or CTR/CSR) field into an optical pulse. The ellipticity introduced into the probe laser is converted into an intensity change with a suitable arrangement of polarisation optics. There are several demonstrated methods for observing this intensity change, each with particular merits. These methods, shown schematically in Fig. 1 are discussed in turn:

Scanning delay sampling: This is the simplest and first demonstrated example EO bunch diagnostics [14]. A short (sub-50fs) laser is used to sample fixed parts of the FIR pulse, and an integrated intensity change in the optical probe is measured. Scanning the relative delay between laser and electron bunch allows the build up of the profile. Multi shot measurements such as this do suffer from time jitter between the laser and electron bunch; however, in even the first demonstration, scanning rates of 2ps per μs were achieved, and over such short measurement periods very small timing jitter (<50fs) can be achieved. The time resolution is in the first instance determined by the sampling pulse duration, although for very short laser pulses (<30fs), group velocity dispersion of the optical pulse may become the dominating factor [15].

Spectral decoding (SD): The measurement of the optical spectrum can be used to directly infer the field temporal profile if a chirp is first applied to the optical pulse, so
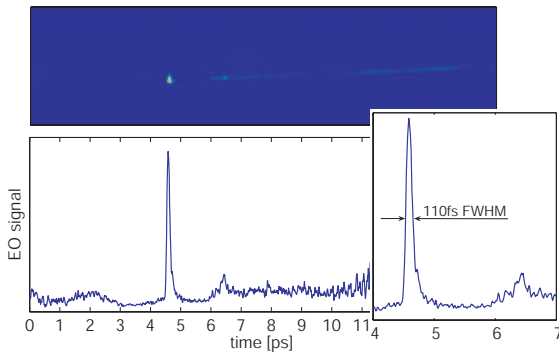
Figure 2: Single shot temporal decoding measurements at FLASH. These measurements are described further in Berden et al. [26].

that there is a known time-frequency relationship in the sampling laser pulse. A lower limit on the bunch duration for which this technique is suitable arises from the intrinsic connection between the temporal modulation of the chirped pulse, and the distortion of the initially known chirp (this limitation can also be shown to be a consequence of the convolution in Eqn. 1). For bunches shorter than this limitation, the measured bunch profile may contain significant artifacts, producing a misleading bunch profile. The limitation can be given approximately as $\tau_{\rm lim} = 2.6\sqrt{T_c T_0}$, where T_c and T_0 are the FWHM of the chirped and transform limited optical pulse durations, respectively [16]. SD characterization of the in-beam-line Coulomb field has been demonstrated at several facilities, including FELIX [17], NSLS [19], and FLASH[20]. The technique has also been demonstrated for single shot characterisation of CSR [21, 22], and CTR [23].

Spatial encoding: This approach has many similarities to the scanning delay line approach, but instead allows for a single-shot measurement. By sampling the Coulomb field with an optical pulse obliquely incident to the EO crystal and the Coulomb field propagation direction, there is a spatial to temporal mapping introduced for the the relative delay of the laser arrival time at the crystal. Imaging the EO crystal, and the intensity changes as a function of spatial position, therefore allows the determination of the field induced intensity changes as a function of relative arrival time at the crystal. An important requirement for spatial encoding is spatially uniform EO materials. The tolerances of this requirement can be difficult to satisfy, with even stress induced birefringence potentially adding significant experiential difficultly. This approach has been demonstrated at SLAC FFTB [24] and at DESY on FLASH [25]. At the FFTB EO signals of 270 fs FWHM were measured, while at FLASH $\sim$ 300 fs FWHM signals have been obtained.

Temporal decoding (TD): Referring to the time domain description of Eqn. 2, it is apparent that for a long duration optical probe, an intensity modulation will be imposed only on portions of the the pulse envelope. TD temporally

resolves this intensity modulation though a process of optical second-harmonic generation, using a non-colinear geometry. Just as in spatial encoding, a time-space mapping is therefore achieved, although in TD this is purely with the optical fields, and is done outside the beamline. TD has been demonstrated at FELIX [18], and more recently at FLASH [26]. In these later experiments an electro-optic signals with FWHM duration of 110 fs were observed. An example of these ultrashort TD measurements is shown in Fig. 2

Benchmarking of Electro-Optic Signals

An important recent advance in electro-optic diagnostics has been the benchmarking of the measured signal with other diagnostics. In recent experiments at FLASH, a variety of longitudinal diagnostics were used to make concurrent measurements. The EO signal has been measured by Temporal Decoding, Spectral Decoding, and Spatial Encoding, together with simultaneously transverse deflecting cavity measurements of the electron bunch immediately following in the bunch train. CTR measurements were also made during the experiments, although not generally simultaneously. The Temporal decoding and transverse cavity measurements have in particular provided explicit confirmation of the exceptional time resolution achieved in the latest TD experiments, and in the faithful reproduction of the bunch profile.

DIRECT ELECTRON BUNCH TECHNIQUES

Direct electron bunch techniques rely on a change to the electron bunch phase space so that the longitudinal projection is converted to a more easily observed projection, such as transverse profile or energy.

Transverse Deflection Cavities: Lola

In RF transverse deflecting cavities, a transverse kick is applied to the bunch which is dependent on the relative phase of the RF with respect to the election arrival time. Extremely fast temporal resolution can be obtained with a sufficiently rapidly varying deflecting force. Cavities capable of producing such a rapidly varying deflecting force were developed at SLAC in the 1960's, and were prosed for particle separates, as well as for fast bunch diagnostics.

More recently these original SLAC cavities have been installed and operated at the SPPS facility, and at FLASH. The transverse deflection cavity at FLASH, known as "Lola" after it original developers, is currently producing the highest time resolution of all the longitudinal diagnostics. Lola operates in a hybrid mode for which the net deflection produced by the combination of electric and magnetic fields is independent of the transverse position of the beam within the cavity (although the individual contributions from magnetic or electric fields does vary across the cavity aperture). The RF-bunch phase is operated at the

zero-deflection point, so that the longitudinal phase space of the bunch is streaked transversely, but does not have a mean deflection. At FLASH the Lola cavity is preceded by a kicker that adds an additional mean deflection, so that a single bunch can deflected onto an off-axis OTR screen. An example of the Lola image, and the projected longitudinal profile is shown in Fig. 3. The temporal resolution of TDC is ultimately restricted by the unstreaked transverse beam size on the OTR screen; for Lola this is $\approx 200\,\mu$m in normal SASE operation conditions, and the maxim streak is 72 fs/mm, from which an ultimate resolution of 15 fs has been inferred [27].

Transverse deflecting cavities such as Lola are intrinsically destructive measurements. They also have large infrastructure requirements, and may require significant beamline space; the Lola cavity is 3.6m in length, compared to the requirement of $\sim$ 10cm for CTR or electrooptic diagnostics. However, the added capability for measuring slice parameters, such emittance, energy, or z-y correlations, makes them a more versatile diagnostic than longitudinal profiling by itself.
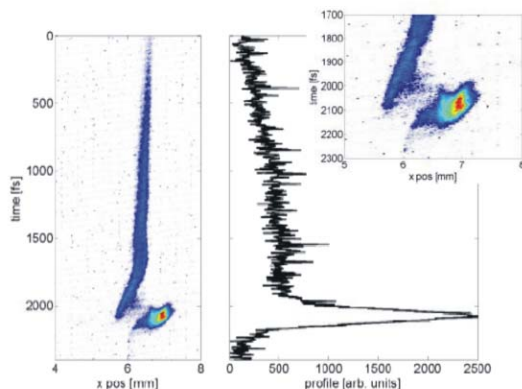

Figure 3: An example of a Lola transverse deflecting cavity measurement (from Hüning et al. [27]).

Optical Replicas

A new technique known as 'optical replicas' has been proposed as a means to obtain femtosecond resolution longitudinal profile diagnostics[28]. The basic concept of the scheme is to impose an optical wavelength density modulation on the electron bunch under investigation, and then cause the bunch to radiate optically by passing this modulated bunch though a resonant undulator.

The full scheme consists of i) an initial undulator resonant at $\lambda = 800$ nm, which is synchronously seeded with an 800nm TiS laser pulse. The interaction of the bunch with the seeded undulator will result in an energy modulation on the bunch with a period of 800nm, or 2.7 fs. The bunch is taken through a drift space to allow the energy modulation to develop into a longitudinal density modulation, again with a period of 800nm. This modulated bunch then

enters a second undulator also resonant at $\lambda = 800$ nm. The pre-modulated bunch will therefore coherently radiate at 800nm, with a radiated intensity dependent on the local charge density of the bunch. Simulations indicate that there will be sufficient intensity in the radiated optical pulse for it to be separately diagnosed with standard ultrafast laser diagnostics. An ultimate time resolution to this technique will be associated with the slippage length of the bunch with respect to the radiation field in the second undulator.

Experimental implementation of a demonstration of the optical replicas concept is currently underway[29]. The system will be installed on FLASH. With a proposed 5 period undulator the achievable time resolution will potentially be 5 cycles of the 800nm resonant wavelength, or 13fs.

REFERENCES

[1] H. Delsim-Hashemi, et al., EPAC 2006, MOPCH016.

[2] H. Delsim-Hashemi, B. Schmidt. Private communication.

[3] H. Delsim-Hashemi, et al., FEL 2005, p. 514.

[4] P. Muggli et al., PAC 2005, p. 4102

[5] A. H. Lumpkin, et al., PAC 2003, p. 2420

[6] A.H. Lumpkin, et al., FEL 2005, p. 608

[7] S. E. Korbly, et al., Phys. Rev. ST Accel. Beams **9** 022802 (2006)

[8] V. Blackmore, et al., EPAC 2006, TUPCH042.

[9] G. Doucas, et al., EPAC 2006, TUPCH043

[10] S. Casalbuoni, et al., TESLA-FEL report 2006-04.

[11] R. Lai, A.J. Sievers, Nucl. Instr. and Meth. A **397** 221 (1997).

[12] O. Grimm, P. Schmüser. Tesla-FEL report 2006-3

[13] S. P. Jamison, et al., Opt. Lett. **31** 1753 (2006).

[14] X. Yan, et al., Phys. Rev. Lett. **85** 3404 (2000).

[15] S. Casalbuoni, et al., PAC 2005, p. 3070.

[16] S.P. Jamison et a., to be published.

[17] I. Wilke, et al., Phys. Rev. Lett. **88**, 124801 (2002).

[18] G. Berden, et al., Phys. Rev. Lett. **93**, 114802 (2004).

[19] H. Loos et al., PAC 2003, p. 2455.

[20] B. Steffen, et al., FEL 2005, p. 549.

[21] S.P. Jamison, et al., Nucl. Instr. and Meth. A **557**, 305 (2006).

[22] G. Berden, et al., DIPAC 2005, p. 69.

[23] G. Berden, et al., EPAC 2006, TUPCH027.

[24] A. L. Cavalieri, et al., Phys. Rev. Lett. **94**, 114801 (2005).

[25] H. Schlarb et al. EPAC 2006, TUPCH024

[26] G. Berden, et al., EPAC 2006, TUPCH026.

[27] M. Hüning, et al., FEL 2005, p. 538.

[28] E.L. Saldin, E.A. Schneidmiller, M.V. Yurkov, Nucl. Instr. and Meth. A **539** (2005) 499

[29] V. Ziemann, et al., EPAC 2006, TUPCH081.

06 Beam Instrumentation and Feedback
T03 Beam Diagnostics and Instrumentation

Chapter 6

Advanced CERN Accelerator School Lectures on Beam Instrumentation and Diagnostics (Trondheim 2013)

Introduction to Beam Instrumentation and Diagnostics

M. Gasior, R. Jones, T. Lefevre, H. Schmickler
CERN, Geneva, Switzerland

K. Wittenburg
DESY, Hamburg, Germany

Abstract

These lectures aim at describing instruments and methods used for measuring beam parameters in particle accelerators. Emphasis will be given to new detection and analysis techniques in each field of accelerator instrumentation. The clear distinction is made between: "instrumentation", the design and construction of the instruments themselves, and "diagnostics", the use of the data from these instruments for running and improving the performance of the accelerator.

1   Introduction

Beam instrumentation and diagnostics combines the disciplines of accelerator physics with mechanical, electronic and software engineering, making it an extremely interesting field in which to work. The aim of the beam instrumentation physicist or engineer is to design, build, maintain and improve the diagnostic equipment for the observation of particle beams with the precision required to tune, operate and improve the accelerators and their associated transfer lines.

This introduction is intended to give an overview of the instrumentation in use in modern accelerators. The choice available today is so vast that inevitably it will not be possible to cover them all. Many of the standard instruments have been covered in previous CAS schools (see for example [1] which also contains a comprehensive list of references) and will therefore be touched upon only briefly. The following subjects will be discussed:

- Beam position measurement

- Beam current and intensity measurement

- Diagnostics of transverse beam motion (tune, chromaticity and coupling)

- Emittance measurement

- Beam loss monitoring

- Longitudinal profile measurement

- Some examples of beam diagnostics

2   Beam Position Measurement

The Beam Position Monitor (BPM) can be found in every accelerator. Its role is to provide information on the position of the beam in the vacuum chamber at the monitor location. For linacs and transfer lines the BPMs are used to measure and correct beam trajectories, while for synchrotrons such monitors are distributed around the ring and used to calculate the closed orbit. In circular machines, their location is usually chosen close to the main quadrupole magnets where the β-functions are largest

1

and so any orbit distortion a maximum. For 90° lattices a typical layout involves placing horizontal monitors near the focusing quadrupoles (where the horizontal β-function is large) and the vertical monitors near the defocusing quadrupoles (where the vertical β-function is large). Apart from closed orbit measurements, the BPMs are also used for trajectory measurements (the first turn trajectory is particularly important for closing the orbit on itself) and for accelerator physics experiments, where turn-by-turn data, and even bunch-to-bunch data is often required.

In the early days a BPM monitoring system simply consisted of an oscilloscope linked directly to the pick-up signals. Since then, enormous advances in the acquisition and processing electronics have been made, turning beam position monitors into very complex systems. Modern BPMs are capable of digitising individual bunches separated by a few nanoseconds, with a spatial resolution of a micrometre or less, while the resulting orbit or trajectory collected from several hundred pick-ups can be displayed in a fraction of a second.

2.1 Pick-ups

The measurement of beam position relies on processing the information from pick-up electrodes located in the beam pipe. Five pick-up families are commonly employed:

- Electrostatic – including so-called 'button' and 'shoe-box' pick-ups
- Electromagnetic – stripline couplers
- Resonant cavity – especially suited for high frequency linacs
- Resistive
- Magnetic

An excellent in depth analysis of most of these pick-ups is presented in Ref. [2]. Here we will briefly describe the three most commonly used, namely the electrostatic, electromagnetic and cavity pick-up.

2.1.1 *Electrostatic (Capacitive)*

The electrostatic or capacitive pick-up is the most widely used in circular accelerators. It consists of metallic electrodes situated on opposite sides of the vacuum chamber at the location where the beam is to be measured. As the beam passes through, electric charges are induced on the electrodes, with more induced on the side which is closer to the beam than the one furthest from the beam. By measuring the difference in the charge induced, the position can be calculated.
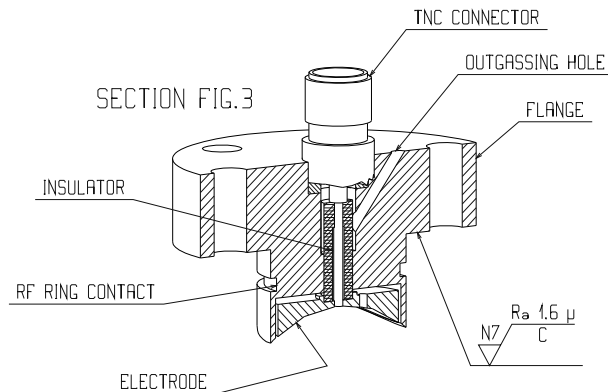

Fig. 1: Cross-section and photo of an LHC button electrode

Let us analyse the properties of button pick-ups (see Fig. 1) since they are the most popular due to their low cost and ease of construction.

The image current associated with the beam will induce a charge on the button which is proportional to the beam intensity and inversely proportional to the position of the beam from the electrode. A schematic representation is given in Fig. 2.
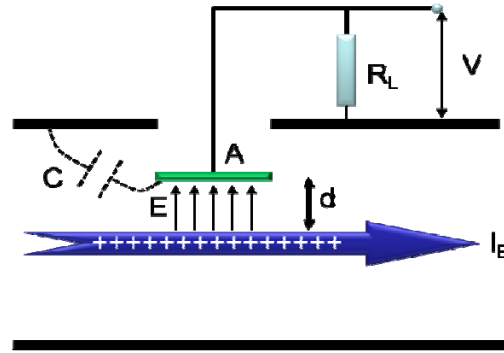

Fig. 2: Schematic of a capacitively coupled electrode

The figure of merit for any electrode is its transfer impedance (the ratio of the pick-up output voltage, V, to the beam current, I_B). For a capacitive pick-up the signal is proportional to the rate of change of beam current at low frequencies, while for high frequencies the capacitance 'integrates' the signal and the transfer impedance tends to its maximum. For the case of a button electrode of area A and capacitance C situated at a distance d from the beam, the maximum transfer impedance (i.e. the value it tends to at high frequency) can be approximated by:

$$Z_{T\infty} = \frac{A}{2\pi d(\beta c) C}$$

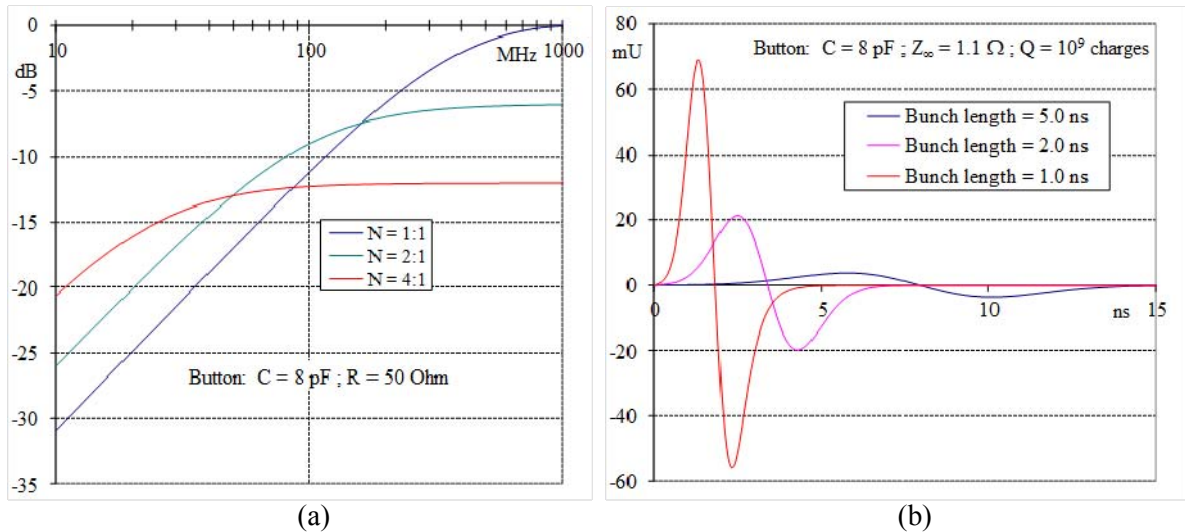where β is the relativistic β and c the speed of light.

Fig. 3: (a) Frequency response and (b) time response of a button electrode

3

Impedance transformation can be used to improve the low frequency response at the expense of that at high frequency. Figure 3(a) shows the frequency response of an 8pF button electrode for the matched 50Ω impedance case (1:1) and after two different impedance transformations. The time response of the button for different bunch lengths can be seen in Fig. 3(b).

When designing such pick-ups care must be taken to limit the impedance variations when the transmission line used for signal extraction passes from the vacuum to a feedthrough or cable dielectric (such as ceramic, glass or air). Any such mismatch will produce unwanted reflections, often at high frequency, which could perturb the processing electronics. For this reason most processing chains introduce a low-pass filter on the button output. Special care must also be taken to pair the electrodes on opposite sides of the chamber to minimise offsets in the position reading. This pairing can be made less sensitive to capacitance variations if the high frequency cut-off for the processing electronics sits on the linear part of the button response, with the disadvantage that the overall signal amplitude is reduced.

2.1.2 *Electromagnetic (stripline)*

The electromagnetic pick-up is a transmission line (stripline) which couples to the transverse electromagnetic (TEM) field of the beam. The transmission line is formed between the stripline and the wall of the vacuum chamber and is excited by the beam only at the gaps on either end of the stripline where a longitudinal field occurs. Figure 4 shows the layout of such an electromagnetic stripline electrode.
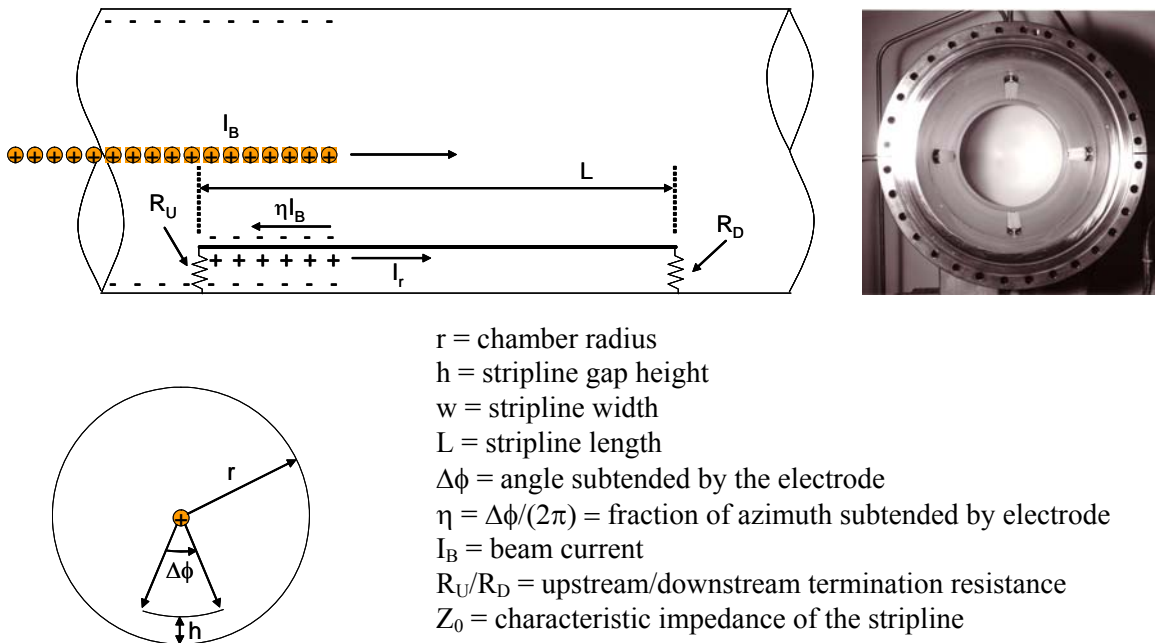

r = chamber radius
h = stripline gap height
w = stripline width
L = stripline length
$\Delta\phi$ = angle subtended by the electrode
$\eta = \Delta\phi/(2\pi)$ = fraction of azimuth subtended by electrode
I_B = beam current
R_U/R_D = upstream/downstream termination resistance
Z_0 = characteristic impedance of the stripline

Fig. 4: Schematic and photo of an electromagnetic stripline pick-up

Consider a bunch travelling from left to right (upstream to downstream). While it is over the upstream port there is a voltage V_r across R_U, causing a voltage wave of that amplitude to be launched to the right. The stripline forms a transmission line with the wall of the vacuum chamber of characteristic impedance Z_0. The voltage wave is therefore accompanied by a right travelling current wave of amplitude $I_r = V_r / Z_0$. This current flows along the bottom surface of the electrode whilst an equal and opposite current flows along the chamber wall. In addition an image current of amplitude ηI_B travels along the top surface of the electrode. The voltage V_r across R_U can therefore be expressed as

$$V_r = (-I_r + \eta I_B)R_U = \eta I_B \frac{R_U Z_0}{R_U + Z_0} \quad \Rightarrow \quad V_r = \tfrac{1}{2}\eta I_B Z_0 \text{ for a matched stripline } (R_U = Z_0)$$

When the beam is over the downstream port it produces a voltage $-V_r = -\tfrac{1}{2}\eta\, I_B Z_0$ across R_D in the same way as it produced a voltage $+V_r$ across R_U. This launches a left-travelling wave of the same magnitude, but different sign to the right-travelling wave, which propagates along the transmission line formed by the stripline and the chamber wall and will produce an inverted signal upon arrival at the upstream port a time L/c later. The final signal observed at the upstream port will therefore be a bipolar pulse with the maxima separated by $2L/c$ (see Fig. 5(a)).

When the RF wavelength of the beam is equal to multiples of $2L$, the reflection and the signal from next bunch will cancel and there will be no net signal from the stripline. A maximum in the frequency response will be observed when L is a quarter of an RF period, and hence the stripline pick-up length is usually chosen accordingly. The full frequency response of a 60cm long stripline is shown in Fig. 5(b) and has a lobe structure, with the minima located at multiples of $c/(2L)$.
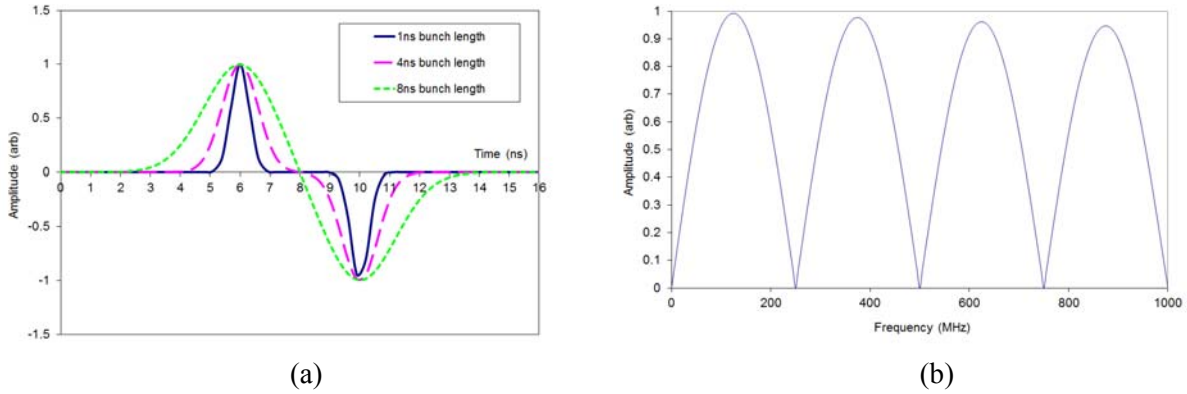

| (a) | (b) |

Fig. 5: (a) Time response and (b) frequency response of a 60cm long electromagnetic stripline pick-up

For a relativistic beam the voltage due to the beam passing the downstream port is produced at the same time as the right-travelling wave propagating between the stripline and the wall arrives at the downstream port. The two equal and opposite voltages therefore cancel producing no net signal at the downstream port. The electromagnetic stripline pick-up is therefore said to be "directional", i.e. a signal is only observed on the upstream port with respect to the beam direction. These pick-ups are therefore used in all locations where there are two counter rotating beams in the same vacuum chamber. Due to imperfections in the stripline and feedthrough impedance matching, the best directivity one can hope to obtain for a real stripline is generally around 25-30dB (i.e. the voltage signal of one beam with respect to the other is attenuated by a factor between 18-32).

2.1.3 *Resonant Cavity*

Resonant structures, e.g. "pill-box" or rectangular cavities, coaxial resonators and more complex waveguide-loaded resonators, have become very popular to fulfil the high resolution, single-pass beam position monitoring demands of next generation, high energy, linear accelerators [3,4], or for driving a SASE-FEL beam-line [5].

These are constructed to exploit the fact that an off-centre beam excites a dipole mode (TM_{110}) in the cavity, with the amplitude of excitation almost linearly dependent on the off-axis displacement of the beam (Fig. 6). This dipole mode has a slightly different frequency from the main monopole mode (TM_{010}) of the cavity, which allows the processing electronics to select only the frequency of interest (dipole TM_{110}) and so suppress much of the large, unwanted, intensity related signal (monopole TM_{010}).

5

Nevertheless, even with this frequency difference, the presence of the fundamental TM_{010} monopole mode still adds a strong common mode component to the dipole-mode position signal, limiting the performance of the cavity BPM. Rather than picking off the signal from the cavity using four symmetrically arranged pin antennas it is therefore preferable to couple to the cavity using waveguides. Selecting the width of the waveguides such that they have a cut-off frequency above the TM_{010} monopole mode results in a very efficient, internal high-pass filter and makes the cavity BPM quasi "common-mode free". Such waveguide-loaded rectangular resonators (Fig. 7) have demonstrated a world record resolution of 8.7 nm at the ATF2 final focus test beam-line [6].
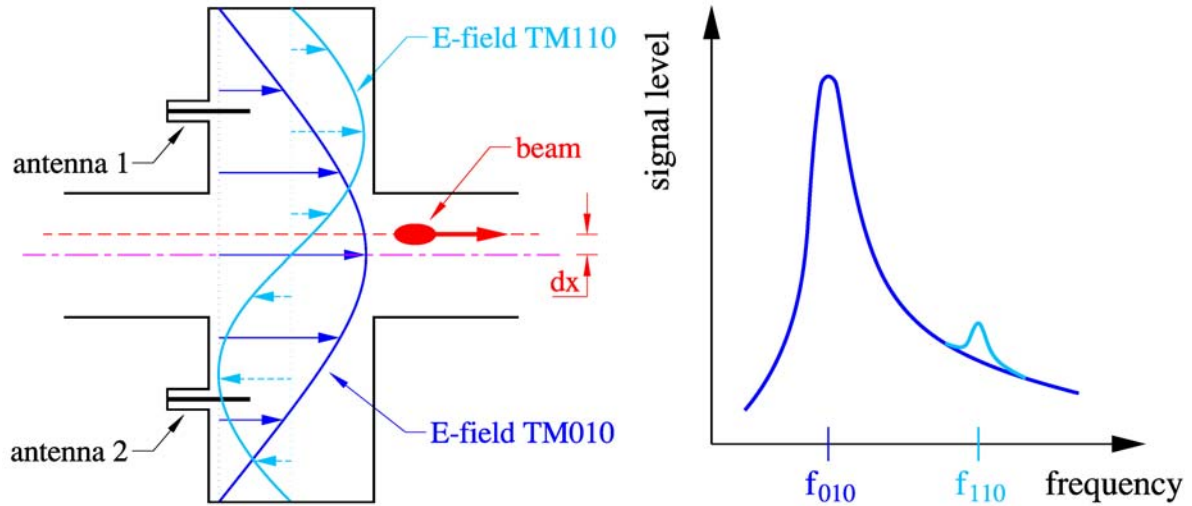

Fig. 6: Principle and frequency response of a cavity BPM
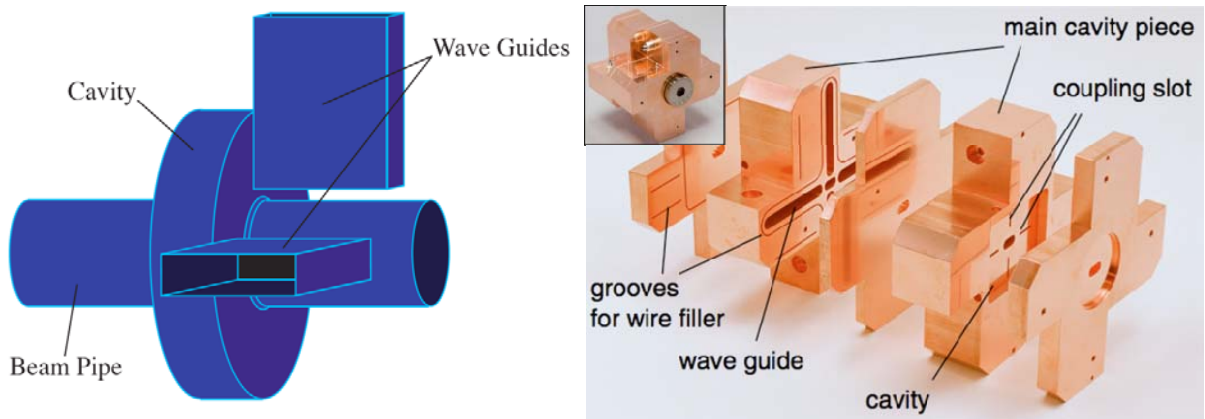
Fig. 7: Principle and example of a waveguide coupled cavity pick-up (ATF2, KEK, Japan)

2.2   Beam Position Acquisition Systems

Once the signals from the opposite electrodes of a pick-up have been obtained, the next step is to convert these signals into a meaningful beam position. The first thing to do is to normalise the position, i.e. to make it independent of the signal amplitude (i.e. beam intensity). This is generally done using one of three algorithms, whose response curves can be seen in Fig. 8.

6

- **Difference over sum (Δ/Σ) -** The sum and difference can be obtained either directly from a cavity BPM, or for the other pick-up types using a 0°/180° passive hybrid, a differential amplifier or calculated by software (after digitising), to give:

$$Normalised\ Position = \frac{A - B}{A + B}$$

  The transfer function of this algorithm can be seen to be highly linear.

- **Logarithmic ratio -** The two input signals are converted into their logarithmic counterparts and subtracted. In practice this is done using logarithmic amplifiers followed by a differential amplifier. This gives:

$$Normalised\ Position = Log(A) - Log(B)\left(= Log\left[\frac{A}{B}\right]\right)$$

  whose response curve is seen to be an reversed S-shape, which becomes highly non-linear when exceeding 70% of the normalised aperture.

- **Amplitude to Phase -** The two input signals are converted by a 90° passive hybrid into signals of equal amplitude but varying phase, with the position dependence of this phase given by:

$$Normalised\ Position = \phi = 2 \times ArcTan(A/B)$$

  Here the transfer function again deviates from the linear in an S form, but does not diverge for large excursions. In addition, the gradient is larger around zero, making it more sensitive towards the middle of the pick-up. A variation on the amplitude to phase algorithm is amplitude to time conversion, the technique used for the beam position system of the LHC [7].
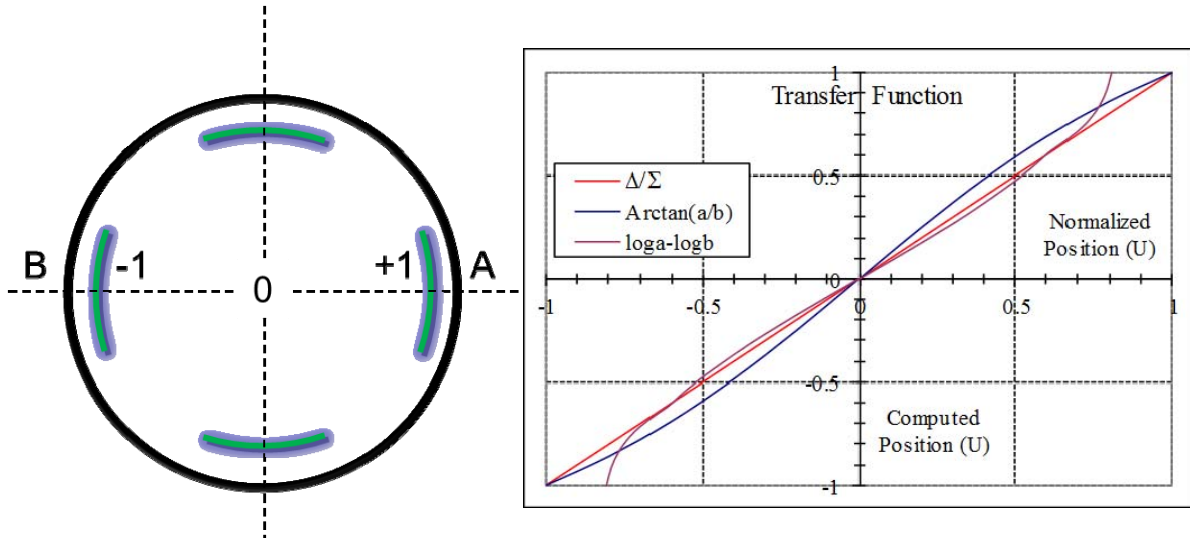
Fig. 8: Transfer functions for three commonly used position normalisation algorithms

The type of algorithm to be used will depend on the choice of processing electronics. In all cases the non-linearity is taken into account by calibration circuits and correction algorithms. A summary of commonly used beam position acquisition systems is given in Fig. 9. Here we will only briefly mention the various families in passing, but detailed descriptions along with the advantages and disadvantages of each system can be found in [8].

MPX (multiplexed) – each of the BPM electrodes is multiplexed in turn onto the same, single electronics acquisition chain. This eliminates channel to channel variations, but since the switching is

7

generally quite slow such an acquisition only tends to be used in circulating machines where the average orbit is of main importance.

Hybrid (Sigma & Delta) – here a 0°/180° passive hybrid is usually used to obtain the sum (Σ) and difference (Δ) signal from the two electrodes. The position (or ratio of the sum and difference signals) can then be obtained in many ways including: direct digitisation, homodyne detection (mixing the sum and delta signals with the sum signal itself) or heterodyne detection (mixing sum and delta signals with an external reference).

Individual Treatment – in this case each electrode is treated separately, but in parallel. The acquisition can either consist of directly digitising each signal or using logarithmic amplifiers as outlined above. The disadvantage of this method is that it requires two (or four depending on the pick-up orientation) very well matched chains of electronics, since the combination of the signals to obtain a position is performed at the very end of the chain.

Passive Normalisation – here the amplitude difference (i.e. position information) in the input signals is directly converted into a phase or time difference. Intensity information is lost in this procedure, but the result is a varying phase or time which is directly proportional to the position.
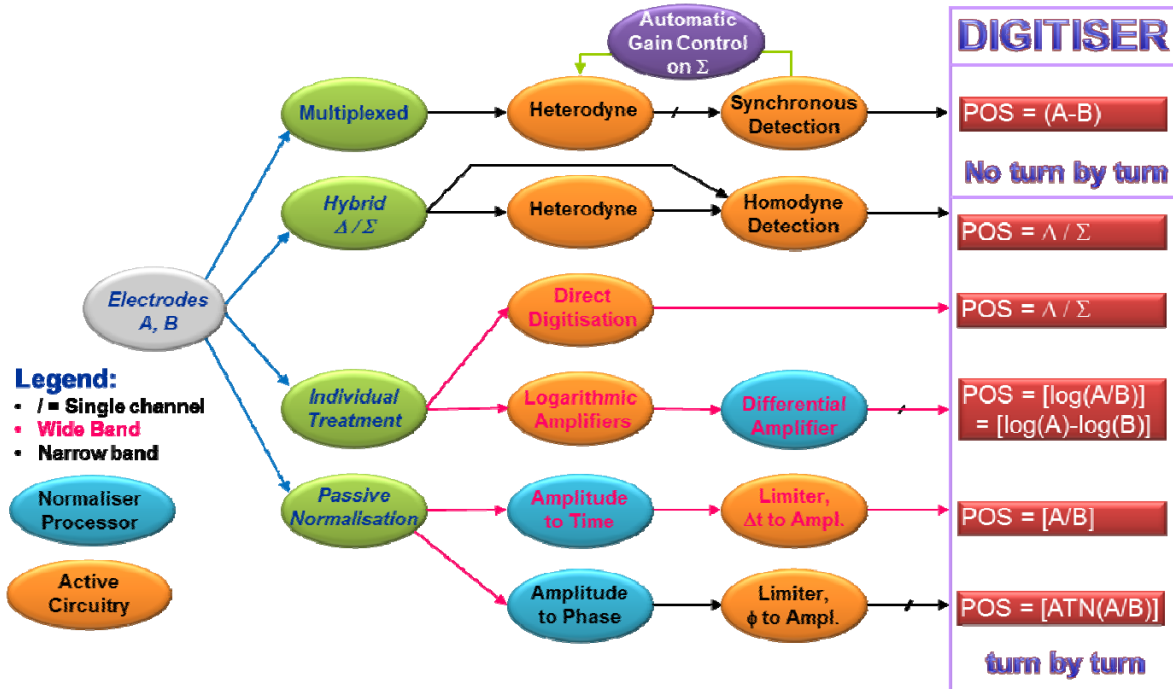
Fig. 9: Schematic representation of the various beam position processing families

2.2.1 *Read-out electronics*

The read-out system interfaces the BPM pickup to the accelerator data acquisition (control) system. This requires signal conditioning, normalisation and linearisation of the BPM signals with conversion to a digital format somewhere along this chain in order to ultimately provide a time-stamped beam position.

Modern BPM read-out electronics are typically based on the individual treatment of the electrode signals using frequency domain signal processing techniques [9]. These techniques were developed for the telecommunications market and make use of the high frequency and high resolution analogue to

digital converters (ADCs) that are now readily available. In such schemes, bandpass filters in the analogue section convert the BPM signals into sinewave-like signal bursts for waveform sampling and processing in the following digital electronics. Microwave and RF analogue components, 12-16 bit pipeline ADCs, Field Programmable Gate Arrays (FPGAs) and clock distribution chips with sub-picosecond jitter are some of the key hardware elements. Figure 10 illustrates a typical electronics arrangement for a broad-band BPM pickup with only 1 of the 4 channels shown. For cavity BPMs the schematic is similar.
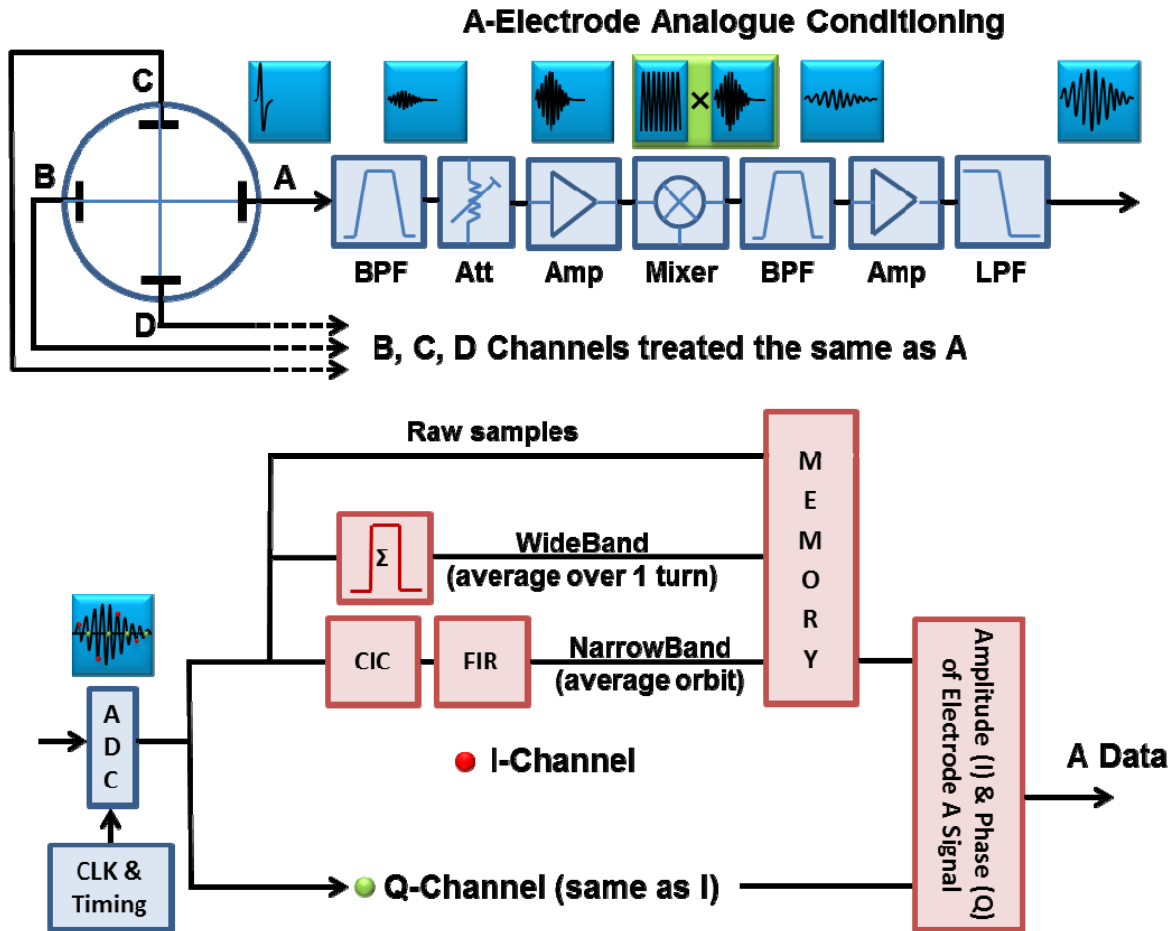

Fig. 10: Key elements of modern BPM read-out electronics

The analogue chain, consisting of bandpass filters, amplifiers and typically a frequency down-conversion stage prepare the electrode signal for sampling by an ADC. In order to reconstruct the input sine wave the ADC is either clocked at some sub-harmonic of the accelerator radio frequency or with an external clock (NCO – numerically controlled oscillator). This clock is typically chosen to give a sampling at 4 times the frequency of the input sine wave or to under-sample the input sine wave by a multiple of 4. This allows I/Q demodulation to be carried out in the digital domain. In-phase / Quadrature (I/Q) demodulation is nothing more than sampling at some 4th multiple or sub-harmonic of the input frequency. The knowledge that the sampled points are then all 90° apart on the sine wave allows for easy computation in the digital domain without the need for sine and cosine lookup tables. If the frequency is correct, and the phase is locked, then all the quadrature samples are zero and only the in-phase samples need to be considered, giving directly the amplitude of the sine wave. These data can then be treated either in their raw form for bunch to bunch measurements, in a wide-band form for turn by turn measurements or in narrow-band for orbit measurements. The narrow band orbit data is

9

typically always available on-line from such systems, with the wideband and raw data available on request for a limited number of turns or bunches respectively. By producing the sum and difference of the amplitudes from opposite electrodes and applying calibration and linearization factors this data can then be converted into a meaningful beam position.

3   Beam Current and Intensity Measurement

The measurement of beam current or bunch intensity is one of the most basic and important measurements performed at any accelerator, used to optimise its operation and to calibrate physics experiments. For determining the time evolution, relative measurements are often sufficient, relying only on a good resolution from a single detector. However, when comparing the intensity read-out from several devices, such as for transfer line or injection optimisation, or when using the system to cross-calibrate other devices, a precise system calibration is mandatory.

3.1   The Beam Current Transformer

The beam intensity is usually measured by means of a "beam current transformer" or BCT. This name originates from the fact that in such a device the beam can be considered as the primary, one-turn winding of a transformer, with its equivalent current "transformed" to the secondary winding output (see Fig. 11).

The transformer is based on two principles: first, that an electric current produces a magnetic field and second that a changing magnetic field within a loaded coil of wire induces a current in the coil (electromagnetic induction). Changing the current in the primary coil changes the magnetic flux that is developed, with the changing magnetic flux inducing a current in the secondary coil.

The BCT relies on a toroid made of ferromagnetic material to capture the magnetic field, passing it through an n-turn secondary winding loaded with a resistance R_L. A beam current I_B passing through the toroid induces a current $I_O = I_B / n$ in the secondary n-turn winding. This current is converted into an output voltage $V_O = I_O \times R_L$. The BCT transfer impedance, i.e. the factor determining the output voltage corresponding to a given beam current, can be defined as $Z_{TR} = R_L / n$.

$$I_O = \frac{I_B}{n}$$

$$V_O = \frac{I_B}{n} R_L$$

$$Z_{TR} = \frac{V_O}{I_B} = \frac{R_L}{n}$$
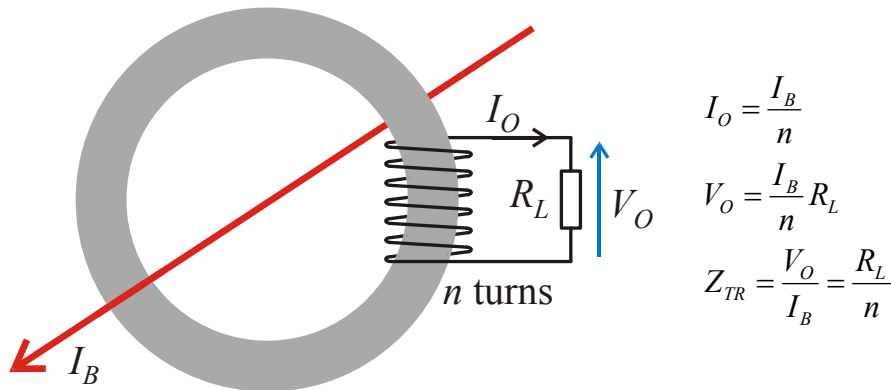
Fig. 11: The principle of a beam current transformer (BCT)

A perfect BCT would reproduce the temporal distribution of the beam current shape with no distortion and amplitudes described with the above equations. Each real BCT has a limited bandwidth, which can be characterised by the low and high cut-off frequencies, f_{cL} and f_{cH}. Typically they are chosen according to the spectral content of the beam to minimise the distortion of the beam pulses.

10

The low cut-off originates from the fact that the impedance of the secondary winding decreases for low frequencies. The secondary winding inductance is given by $L_S = A_L \times n^2$, where A_L is the toroid inductance constant having the unit of nH / turn^2. A_L depends on the toroid material and its geometry, in particular the length to cross-section ratio. At the cut-off frequency f_{cL} the inductive reactance $X_L = 2\pi f_{cL} L_S$ of the secondary equals the load R_L, giving the BCT low cut-off frequency

$$ f_{cL} = \frac{R_L}{2\pi A_L n^2} $$

For modern, high permeability materials A_L is in the order of 10000 nH / turn^2. For a BCT with such a toroid, a secondary winding with $n = 30$ turns and load $R_L = 10\ \Omega$, the low cut-off frequency would be some 180 Hz.
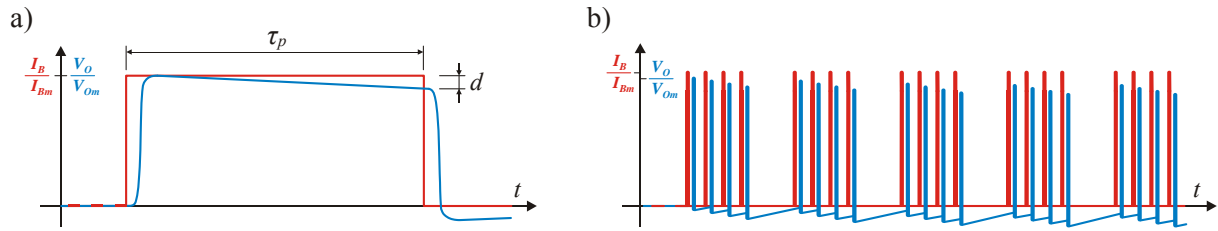

Fig. 12: Influence of the limited BCT low cut-off frequency: (a) signal droop and (b) base line shift

The fact that the BCT has a low frequency cut-off implies that the output signal will have no DC component, which results in a distortion of the signal. For long pulses with a low duty cycle (e.g. from a linac) the distortion is called "droop" and is sketched in Fig. 12(a). The amount of droop at the end of the pulse depends on the ratio of the pulse length τ_p and the time constant $\tau_{cL} = (2\pi f_{cL})^{-1}$. For $\tau_p \ll \tau_{cL}$ the dependence is linear. Pulse trains of short bunches suffer from a phenomenon known as "base line shift", depicted in Fig. 12(b), where the steady-state integral of the BCT output signal is zero. This is typical for circular accelerators and is also a consequence of the low frequency response and lack of DC component. Special compensation techniques are therefore often required to restore the missing DC response and are known as "base-line restoration" techniques. In the past this was done electronically, often requiring complicated switching circuitry and timing, whilst nowadays it can be efficiently performed in the digital domain.
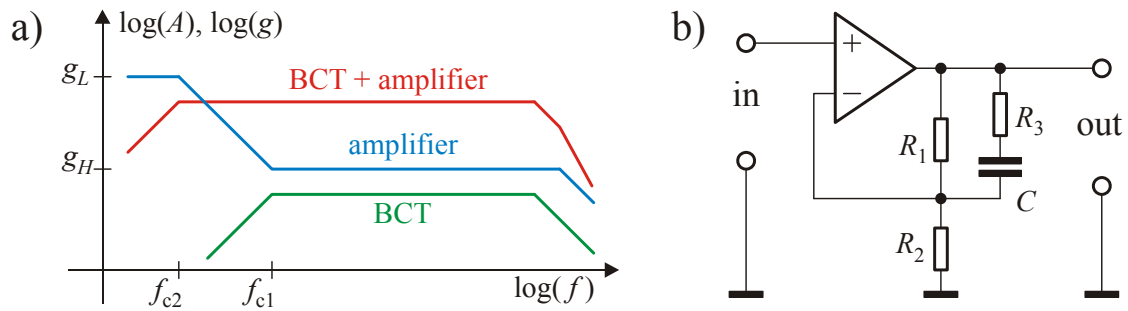
Fig. 13: (a) Simplified frequency characteristics of a BCT with a correcting amplifier and (b) an implementation example using an operational amplifier

If the BCT frequency characteristic below the low cut-off frequency f_{cL} is defined by the first-order high-pass of the secondary winding inductance and its load, it can be compensated by an analogue circuit. This can be achieved using an amplifier having more gain for these low frequencies, as sketched in Fig. 13. Such a circuit can be built using an operational amplifier with the feed-back circuit shown. For low frequencies its gain is given by $g_L = R_1 / R_2 + 1$, while for high frequencies the

gain is given by $g_H = (R_3 || R_1) / R_2 + 1$, where $(R_3 || R_1)$ is the resistance of R_3 and R_1 in parallel. Capacitance C is chosen according to f_{cL} in order to achieve a flat overall frequency response. The price to pay for this higher low frequency gain of the amplifier is deterioration in the noise performance for the compensated frequency band.

The high frequency response of a BCT depends on many factors, making it very difficult to calculate and even to simulate with modern electromagnetic finite-element simulators. In practice the high frequency response is therefore still often optimised on prototypes. It depends on the toroid material, toroid size, toroid winding load, the ceramic insert and winding technique used, but always decreases with the number of turns. BCTs optimised for bandwidth can cover a range of 6–7 decades in frequency, with the low cut-off typically ranging from 100 Hz to 1 kHz and the high cut-off from 100 MHz to 1 GHz.
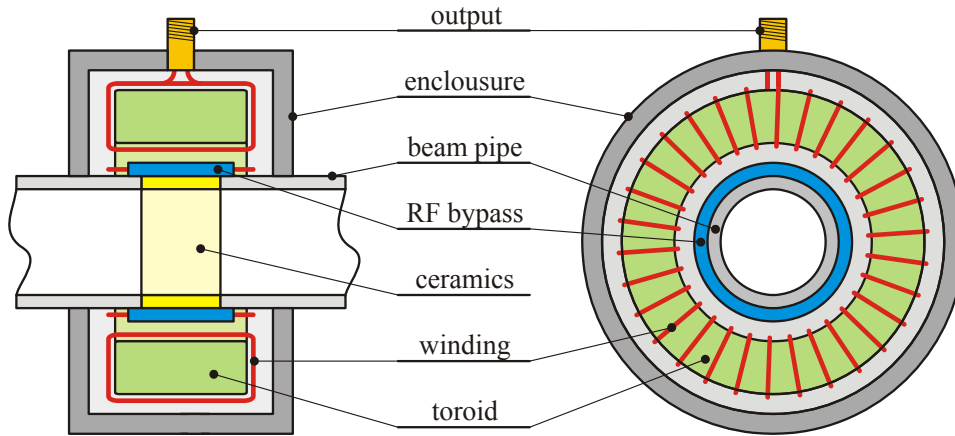
Fig. 14: The beam current transformer

An example of a BCT construction is sketched in Fig. 14. In order for the transformer to interact with the magnetic field of the beam it has to be placed over a ceramic gap in the vacuum chamber. To keep the impedance seen by the beam as low as possible an RF bypass (either a thin metallic coating or external capacitors on the ceramic) is required for the very high frequency wall current components. In addition, to keep the vacuum chamber continuity, the transformer is enclosed in a housing connected galvanically to the beam pipe.

An example of a wide-bandwidth BCT system is the one installed on the CERN-SPS [10], with a

Fig. 15: The integrator of the CERN-SPS BCT and a beam measurement example

12

bandwidth from 200 Hz to 1 GHz. Such a bandwidth is obtained by using a ferromagnetic core wound of high permeability amorphous metal tape. With this system operators can observe the bunch-by-bunch intensity evol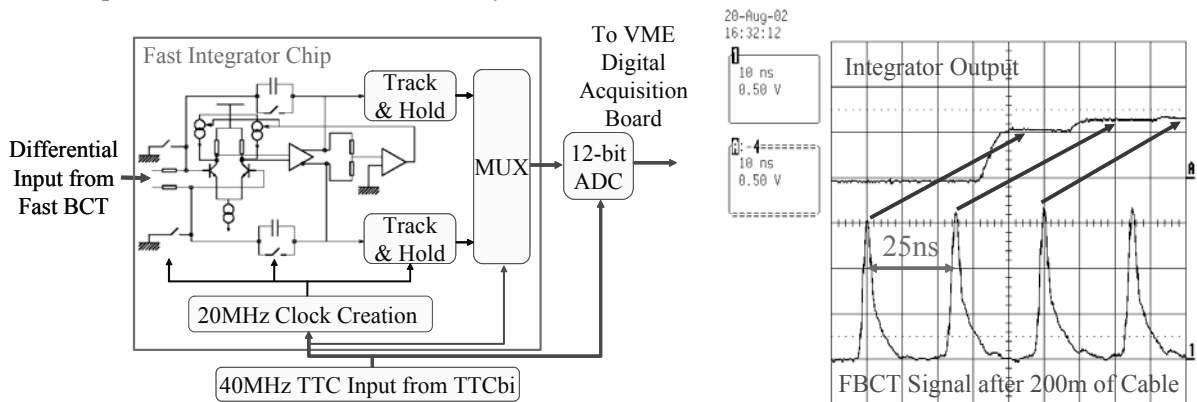ution of beams throughout the SPS acceleration cycle. In order to obtain the total charge in each bunch, fast integrators are used, capable of working at repetition frequencies of up to 40 MHz. The integrators are based on a dedicated chip, developed primarily for capturing photomultiplier signals in the LHC-b experiment [11]. A schematic of the integration principle and the resulting signals as measured in the CERN-SPS are shown in Fig. 15. The chip works using two integrators operating in parallel. As one integrates the other is discharged, with the output switched from one to the other on each clock cycle. The resulting integrated signals are directly digitised, with all integrator linearization and base line restitution performed in the digital domain.

3.2 The DC Beam Current Transformer

In storage rings and accelerators with cycle times of several seconds, a DC beam transformer can be used to measure the total current. Such an instrument was developed for the CERN-ISR (Intersecting Storage Rings) in the early 1980's, the first machine to sustain beams for hours [12]. A DC transformer is based on a pair of matched, toroidal, ferromagnetic cores, which are driven into saturation by a modulation current at frequencies of up to a few kHz. The principle of operation is shown in Fig. 16, and makes use of the hysteresis loop of the toroid.

If an equal but opposite modulation current (the triangular waveforms in Fig. 16) is applied to both
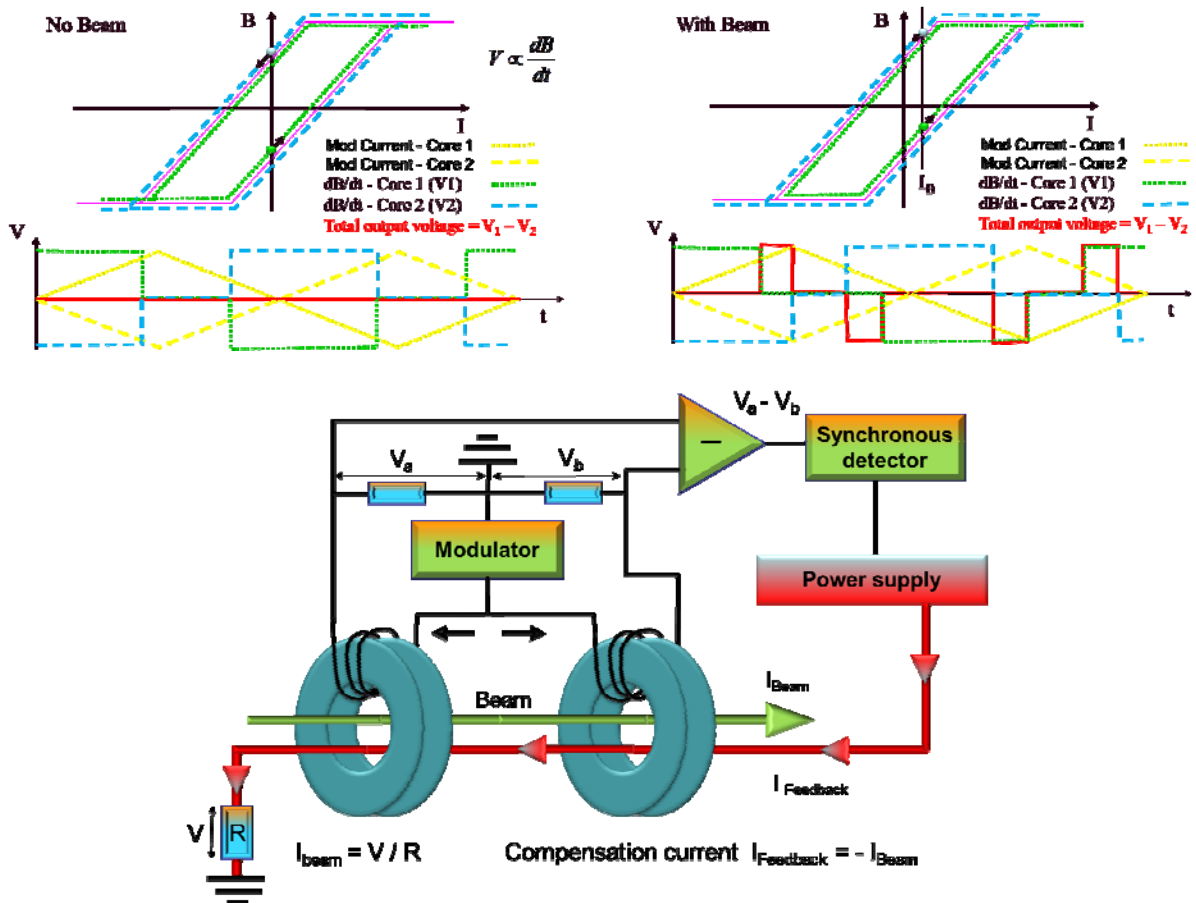

Fig. 16: The principle and schematic of a DC beam current transformer

cores with the beam not present, then the voltage induced in the detection windings on each core will be equal but opposite. When, however, there is a beam current I_B present, the starting point in the

hysteresis loop for zero modulation current is offset due to the static magnetic field generated by the beam current. Since the modulation is in opposite directions in each toroid, the time spent in saturation will be different for the two branches of the hysteresis loop. This results in the generation of voltage pulses at twice the modulation frequency when the induced voltage in the detection windings on each core is combined. The demodulation of this signal gives a train of pulses, with the width of each pulse being a direct measure of the beam current, i.e. by how much the hysteresis curves are offset.

In the "zero flux detector" implementation of the DC beam transformer, the result of the demodulation is fed back into a compensating current loop (see Fig. 16). Once the compensation current and the beam current are identical the net static magnetic field seen by the toroids is zero (hence zero flux) and the output from the demodulator is also zero. The beam current can then be obtained by simply measuring the voltage produced by this compensation current across a known resistor.

For modern DC transformers such a zero flux detector is used to compensate the droop of the simple beam current transformer described in section 3.1. This significantly increases the bandwidth of the system, allowing measurement from DC to a few MHz.

4   Diagnostics of Transverse Beam Motion

The instrumentation used to observe transverse beam motion is very important for the efficient operation of any circular accelerator [13]. There are three main parameters which can be measured using such diagnostics, namely the betatron tune, chromaticity and coupling, all of which are discussed in detail below.

4.1   Tune Measurement

Measuring and optimising the betatron tune through the whole operational cycle of a circular accelerator is one of the most important and basic control room tasks, and strongly influences the beam lifetime and quality. Since the betatron oscillations are typically only detected at one point in the machine the measurement gives the fractional part of the tune, which is the quantity of interest for beam optimisation. Separate measurements are normally performed in order to obtain the tune in both the horizontal and vertical plane. The quality of the tune measurement is very important for measuring other crucial beam parameters, such as chromaticity and betatron coupling, which are traditionally derived from tune measurements.
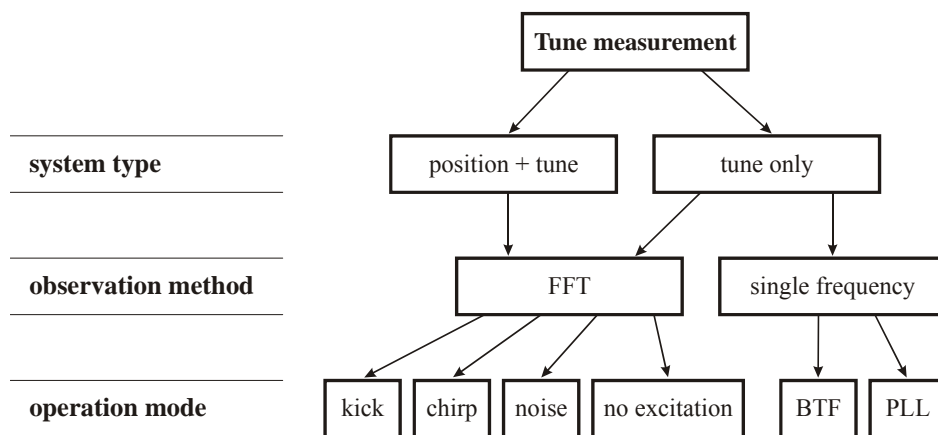

Fig. 17: Categories of tune measurement systems

Tune measurement systems can be divided into two main categories of system (see Fig. 17), those based on turn-by-turn BPM measurements followed by special tune signal processing and those constructed as dedicated systems optimised for detecting only the oscillations of the beam. The

14

"observation method" can either be wide-band, i.e. yielding a full response function over the frequency range of interest, or narrow-band, detecting only the response at a given frequency. In order to be able to observe an oscillation an appropriate excitation has to be applied to the beam, the "operation mode".

4.1.1   *Tune measurement systems*

A tune measurement system can be based upon turn-by-turn readings from a regular beam position acquisition system, such as those described in Section 2. Signal processing of these signals typically result in spectra showing the oscillation frequencies present in the transverse beam motion. Such a universal system is, in many cases, sufficient, especially for machines that can tolerate relatively large beam excitation (such as electron machines, where radiation damping counters any emittance blow-up introduced by exciting the beam for a short period). Its main limitation is sensitivity, originating from the fact that, in most cases, the BPM system is optimised for accurate position measurements over a large dynamic range in both position and beam intensity. For example, if the system has to measure positions over ±10 mm, then to detect oscillations with 1 μm amplitude, a dynamic range of 10000 is required in turn-by-turn mode. This is in practice difficult to achieve, with position measurements typically averaged over many hundreds of turns to achieve such a resolution. This can be improved significantly by building dedicated systems optimised for beam oscillation detection. In such systems the static beam position is rejected at a very early stage with only the oscillation signal used for further processing. An example is the so called Base-Band Tune (BBQ) system, based on a direct diode detection method initially designed for the LHC [14]. This allows a reliable tune measurement with micrometre beam oscillations, which in some machines is always present without the need for additional, explicit excitation.
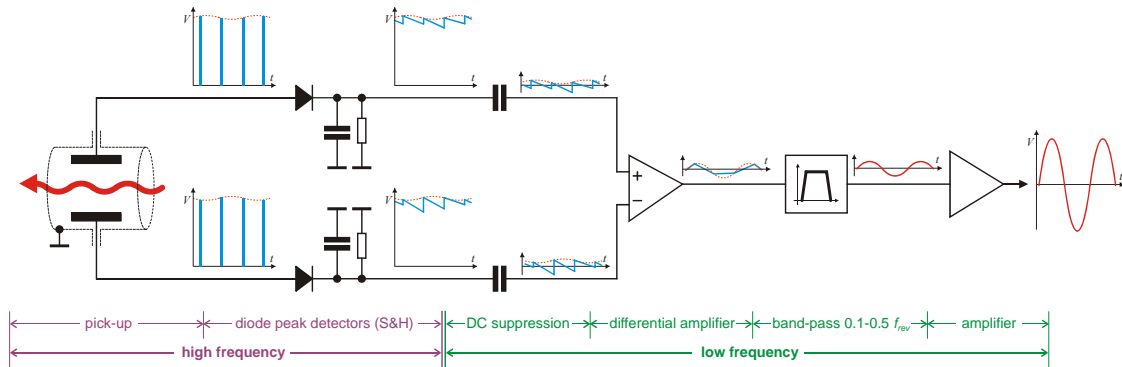

Fig. 18: Principle of the Base Band Tune Measurement system using Direct Diode Detection

In this technique the electrode signals from a beam position pick-up undergo envelope demodulation with diode peak detectors, which can be considered as a simple, fast, sample-and-hold circuit (see Fig. 18). Most of the pick-up signal does not change from one turn to another and gets converted to DC, while the small beam oscillation modulation is kept as ripples on this DC offset. A series capacitor blocks the large DC component related to the intensity and static beam orbit, while allowing the small ripples to pass and be amplified. As the beam oscillation modulation from opposite pick-up electrodes is of opposite phase, enhancement of the signal is possible by subtraction using a differential amplifier, with all common mode interference and remaining intensity and orbit signals further suppressed. The tune range of interest typically corresponds to half the machine revolution frequency ranging from tens of kHz to MHz depending on the size of the accelerator. The beam oscillations of importance after the diode peak detectors are therefore of relatively low frequency and as such can be easily filtered, amplified and digitised with high resolution ADCs. Further details on

15

the direct diode detection technique along with some adventures encountered during its development can be found in [15], which also includes a list of references related to the subject.

4.1.2 *Tune measurement observation methods*

Narrowband tune observation was popular in the past when high frequency digitisation and processing of RF signals was expensive and difficult to achieve with enough precision. In such cases most of the signal processing was performed in the analogue domain with RF mixers and filters with only the resulting low frequency content digitised and analysed. They always involve locking the detection frequency to the excitation frequency, and measuring the beam response at that particular frequency. Beam transfer function (BTF) measurements and phase-locked loop (PLL) measurements are the two main examples of narrow-band tune observation and will be discussed further in the next section.

With the recent advance in high resolution, high frequency digital electronics, most modern tune observation is performed wide-band. The advantage of wide-band tune observation is that it yields a complete spectrum of the transverse beam motion. In addition to tune measurement this then allows detection of beam instabilities and abnormal sources of beam excitation, typically originating from malfunctioning of an accelerator system, such as the RF system or magnet power supplies. Wideband observation is based on a fast sampling of the input signal followed by analysis using Fast Fourier Transform (FFT). In the simplest case the tune is localised in the beam spectrum as the frequency corresponding to the highest spectral peak. In practice, however, the beam spectrum is often much more complicated. Use of wideband observation in such cases is a big asset, as it allows tune determination using algorithms of practically unlimited complexity, something which is simply not possible in single frequency systems.

4.1.3 *Tune measurement operation modes*

In a circular accelerator each particle in the beam undergoes a transverse harmonic motion around the ideal orbit defined by the magnetic lattice. However, the resonant frequency (tune) of each particle is slightly different, resulting in an incoherent motion. To an external observer (such as a beam position pick-up), who looks just at the centre of mass of all these moving charges, this yields a constant signal which is directly proportional to the total intensity and the average position. In order to measure the average resonant frequency (tune) and the spread in frequencies (tune spread) the movement of the particles need to be synchronised, something which is achieved using externally applied excitation.

4.1.3.1 *Excitation techniques for FFT based measurements*

A classical tune measurement consists of applying a transverse kick to the beam, typically by discharging a capacitor bank to generate a large deflecting current in a kicker magnet. An example of such a measurement is shown in Fig. 19.

The kick has the effect of offsetting all the particles by the same amount from the reference orbit, from which they then continue to perform their individual harmonic motion. The average frequency of this motion is what is known as the tune. The decay in the amplitude of the oscillation, as seen in the pick-up signal, is a result of the slightly different frequencies of the individual particles. After a while this results in the motion becoming incoherent, observed as a damping of the oscillation signal. What should not be forgotten is that in a hadron machine all particles still undergo the original harmonic motion, which is now higher in amplitude due to the applied kick. This results in an increase of the effective beam size, and hence emittance. In order to follow the tune evolution along an acceleration cycle the kicks can be repeated, giving a full time resolved beam spectrum as shown in Fig. 19.
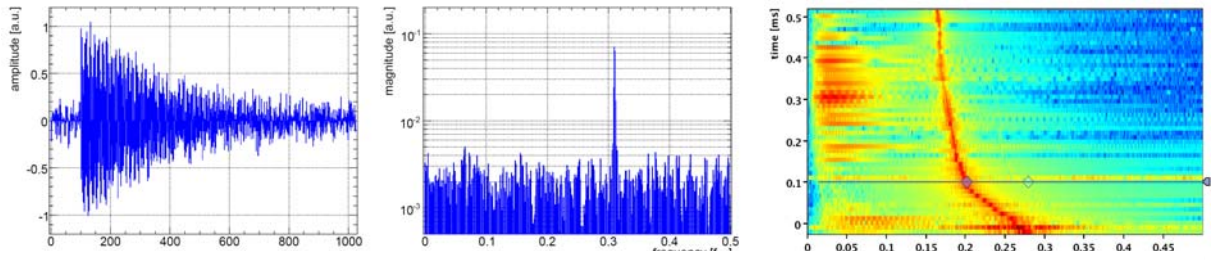
16

Fig. 19: Proton beam response to single kick excitation (left) with corresponding magnitude spectrum (middle). Tune measurement example from the CERN Booster Synchrotron (right) with kicks every 10 ms.

Another commonly used excitation technique is the so called "chirp". This involves sweeping the applied excitation frequency over a certain range where the tune is expected to sit. The name "chirp" comes from the fact that if listened to at audio frequencies such a signal sounds like the chirp of a bird.

The sweep time should be short enough so that the machine tune can be assumed to remain constant during the excitation time. Typically tune changes are slow compared to the revolution frequency. The sweep range and time can therefore be chosen in such a way that the beam gets coherent kicks over several machine turns when the sweep reaches the right frequency. Beam oscillations of sufficient amplitude can thus be achieved with much smaller peak excitation power than with the single kick method. Chirp excitation trades the excitation strength with the excitation duration and can often be applied to the beam through a direct input to the transverse feedback system.

Noise excitation, an alternative to chirp excitation, continuously puts power into the beam spectrum at all frequencies. This has the advantage that it does not require any synchronisation between the excitation source and the beam signal acquisition. In some machines various unwanted noise sources result in sufficient "natural" beam oscillations that no additional excitation is required for tune measurement.

4.1.3.2 Excitation techniques for single frequency based measurements

A Beam Transfer Function (BTF) measurement consists of exciting the beam with a steady sinusoidal signal and measuring the resulting beam motion at this specific frequency. The excitation frequency is then changed and a new measurement made, with this process repeated until the range of interest is covered. Both the amplitude and phase of the resulting beam oscillation can be precisely determined as the excitation frequency is known. A BTF measurement typically takes quite a long time during which it must be assumed that all machine conditions remain constant. This is why the BTF method
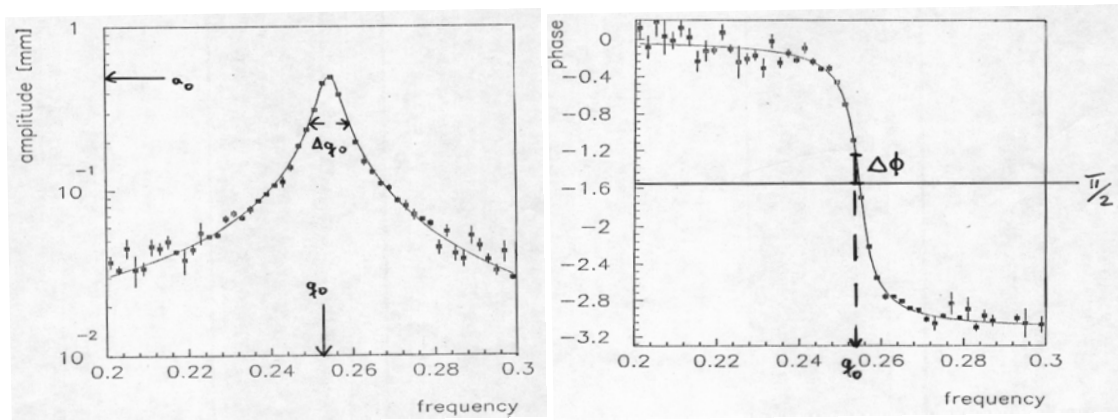

Fig. 20: Complete beam transfer function measured on the CERN-LEP

17

cannot be used for studying dynamic phenomena.

An example of a beam transfer function is shown in Fig. 20. Notice how the phase jumps by 180° as the excitation is applied either side of the central betatron tune frequency. Such a response is typical for any harmonic oscillator.

This 180° phase jump is the basis for a Phase-Locked Loop (PLL) tune tracker. Its basic principle is sketched in Fig. 21. A voltage or numerically controlled oscillator (VCO or NCO) is used to put a harmonic excitation $A \cdot \cos(\omega t)$ onto the beam. The beam response to this signal is then observed using a position pick-up. The response is of the form $B \cdot \cos(\omega t + \phi)$, where A and B is the amplitude of the excitation and oscillation respectively, ω is the tune expressed as angular frequency and ϕ is the phase difference between the excitation and the observed beam response. In the phase detector both signals are multiplied, resulting in a signal of the form

$$\tfrac{1}{2} \cdot A \cdot B \cdot \cos(\phi) + \tfrac{1}{2} \cdot A \cdot B \cdot \cos(2\omega t + \phi)$$

which has a DC component proportional to the cosine of the phase difference. This DC component is therefore zero when the phase difference is 90° which, as can be seen in Fig. 20, is when the amplitude response has a maximum, i.e. at the tune frequency. The aim of the PLL is therefore to "lock-in" to this 90° phase difference between excitation and observed signal by correcting the VCO frequency until the DC component of the phase detector output is zero. Since the PLL always tries maintaining this 90° phase difference, the VCO frequency tracks any tune changes, resulting in a continuous tune measurement.

In practice the PLL tracker operation is influenced by many parameters, which have to be optimised so that the PLL finds, locks-in and subsequently tracks the tune changes. The beam spectra and dynamics have to be well understood if the PLL is not to lock or jump to a synchrotron sideband or an interference line. In addition, for hadron machines, the continuous excitation required leads to emittance blow-up.

PLL tune tracking has been used on many machines, and is the basis upon which simultaneous feedback on tune, chromaticity and coupling was made possible at the Relativistic Heavy Ion Collider (RHIC) Brookehaven National Laboratory (USA) [16].
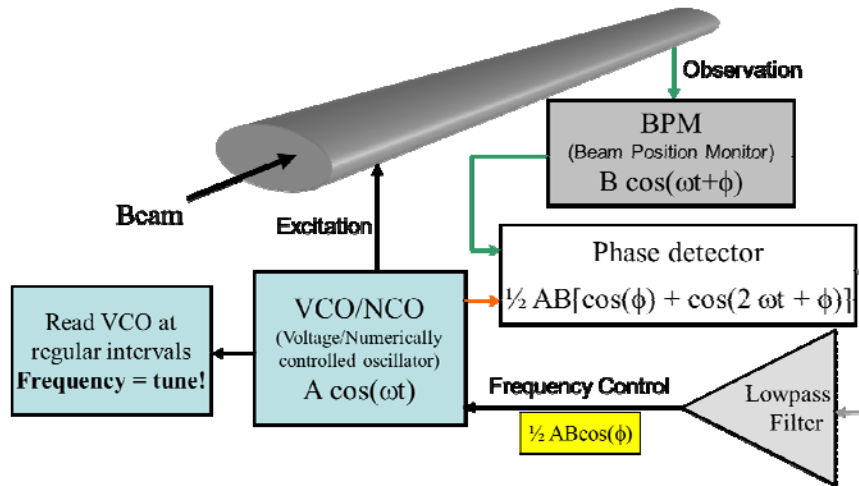

Fig. 21: Principle of a phase locked loop tune tracker

4.2 Chromaticity Measurement

For any high energy synchrotron, the control of chromaticity is very important. If the chromaticity is of the wrong sign (corresponding to positive below the transition energy or negative above it) then the beam quickly becomes unstable due to the head-tail instability. If the chromaticity is too big then the tune spread becomes large and some particles are inevitably lost as they hit resonance lines in tune space. The most common method of measuring the chromaticity of a circular machine is to measure the betatron tune as a function of the beam energy and then to calculate the chromaticity from the resulting gradient. This is usually done by varying the RF frequency, keeping the magnetic field static. The equations of interest are:

$$\Delta Q \;=\; (\xi Q)\frac{\Delta p}{p} \;=\; Q'\frac{\Delta p}{p} \;=\; Q'\gamma_t^2\frac{\Delta R}{R} \;=\; Q'\left(\frac{-\gamma_t^2\gamma^2}{\gamma^2-\gamma_t^2}\right)\frac{\Delta f}{f}$$

where ΔQ is the change in tune, $\Delta p/p$ the momentum spread (or relative change in momentum), $\Delta R/R$ the relative change in radius, $\Delta f/f$ the relative change in RF frequency, γ and γt the relativistic γ and γ at transition respectively, and ξ the chromaticity. Please note that the chromaticity, ξ, is often expressed as $Q' = Q\,\xi$, where Q is the total betatron tune including the integer part.

In the CERN-SPS, for example, a chromaticity measurement consists of performing a tune measurement for three different RF frequency settings. Instead of noting the exact RF frequency, what is actually measured is the change in closed orbit, from which the relative change in radius can be calculated. These three points are then plotted, with the gradient giving the chromaticity.

In order to obtain continuous chromaticity measurements this technique of RF modulation is combined with one of the tune measurement methods described in the previous section. By tracking the tune during this time and knowing the magnitude of the RF change, the chromaticity can be calculated and measured on-line.

4.3 Coupling Measurement

The control of coupling (the degree to which horizontal and vertical betatron motion is linked) is also important for circular accelerators. Excessive coupling will make tune and chromaticity measurements almost impossible, as the information from both planes are mixed-up in the observed signal. A very good and comprehensive summary of linear betatron coupling can be found in [17].
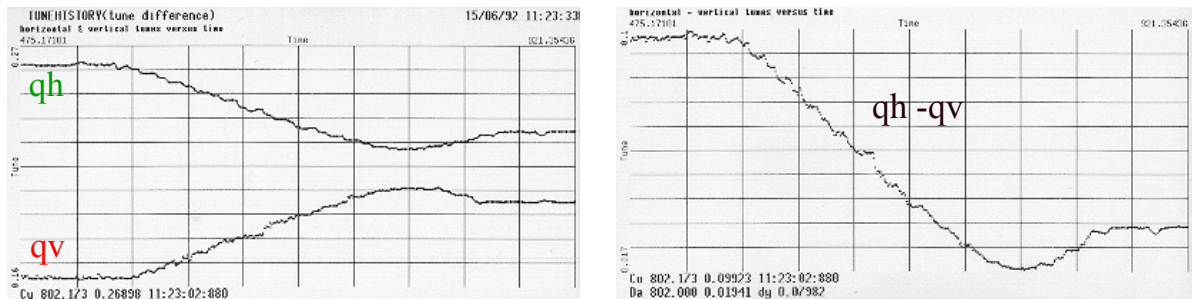
4.3.1 *Closest Tune Approach*

Fig 22: LEP coupling measurement

For this method, both betatron tunes are measured during a linear quadrupole power converter ramp which crosses the values of the horizontal and vertical tunes. The remaining separation of the tune

traces is a direct measure for the total coupling coefficient |c|. A measurement example from the CERN-LEP, using a phase locked loop tune measurement is shown in Fig. 22. In order to ensure that the PLL keeps tracking both tunes, even when they approach each other, the measurements are performed on two different bunches.

4.3.2 *Kick and PLL Methods*

The above method does not allow for diagnostics during machine transitions. A better tool for the measurement of small coupling coefficients, although demanding quite large beam excitations, consists of applying a single kick in one plane and observing the time evolution of the betatron oscillations in both planes. This method is described in [13].

Alternatively the PLL described in Section 4.1.3.2 can be used in a special configuration to measure both the amplitude and phase of the excitation seen in the other plane. This allows an on-line coupling measurement with minimal excitation and, in the presence of strong coupling, is essential for robust phase locked loop tune control [18].

5　Emittance Measurement

The ultimate luminosity of any collider is inversely proportional to the transverse emittance of the colliding beams. Preservation of emittance and hence emittance measurements are therefore of particular importance in the long chain of accelerators and storage rings of big hadron colliders as the emittance of a hadron bunch is not appreciably reduced through mechanisms such as the radiation damping associated with lepton machines.

In lepton machines, achieving the smallest possible vertical emittance is a common goal for damping rings for linear colliders, for particle factories based on the crab-waist collision scheme, and for light source storage rings providing photon beams of highest brightness. The measurement of such small emittance beams is therefore very important and is one of the main challenges for modern day beam instrumentalists.

Good explanations of emittance can be found in Refs [19,20]. The emittance which includes about 98% of the beam-particles can be defined as

$$\varepsilon(98\%) = \frac{beamwidth^2 - \left(\frac{\Delta P}{P} \cdot D_m\right)^2}{\beta_m} = \frac{FWHM^2 - \left(\frac{\Delta P}{P} \cdot D_m\right)^2}{\beta_m}$$

where FWHM is the measured full width at half height (2.35σ) of the beam, $\Delta P/P$ the FWHM of the momentum spread, D_m the value of the dispersion-function and β_m the value of the beta-function at the monitor position. From this equation one can immediately see that the measurement of emittance depends on many parameters. This limits the accuracy to which emittance can be calculated, which is generally with a precision no better than around 10%. A number of instruments are capable of measuring the beam profile quite precisely, but in calculating the emittance one also relies on knowledge of the beam optical parameters at the position of the instrument and these are often fraught with considerable uncertainties.

The remainder of this section is devoted to the measurement of beam size from which the emittance is then calculated.

5.1 Scintillator and Optical Transition Radiation Screens

Scintillator screens have been used for nearly a century and are the simplest and most convincing device when one has to thread a beam through a transfer line and into and around an accelerator. The modern version consists of a doped alumina screen which is inserted into the beam and can stand high intensities and large amounts of integrated charge. In its simplest form a graticuled screen is observed using a TV-camera. It can deliver a wealth of information to the eye of an experienced observer, but only in a semi-quantitative way. Much can be done about that with modern means of rapid image treatment, but questions concerning the linearity of these screens at high beam densities remain.

(OTR) screens are a cheap substitute for scintillator screens. OTR radiation is generated when a charged-particle beam transits the interface of two media with different dielectric constants (e.g. vacuum to metal or vice versa) [21]. Since this is a surface phenomenon, the screens can be made of very thin foils which reduces beam scattering and minimises heat deposition. The radiation produced is emitted in two cones around the angle of reflection for backward (vacuum to metal) OTR so that if the foil is placed at 45° to the beam direction, the radiation produced is at 90° to the beam direction. In addition two cones of forward OTR (metal to vacuum) are produced around the beam direction (see Fig. 23). The angular distribution of the emitted radiation has a central hole and a peak located at $1/\gamma$. The higher the value of γ the sharper the peaks and the more light can be collected, which is why OTR is generally suited to lepton or high energy hadron machines. However, the experience from modern, Linac based, 4th generation light sources (free electron lasers, FELs) shows that OTR diagnostics fail because of coherence effects in the OTR emission process. As a consequence such machines have reverted to the use of scintillating screen monitors for transverse beam profile measurements, with additional effort to reach high resolution imaging [22].
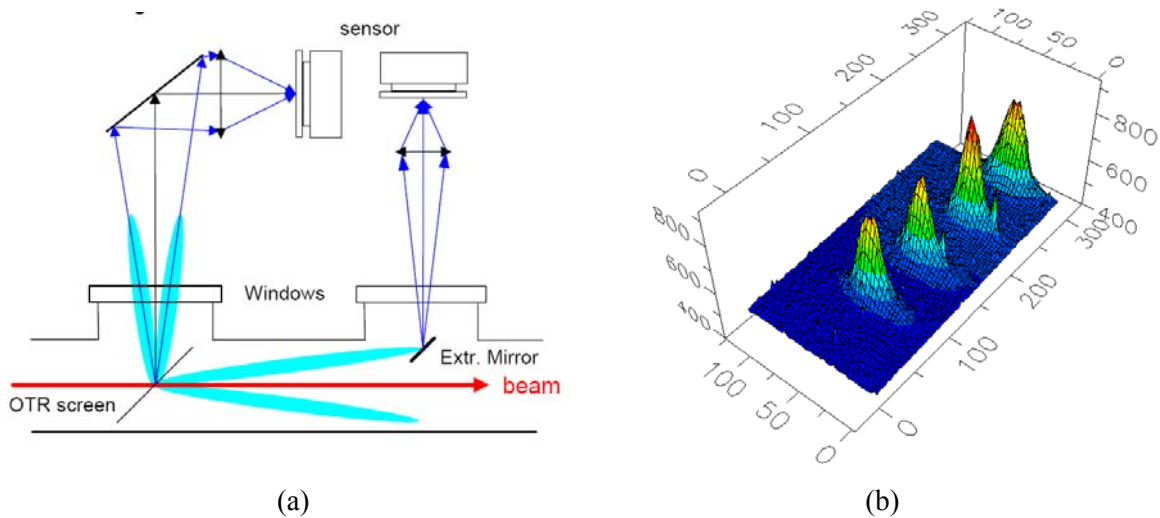

(a)   (b)

Fig. 23: (a) Backward and forward OTR patterns with their imaging schemes.
(b) Example of 2D OTR images taken every four turns at injection in the CERN-SPS.

5.2 SEM-Grids

Secondary Emission (SEM) Grids, also known as harps, consist of ribbons or wires which are placed in the beam. As the beam intercepts the grid, secondary emission occurs, leading to a current in each strip which is proportional to the beam intensity at that location. By measuring this current for all strips a beam profile is obtained. SEM-grids are the most widely used means to measure the density profile of beams in transfer lines and low energy hadron linacs. In addition, sets of three, properly spaced (i.e. with the right phase advance between monitors), allows a determination of the emittance ellipse. What makes them popular is their simple and robust construction, the fact that there is little doubt about the measured distribution, and their high sensitivity, in particular at low energies and for

ions. At higher energies they can be considered semi-transparent. Amongst their drawbacks are the limited spatial resolution (difficult to get the wire spacing much below 0.25mm) and the rather high cost for the mechanisms and electronics.

5.3 Wire Scanners

Of all the instruments used for measuring the emittance of circulating beams, wire-scanners are considered to be the most trustworthy. They come in two different types; rotative and linear. Rotative wire scanners consist of a thin wire (some tens of microns in diameter) mounted on a fork which is attached to a rotating motor (see Fig. 24), while linear scanners use motors which push/pull the wire across the beam. There are two ways of obtaining a beam profile with wire scanners; by measuring the secondary emission current as a function of wire position (similar to the SEM-grid acquisition mentioned above) or by measuring the flux of secondary particles created as the beam interacts with the wire. The latter technique is often used for high intensities, where the heating of the wire produces thermal emission which falsifies the secondary emission results. It relies on the use of radiation detectors, typically scintillators followed by photo-multipliers, placed downstream of the wire scanner to detect the γ-radiation and secondary particles produced when the wire intercepts the beam. To make the flux collected independent of the beam position may require the summation of the signals from two or more detectors positioned around the beam chamber.

Fast wire scanners are nearly non-destructive and can be used over a wide range of energies. Their spatial resolution can reach the micrometre range and, with fast gated electronics, can provide the profile of individual bunches. Their great sensitivity also allows them to be used for the study of beam halos.
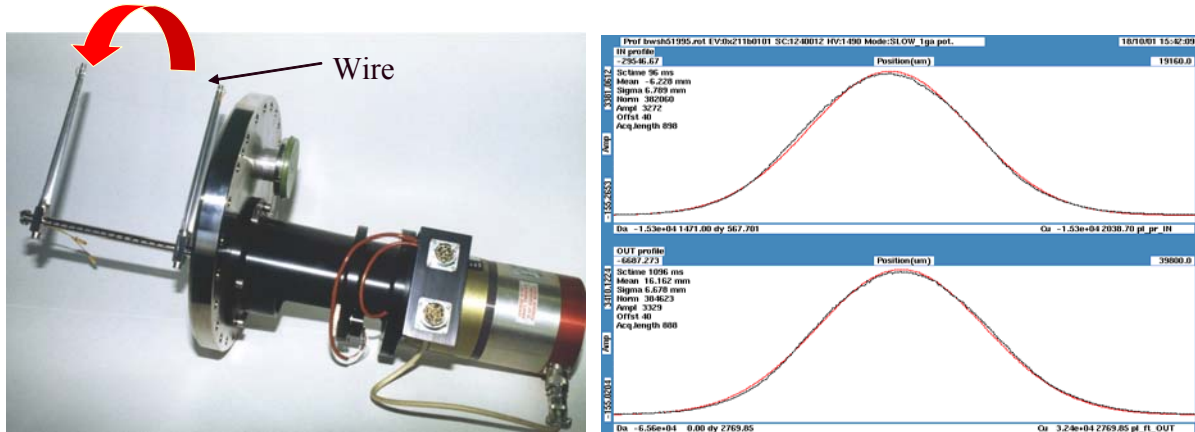
Fig. 24: Rotative wire scanner and an example of a wire scanner profile measurement.

5.4 Residual Gas Monitors

5.4.1 *Ionisation Profile Monitors*

Ionisation profile monitors are used in many high energy accelerators in order to reconstruct transverse beam distributions (see e.g. Ref. [23]). The signal results from the collection of either the ions or the electrons produced by the beam ionising the small amount of residual gas in the vacuum chamber. These ions or electrons are accelerated using a bias voltage of several kilovolts and collected on a micro channel plate (MCP). The avalanche of electrons produced by the MCP then either hits a phosphor screen, giving an image of the beam profile which can be monitored using a CCD camera (see Fig. 25), or impinges on a strip detector which can be read-out to give a profile. Due to their

22

rigidity, ions are less sensitive to the distorting effects of the space charge from the circulating beam, but their slow drift time, even with high bias voltages, means that they spend a long time in this beam field, making it difficult to analyse rms beam dimensions smaller than one millimetre. In order to use electrons to produce an image, a transverse magnetic field needs to be added, around which the electrons spiral on their way to the MCP. This eliminates, to a large extent, the space charge effects of the beam and allows sharper images to be produced than with ions. This additional magnetic field, however, is also seen by the beam and has to be compensated by corrector magnets either side of the ionisation profile monitor.
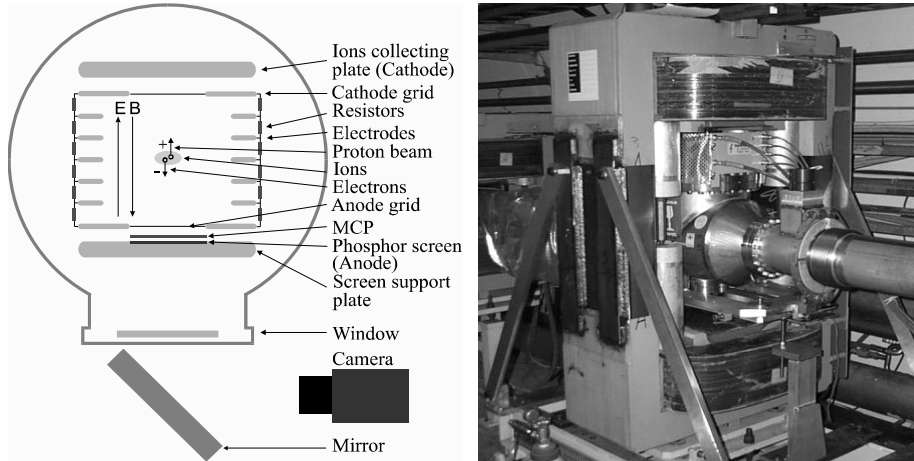

Fig. 25: Principle of a residual gas ionisation profile monitor and an example from the CERN-SPS

5.4.2   *Luminescence Monitors*

Luminescence monitors (see e.g. Ref. [24]) also rely on the interaction of the beam with a gas in the vacuum chamber. The traversing beam excites electrons in the gas molecules from the ground state to a higher energy level. Once the beam has passed the electrons return to the ground state and emit photons of a precise wavelength. In the case of nitrogen the dominant photon wavelength is 391.3 nm, corresponding to light at the lower end of the visible range, for which many detectors are available. In general, the residual gas alone does not produce enough photons for accurate imaging and hence a local pressure bump is usually created by injecting a small amount of gas to enhance the photon production. The principle of luminescence monitoring and a schematic layout of such an instrument are shown in Fig. 26.
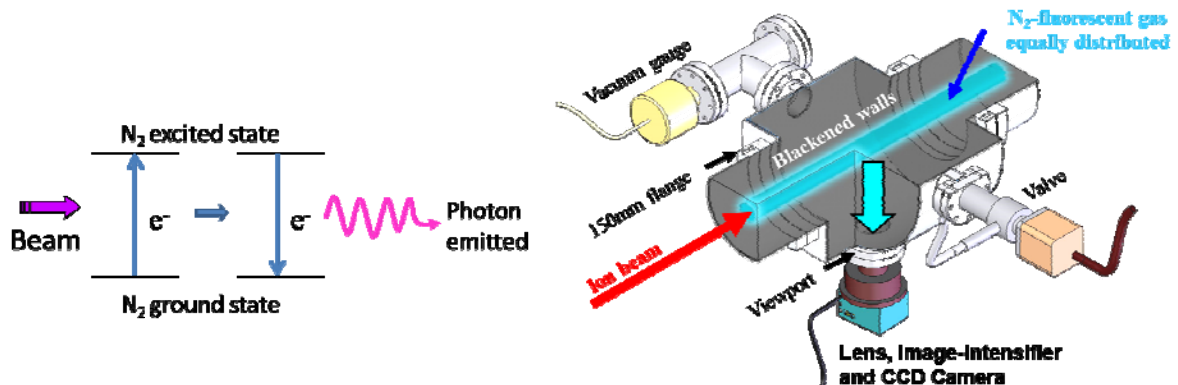

Fig. 26: Principle of luminescence monitoring and an example set-up

Most users consider both the residual gas ionisation and luminescence profile monitors to be semi-quantitative and not be relied upon for absolute emittance measurements, even after calibration against some other instrument such as a wire scanner. Their virtual transparency for the beam, however, make them useful for the continuous on-line tracking of beam size.

5.5   Synchrotron Radiation Monitors

Synchrotron radiation monitors are limited to highly relativistic particles and offer a completely non-destructive and continuous measurement of the 2-dimensional density distribution of the beam. These monitors make use of the light produced when highly relativistic particles are deflected by a magnetic field. They are therefore usually positioned to make use of parasitic light produced by a dipole magnet in the machine or behind a purpose built "wiggler" or "undulator" magnet in which the beam is deflected several times to enhance the photon emission.

The most common way of measuring the beam size with synchrotron radiation is to directly image the extracted light using traditional optics and a camera. The spatial resolution for such systems is usually limited by diffraction and depth-of-field effects. If the beam is sufficiently relativistic then the photon emission extends into the hard X-ray region of the spectrum and X-ray detectors can be used, for which diffraction effects can be almost disregarded. High brilliance 3rd generation synchrotron light sources use special X-ray optics (e.g. pinhole, compound refractive lens, coded aperture, Fresnel zone plate, …) to achieve the required resolution ($\approx$ 1 micron) for their small beam sizes. A way to overcome the resolution limits in the optical range is to use interferometry or point spread function analysis of the π-polarization of the visible synchrotron light [25,26].

6   Beam Loss Monitoring

Beam loss monitors (BLMs) have three main uses in particle accelerators:

- **Damage prevention** - Beam loss may result in damage to accelerator components or the experimental detectors. One task of any BLM system is to avoid such damage. In some accelerators it is an integral part of the protection system, signalling the beam abort system to fire if a certain loss rate is exceeded. This is of vital importance to the new generation of superconducting accelerators, for which even fairly small beam losses in the superconducting components can lead to magnet quenches.
- **Diagnostics** - Another task of BLM systems is to identify the position (and time) of unacceptable beam losses and to keep the radiation level in the accelerator and its surroundings as low as possible.
- **Luminosity optimisation** - BLMs can also help in the tuning of the machine in order to produce the long lifetimes necessary for improved luminosity.

The job of the BLM system is to establish the number of lost particles at a certain position within a specified time interval. Most BLM systems are mounted outside the vacuum chamber, so that the detector normally observes the shower caused by the lost particles interacting in the vacuum chamber walls or in the materials of the magnets. The number of detected particles and the signal from the BLM should be proportional to the number of lost particles. This proportionality depends on the position of the BLM with respect to the beam, the type of lost particles and the intervening material. It also, however, depends on the momentum of the lost particles, which may vary by a large amount during the acceleration cycle. One has to distinguish between two types of losses:

- **Fast losses** – where a large amount of beam is lost in a very short time.
- **Slow losses** – where partial beam loss occurs over some time (circular machines) or distance (LINAC, transport lines).

In storage-rings, the lifetime is defined by slow losses. There are many reasons for these losses and a BLM system is very helpful for finding out what is happening in the machine. In superconducting accelerators a BLM system can also prevent beam loss induced quenches caused by these slow losses.

The fact that BLM systems have to cover both of these cases means that they are required to function over a very large dynamic range, typically in the region of $> 10^6$.

6.1 Long Ionisation Chambers

In 1963, Panowsky [27] proposed a BLM system for SLAC which consisted of one long (3.5 km) hollow coaxial cable filled with Ar (95%) + CO_2 (5%), mounted on the ceiling along the LINAC, about 2m from the beam (PLIC). When a beam loss occurs, an electrical signal is produced which propagates to both ends of the cable. Position sensitivity is achieved by comparing the time delay between the direct pulse from one end and the reflected pulse from the other. The time resolution is about 30ns (~ 8 m) which, for shorter versions, can be reduced to about 5ns. This principle of space resolution works for linear accelerators and transport lines with a bunch train much shorter than the machine and with relativistic particles. For particles travelling significantly slower than the signal in the cable the resolution of multiple hits in the cable becomes difficult. In this case, and for circular machines, it is necessary to split the cable. Each segment has to be read out separately, with a spatial resolution which becomes approximately equal to their length.

6.2 Short Ionisation Chambers

Short ionisation chambers are used in many accelerators (see e.g. Ref. [28]). They are more or less equally spaced along the accelerator with additional units at special positions such as aperture restrictions, targets, collimators, etc. The chamber provides some medium with which the secondary particles created by the beam loss can interact, typically a gas such as nitrogen or argon. This interaction produces electron-ion pairs which are collected by a series of high voltage gaps along the length of the chamber. The resulting current is then measured and is proportional to the beam loss at the location of the monitor. An example of a CERN-LHC ionisation chamber is shown in Fig. 27.
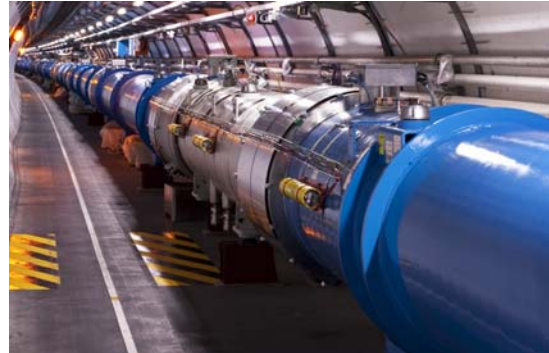
Fig. 27: A CERN-LHC ionisation chamber used for beam loss monitoring

6.3 Scintillation Counters

In the case where losses occur in a machine without a full BLM system, a plastic scintillator with photomultiplier readout is often temporarily installed. Such systems have a well-known behaviour, but the radiation damage of the plastic scintillator restricts their long term use. Liquid scintillators are not susceptible to such damage and have been installed in some accelerators [29, 30]. Such BLMs can be very fast, with pulse rise times of around 10ns, but suffer from drift in the photomultiplier gain.

25

6.4   Aluminum Cathode Electron Multipliers

In such detectors the sensitivity of photomultipliers to ionising radiation is increased by replacing the photocathode with an aluminium foil. This foil then works as a secondary electron emitter when irradiated. A BLM system consisting of Aluminum Cathode Electron Multipliers (ACEMs) is installed in the CERN-PS and PS-Booster [31]. It is very fast, with signal rise times in the order of 10ns, but is rather expensive since the ACEM is not a standard tube of photomultiplier manufacturers.

6.5   PIN Photodiodes

For circular electron accelerators, which emit hard synchrotron radiation it is difficult to distinguish between the beam loss distributions and the synchrotron radiation background using traditional BLM techniques. In DESY-HERA, an electron-proton collider, the warm electron and a superconducting proton rings were in the same tunnel. Protection of the superconducting proton beam magnets from beam loss induced quenches therefore relied on a BLM system which saw only the proton beam losses and not the synchrotron radiation background. In this case back to back PIN photodiodes were used to distinguish between the hadronic shower created by beam losses and the synchrotron radiation [32]. The charged particles interacted with both photodiodes, giving a coincidence signal, while the photons were absorbed by the first diode. In contrast to the charge detection of most other BLM systems, PIN photodiode detection depends on counting coincidences, with the count rate proportional to the loss rate so long as the number of overlapping coincidences is small.

6.6   Optical Fibres

Cherenkov light created in long optical fibres can be used in the same way as a single long ionisation chamber to reduce the costs of a BLM system while maintaining full coverage. It allows real time monitoring of loss location and loss intensity as for PLICs (section 6.1).
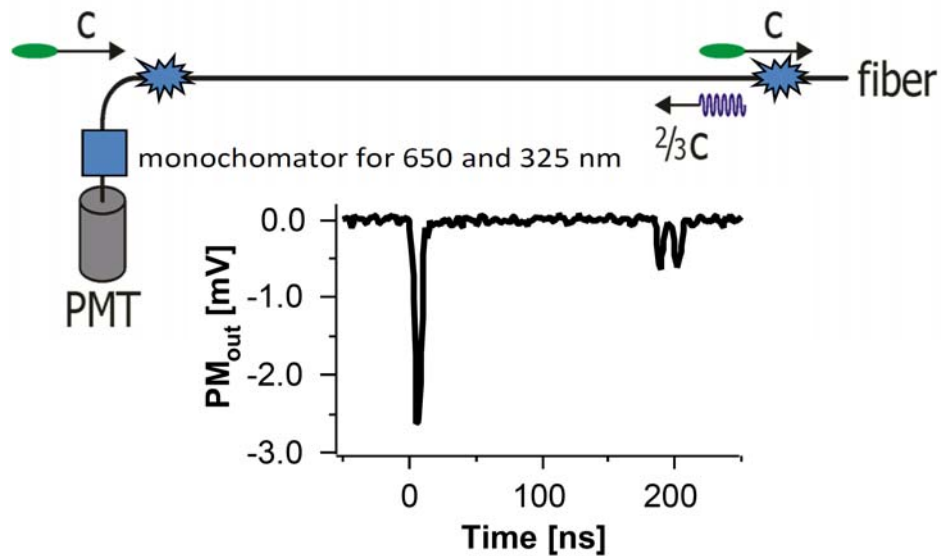
Fig. 28: A time measurement provides the position of the beam loss along the fibre while the amplitude gives the amount lost. Due to dispersion, the emission at 650 nm reaches the photodetector earlier than the emission at 325 nm, thus producing the double peak (Tesla-Report 2000-27).

A Cherenkov detector is nearly insensitive to X-rays because the Cherenkov effect only occurs when the velocity of a charged particle traversing a dielectric medium is faster than the speed of light in that medium. The fast response of the Cherenkov signal is detected with photomultipliers at the end of the irradiated fibres (Fig 28). A time measurement provides the position of the loss along the fibre while the integrated light is proportional to the size of the loss. A longitudinal position resolution of 20 cm

(= 1ns at v = 0.66c) is possible with this technique. High purity quartz fibres (Suprasil®) are often used for such installations as they only produce Cherenkov emission (no scintillation) and are radiation hard, capable of withstanding tens of MGy of irradiation. Scintillating fibres, on the other hand, give about 1000 times more light output but are much more sensitive to radiation damage.

7 Longitudinal profile diagnostics

The time structure of a charged particle beam is related to the characteristics of the accelerating field. Electrostatic accelerators produce DC particle beams that have no variation in time. Radio-Frequency (RF) accelerators generate beams with a time structure defined by the frequency of the electromagnetic field in use. Nowadays RF accelerators may operate at frequencies up to tens of Gigahertzs, which means that particle bunches can naturally be as short as a few picoseconds or less. For some applications, such as Free Electron Lasers or TeV Linear Colliders, the bunch length is further compressed down to 10-100 femtoseconds. Moreover, since the late 1990's, the use of ultra-short intense laser pulses has contributed to the development innovative acceleration schemes such as Laser Plasma Wakefield Acceleration (LPWA). Here the accelerating field is generated by the interaction of a laser beam with a gas cell. The resulting plasma wave has a very high electric field that may oscillate at frequency up to Terahertzs with the corresponding bunch length in the order of a few femtoseconds.

In order to measure the longitudinal structure of particle beams, many different instruments have been developed during the last three decades. They can be regrouped into four different categories:

- **Direct Beam Observation**, where the longitudinal structure of the beam is measured by means of fast detectors.

- **Detection of Coherent Radiation**, where the bunch length can be retrieved by measuring the radiated power spectrum for wavelengths of the order or longer than the bunch length.

- **Radio Frequency Manipulation**, where the longitudinal beam profile is encoded into the modulation of its transverse spatial profile.

- **Sampling Techniques**, where a short laser pulse is used to scan through the longitudinal bunch profile.

7.1 Direct Beam Observation

For relatively long bunches, the beam time structure can be measured using Wall Current Monitors (WCMs) [33] and fast sampling oscilloscopes. WCMs have already demonstrated bandwidths in excess of 10GHz and state of the art oscilloscopes are improving their performance every year with sampling rates as high as 80GSa/s now available. To provide even better time resolution optical methods need to be used. An optical replica of the longitudinal beam distribution must first be generated through the use of synchrotron radiation, transition radiation, diffraction radiation, or Cherenkov radiation, with the corresponding light pulses measured by an appropriate detector.

7.1.1 *Single photon counting*

A way of providing both time resolution in the order of tens of picoseconds and a high dynamic range is through the use of time-correlated single-photon counting [34]. This principle is illustrated schematically in Fig. 29. The system is well adapted to ring accelerators, where each particle bunch passes the detector once every revolution with the light attenuated such that on average less than one photon reaches the detector per bunch passage. The detector typically used is an avalanche photodiode (APD) which produces an electrical pulse when it detects an incoming photon. This is time-stamped by a time-to digital converter (TDC) and a histogram of arrival times is created. In order to construct a

meaningful bunch profile the data have to be collected over thousands of turns. The longer the acquisition, the more counts are added to the histogram and the higher the dynamic range of the measurement.
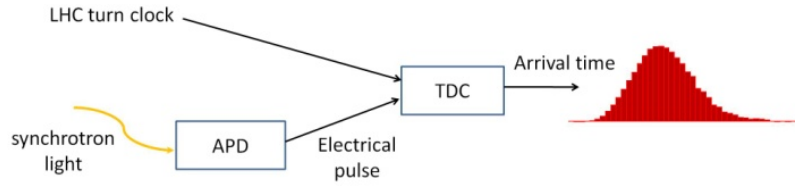

Fig 29: Schematic of a single photon counting longitudinal density monitor

An example of a typical profile measured on the Large Hadron Collider at CERN is shown in Fig. 30, illustrating the large dynamic range that can be achieved when applying all the appropriate signal corrections. A long integration time of several minutes is necessary in order to make a high-dynamic range profile showing small satellites at the 10^{-4} level of the main bunches.
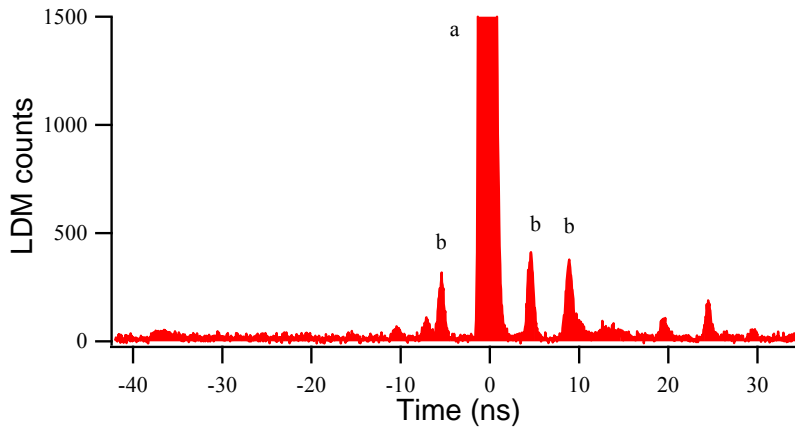

Fig. 30: Longitudinal density measurement in the LHC showing a main proton bunch (a) with peak at 1.3×10^5 counts and small satellite bunches (b).

7.1.2 *Streak Camera*

Another very popular method to measure longitudinal bunch profiles using optical signals relies on the use of streak cameras [35]. In order to achieve a good time resolution, the photons from the radiation to be analysed are converted to electrons, which are then accelerated and deflected using a ramped, time-synchronised, High Voltage (HV) electric field, as shown in Fig. 31. The signal from the electrons is subsequently amplified with a micro channel plate (MCP), converted to photons via a phosphor screen and finally detected using an imager such as a CCD array. In this way the time variation of the intensity of the incoming photon pulse, which is a replica of the longitudinal bunch profile, is converted into a spatial intensity variation. The time resolution of a streak camera is limited by the transverse size of the collimation slit, the initial velocity spread of the photo-electrons and the dispersion of the optical system. State of the art streak cameras can provide a time resolution better than 500 femtoseconds.
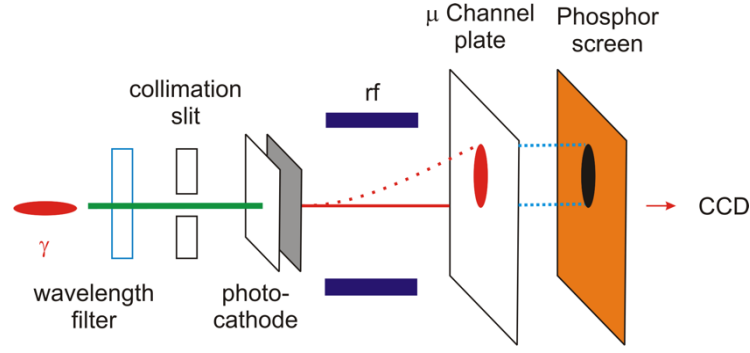
28

Fig. 31: Principle of the streak camera

7.2 Coherent Radiation

For wavelengths shorter than the bunch length, the particles within the bunch radiate incoherently, with the power emitted proportional to the number of particles. However, for wavelengths equal to or longer than the bunch length, the particles emit radiation in a coherent way with the emitted power dependent on the bunch length and scaling as the square of the number of particles. This can be described by the following equations:

$$\underset{\Downarrow}{incoherent\ term}\quad \underset{\Downarrow}{coherent\ term}$$

$$S(\omega) = S_p(\omega)\left[N + N(N-1)F(\omega)\right] \qquad F(\omega) = \left|\int_{-\infty}^{\infty} \rho(s)\, e^{-i\frac{\omega}{c}s}\, ds\right|^2$$

where $S(\omega)$ represents the radiation spectrum, $S_p(\omega)$ the single particle spectrum, N the number of particles and $F(\omega)$ the longitudinal bunch form factor, which depends on the longitudinal particle distribution $\rho(s)$.

Measuring the power spectrum therefore allows the form factor to be calculated from which an indirect estimate of the bunch length is possible. This method is relatively simple to implement and has already demonstrated its capacity for the measurement of extremely short bunches.
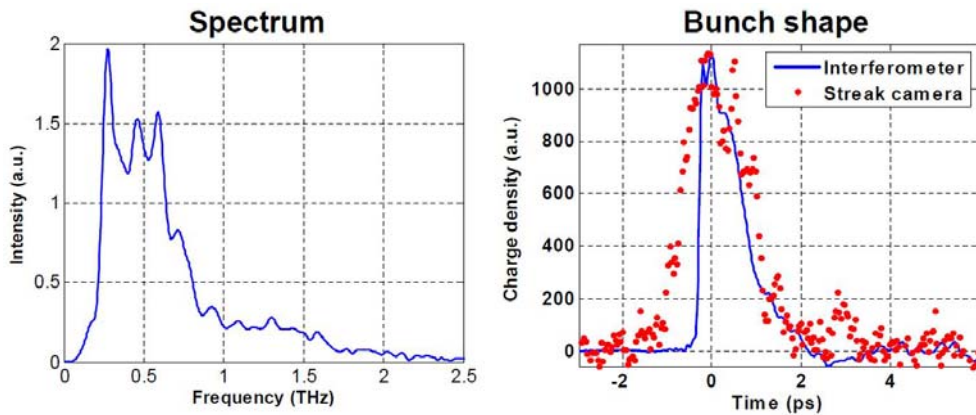

Fig. 32: Measured coherent synchrotron radiation spectrum (left) and reconstructed bunch shape (right)

The advantage of coherent radiation monitors is that their resolution does not have any theoretical limit. What is obtained, however, is the form factor rather than the longitudinal distribution. In order to

reconstruct the longitudinal bunch profile it is necessary to perform an inverse-Fourier transformation using phase recovery algorithms making use of the Kramers-Kronig relation.

The detection can be based on an autocorrelation technique using either Michelson or Martin-Puplett interferometers. Scanning the interferometer over the frequency range of interest allows a measurement of the radiated power spectrum, $S(\omega)$, from which the longitudinal bunch profile can be reconstructed. An example of such a measurement performed on the Flash FEL facility at DESY [36] is depicted in Fig. 32 showing the measured power spectrum and the reconstructed bunch profile compared with a streak camera measurement. Single-shot measurement devices have also been developed using gratings combined with a large array of detectors [37].

7.3 Radio-frequency manipulations

The principle of Radio-Frequency manipulation techniques is to encode the longitudinal structure of the beam into spatial information, which is easier to measure. Two such techniques, a bunch shape monitor for hadron Linacs and an RF deflecting cavity for Free Electron Lasers (FEL) or e^+-e^- Linear Colliders, are described below.

7.3.1 *Bunch Shape Monitor*

For non-relativistic beams ($\beta<<1$) the electromagnetic field of a bunch is not purely transversal and therefore does not represent its longitudinal charge distribution. Hence a bunch shape monitor based on secondary emission has been developed to measure the longitudinal bunch profile in a non-invasive way [38]. These monitors are used in many proton, H$^-$ and ion Linacs. Their principle of operation is presented in Fig. 33.

Configuration of Bunch Shape Monitor (1 - target, 2 - input collimator, 3 - rf deflector combined with electrostatic lens, 4 - output collimator, 5 – bending magnet, 6 – collimator, 7 – Secondary Electron Multiplier).
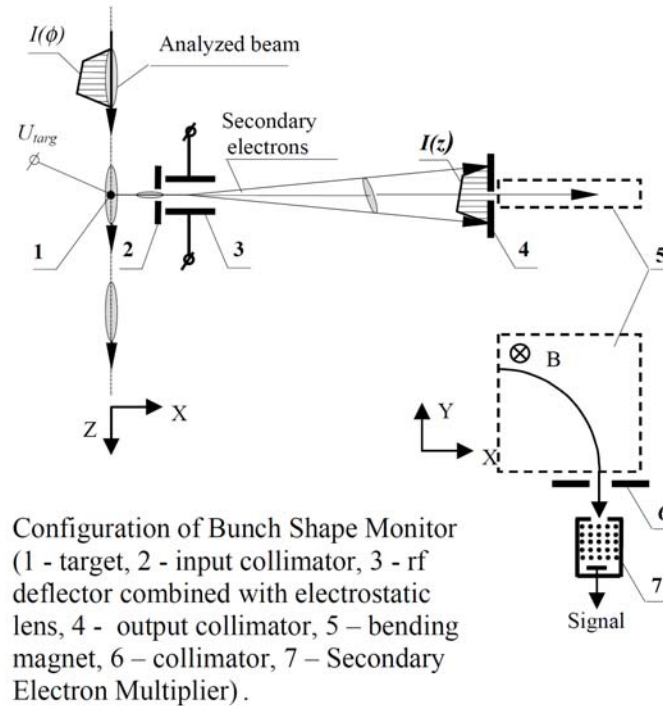
Fig. 33: Principle of operation of the Bunch Shape Monitor

As the beam hits a thin metal wire, low energy secondary electrons of a few eV are released almost instantaneously. These electrons are quickly accelerated away by applying a negative bias voltage ($U_{targ} \approx$ -10 kV) on the wire. The secondary electron beam is then collimated and deflected by a time-varying transverse RF field. Similar to the principles behind the streak camera, the arrival time of the

electrons is thereby transformed into a spatial distribution that can be measured by various detectors, such as a phosphor screen coupled to a CCD camera, a multichannel electron detector or a scanning slit and collector. State of the art BSMs have achieved resolutions in the order of some 10 ps.

In the special case of an H⁻ beam, the detached electrons originating from the dissociation of the H⁻ ions on the target wire contribute to the background signal. Energy separation by an additional spectrometer behind the second slit can be used to reduce this background enabling measurements of the longitudinal halo with a dynamic range of 10^5.

The energy deposition of the beam in the wire must remain small in order to avoid the creation of thermal electrons and ultimately the melting of the wire. This clearly imposes operational limitations when using a BSM with high charge beams.

7.3.2 *RF Deflecting Cavities*

The principle of operation of a longitudinal bunch profile monitor using an RF deflecting cavity [39] is shown in Fig. 34.
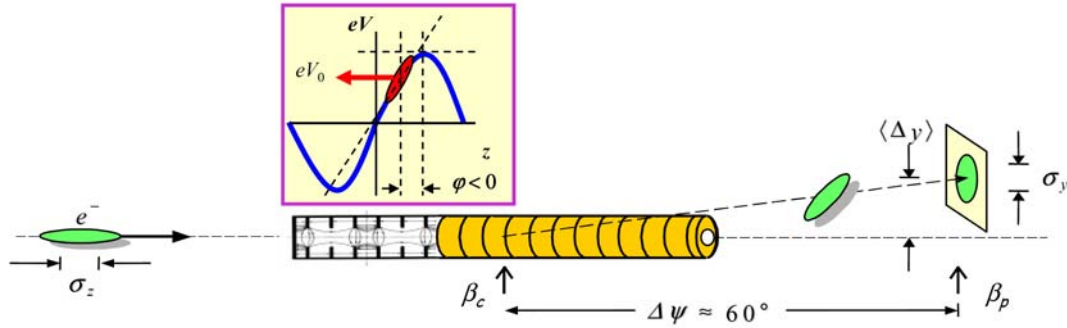

Fig. 34: Principle of operation of a longitudinal bunch profile monitor using an RF deflector

Again the idea is to transform a longitudinal bunch distribution into a transverse distribution. The cavity is designed to provide a time-varying deflecting field. By adjusting the arrival time of the bunch with respect to the phase of the electric field, the particles will experience different transverse kick strengths depending on where they are located along the bunch. By measuring the transverse beam size downstream, one can then reconstruct the longitudinal bunch profile. Assuming a deflection in the vertical plane, the vertical beam size σ_y can be expressed as follows:

$$\sigma_y = \sqrt{\sigma_{y_0}^2 + \sigma_z^2 \beta_c \beta_p \left(\frac{2\pi}{\lambda} \frac{eV_0}{E_0} \sin(\Delta\Psi)\cos(\varphi) \right)^2}$$

with σ_{y0} the vertical beam size measured on the screen when the deflector is turned off, σ_z the bunch length, β_c and β_p the beta-function at the position of the cavity and the screen respectively, $\Delta\psi$ the betatron phase advance between the cavity and the screen, λ the RF cavity wavelength, V_0 the RF voltage in the cavity, φ the phase of the RF field and E_0 the beam energy.

RF deflectors have demonstrated the capability of measuring very short bunches down to few femtoseconds but have the drawback of being destructive to the measured beam and having a very high cost.

7.4   Sampling techniques

Sampling techniques rely on the use of very short laser pulses. Over the past 15 years, several monitors have been tested using different processes such as electro-optic Pockel and Kerr effects [40]

or Compton scattering [41]. Whatever the physics process involved, these techniques always require laser pulses shorter than the particle bunch length and a precise laser-to-beam synchronization. Only the electro-optic techniques will be described in more detail here.

7.4.1 *Principle of electro-optic diagnostics*

The aim of electro-optic (EO) longitudinal diagnostics is to accurately measure the temporal profile of the Coulomb field of a relativistic particle beam using the optical non-linearity induced in an electro-optic crystal. This only provides an accurate replica of the longitudinal bunch profile for highly relativistic beams, where the accompanying Coulomb field has an opening angle much smaller than the bunch length. The coulomb field is probed by placing an electro-optic crystal adjacent to the particle beam (Fig. 35), with no need for the beam to traverse the crystal, making this a completely non-intercepting technique.
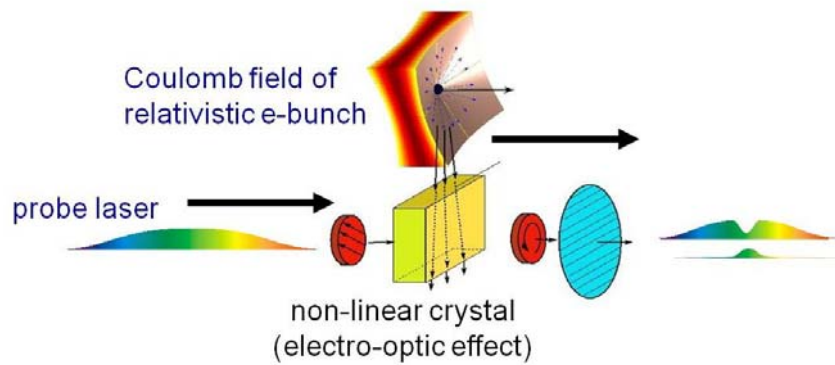

Fig. 35: Principle of electro-optic detection

The Coulomb field sweeping through the crystal renders the material bi-refringent during its transit. This birefringence is probed using a chirped (or sometimes ultra short) optical probe laser pulse that is passed through the crystal parallel to the particle beam axis in synchronism with the particle bunch. The bi-refringence results in a rotation of the polarization of the optical pulse. This can be sensitively detected using optical techniques to yield a temporal evolution of the Coulomb field, hence measuring the longitudinal charge density profile of the bunch.

7.4.2 *Encoding and Decoding Techniques*

The temporal resolution of the longitudinal profile obtained with EO detection depends both on the processes occurring within the non-linear crystal during the encoding, and by the method of decoding the temporal information from the resulting optical pulse. For all techniques the time resolution is also limited by the Lorentz factor of the particles, which dictates how faithful a reproduction of the bunch charge density profile the Coulomb field actually is. In practice, for the GeV electron beams for which such techniques are typically used, this is not a limitation.

The encoding limitations arise from the EO crystal response, and are best viewed as a frequency cut-off, rather than directly as a temporal resolution. For example, a 0.2 mm thick ZnTe crystal can efficiently detect frequencies up to 2.8 THz, while a similar thickness GaP crystal works up to about 8 THz. For ultra-short bunches with a frequencies above this cut-off, the resulting profile will no longer be an accurate reproduction of the traversing Coulomb field.

For decoding the information, the two techniques most widely used are spectral decoding and single-shot temporal decoding (Fig. 36). In both cases the optical pulse from an ultrafast laser is synchronized to the particle bunch train. Such an ultra-short pulse, by definition, contains a certain spread in wavelengths. This fact can be used to stretch the optical pulse, through the use of gratings or

dispersive media, so that it is longer than the bunch length to be measured, and has a time to wavelength correlation. The stretched laser pulse passes through a polarizer and is focused onto the electro-optic crystal. The bi-refringence induced in the EO crystal during the passage of the bunch is translated into a change in polarisation and subsequently, through the use of polarizers, into intensity modulation on the laser pulse.
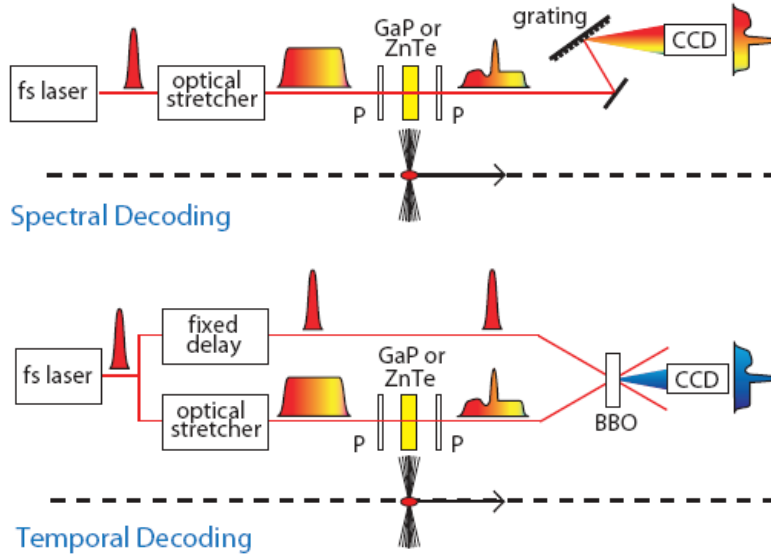

Fig 36: General layout for spectral decoding (top) and temporal decoding (bottom)

Spectral decoding makes use of the fact that there is a correlation between time and wavelength to resolve the bunch profile using a spectrometer, and can measure bunch lengths down to 500 fs.

For temporal decoding the laser beam is split into two, providing a probe and a gate pulse. The probe, as for spectral decoding, is stretched, polarized and focused onto the crystal. The resulting intensity modulated probe is then passed through a β-Barium Borate (BBO) crystal at the same time as the short gate pulse. By selecting the right angles of incidence the short gate pulse can be made to scan across the longer probe pulse within the BBO crystal, producing frequency doubled light with the same intensity profile as the probe.

Temporal decoding has significantly better time resolution capabilities than spectral decoding, and has been used to measure electron bunches shorter than 100 femtoseconds at DESY-FLASH (Fig. 37) [42]. However, the price to pay is the requirement for much higher laser power.
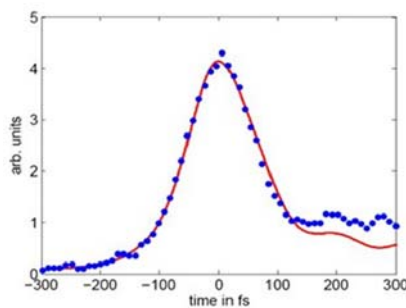

Fig. 37: Shortest measured electron bunch profile using temporal decoding at DESY FLASH. The optimum fitted Gaussian curve sigma is 79.3 ± 7.5 fs.

33

8 Some examples of beam diagnostics

This section is meant to serve as general entertainment for those readers who have made it this far! Two examples from CERN-LEP operation have been selected, and show how difficult it can be to interpret primary measurements and decide on the right actions for solving a problem in an accelerator.

8.1 The CERN-LEP beam does not circulate!

The LEP accelerator had a very regular operation schedule. Every year it was used for about 8 months for physics, followed by a 4 month maintenance and upgrade shutdown. During this shutdown major intervention work was sometimes carried out on the machine. At the next start-up it was often expected that typical problems, such as inverted magnet polarities, would have to be overcome. One year the start-up was particularly bad, with neither the electron beam nor the positron beam capable of being made to circulate. Several hours were devoted to checking all vacuum conditions, power supply currents, settings of the radio frequency system, injection deflectors and so on, but nothing indicated a severe problem. Finally people started to look in detail at the measured beam trajectory from the injection point onwards. A typical example for the positron beam is shown in Fig 38.
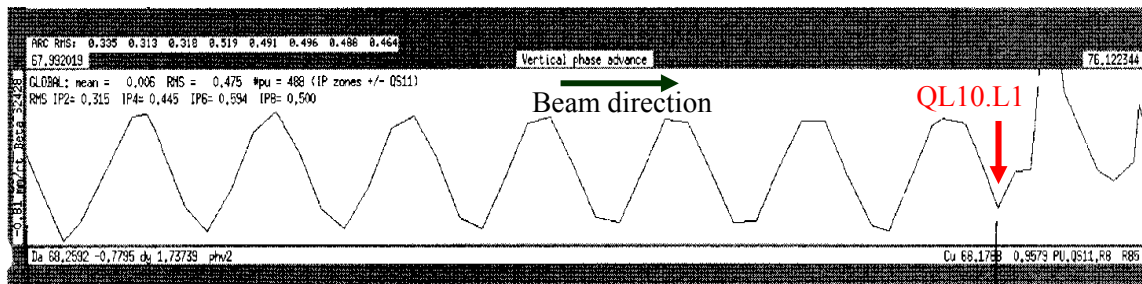
Fig. 38: Measurement of the LEP phase advance when beams did not circulate

What is actually shown in Fig. 38 is the phase advance from one beam position monitor to the next, as calculated from the measured beam trajectory. At a particular quadrupole (QL10.L1) the regular pattern is distorted. Additional measurements also indicated that most of the beam was lost at this point. The first conclusion was to suspect a problem with this quadrupole. People went in, measured the current in the quadrupole, checked its polarity, inspected its coils, but could not find anything abnormal.

Fig. 39: The mystery of the beam circulation problem in LEP is solved!

34

The indications of the beam measurements, however, clearly pointed to a problem at this location. After many discussions and potential hypotheses it was decided to open the vacuum chamber. It should be noted that this was a major intervention, causing a stop of the accelerator for at least one day. One can understand the surprise of the intervention team when they looked into the open vacuum chamber and saw a beer bottle!!! Duri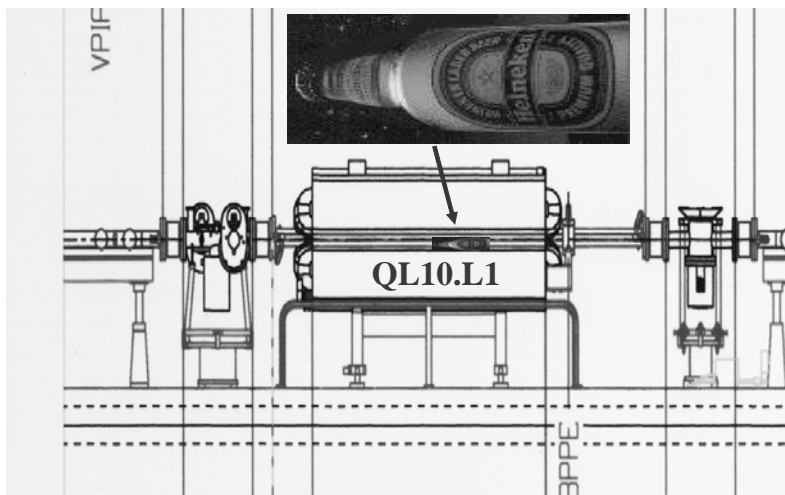ng the shutdown intervention, somebody had sabotaged the LEP accelerator and inserted a beer bottle into the beam pipe (Fig. 39)! What had upset the operation team most at the time was the fact that it was a very unsociable form of sabotage - the bottle was empty!

8.2   The beam gets lost during the beta squeeze

This again is one of the stories from LEP operation which took several hours using beam diagnostics to solve. The problem in itself is pretty complex, and therefore requires some additional explanations beforehand.

The acceleration of the particle beams and the change of the lattice function in the insertion regions in order to get smaller values of the beta-function at the crossing point (hence higher luminosity) are so-called "dynamic processes". The presence of the beam requires that all actions are well synchronised. For example, the power converters of all relevant magnetic circuits have to be controlled such that beam parameters such as the closed orbit, tunes and chromaticities stay within tolerance during the dynamic process. In order to achieve this, the behaviour of these beam parameters is periodically measured as a function of time and the corresponding power converter tables are updated.

During one period of LEP operation it was found that the beams were lost during the beta squeeze. Shortly before the total loss of the beams a significant beam loss was measured. As standard practice when encountering such problems, the engineer in charge (EIC) launched a new machine cycle with diagnostic facilities such as "tune history" (the measurement of the betatron tunes as a function of time – see Section 4) switched on. This indicated that the vertical tune moved out of tolerance during the beta squeeze. Fig. 40 shows an excerpt from the actual LEP logbook entry of this event.

Fig. 40: Excerpt from the LEP logbook when beams were lost during the beta squeeze

As a result of this observation, the EIC launched another cycle, but inserted a breakpoint (to stop the accelerator cycle) just before the critical moment in the beta squeeze when the deviation in tune occurred. Having reached that breakpoint the tunes were measured statically and found to be perfectly within tolerance. The beta squeeze was then executed step by step, and to the big surprise of the operations crew, the tunes were found to be correct at all times. The beam had passed the beta squeeze

35

like on an ordinary day! But on the next attempt, without a break in the cycle, the beam was again lost at the same moment, and several people scratched their heads to find an explanation.

Finally, the following measurement was made. The machine was prepared and a breakpoint again inserted just before the critical beam loss. Once this point was reached, the EIC requested the execution of one further step in the beta squeeze. The facility by which one could execute a single step in a dynamic process had the additional feature that one could specify the rate of current change of any machine element. This current rate limitation was changed from 5A/s (nominal) down to 2.5 A/s on consecutive steps. The corresponding tune history (the result from the vertical plane is plotted on the lower graph) is shown in Fig 41.
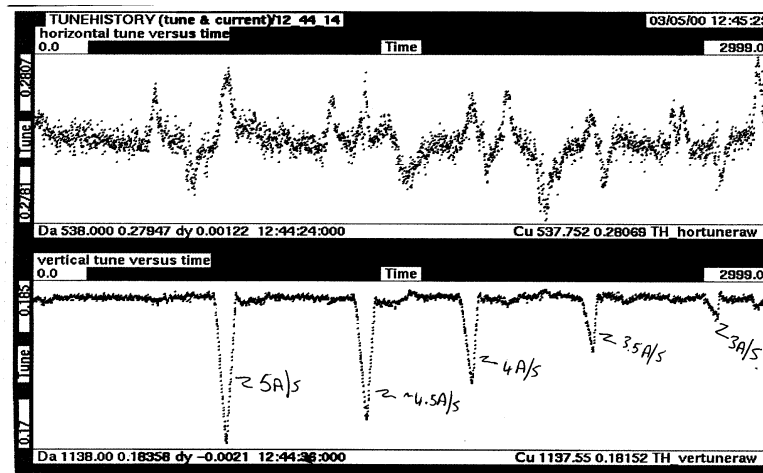

Fig. 41: The LEP tune history during the beta squeeze for various power converter ramp rates

One can clearly see that a huge (negative) tune excursion occurred when the step was executed at the nominal rate. This observation led the EIC to the right conclusion, which was that one of the power supplies was able to deliver the demanded current statically, but not dynamically. When this was discussed with experts from the power converter group, they indicated that the power supplies for the superconducting insertion quadrupoles were built as two blocks in series, each of them able to deliver the necessary current (each block typically 1000 A/10 V). Both of these blocks were required to have enough voltage margins to enforce a current change against the inductance of the quadrupole coil. This then explained the whole story. One of these blocks was faulty, but since the remaining working block could deliver its static current, it was not detected by an alarm or surveillance circuit. If the dynamic rate was too high, however, this single block could not provide enough current leading it to lose synchronism with the other power converters. This resulted in the large tune change observed and ultimately the total beam loss.

These two examples show the enormous potential of beam instrumentation if they are used in the right combination by intelligent people.

9   REFERENCES

[1]   CERN Accelerator School, Beam Diagnostics, Dourdan, France, 28 May – 6 June 2008, CERN–2009–005
[2]   D.A. Goldberg, G.R. Lambertson, "Dynamic devices : a primer on pickups and kickers ", US Part. Acc. School, 1991. AIP Conf. Proc., 249,1992.

36

[3] S. Walson, et.al., "Performance of a High Resolution Cavity Beam Position Monitor System," NIM-A, 578 (2007), pp. 1-22.

[4] S. T. Boogert, et.al., "Cavity Beam Position Monitor System for ATF2," IPAC'10, Kyoto, Japan, May 2010, MOPE070, pp. 1140-42 (2010).

[5] S. Smith, et.al., "LCLS Cavity Beam Position Monitors," DIPAC'09, Basel, Switzerland, May 2009, TUOC03, pp. 285-287 (2009).

[6] T. Nakamura, et.al., "High Resolution Cavity BPM for ILC Final Focus System (IP-BPM)," LCWS/ILC 2007, Hamburg, Germany, May/June 2007, arXiv:0709.2254v1, eConf C0705302.

[7] D. Cocq, "The Wide Band Normaliser : a New Circuit to Measure Transverse Bunch Position in Accelerators and Colliders", Nucl. Instrum. Methods Phys. Res., A 416 (1998) 1.

[8] G. Vismara, "Signal Processing for Beam Position Monitors", 9th Beam Instrumentation Workshop, BIW 2000, Cambridge, MA, USA , May 2000, AIP Conf. Proc. 546, pp36-60.

[9] V. Schlott, et.al., "First Operational Experience with the Digital Beam Position Monitoring System for the Swiss Light Source," EPAC'00, Vienna, Austria, June 2000, pp. 1809-11.

[10] H. Jakob et al., "A 40 MHz Bunch by Bunch Intensity Measurement for the CERN SPS and LHC", 6th European Workshop on Beam Diagnostics and Instrumentation for Particle Accelerators, DIPAC 2003, Mainz, Germany , May 2003.

[11] G. Bohner et al., "Very front-end electronics for the LHCb preshower", LHCb-2000-047, CERN, 2000.

[12] K. Unser, "A Toroidal DC Beam Current Transformer with High Resolution", IEEE Trans. Nucl. Sci.: 28 (1981) pp.2344-2346.

[13] H. Schmickler, "Diagnostics and Control of the Time Evolution of Beam Parameters", 3rd European Workshop on Beam Diagnostics and Instrumentation for Particle Accelerators, DIPAC '97, Frascati, Italy, Oct 1997.

[14] M. Gasior and R. Jones, "High Sensitivity Tune Measurement by Direct Diode Detection", 7th European Workshop on Beam Diagnostics and Instrumentation for Particle Accelerators, Lyon, France, 6 - 8 Jun 2005, pp.310

[15] M. Gasior, "Faraday Cup Award: High Sensitivity Tune Measurement using Direct Diode Detection", 15th Beam Instrumentation Workshop BIW2012, Newport News, VA USA, 15-19 April 2012, pp. 1-8, CERN-ATS-2012-246.

[16] M. Minty et al, "Simultaneous Orbit, Tune, Coupling and Chromaticity Feedback at RHIC", Proc. of PAC11, New York, NY (2011).

[17] P. Bryant, "A simple theory for weak betatron coupling", CAS, CERN 89-03, 1989.

[18] Jones, R ; Cameron, P ; Luo, Y, "Towards a robust phase locked loop tune feedback system", 7th European Workshop on Beam Diagnostics and Instrumentation for Particle Accelerators, Lyon, France, 6 - 8 Jun 2005, pp.296

[19] E. Wilson, "Transverse Beam Dynamics", CAS, CERN 85-19, Vol. 1, 1985.

[20] J. Buon, "Beam Phase Space and Emittance", CAS, CERN 91-04, 1991.

[21] J. Bosser et al., "Optical Transition Radiation Proton Beam Profile Monitor", CERN/SPS 84-17, (1984).

[22] Ch. Wiebers, et al., "Scintillating Screen Monitors for Transverse Electron Beam Profile Diagnostics at the European XFEL"; Proc. IBIC2013, Oxford, UK, 16-19 September, 2013.

[23] T. Giacomini, P. Forck, et al., "Ionization Profile Monitors - IPM @ GSI", Proc. DIPAC2011, Hamburg, Germany, 16-18 May, 2011.

[24] F. Becker, "Beam Induced Fluorescence Monitors", Proc. DIPAC2011, Hamburg, Germany, 16-18 May, 2011.

[25] S. Takano, "Beam Diagnostics with Synchrotron Radiation in Light Sources", Proc. IPAC'10, Kyoto, Japan, 23-28 May, 2010.

[26] A.S. Hernandez et al., "The New SLS Beam Size Monitor, First Results" Proc. of 4th IPAC2013, Shanghai, China, May 13-17, 2013.

[27] W. Panofsky, SLAC Internal Report TN-63-57, (1963).

[28] V. Agoritsas, "Air Ionisation Chamber as Detector of the Beam Losses in the CPS Ring", Internal Report CERN MPS/Int.CO 66-23, (1966).

[29] J.R. Parker et al., "A Beam-Spill Monitor for LAMPF", IEEE Trans. on Nucl. Science Vol. 18 No. 3, (1971), p. 825-826.

[30] R.A. Lundy et al., "A System for Monitoring Proton Losses from the NAL Main Accelerator", IEEE Trans. on Nucl. Science Vol. 20 No. 3, (1973), p. 596-598.

[31] V. Agoritsas et al., "Aluminum Cathode Electron Multipliers: CERN TESTS", CERN MPS/CO Note 71-51, (1971).

[32] S. Schlögl et al., "A Beam Loss Monitor System for HERA", Proc. 15th Int. Conf. on high Energy Accel., Hamburg, (1992), p. 254-256.

[33] P. Odier, "A New Wide Band Wall Current Monitor", Proc. DIPAC2003, Mainz, Germany, 2003 pp.216

[34] W. Becker, "Advanced Time-correlated Single Photon counting techniques", Berlin Heidelberg: Springer, 2005.

[35] M. Uesaka et al, "Precise measurement of a subpicosecond electron single bunch by the femtosecond streak camera", Nuclear Instruments and Methods in Phys. Res. A 406 (1998) 371.

[36] O. Grimm, "Coherent Radiation Diagnostics for Short Bunches", Proc. PAC2007, Albuquerque, New Mexico, USA, (2007) pp.2653

[37] T. Watanabe et al, "Overall comparison of subpicosecond electron beam diagnostics by the polychromator, the interferometer and the femtosecond streak camera", Nuclear Instruments and Methods in Phys. Res. A 480 (2002) 315–327

[38] A. Feschenko et al, "The First Results of Bunch Shape Measurements in SNS Linac", Proc. LINAC04, Lübeck, Germany, 2004 pp.408

[39] P. Krejcik et al, "Commissioning the New LCLS X-band Transverse Deflecting Cavity with Femtosecond Resolution", Proc. IBIC13, Oxford, UK, 2013 pp.308

[40] S.P. Jamison et al, "Femtosecond Resolution Bunch Profile Measurement", Proc. EPAC06, Edinburgh, UK, (2006) pp.915

[41] W.P. Leemans et al, "X-ray Based subpicosecond Electron Bunch Characterization using 90o Thomson Scattering", Physical Review Letters 77, (1996), 4182

[42] B. Steffen et al., "Electro-optic time profile monitors for femtosecond electron bunches at the soft x-ray free-electron laser FLASH," Phys. Rev. ST Accel. Beams 12, 032802 (2009).

38

Chapter 7

Beam Parameter Specifications for Various Types of Accelerator

Name	Electron Positron Collider
Acronym	
WebPage	
Laboratory	
AcceleratorState	Not in operation
AcceleratorType	Synchrotron and Storage ring
AcceleratorPurpose	High energy experiments
ParticleTypes	e- , e+
Length-m	26600
EnergyMin-GeV/u	14
EnergyMax-GeV/u	103
Beam current [mA]	3
Single bunch current [mA]	≤ 0.7
EmitH-nm rad	25
EmitV-pm rad	250
BeamSizeH-um	$\sigma_x = \beta_x\, \varepsilon_x$
BeamSizeV-um	$\sigma_v = \beta_v\, \varepsilon_v$
Gamma	2800- 20000
BunchSpacing min.-µs	22
BeamLongSize-mm	
BunchLength-ps	5 – 50
UpstreamAcc	
RF Frequency [MHz]	352
RF peal voltage [MV]	
Harmonic number	31320
NbOfBunchesMax	4
Tune hor. / vert.	70.34 / 78.21
Energy spread	
Corrected Chromaticity hor./vert	
Betafunc. max hor. / vert / Dx [m]	12 / 12 / 2.2
Betafunc. min hor. / vert / Dx [m]	0.02 / 0.02 / 0
Critical photon energy [keV]	522
Damping times (h/v/l) [ms]	60 turns at top energy
Beam lifetime [h]	2.5 (Quantum lifetime)
Synchrotron tune vs *10^-3	

Name	Proton Synchrotron
Acronym	
WebPage	
Laboratory	
AcceleratorState	in operation
AcceleratorType	Synchrotron
AcceleratorPurpose	ParticlePhysics-FixedTarget; PreInjector
ParticleTypes	Pb 54+
Length-m	628
EnergyMin-GeV/u	0.072
EnergyMax-GeV/u	5.88
Beam current [mA]	
Single bunch current [# Ions]	1.2 * 10^8 / bunch
EmitH-mm mrad (2 sigma)	1
EmitV-mm mrad (2 sigma)	1
BeamSizeH-um	$\sigma_x = \beta_x \, \varepsilon_x$
BeamSizeV-um	$\sigma_y = \beta_y \, \varepsilon_y$
Gamma	1.08 − 7.3 (Gamma transition = 8)
BunchSpacing min.-ns	100
BeamLongSize-mm	
BunchLength-ns	11 (4 sigma)
UpstreamAcc	
RF Frequency [MHz]	80
RF peal voltage [MV]	
Harmonic number	169
NbOfBunchesMax	4
Tune hor. / vert.	6.18 / 6.21
Energy spread	01 * 10^-4
Corrected Chromaticity hor./vert	
Betafunc. max hor. / vert / Dx [m]	23.1 / 23.7 / 2
Betafunc. min hor. / vert / Dx [m]	12 / 12 / 0.5
BeamIn [s]	1.2
Damping times (h/v/l) [ms]	
Beam lifetime [h]	
Synchrotron tune vs *10^-3	

Name	ION Synchrotron
Acronym	
WebPage	
Laboratory	
AcceleratorState	planned
AcceleratorType	Synchrotron, Superconducting , fast ramp rate of 4 T/s, B_{max} = 1.9 T
AcceleratorPurpose	ParticlePhysics-FixedTarget; PreInjector
ParticleTypes	Protons and heavy ions U^{28+}, U^{92+}
Length-m	1083.6
EnergyMin-GeV/u	0.400
EnergyMax-GeV/u	2.7 (29 GeV for protons)
Beam current [mA]	5 x 10^{11} U^{28+} and 4 x 10^{13} p, 3 x 10^{10} U^{92+} in one machine cycle every seconds
Single bunch current [# Ions]	
EmitH-mm mrad (2 sigma)	ε_h = 6.4 at 2.7 GeV/u, 24 at 0.4 GeV/u
EmitV-mm mrad (2 sigma)	ε_v = 2.7 at 2.7 GeV/u, 10 at 0.4 geV/u
BeamSizeH-um	$\sigma_x = \beta_x \, \varepsilon_x$
BeamSizeV-um	$\sigma_v = \beta_v \, \varepsilon_v$
Gamma transition (GeV/c)	15.63
BunchSpacing min.-ns	
BeamLongSize-mm	
BunchLength-ns	50 - 100 (4 sigma)
UpstreamAcc	
RF Frequency [MHz]	1.1 − 3.2
RF total peak voltage [kV]	280, Gap voltage 0.03 − 20 kV
Harmonic number	10
NbOfBunchesMax	8
Tune hor. / vert.	Q_h=18.84, Q_v=18.73 (ion operation)
Energy spread	dp/p=1 %
natural Chromaticity hor./vert	-1.19 / -1.2
Betafunc. max hor. / vert / Dx [m]	19.0 / 19.1 / 1.76
Betafunc. min hor. / vert / Dx [m]	/ / -0.09
BeamIn [s]	0.5
Damping times (h/v/l) [ms]	
Beam lifetime [h]	
Synchrotron tune $vs *10^{-3}$	

Name	Synchrotron Light Source
Acronym	
WebPage	
Laboratory	
AcceleratorState	Operational
AcceleratorType	Storage ring with top-up injection
AcceleratorPurpose	Synchrotron Light Source User Facility
ParticleTypes	e-
Length-m	288
EnergyMin-GeV/u	2.4
EnergyMax-GeV/u	2.4
Beam current [mA]	400
Single bunch current [mA]	≤ 10
EmitH-nm rad	5
EmitV-pm rad	1 – 7
BeamSizeH-um	$\sigma_x = \beta_x\,\varepsilon_x$
BeamSizeV-um	$\sigma_v = \beta_v\,\varepsilon_v$
Gamma	4697
BunchSpacing min.-ns	2
BeamLongSize-mm	3.5
BunchLength-ps	35
UpstreamAcc	100 MeV linear Accelerator -> energy injector booster synchrotron
RF Frequency [MHz]	500
RF peal voltage [MV]	2.6
Harmonic number	480
NbOfBunchesMax	448
Tune hor. / vert.	20.41 / 8.67
Energy spread	0.858 * 10^-3
Corrected Chromaticity hor./vert	5 / 5
Betafunc. max hor. / vert / Dx [m]	23.1 / 23.7 / 0.35
Betafunc. min hor. / vert / Dx [m]	0.46 / 0.8 / 0
Critical photon energy [keV]	5.4
Damping times (h/v/l) [ms]	9 / 9 / 4.5
Beam lifetime [h]	3 - 10
Synchrotron tune *vs *10^-3*	1.9 – 4.8

Name	H- LINAC
Acronym	
WebPage	
Laboratory	
AcceleratorState	Operational
AcceleratorType	H- Linac ; superconducting
AcceleratorPurpose	Neutron user facility
ParticleTypes	H-
Length-m	251
EnergyMin-MeV	2.5
EnergyMax-GeV	1.0
BunchChargesMin [nC]	
BunchChargesMax [nC]	2
EmitHMin-mm.mrad	**0.2**
EmitHMax-mm.mrad	0.4 rms normalized
EmitVMin-mm.mrad	0.2
EmitVMax-mm.mrad	0.4 rms normalized
BeamSize H/VMax-mm	3 / 3
BeamSize H/VMin-mm	1 / 1
Beta x/y [m]	
Dispersion X / Y [m]	
AvailableRF-MHz	805
BunchSpacing-ns	1.24
BeamLongSize-ps	
SourceCurrentMin-μC/pulse	24
SourceCurrentMax-nC/bunch	
PulseLengthMin-ms	1
PulseLengthMax-ms	1
NbOfBunchesMax	837 200
RepetitionRateMin-Hz	60
RepetitionRateMax-Hz	60
Energy spread [MeV]	0.33